Improved analyses of the tapered inset dielectric guide antenna

Hannigan, A. B.

Award date:
2000

Awarding institution:
University of Bath

IMPROVED ANALYSES OF THE TAPERED INSET DIELECTRIC GUIDE ANTENNA

submitted by A.B. Hannigan

for the degree of PhD

of the University of Bath

2000

ProQuest LLC
789 East Eisenhower Parkway
P.O. Box 1346
Ann Arbor, MI 48106-1346

Acknowledgements

My greatest debt is to my supervisors, Dr. Steve Pennock and Dr. Peter Shepherd, whose help and advice throughout the whole of the project has been invaluable, and whose support eased my painful transition from industry back into an academic environment.

I must also thank Mr. Dave Hatten for the help he has provided with the practical aspects of the project, and Mr. Trevor Ryan for constructing the circuit boards.

In addition, I am most grateful to EPSRC who provided the financial support for this work, under reference 96306671.

Summary

The tapered inset dielectric guide antenna is a broadband radiating structure for use at microwave and millimetre wave frequencies. It is constructed from a tapered dielectric-filled slot cut into a ground plane, and is typically fed using rectangular waveguide. The structure is simple, rugged, lightweight and inexpensive to manufacture. The width and orientation of the main radiated beam is determined by the slot and ground plane geometry. For example, elevation plane beams from near-endfire to near-broadside can be produced.

This thesis is chiefly concerned with the development of analytical and numerical methods for predicting the far field radiation patterns of the tapered inset dielectric guide antenna. A new analytical method is presented that includes, for the first time, a full model of the fields on both the slot and ground plane surfaces. Results generated by this method compare well with measurements and show improvements over results obtained using an earlier analytical method.

Further, an improved numerical method is presented which dispenses with the approximations used by earlier methods, and additionally models the surfaces of the antenna mounting block and feed waveguide. Besides producing accurate radiation pattern predictions, this method provides insight into the operation of the structure. As such, the important role played by the ground plane of antennas with certain slot geometries has now been recognised.

A range of experimental results are also presented which study various characteristics of the antenna. The broadband and pure polarisation properties of the structure are demonstrated, and several novel antenna geometries are investigated. New types of feed are proposed and evaluated which allow the antenna to integrate directly with planar circuitry for the first time. A novel dual polarised antenna is described from which some interesting results have been obtained.

Publications Arising from this Work

1. A.B. Hannigan, S.R. Pennock, and P.R. Shepherd, "Analysis of Endfire Tapered Slot Antennas", in *Proceedings of IEEE High Frequency Postgraduate Colloquium*, Leeds, United Kingdom, September 1997, pages 106-111.

2. A.B. Hannigan, S.R. Pennock, and P.R. Shepherd, "Analysis of Tapered IDG Antennas in Finite Ground Planes", in *Proceedings of 28th European Microwave Conference*, Amsterdam, Netherlands, October 1998, volume 1, pages 36-41.

3. A.B. Hannigan, S.R. Pennock, and P.R. Shepherd, "The Estimation of Radiation Losses from a Tapered H-Guide: Application to the Analysis of IDG Antennas", in *Proceedings of IEE National Conference on Antennas and Propagation*, York, United Kingdom, March 1999, pages 328-331.

4. A.B. Hannigan, S.R. Pennock, and P.R. Shepherd, "Improved Modelling of Tapered IDG Antennas", in *Proceedings of 29th European Microwave Conference*, Munich, Germany, October 1999.

Abbreviations

2D	Two Dimensional
ABC	Absorbing Boundary Condition
BMM	Bounded Mode Matching
CF	Correction Factor
CP	Contour Path
CPFDTD	Contour Path Finite-Difference Time-Domain
CPW	Coplanar Waveguide
DFT	Discrete Fourier Transform
FDTD	Finite-Difference Time-Domain
IDG	Inset Dielectric Guide
IDG-TSA	Inset Dielectric Guide Tapered Slot Antenna
LSE	Longitudinal Section Electric
LSM	Longitudinal Section Magnetic
MLIDG	Microstrip Loaded Inset Dielectric Guide
PEC	Perfect Electric Conductor
PMC	Perfect Magnetic Conductor
RG	Ritz-Galerkin
RWG	Rectangular Waveguide
TE	Transverse Electric
TM	Transverse Magnetic
TRD	Transverse Resonance Diffraction
TSA	Tapered Slot Antenna
TWA	Travelling Wave Antenna
VBMM	Variable Bounded Mode Matching
VSWR	Voltage Standing Wave Ratio

Symbols

β	Propagation Constant
γ	Complex Propagation Constant
δ	Kronecker Delta
ϵ_0	Permittivity of Free Space
ϵ_r	Relative Permittivity
θ	Elevation Angle
κ	Singularity Factor
λ	Wavelength
λ_g	Guided Wavelength
λ_0	Free Space Wavelength
μ	Permeability
μ_0	Permeability of Free Space
ν	Singularity Factor
ρ	Charge Density
ϕ	Angle of Rotation
φ	Scalar Potential
χ	Singularity Factor
ω	Angular Frequency
Γ	Reflection Coefficient
$\mathbf{\Pi}$	Hertzian Vector Potential
Φ_e	Scalar Electric Potential
Φ_m	Scalar Magnetic Potential
c	Velocity of Light in Free Space
k_0	Free Space Propagation Constant
$S\{x\}$	$\sin(x)/x$

Contents

Chapter 1

Overview

1.1 Introduction

Modern microwave systems place many demands on their antenna subsystems. For instance, broadband operation is often sought. However, many antenna structures operate satisfactorily only over a narrow band due to limitations and variations in input match or beam steer with frequency. For example, the input match of the microstrip patch antenna is quite narrowband, whilst arrays of such elements either show a frequency dependent beam angle or require a well designed feed network in order to maintain the required inter-element phase relationships.

In addition to the need for broadband operation, a high degree of polarisation control is commonly required. This represents a problem when using the microstrip patch antenna. Physically, it is often desirable that a radiating element be compact, lightweight, rugged, and inexpensive to manufacture.

For applications where a moderate gain is required, a radiating structure which possesses the above mentioned features is the tapered inset dielectric guide antenna. This structure, shown in Fig. 1.1, is the subject of the work presented in this thesis.

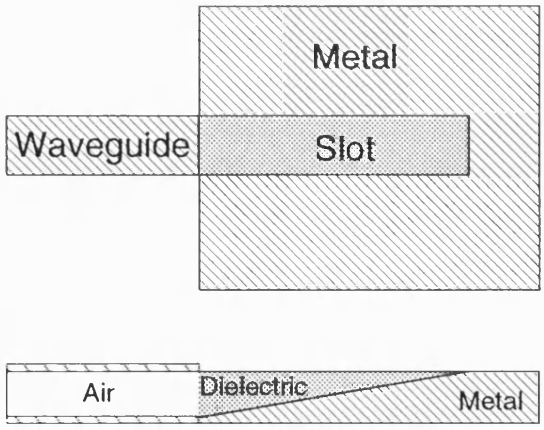

Figure 1.1: Structure of the tapered inset dielectric guide antenna. Top and side views.

The antenna consists of a rectangular waveguide connected to a tapered slot filled with dielectric, flush mounted in a ground plane. The tapered slot can be considered as a section of non-uniform inset dielectric guide, IDG. This simple structure produces a rugged, inexpensive antenna. Construction using spray metallised plastic components, rather than a solid metal block, would lead to an extremely lightweight structure. In addition, the antenna presents an aerodynamic profile when mounted in a surface, a feature frequently demanded in avionic and automotive applications.

The design of the taper exerts control over the orientation and width of the main radiated beam, and the slot dimensions can be altered to give nearly pure polarisations. In a narrow deep slot, nearly pure horizontally polarised radiation is obtained whilst a wide shallow slot gives nearly pure vertically polarised radiation.

The broadband nature of this antenna has long been established, with 2:1 and 4:1 bandwidths having been reported [1, 2]. The antenna input/output is a dielectric-filled waveguide, allowing relatively straightforward integration with other circuitry for realising complete systems. The tapered inset dielectric guide antenna therefore represents a viable solution to the problem of antenna selection for modern communication systems.

1.2 Objectives of the Thesis

This thesis focuses on the development of methods of analysis applicable to the tapered inset dielectric guide antenna. In previously published work two methods have been used to predict the far field radiation pattern of the structure; an analytical method based on the H-guide [3] and the numerical finite-difference time-domain (FDTD) method [4]. The H-guide method is based on the assumption that it is possible to represent the field distribution of the dielectric filled slot by that of an H-guide. This method has been shown to provide quick, reasonable predictions of the antenna far fields. However, comparison with measured results has demonstrated the superior accuracy of the FDTD method. The penalty for this increased accuracy lies in the extended computing times required by this method. Furthermore, certain antenna geometries, such as those where the slot flares out in width, can become unmanageable in terms of the computing resources required.

Given the foregoing, it is desirable that further consideration be given to analytical methods, such as the H-guide method, which can rapidly provide accurate results and which are suitable for use with a wide range of geometries. This forms the most important aim of the work carried out for this thesis. A new analytical method has been developed based on an improved H-guide model of the antenna structure.

A second objective is to develop the FDTD model of the IDG antenna. The existing implementation incorporates an approximate model of the finite ground plane, and does not process all parts of the antenna structure. The work presented in this thesis aims to remove these limitations and approximations.

A third, related, aim of the work has been to characterise the antenna and investigate its operation to a greater degree than has been done previously. This is, to some extent, necessary as part of the development of the theoretical models and to facilitate explanation of the results that are obtained from them.

1.3 Thesis Structure

The following paragraphs give a brief résumé of the contents and structure of the remaining chapters of the thesis.

Chapter 2 comprises an introduction to the subject matter considered in the thesis, and presents a survey of the relevant literature. The properties of IDG are discussed, and the techniques that have been used to characterise it are reviewed. A general consideration of tapered slot antennas is then given, and the place of the tapered IDG antenna within this category is highlighted. Methods for the analysis of waveguide discontinuities are also reviewed.

Building on the contents of Chapter 2, the state of the art in tapered IDG antenna theory is considered in detail in Chapter 3. Two methods for uniform IDG analysis are described, together with a method for characterising field behaviour close to metal edges. A general theory for aperture antennas is developed, and the two methods that have been applied to tapered IDG antennas in the past are discussed.

Chapter 5 develops the theory of the H-guide and carries out a study of the fields of IDG. The latter enables the validity of the H-guide model of IDG to be investigated.

As part of the development of an analytical method for the antenna, the power losses of the fundamental mode as it propagates on the IDG taper are sought. Chapter 4 considers in detail a mode matching scheme based on a bounded structure for analysing step discontinuities in waveguides. The technique is extended and applied to H-guide steps and tapers in Chapter 6

Chapters 7 and 8 detail the development of the new analytical and numerical models of the tapered IDG antenna respectively, and give comparisons between theoretical and experimental results. The models are further tested, and compared against each other, in Chapter 9, which also considers the effect of siting antennas

of both polarisations in a mounting surface. FDTD results are used in this chapter to reveal the field distribution around the antenna and its mounting block.

Chapter 10 contains a number of results, most of which are experimental, studying the characteristics of the tapered IDG antenna. New types of feed are proposed and evaluated. Antenna input impedance, gain, polarisation properties, and higher frequency operation are investigated. A novel dual polarised structure is described and some results presented.

Finally, Chapter 11 draws together the foregoing chapters with some concluding remarks. The main achievements of the work carried out are highlighted, as are those areas where further work could usefully be done.

1.4 Chapter Summary

The tapered IDG antenna has been identified as a viable structure for use in modern communication systems. The current situation as regards theoretical analysis of the antenna structure has been introduced. A requirement for an improved analytical method has been noted. An investigation into the development of such a method has been identified as the key objective of the work presented in this thesis.

Chapter 2

Review of Past Developments

The aim of this chapter is to give an introduction to the main subject areas that are considered in this thesis, and to provide a survey of the relevant literature. The chapter is split into three sections which deal with inset dielectric guide, tapered slot antennas, and the analysis of waveguide discontinuities respectively.

2.1 Inset Dielectric Guide

2.1.1 Introduction

The type of antenna under consideration in this thesis is constructed from a length of inset dielectric guide (IDG) of non-uniform cross section. Before examining the antenna structure itself, it is useful to consider the properties of uniform IDG as a transmission medium, and to review the methods that have been used to analyse it.

The structure of IDG is shown in Fig. 2.1. It consists of a slot filled with dielectric material, flush mounted in a ground plane.

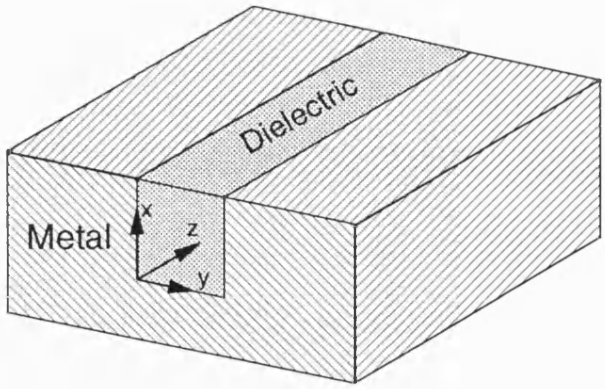

Figure 2.1: Structure of IDG.

IDG is a low loss transmission medium suitable for use at microwave and millimetre wave frequencies. It is a development of trapped image guide, which consists of a dielectric block located in a metal trough. Trapped image guide combines the low losses of image guide with improved field confinement at curved sections [5]. However, trapped image guide is not straightforward to manufacture. IDG was thus proposed as an easy-to-manufacture, and therefore lower cost, alternative to trapped image guide [6]. IDG provides a high degree of field confinement and low loss at discontinuities, allowing energy to be directed around reasonably tight bends.

IDG can be fabricated in a number of ways. The most obvious method is to cut a slot in a metal sheet or block and then fill it with dielectric. Either low melting point dielectric in liquid form can be poured into the slot, or a dielectric slab can be cut to the required dimensions before fitting into the slot. Equally, a plastic mould can be used which can be spray-metallised. Other options exist for prototyping work, especially at lower (i.e. X-band) frequencies. As part of the work for this thesis, IDG has been fabricated from plastic sheeting covered with aluminium foil. A wooden block has also been used instead of plastic sheeting.

Thus, the positive physical attributes of IDG are its strength, simplicity, light weight and its ability to be flush mounted into a surface.

2.1.2 IDG Fields

In general the modes of IDG are hybrid, having three magnetic and three electric components. However, the analysis of IDG can be significantly simplified if certain slot geometries are chosen. For wide shallow slots the Longitudinal Section Magnetic (LSM) five field approximation may be used. In a narrow deep slot the Longitudinal Section Electric (LSE) approximation can be applied [7]. By using these slot geometries, nearly pure polarisations can be obtained [8, 9].

2.1.3 Applications

Since IDG was originally proposed, a number of researchers have investigated variations on the basic guide structure for use in various applications. The following is a review of the most important work that has been carried out to date:

Linear Arrays: The polarisation properties of IDG can be exploited to produce linear arrays with very low cross polarisation. This has been done by laying conducting strips onto the guide surface. Currents are induced in the strips leading them to act as dipole radiators. In [9] transverse strips were laid on a deep slot IDG to couple to the fundamental LSE mode, whilst in [8] longitudinal strips were laid on the surface of shallow slot IDG in order to couple with the fundamental LSM mode. This principle has been extended to a two-dimensional LSM polarised array [10].

Microstrip Loaded IDG (MLIDG): This structure was proposed by Rozzi *et al.* [11]. It consists of a longitudinal strip placed on the air/dielectric interface of IDG. The proposal of MLIDG was a result of the work on linear arrays cited above. Indeed, the LSM polarised linear array can be considered as consisting of a cascade of alternating MLIDG and IDG sections. MLIDG could be used to feed such an array, and would seem to be suitable for integration with other planar

structures such as microstrip. Additionally, it may offer an alternative to microstrip at millimetre wave frequencies. MLIDG supports two types of mode; microstrip-type modes due to the presence of two conductors, and dielectric modes similar to those of IDG. A rigorous analysis has been carried out in [12]. An extension to the MLIDG structure, where a multi-layer, multi-conductor circuit is contained within an IDG slot is considered by Izzat *et al.* in [13].

Multi-layer Structures: In [14, 15] an investigation into the influence of the dielectric filling on the IDG monomode bandwidth is carried out. It is demonstrated that the monomode bandwidth with a single dielectric filling may be made greater than that of comparable metal rectangular waveguide (RWG) by appropriate choice of permittivity of the dielectric. Additionally, it is shown that by using two dielectric layers in the IDG slot, the monomode bandwidth can be greater than that of a standard double ridge waveguide. Twin layer IDG, therefore, is an attractive medium for wideband applications at microwave and millimetre wave frequencies.

Ferrite Loaded IDG: Analysis of a double-layered IDG containing a magnetised ferrite has demonstrated that the non-reciprocity of the propagation constants can be controlled by varying the relative permittivity of the dielectric layer [16]. Such a structure is suitable for application in non-reciprocal phase shifters. Further work on ferrite loaded IDG in [17] has shown that much higher differential phase shift values can achieved using three-layer structures.

Coplanar Waveguide (CPW) Loaded IDG: This structure was proposed by Fan and Pennock in [18], and consists of CPW placed on the surface of IDG. It is claimed that this arrangement combines the advantages of CPW and IDG whilst shedding some of the problems associated with CPW. The advantages of CPW loaded IDG over standard CPW include the removal of the need for air bridges for ground equalisation, improved mechanical tolerance and heat sinking, better field confinement, suppression of surface modes, and a wide range of possible characteristic impedances due to the large number of degrees of freedom available

in the guide design.

Coupled IDG: Various investigations have been carried out into the characteristics of coupled lines in order to facilitate the design of directional couplers in IDG. Pennock *et al.* [19] have performed an analysis of coupled IDG for the limiting cases of deep and shallow slots. In [20], Fan and Pennock present an analysis that removes these limitations. The results of their investigation show that with appropriate choice of slot depth, the IDG coupler shows quite broadband flat coupling characteristics. Broadside coupled strip IDG has been investigated in [21] and [22]. Fan and Antar have recently considered a number of more elaborate coupling structures [23, 24].

Detector Diode Mounting: Pennock *et al.* [25] have shown that a detector diode can be mounted in deep slot IDG, across the narrow slot dimension, as can be done in RWG. Diode performance is comparable with that achievable in RWG. Diode mounts such as this enable the fabrication of simple receiver front ends entirely in IDG (i.e. antenna, coupler, detector/mixer) without having to introduce lossy transitions to other media.

The use of IDG in endfire antennas has been omitted from the above list. This particular application is considered in detail in Section 2.2.3.

2.1.4 Methods of Analysis

A number of techniques have been employed to analyse the various forms of IDG. These are summarised below.

Effective Dielectric Constant Method: Zhou and Itoh [26] used the effective dielectric constant (EDC) method to analyse trapped image line. In their analysis, IDG is used as an equivalent structure to trapped image line, though it is not specifically identified as a viable transmission structure by the authors. The transverse

resonance condition is then applied at the air/dielectric interface of the equivalent structure. Reasonable values for the propagation constant of the fundamental mode were obtained using this method.

Transverse Resonance Diffraction: An important feature of IDG is the singularity in the transverse fields due to the 90° metal edges of the structure. Any accurate analysis must take this feature into account. The transverse resonance diffraction (TRD) method [6] was the first rigorous analysis of IDG to be carried out. TRD takes account of the field singularities whereas the EDC technique ignores them.

TRD is a space domain variational analysis in which sets of integral equations are derived from potential functions by application of the relevant boundary conditions. These sets of equations are solved for the propagation constant. This is done using Galerkin's method [27, chapter 7], with the unknown function being expanded by a suitable set of basis functions. By using Gegenbauer polynomials as the basis terms, the field singularities at the 90° edges are taken into account and convergence is rapid. Using this method accurate values for the propagation constants of the first few discrete modes were obtained [6].

Following on from the above work, TRD was used by Rozzi and Ma [7] to characterise the continuous modes of LSE and LSM polarised IDG.

The TRD technique has also been used to analyse coupled IDG under LSE and LSM polarisations [19], twin-layer IDG [14], and microstrip loaded IDG [12]. Izzat *et al.* [13] presented a generalised TRD method for analysing multi-layer, multiconductor circuits housed within IDG.

Characteristic Green's Function Approach: In [28], Rozzi and Sewell developed a method for the derivation of the continuous spectrum of open waveguides of non-separable cross section in full hybrid form. Previous work on the continuum of IDG ([7], see above) used an expansion in plane waves of the air space above the

guide without enforcing satisfaction of boundary and edge conditions on each individual spectral component. In [29], the characteristic Green's function approach is applied to the specific geometry of IDG, and the continuous spectrum is rigorously derived.

Mode Matching: Ma *et al.* [30] have developed a simplified model of IDG to which a mode matching technique is applied. The model is based upon the fact that the transmission of power in IDG is confined mostly around the slot, so that if lateral metal walls are placed at some distance away from the slot, the propagation characteristics of the guide are little affected. The fields in both the slot and in the air can then be expanded in terms of parallel plate modes, and the characteristic equation can be obtained using the transverse scattering matrix technique [31].

Compared to TRD this analysis is straightforward, and it demonstrates rapid convergence. The method is able to generate values for the bound mode propagation constants that are within 1% of those calculated by TRD in [6]. However, the authors concede that modelling of the fields above the guide and of the singularities at the guide edges is done better by TRD.

It is claimed that this technique is easy to modify for variations on the basic IDG structure. Indeed, the method has been applied to IDG with a trapezoidal shaped slot and the results from this show that some manufacturing variation in the slot shape does not make much difference to the guide propagation constants. This is an important feature of IDG, and is particularly useful when fabricating components for use at millimetre wave frequencies.

Extended Spectral Domain Method: The spectral domain method for calculating the propagation constants of microstrip lines was originally proposed by Itoh and Mittra [32], and was successfully applied to several microstrip structures [33, 34]. The method is based on the application of Galerkin's method in the finite Fourier transform (spectral) domain. Itoh later generalised the tech-

nique [35]. In general terms, there is much similarity between the spectral domain and TRD methods. In both cases, sets of integral equations are derived from potential functions. In the (space domain) TRD approach, these integrals are solved directly by Galerkin's method, with the unknown functions being expanded by a suitable set of basis functions. In the spectral domain approach, the integral equations are Fourier transformed before solution by Galerkin's method.

More recently, the spectral domain method was extended and used to analyse a number of IDG structures, including ferrite loaded IDG [16, 17], coplanar waveguide loaded IDG [18] and coupled inset dielectric guides [21, 22, 20, 23, 24]. Work on this technique still continues, with further enhancements having been published recently by Fan and Antar [36].

Finite Difference Time Domain Techniques: The finite-difference time-domain (FDTD) method was introduced by Yee [37], and is a numerical technique used to solve electromagnetic scattering problems. The starting points for an FDTD analysis are the two Maxwell curl equations in derivative form in the time domain. These are expressed in a linearised form as finite-difference equations. This is possible as the problem space is broken into many cells. The FDTD algorithm works on the assumption that the field behaviour between adjacent cells can be approximately described by a linear function. The waves propagating from a source are modelled by repeatedly iterating these linearised equations. Time stepping is continued until steady state conditions are reached. Good discussions of the basic FDTD method and its applications are given in [38] and [39].

The FDTD equations cannot be applied to the nodes on the outer boundaries of the computational space as certain field components required for the finite-difference equations fall outside it and so are unavailable. Absorbing boundary conditions must be enforced such that outgoing waves are not reflected back into the problem space, thereby distorting the solution. There is much literature discussing FDTD boundary conditions, for example [40, 41, 42].

The advantages of FDTD lie in its being both rigorous and very versatile, as well as being straightforward to apply. It is applicable to conducting, dielectric or magnetic bodies, which may be either homogeneous or inhomogeneous, and which may have arbitrary shapes.

Two dimensional FDTD techniques have been used to analyse a wide range of structures, with a three dimensional technique having more recently been applied to open dielectric structures [43]. Antenna structures have also been modelled [44, 45, 46].

A three dimensional Finite Difference Time Domain method has recently been developed and applied to deep and shallow slot inset dielectric guide, and has also been used to characterise the rectangular waveguide to IDG transition [47, 48]. Good agreement has been noted between FDTD, TRD, and experimental results [47]. Whilst the TRD and extended spectral domain methods discussed above have been found to give accurate results for IDG structures with uniform cross sections, they become rather more awkward to apply for structures with non-uniform cross sections, such as flared antennas [3]. This increased difficulty in the application of the earlier techniques was the motivating factor for the development of an FDTD code, the flexibility of which is ideal for such applications.

H-Guide Analysis: As has been stated, the TRD and extended spectral domain methods become more difficult to implement for IDG structures with non-uniform cross sections. FDTD gives good results, and is relatively easy to implement for such structures, but is very demanding in terms of computing resources, and run times can be long. With these problems in mind, an approximate analytical method based on the so-called H-guide has been developed.

The H-guide was first proposed by Tischer [49] as a low loss microwave transmission medium which would simplify the manufacture of complex microwave circuits. The structure of H-guide is shown in Fig. 2.2(a), in cross section.

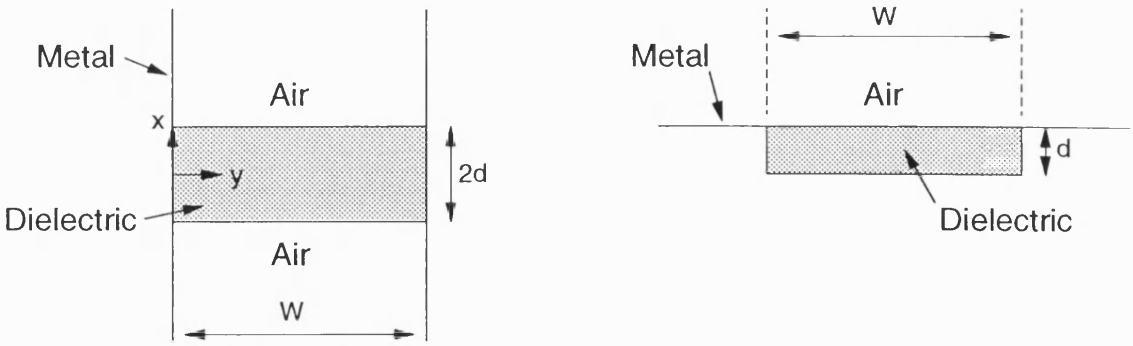

Figure 2.2: (a) Structure of H-guide, (b) Alternative structure.

The analysis of H-guide was further developed by Tischer [50] and by Walter [51]. The modes of H-guide, together with those of the closely related non-radiative dielectric (NRD) guide are studied in [52]. The H-guide analysis is applicable to a reasonable approximation to the structure shown in Fig. 2.2(b), which is effectively IDG, so that the H-guide analysis can be used to approximately characterise IDG. The analysis is straightforward and can be performed very rapidly by computer. The H-guide analysis, therefore, offers a rapid and reasonably accurate alternative to FDTD for use with IDG structures with non-uniform cross sections. Application of this method to antenna geometries has been carried out and reasonable results have been achieved when compared to FDTD, extended spectral domain, and experimental results [3, 4, 53].

The accuracy of the H-guide model is clearly limited by the fact that, like the EDC technique, the field singularities are not modelled due to the assumption that there are vertical metal walls on either side of the slot.

2.2 Tapered Slot Antennas

2.2.1 Introduction

The tapered IDG antenna is a member of the class of structures known as travelling wave antennas (TWAs). A TWA can be defined as an antenna for which the fields that produce the radiation pattern may be represented by one or more travelling waves [51]. Based on this definition, a variety of structures can be classified as endfire TWAs. The simplest of these is the long wire antenna. Other common examples are dielectric rod, corrugated rod, and helical antennas.

Tapered slot antennas (TSAs) are a sub-class of endfire TWAs. In recent published material, the term tapered slot antenna has generally been used to refer to printed planar structures. Structural differences aside, the tapered IDG antenna shares many characteristics with such planar TSAs. Indeed, for applications where one could contemplate the use of a tapered IDG antenna, it is likely that a planar TSA could also be considered as an alternative solution. To some extent, the current research into IDG antennas was motivated by the recent activity in planar TSA research. In order to emphasise and reinforce its relationship to the planar TSA, the IDG tapered slot antenna is hereafter referred to as the IDG-TSA.

The objective of this section of the thesis is firstly to review the development history of some of the common types of planar TSA and to summarise their properties. Secondly, the state of research into the IDG-TSA is reviewed and its characteristics are considered and compared to those of planar TSAs.

2.2.2 Planar Tapered Slot Antennas

Structure

Research interest in planar endfire TSAs was revived by Gibson [54] with the introduction of the Vivaldi antenna. This structure consists of an exponentially tapered slot cut in a thin metal film on a dielectric substrate. Some common variations on this theme include the linearly tapered slot antenna (LTSA) [55] where the exponential taper of the Vivaldi is replaced by a linear taper, and the partially constant width slot antenna (CWSA) [56] where a linearly tapered section is followed by a constant width section. A range of further taper profiles have been investigated experimentally more recently in [57].

A currently popular type of planar antenna is the microstrip patch. One can see that the planar TSA maintains all the structural advantages of the patch, i.e. low profile, light weight, low cost construction, and apparent ease of integrability into microstrip systems. Additionally, the planar structure and endfire properties of the TSA make it suitable for building into very compact arrays. An important advantage of the TSA over the patch is the much wider operating bandwidth that it offers.

Mode of Operation

In general, a TWA can be classified as a slow wave or a fast wave structure. In the slow wave case, the phase velocity v_p of the travelling wave is less than the velocity c of a plane wave in free space. So $v_p < c$ or $\beta > k_0$, where β and k_0 are the propagation constants of the travelling wave in the medium and in free space respectively. For fast wave structures, $v_p > c$ and $\beta < k_0$.

Considering for a moment uniform rather than tapered structures, waves travelling

thereon may be classed as either leaky waves or surface waves. Leaky waves continuously lose energy to radiation as they move along the medium. Most fast wave antennas are leaky wave structures. On the other hand, surface waves propagate along an interface between two media without loss of energy. The wave is bound to the surface, and only loses energy at discontinuities. A characteristic of surface waves is that their velocity is less than that in the surrounding medium. As such, slow wave antennas are usually surface wave structures. The terms leaky wave and surface wave are usually applied to uniform structures.

The radiation mechanism of the TSA is not yet fully understood [57]. Opinion is divided on whether radiation is based on leaky waves [54] or surface waves [56]. Different structures may indeed produce radiation by different means. Certainly, those antennas where there is no supporting dielectric substrate must be leaky wave structures. Indeed, a given tapered structure may support both surface and leaky waves as the propagation constant varies along the taper.

Properties

One advantageous feature of planar TSAs is their good performance over a wide frequency band. Gibson [54] reported satisfactory operation of a Vivaldi antenna over a bandwidth extending from 2GHz to 40GHz. In addition to having a wider bandwidth than a comparable microstrip patch, reported planar TSAs also display narrower beamwidth and higher gain [58]. Despite the planar nature of the TSA, it can produce symmetrical radiation patterns. These structures are suitable for use at millimetre and sub-millimetre frequencies [59, 60], due in part to their compact geometry and ease of integration with other planar devices.

The antenna properties - gain, radiation pattern, cross-polarisation - are dependent on the field distribution on the antenna surface. These may be controlled by varying the physical properties of the structure, such as the length, width, substrate

permittivity and thickness, and the taper shape.

A limitation on the use of the planar TSA in broadband applications is the difficulty of obtaining a sufficiently broadband transition onto the antenna at the feed. The feed section of a planar TSA is usually a slot-line. Integration into a system often requires a transition to microstrip. Early designs made use of an existing microstrip to slot-line transition [61] but this is band-limited due to the inclusion of a $\lambda/4$ length of line in the design. Various improved feeds for TSAs have been proposed [62]. A smooth transition between microstrip and slot-line, via parallel strip-line, is achieved by the so-called antipodal Vivaldi antenna [63] whereby metallisations on either side of the substrate are flared in opposite directions in order to form the tapered slot. This transition has been shown to perform well and to restore wideband characteristics to the combined structure [64].

Another problem area with planar TSAs is the level of cross-polarised radiation. The antipodal Vivaldi antenna has been found to exhibit high cross-polarisation, a figure of -11dB was quoted in [65] whilst variation between -5 and -15dB was observed in [64]. The cross-polarisation characteristics of the standard Vivaldi antenna are better than the antipodal structure but are still not good. In [64, 66], measured cross-polarised radiation was reported to be generally between -10 and -20dB, but sometimes rising to be close to the co-polarised level. In the latter reference, the cross-polarisation levels were much higher than FDTD predictions and were considered to be due to difficulties in manufacturing a perfectly symmetrical antenna and feed arrangement.

More recently, a balanced antipodal Vivaldi antenna has been proposed [64] to try to combat cross-polarisation problems, which are attributed to a skew in the slot fields close to the throat of the flare. The new structure adds a further dielectric layer together with an additional layer of metallisation. The structure has demonstrated lower cross-polarisation levels, whilst maintaining the wideband characteristics of the antipodal antenna. Good performance was observed over a 3:1

band, with approximately equal E- and H-plane beamwidths and cross-polarisation typically below -20dB. Whilst these antennas seem to give good performance, the increased complexity of the manufacturing process must be borne in mind.

Methods of Analysis

Analytical methods for use with TSAs have been slow to develop, with design methods being essentially empirical for a number of years. The analysis of these antennas is complex due to the non-uniformity of the fields in the tapered slot.

The method of Janaswamy *et al.* [67] was the first analytical method to be proposed. This two-step method firstly determines the tangential E-fields in the slot using a spectral domain technique, before obtaining the radiated far fields using a Green's function. The continuously varying slot profile is approximated by a series of steps, so that the problem can be considered as a set of uniform lines connected end to end. The main problem with this stepped approximation method is that it does not take into account the finite extent of the ground plane. To overcome this problem, a technique based on the moment method (MM) was proposed in [68]. This method is accurate for air-dielectric antennas but approximate for those antennas with a supporting dielectric substrate.

Ndagijimana *et al.* [69] have applied a three-dimensional transmission line matrix (TLM) technique to a TSA. This appears to be the first published numerical analysis of a TSA, and provides some interesting physical insights into the antenna operation. However, no comparisons to measurement were made in order to validate the method.

The finite-difference time-domain (FDTD) method has been applied to single and double flare Vivaldi antennas, and to single and arrayed 'quad' elements by Thiele and Taflove [66] and to the balanced antipodal Vivaldi antenna by Langley *et al.* [64]. Good results have been obtained using this method.

Of the above methods, MM, TLM, and FDTD require significant computing resources and are better suited to shorter structures where run times are less prohibitive. Only the stepped approximation technique can provide reasonably accurate results rapidly.

2.2.3 Inset Dielectric Guide Tapered Slot Antennas

Structure

The structure of the IDG-TSA has already been introduced (Fig. 1.1). Research was carried out in the 1950s by Stephenson and Walter [1] and by Eberle *et al.* [2] into a structure similar to the IDG-TSA. At this stage inset dielectric guide had not been 'invented' so the antenna was described as being constructed from a tapered dielectric loaded rectangular waveguide with a broad wall removed. Both tapered depth and flared width structures were examined.

Recently, there has been renewed interest in these structures. As has already been mentioned, this is due in part to the general increase in research interest in planar antennas. In addition, as applications at millimetre wave frequencies are now more common, there will be an increasing requirement for antennas that can operate at these frequencies. IDG is known to be a suitable transmission medium for millimetre wave frequencies. It is natural, therefore, that radiating structures that can be integrated with it should be investigated.

Recent work on the IDG-TSA has been carried out by Stoiljković *et al.* both at X-band [3, 4] and Ka-band [53] frequencies. The ease of manufacture of IDG and its relative tolerance, in terms of performance, to manufacturing variations makes it particularly attractive as a millimetre wave antenna medium.

Mode of Operation

The IDG-TSA is a slow-wave structure. Thus, the structure radiates due to perturbation of the surface wave by the discontinuities introduced by the depth taper and/or width flare. By tapering the IDG depth down to a point, the discontinuity at the end of the slot is minimised and so back radiation is reduced.

Properties

The radiation patterns generated by the IDG-TSAs investigated to date are near-endfire in the elevation plane. Pure endfire operation is not possible due to the effect of the ground plane. As with the planar TSAs discussed in the previous section, the antenna structure by itself is capable of wideband operation. The practical bandwidth is limited mainly by the characteristics of the feed structure and by the discontinuity at the beginning of the slot.

Stephenson and Walter [1] noted that the measured radiation patterns differed somewhat from those predicted by simple theory. This discrepancy was attributed firstly to the effect of the finite ground plane and secondly to the discontinuity at the feed. To characterise the first of these effects a useful approximate theoretical model was proposed, and later elaborated upon in [51]. Attempts were made to reduce the latter effect by the use of discontinuity minimisers at the feed. These investigators constructed a large-aperture antenna which produced a satisfactory pencil beam over a 2:1 bandwidth with sidelobes in the horizontal pattern at least 20dB down. The VSWR was less than 1.4 over the 2:1 band with a discontinuity minimiser fitted, or less than 2.2 without.

Eberle *et al.* [2] further developed the design and obtained a moderately directive pencil beam over a 4:1 frequency band. Both horizontally and vertically polarised forms of the antenna were considered. The pure polarisation properties of IDG

would lead one to expect these antennas to exhibit low cross-polarisation when compared to planar TSAs. Eberle *et al.* report that for a vertically polarised structure, cross-polarised radiation was 15dB below the co-polarised component, although no figures are given for a horizontally polarised antenna.

The research to date indicates that feeding problems with the IDG-TSA are less acute than with planar TSAs. The use of discontinuity minimisers in order to obtain a reasonably wideband input VSWR has already been mentioned. Equally, a rectangular waveguide to deep-slot IDG transition utilising a tapered dielectric section has been demonstrated in [6] to give a VSWR of less than 1.12 at X-band frequencies. Also, integration of IDG with other planar structures seems feasible [12], raising the possibility of a microstrip feed. It would be possible to integrate an IDG-TSA with a complete front-end receiver system fabricated from IDG, as IDG couplers [19, 20] are available and detector/receiver diodes can be mounted in it [25].

Methods of Analysis

To date, analytical methods have concentrated on long-aperture, vertically polarised structures.

Two theoretical analyses have so far been used to predict the IDG-TSA radiation pattern. In [3] a two-step method is described. In the first step the electric field distribution in the slot is obtained, and in the second step the far fields radiated by the equivalent magnetic current in the slot are calculated by breaking the aperture into a large number of small rectangular elements. The aperture distribution is determined in one of two ways; either using a spectral domain method or by approximating the IDG by an H-guide. FDTD has also been applied to the IDG-TSA [4, 53].

The above methods include the simple approximate technique proposed by Wal-

ter [51] to take account of the finite size of the ground plane. Each of the methods has appeared to provide reasonable results when compared to measured data, with FDTD being the most accurate but most demanding in terms of computing time and resources.

These methods form the starting point for the theoretical aspects of the work presented in this thesis. Further comment upon them will be suspended until Chapters 7 and 8, where comparison with more recent results will allow greater insight into both the characteristics of the IDG-TSA and into the efficacy of the methods.

2.3 Analysis of Waveguide Discontinuities

2.3.1 Introduction

As part of the development of an analytical method for predicting the characteristics of the IDG-TSA it was considered desirable to assess ways of quantifying the mode conversion occurring on the IDG taper. It is important to do this in order to provide data on how the amplitude of the first bound mode on the structure decays as it passes along the aperture due to transfer of energy to other bound modes and to radiation.

The methods available to analyse a waveguide taper can be divided into two broad categories. The first set of methods are those that have been developed to analyse transverse steps in waveguides. These include mode matching and integral-equation techniques. Clearly such methods can be used for taper analysis by breaking the taper into a cascade of steps. The second set of methods may be referred to as differential equation techniques. These methods have been developed specifically for application to continuously varying waveguide profiles such as tapers. The next

two sections review some of the important contributions to the development of both sets of techniques with the eventual aim of selecting methods suited to the analysis of the IDG taper.

2.3.2 Analysis of Transverse Steps in Waveguide

The waveguide discontinuity problem is very common in microwave engineering and so has received much attention over the years. The equivalent circuits of a large number of configurations were calculated in the period 1940 to 1950 by a variety of analytical techniques [70]. In a small number of cases, exact solutions are available using the integral-transform technique, but approximations are usually necessary. Of the early approximate techniques the variational and integral-equation approaches have proved useful [71, 72].

Problems with these early methods include the complexity of their formulation and the difficulty of using them for the case of a discontinuity where more than one propagating mode exists [73]. These techniques were tailored towards producing solutions that could be obtained by hand calculation. This usually necessitated the inclusion of a number of approximations. The availability of reasonably powerful digital computers from the mid 1960s onwards allowed less approximate techniques to be employed which were simpler in their formulation and were able to cope with multiple modes, but required long and repetitive calculations to be carried out. A class of techniques falling into this category are known as mode matching methods.

In [74], Clarricoats and Slinn proposed a mode matching method applicable to small steps in the dielectric loading of a circular waveguide. Transverse modes are matched at the discontinuity and the orthogonality condition is used to derive two infinite sets of equations in the mode amplitudes. These equations are truncated for solution on a computer. Clarricoats and Slinn extended the method in [70] to a wider range of discontinuities in closed waveguides. Masterman [73] proposed

modifications to allow mode matching to be applied to thin irises.

Extension of the mode matching technique to open waveguides, such as the dielectric slab and IDG, is not straightforward. The difficulties arise from the infinite cross section of the open guide and from the necessity of including the infinite continuum of radiation modes. Mode matching is not therefore ideally suited to the open waveguide problem. Certainly, an exact solution does not appear possible. However, various approximate methods have been proposed.

Marcuse [75] proposed an approximation to calculate the radiation loss at a small step in a monomode dielectric slab waveguide. This is then extended to tapers by discretising the boundary. Given the limits of its application, this method provides satisfactory results.

Clarricoats and Sharpe applied the mode matching method to a discontinuity in a planar surface waveguide in [76]. Their approach assumes that the waveguide step is surrounded by a finite layer of cladding of a lower permittivity than the waveguides. By judicious choice of permittivities the authors show that coupling to radiation is small and can be neglected. Accurate results are obtained using this simple method but it becomes invalid if the discontinuity is surrounded by air, due to the increased coupling of energy to the radiation spectrum. As such, this method is of little use for antenna structures. Hockham and Sharpe [77] applied an integral-equation method to the same problem and their results show agreement with those in [76]. However, the integral-equation method is still valid for a step surrounded by air. Backward radiation from the junction is neglected in this method. This is justified as it is known that the radiation pattern of this type of discontinuity is predominantly in the forward direction [78].

Mahmoud and Beal [79] extended the mode matching method of Clarricoats and Slinn to open waveguides in a more general manner. The infinite integrals in the equations produced by the mode matching are converted into discrete summations

by expressing the radiation mode amplitudes in terms of known functions (Laguerre polynomials). One advantage of using Laguerre polynomials is that their form is such that they effectively and efficiently model the physical situation. As the order of the polynomial increases, its decay with wavenumber becomes slower. Hence, the part of the continuous spectrum corresponding to high values of wavenumber, i.e. the evanescent modes with β imaginary, will be effectively represented by the higher order Laguerre functions.

A rigorous analysis of a step discontinuity of arbitrary size in a planar dielectric slab was presented by Rozzi [80]. This method is based on an extension of the Ritz-Galerkin (RG) variational approach previously expounded by Rozzi in a number of papers ([81, 82] for example), which had been developed for application to closed systems. In this technique, Laguerre polynomials are chosen as the basis functions for the expansion. The method is extended in [83] to cascades of step discontinuities.

Brooke and Kharadly [84, 85] proposed a 'variable bound' method based on mode matching that has shown close agreement with the results obtained by Rozzi using the RG approach. In this method, the dielectric waveguide step is bounded by perfect electric or magnetic conductors, and the continuous spectrum is thus discretised. The equivalence between the modes of the open and bounded structures is shown. This technique has the advantage of being mathematically less complex than most other methods, and it provides some degree of physical insight into the problem. The method was later used to calculate the radiation pattern produced by steps in dielectric waveguides [86].

2.3.3 Differential Equation Techniques (Taper Analysis)

A number of techniques fall into this category. They have been proposed by different researchers and carry various names. These include Coupled Mode Theory, the

Cross Section Method, and the Theory of Local Modes. The methods are in general similar, and have the common feature that the analysis results in sets of differential equations containing terms that may be referred to as coupling coefficients.

An early contribution to the theory was made by Reiter [87], who showed that the fields in a waveguide with non-uniform cross section can be represented by an infinite set of modes. The waveguide can be considered as having an equivalent circuit consisting of an infinite number of transmission lines, each of which supports a single mode and which are coupled by transformers. Reiter expressed the transverse fields in the waveguide, $\mathbf{E}_t$ and $\mathbf{H}_t$, as a sum of uniform waveguide modes corresponding to a uniform waveguide with the same cross section as the non-uniform guide at that point:

$$\begin{aligned} \mathbf{E}_t(x,y,z) &= \sum_{m=1}^{\infty} V_m(z)\mathbf{e}_m(x,y,z) \\ \mathbf{H}_t(x,y,z) &= \sum_{m=1}^{\infty} I_m(z)\mathbf{h}_m(x,y,z) \end{aligned} \tag{2.1}$$

where $\mathbf{e}_m$ and $\mathbf{h}_m$ are the uniform waveguide modes, z is the direction of propagation, and the amplitude terms $V_m(z)$ and $I_m(z)$ are equivalent voltages and currents.

Equations for the transverse fields can be derived from Maxwell's equations by resolving the $\mathbf{E}$ and $\mathbf{H}$ fields and the Hamiltonian operator into longitudinal and transverse components. The longitudinal components can then be eliminated from Maxwell's equations to yield:

$$\begin{aligned} -\frac{d\mathbf{E}_t}{dz} &= j\omega\mu(\mathbf{H}_t \times \mathbf{z}_0) - \frac{1}{j\omega\epsilon}\nabla_t \cdot [\nabla_t \cdot (\mathbf{H}_t \times \mathbf{z}_0)] \\ -\frac{d\mathbf{H}_t}{dz} &= j\omega\epsilon(\mathbf{z}_0 \times \mathbf{E}_t) - \frac{1}{j\omega\mu}\nabla_t \cdot [\nabla_t \cdot (\mathbf{z}_0 \times \mathbf{E}_t)] \end{aligned} \tag{2.2}$$

Application of orthogonality conditions to these equations eventually leads to the following system of differential equations in the unknown equivalent voltages and currents [88]:

$$\begin{aligned} \frac{dV_m}{dz} &= -j\beta_m Z_m I_m + \sum_{n=1}^{\infty} T_{mn} V_n \\ \frac{dI_m}{dz} &= -j\frac{\beta_m}{Z_m} V_m + \sum_{n=1}^{\infty} T_{nm} I_n \end{aligned} \tag{2.3}$$

where β_m and Z_m are the propagation constant and impedance of the mth mode. The coupling coefficients T_{mn} describe the coupling between the nth and mth modes, and are defined by the following integral across the guide cross section:

$$T_{mn}(z) = \iint_S \frac{d\mathbf{e}_m}{dz} \cdot \mathbf{e}_n \, dx \, dy \tag{2.4}$$

The set of equations (2.3) are known as the Generalised Telegraphist's equations.

The above theory was originally proposed for use with closed non-uniform waveguiding structures. The formulation has been extended to open structures where radiation modes also need to be accounted for. Such an extension has been presented by Snyder [89] and in [90] Marcuse gives a lucid description of coupled mode theory for optical waveguides. He performs an expansion of the fields of a non-uniform guide in terms of forward and backward travelling waves, rather than the equivalent voltage and current representation favoured by Reiter and others. These two sets of amplitude terms are related through simple relationships [91].

In parallel with the above work, researchers in the Soviet Union were working along similar lines. Katsenelenbaum [92, 93] proposed the cross-section method whereby the fields at any point in a non-uniform waveguide are represented by a superposition of the fields of a regular waveguide of the same cross section as the non-uniform guide at that point. The amplitudes of the modes of the uniform

guides satisfy a set of differential equations, the coefficients of which are referred to as coupling coefficients. Given this description of the method, it is clear that it is broadly similar to the methods described above. The cross section method is discussed in detail in a recent book [94].

The work of Katsenelenbaum was extended in the monograph by Shevchenko [78]. In this work, the cross section method is used as the basis for an analysis of open waveguides. Rozzi refers to the method of Shevchenko as the local modes approach, and has applied it to curved dielectric ridge waveguides [95, 96]. The local modes method results in sets of equations similar to those derived by Marcuse in [90], which are considered in more detail in Chapter 4.

Various authors have applied coupled mode theory to a number of (mostly closed) structures. Saad *et al.* [97] presented a general computer analysis of gradually tapered waveguides of irregular cross section. In [98] Mirshekar-Syahkal and Davies proposed a combination of coupled mode theory and the spectral domain approach to analyse general tapered planar transmission lines. In this paper some simplifications are made which allow a closed form solution for the coupled mode equations to be obtained. These simplifications include considering only one forward and one backward travelling wave, and assuming that the system does not radiate.

A variety of types of waveguide taper and methods of solution for larger sets of differential equations are discussed in [91, 99, 100, 88]. Mode coupling in co-axial cable with variations in the radius of the conductors is analysed in [101] using the method of cross sections, and the coupling coefficients are derived.

In [88], Huting and Webb performed a comparison of differential equation and mode matching techniques and came to the conclusion that the methods give identical results for gradual transitions, and similar results for steeper transitions. These results were obtained from a study of the Marie transducer, a closed rectangular to circular waveguide transition. As the mode matching methods use a stepped

approximation of the transition, whereas differential equation methods assume a smooth transition, it was considered that the latter technique may be more generally applicable to continuous functions.

2.4 Chapter Summary

The following have been identified as being the main areas of interest of this work, and key past developments in these areas have been reviewed:

- Inset dielectric guide: research to date has shown this to be a versatile open waveguiding structure suitable for use at microwave and millimetre wave frequencies.
- Tapered slot antennas: this class of antenna has good physical and radiation properties, and operates over a broad bandwidth. In this chapter the tapered IDG antenna is identified as a member of this class.
- Analysis of waveguide discontinuities: a review of such methods is included in this chapter with a view to selecting methods suitable for application to an IDG taper.

Chapter 3

IDG-TSA Theory: State of the Art

Having introduced a number of areas of interest in Chapter 2, the current chapter and Chapter 4 focus on specific aspects of the theory. The theory discussed in these two chapters was in general developed by other researchers prior to the start of the current work.

In this chapter the analysis of uniform IDG is considered using both space domain and FDTD approaches. Secondly, an analytical method for modelling singularities is considered, and finally theory that can be applied to IDG antenna structures is introduced.

3.1 Space Domain Analysis of IDG

In Chapters 5 and 7 of this thesis, use is made of propagation constant values calculated using a rigorous space domain analysis of IDG. This technique, the Transverse Resonance Diffraction (TRD) method, was introduced in Section 2.1.4.

TRD is known to provide accurate values for the propagation constants of the bound modes [6].

No development of the TRD method has been carried out as part of the current project. The results used in this work were obtained using the computer program developed by Pennock *et al.* for their investigation into the bandwidth characteristics of single dielectric and layered dielectric IDG [14, 15].

Details of the TRD analysis of IDG are available from a number of sources [6, 14, 102], so only an outline of the method is given here. Referring to the IDG structure of Fig. 3.1, the full six component hybrid fields can be expressed as a superposition of LSE and LSM fields. Thus the hybrid modes can be derived from y-directed Hertzian vector potentials $\mathbf{\Pi}_h$ and $\mathbf{\Pi}_e$:

$$\begin{aligned} \mathbf{\Pi}_e &= \hat{\mathbf{y}}\varphi_e(x,y)e^{-j\beta z} \\ \mathbf{\Pi}_h &= \hat{\mathbf{y}}\varphi_h(x,y)e^{-j\beta z} \end{aligned} \tag{3.1}$$

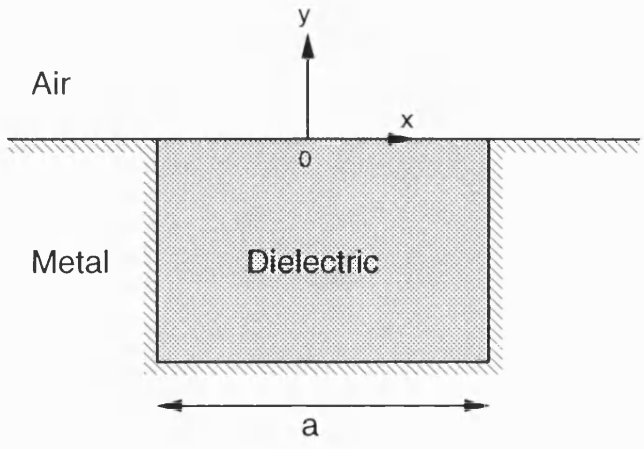

Figure 3.1: IDG structure for TRD analysis.

The **E** and **H** fields can be written in terms of these vector potentials [6]. The scalars $\varphi_e(x,y)$ and $\varphi_h(x,y)$ must be chosen to satisfy the boundary conditions.

Suitable expressions for these scalars in the air and dielectric regions are given by Pennock *et al* in [14]. Considering only the modes with even parity with respect to E_x, the analysis leads to a dispersion equation of the form:

$$\begin{bmatrix} \tilde{Y}_{11} & \tilde{Y}_{12} \\ \tilde{Y}_{21} & \tilde{Y}_{22} \end{bmatrix} \begin{bmatrix} E_x(x,0) \\ \delta_x E_z(x,0) \end{bmatrix} = 0 \tag{3.2}$$

where $\tilde{Y}_{ii}$ are integral admittance operators, the forms of which are given in [14], and are defined in terms of the potentials given above. This equation expresses the condition of continuity of the fields at the air/dielectric interface. Solution of equation (3.2) is by Galerkin's method [6] whereby the fields are expressed in terms of a complete set of basis functions:

$$\begin{aligned} E_x(x,0) &= \sum_{i=0}^{\infty} X_i E_{xi}(x) \\ \delta_x E_z(x,0) &= \sum_{i=0}^{\infty} Z_i E'_{zi}(x) \end{aligned}$$

In order to obtain rapid convergence of the solution to the dispersion equation, the following weight function is introduced into the basis functions:

$$W(x) = \left[1 - \left(\frac{2x}{a}\right)^2\right]^{-\frac{1}{3}}$$

This term takes account of the singularity at the 90° metal edge of IDG. A choice of functions that are orthogonal to these weighting functions are the Gegenbauer polynomials $C_m^{\frac{1}{6}}(x)$ [103]. Finally, after taking the inner product of the basis functions with equation (3.2), the following determinant equation is obtained [14]:

$$\begin{bmatrix} \langle E_{xi}\tilde{Y}_{11ij}E_{xj}\rangle & \langle E_{xi}\tilde{Y}_{12ij}E'_{zj}\rangle \\ \langle E'_{zi}\tilde{Y}_{21ij}E_{xj}\rangle & \langle E'_{zi}\tilde{Y}_{22ij}E'_{zj}\rangle \end{bmatrix} \begin{bmatrix} \mathbf{X} \\ \mathbf{Z} \end{bmatrix} = 0 \tag{3.3}$$

A search for the zeros of the determinant gives the solutions for the required propagation constants. It is found that the solutions converge quickly, with convergence to three significant figures achieved using only two sets of basis functions for each of the tangential electric field components at the air/dielectric interface.

3.2 The Analysis of IDG by FDTD

3.2.1 Introduction

The finite-difference time-domain method was introduced in Section 2.1.4. It has been applied by Stoiljković *et al.* both to uniform IDG [48, 47] and to the IDG-TSA [4, 53]. The computer code produced by Stoiljković formed the foundation for the FDTD work carried out during the current project. The original code has been considerably extended.

The objective of this section is to describe the operation of the program used to analyse uniform IDG. The core of this code can be applied directly to the IDG-TSA structure. The modifications and extensions to the code required to do this are discussed in Section 3.4.5.

There are a number of papers and several books ([38, 104] for example) dealing with the FDTD method, and its basic operation is well known. As such, the following sections avoid presenting detailed analysis except where doing so is necessary as a basis for work presented in later sections of the thesis.

3.2.2 Basic Formulation

The FDTD method was proposed by Yee in 1966 [37]. It is based on the differential form of Maxwell's equations. The method requires that both space and time be discretised such that space is divided into a regular lattice of cells with sides of length Δx, Δy and Δz, and time is incremented in steps of Δt. The differential terms in the Maxwell equations are approximated using finite difference equations, and **E** and **H** field components are evaluated at alternative half time steps. This finally results in a set of six equations for the field components where the current value of a component is defined in terms of its value at the last time step together with the values of some of the components adjacent to it. Such an algorithm is amenable to computer implementation.

For the purposes of this work, it is more useful to consider the derivation of the FDTD equations from the integral forms of Maxwell's equations. This is known as contour path FDTD, or CPFDTD [105]. For a uniform grid, CPFDTD gives the same set of finite difference equations as Yee FDTD. However, the CPFDTD formulation lends itself more readily to the modelling of shaped surfaces and the fields around fine material details such as wires, points, and edges. Some of these applications of CPFDTD are considered later.

The integral forms of Maxwell's equations are Ampere's and Faraday's laws:

$$\oint_C \mathbf{H} \cdot d\mathbf{l} = \frac{\partial}{\partial t} \int_S \epsilon \mathbf{E} \cdot d\mathbf{S} \tag{3.4}$$

$$\oint_C \mathbf{E} \cdot d\mathbf{l} = -\frac{\partial}{\partial t} \int_S \mu \mathbf{H} \cdot d\mathbf{S} \tag{3.5}$$

Ampere's law states that the sum of **H** around a contour C is equal to the rate of change of the electric flux density through the surface S defined by the contour.

Faraday's law can be similarly expressed. These laws can be implemented on an array of electrically small spatially orthogonal contours [106]. In Fig. 3.2, Ampere's law has been applied for the E_y component, and in Fig. 3.3 Faraday's law has been applied for the H_y component.

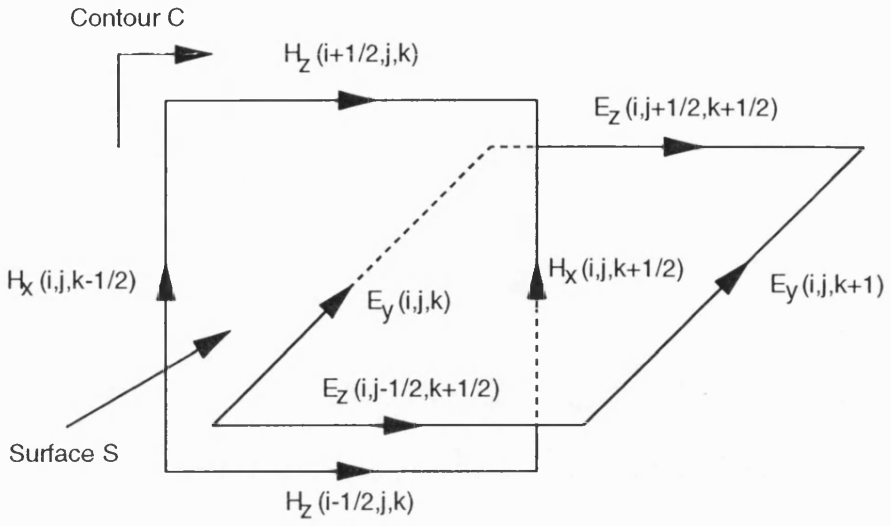

Figure 3.2: CPFDTD contour for the E_y component.

If the two structures in Figures 3.2 and 3.3 are joined together the cell shown in Fig. 3.4 is created. This matches the original Yee cell [37], differences in axis labelling excepted, so without having to do any analysis one can see immediately that the Yee and CPFDTD approaches are equivalent for uniform cells.

To generate the CPFDTD time stepping equations the line and surface integrals of Ampere's and Faraday's law must be replaced by approximations [107]:

$$\oint_C \mathbf{F} \cdot d\mathbf{l} = \hat{F} \Delta l \tag{3.6}$$

$$\int_S \mathbf{F} \cdot d\mathbf{S} = \hat{F} \Delta x \Delta y \tag{3.7}$$

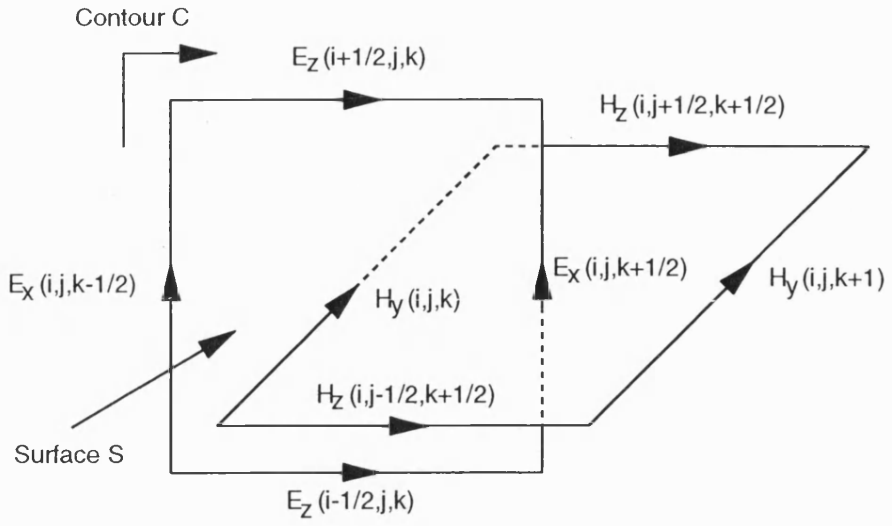

Figure 3.3: CPFDTD contour for the H_y component.

where $\hat{F}$ is the value of the field $\mathbf{F}$ that lies in the centre of each integral domain. For a uniform square grid the integral domains are the cell side length Δl in the line integral case, and the area $(\Delta l)^2$ for the surface integral. The field value at the midpoint of a contour or at the centre of a surface is therefore assumed to be the average field value along the contour or over the surface.

The difference equation for the E_y component in air is derived below. Note that the field component at the point in space $(i\Delta x,j\Delta y,k\Delta z)$ is denoted by (i,j,k) and that the value of a component $\hat{F}$ at a time $n\Delta t$ is denoted by $\hat{F}^n$. Letting $\Delta x = \Delta y = \Delta z = \Delta l$, Ampere's law for E_y applied in Fig. 3.2 gives:

$$(\Delta l)^2 \epsilon_0 \frac{d}{dt} E_y(i,j,k) = \Delta l \Big(H_z(i+\frac{1}{2},j,k) + H_x(i,j,k-\frac{1}{2}) \\ -H_z(i-\frac{1}{2},j,k) - H_x(i,j,k+\frac{1}{2}) \Big) \qquad (3.8)$$

after application of the assumptions of equations (3.6) and (3.7). Introducing the

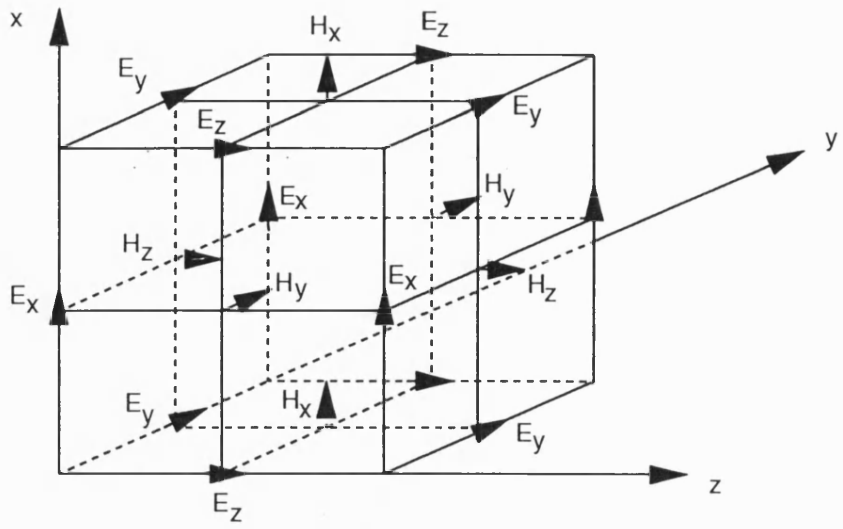

Figure 3.4: CPFDTD cell (Yee cell).

following difference expression for the time derivative:

$$\frac{d}{dt}\hat{F}^n(i,j,k) = \frac{\hat{F}^{n+1}(i,j,k) - \hat{F}^n(i,j,k)}{\Delta t} \tag{3.9}$$

yields the difference equation for E_y:

$$E_y^{n+1}(i,j,k) = E_y^n(i,j,k) + \frac{\Delta t}{\epsilon_0 \Delta l}\left[H_z^{n+\frac{1}{2}}(i+\frac{1}{2},j,k) - H_z^{n+\frac{1}{2}}(i-\frac{1}{2},j,k) + H_x^{n+\frac{1}{2}}(i,j,k-\frac{1}{2}) - H_x^{n+\frac{1}{2}}(i,j,k+\frac{1}{2})\right] \tag{3.10}$$

Using Fig. 3.3, the expression for H_y is found to be:

$$H_y^{n+\frac{1}{2}}(i,j,k) = H_y^{n-\frac{1}{2}}(i,j,k) - \frac{\Delta t}{\mu_0 \Delta l}\left[E_x^n(i,j,k-\frac{1}{2}) - E_x^n(i,j,k+\frac{1}{2}) + E_z^n(i+\frac{1}{2},j,k) - E_z^n(i-\frac{1}{2},j,k)\right] \tag{3.11}$$

The x and z components of the fields can be derived in a similar manner, starting from the contour diagram for each component in turn. The resulting difference equations are given here for reference:

$$E_x^{n+1}(i,j,k) = E_x^n(i,j,k) + \frac{\Delta t}{\epsilon_0 \Delta l}\left[H_z^{n+\frac{1}{2}}(i,j-\frac{1}{2},k) - H_z^{n+\frac{1}{2}}(i,j+\frac{1}{2},k) + H_y^{n+\frac{1}{2}}(i,j,k+\frac{1}{2}) - H_y^{n+\frac{1}{2}}(i,j,k-\frac{1}{2})\right] \quad (3.12)$$

$$E_z^{n+1}(i,j,k) = E_z^n(i,j,k) + \frac{\Delta t}{\epsilon_0 \Delta l}\left[H_y^{n+\frac{1}{2}}(i-\frac{1}{2},j,k) - H_y^{n+\frac{1}{2}}(i+\frac{1}{2},j,k) + H_x^{n+\frac{1}{2}}(i,j+\frac{1}{2},k) - H_x^{n+\frac{1}{2}}(i,j-\frac{1}{2},k)\right] \quad (3.13)$$

$$H_x^{n+\frac{1}{2}}(i,j,k) = H_x^{n-\frac{1}{2}}(i,j,k) - \frac{\Delta t}{\mu_0 \Delta l}\left[E_z^n(i,j-\frac{1}{2},k) - E_z^n(i,j+\frac{1}{2},k) + E_y^n(i,j,k+\frac{1}{2}) - E_y^n(i,j,k-\frac{1}{2})\right] \quad (3.14)$$

$$H_z^{n+\frac{1}{2}}(i,j,k) = H_z^{n-\frac{1}{2}}(i,j,k) - \frac{\Delta t}{\mu_0 \Delta l}\left[E_y^n(i-\frac{1}{2},j,k) - E_y^n(i+\frac{1}{2},j,k) + E_x^n(i,j+\frac{1}{2},k) - E_x^n(i,j-\frac{1}{2},k)\right] \quad (3.15)$$

In order to implement difference equations such as these in computer code it is necessary to define a cell on which the components to be computed are fixed. Such a cell is shown in Fig. 3.5.

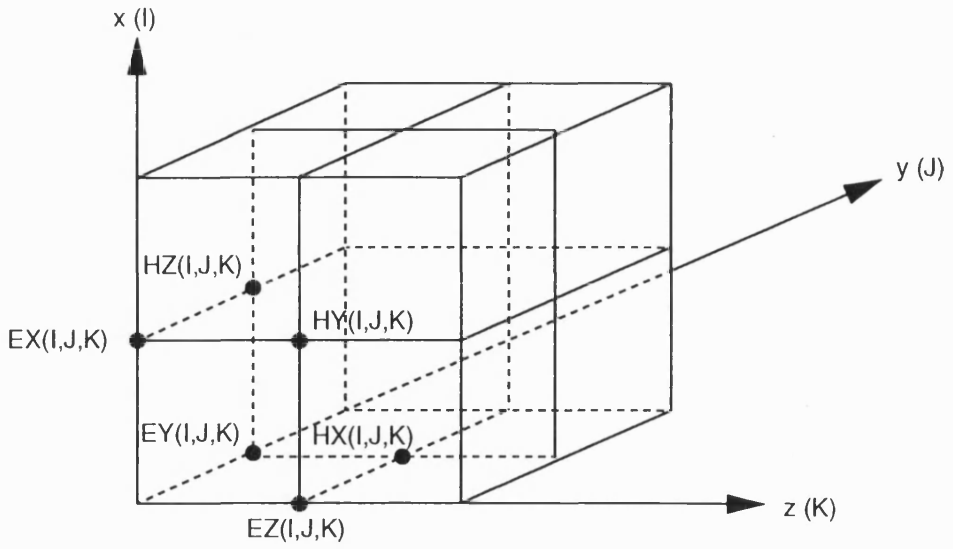

Figure 3.5: Positions of field components for computation.

This cell is referred to as the I, J, K-th cell so that the computer variable EX(I,J,K) is a shorthand for $E_x(i+\frac{1}{2}, j, k)$. The other equivalent notations are:

$$\begin{aligned} EY(I,J,K) &\equiv E_y(i, j+\frac{1}{2}, k) \\ EZ(I,J,K) &\equiv E_z(i, j, k+\frac{1}{2}) \\ HX(I,J,K) &\equiv H_x(i, j+\frac{1}{2}, k+\frac{1}{2}) \\ HY(I,J,K) &\equiv H_y(i+\frac{1}{2}, j, k+\frac{1}{2}) \\ HZ(I,J,K) &\equiv H_z(i+\frac{1}{2}, j+\frac{1}{2}, k) \end{aligned} \tag{3.16}$$

Using this notation, the above difference equations can be rewritten in a form directly suitable for computer implementation:

$$EX(I,J,K) = EX(I,J,K) + \frac{\Delta t}{\epsilon_0 \Delta l}[HZ(I,J-1,K) - HZ(I,J,K) + HY(I,J,K) - HY(I,J,K-1)] \quad (3.17)$$

$$EY(I,J,K) = EY(I,J,K) + \frac{\Delta t}{\epsilon_0 \Delta l}[HZ(I,J,K) - HZ(I-1,J,K) + HX(I,J,K-1) - HX(I,J,K)] \quad (3.18)$$

$$EZ(I,J,K) = EZ(I,J,K) + \frac{\Delta t}{\epsilon_0 \Delta l}[HY(I-1,J,K) - HY(I,J,K) + HX(I,J,K) - HX(I,J-1,K)] \quad (3.19)$$

$$HX(I,J,K) = HX(I,J,K) - \frac{\Delta t}{\mu_0 \Delta l}[EZ(I,J,K) - EZ(I,J+1,K) + EY(I,J,K+1) - EY(I,J,K)] \quad (3.20)$$

$$HY(I,J,K) = HY(I,J,K) - \frac{\Delta t}{\mu_0 \Delta l}[EX(I,J,K) - EX(I,J,K+1) + EZ(I+1,J,K) - EZ(I,J,K)] \quad (3.21)$$

$$HZ(I,J,K) = HZ(I,J,K) - \frac{\Delta t}{\mu_0 \Delta l}[EY(I,J,K) - EY(I+1,J,K) + EX(I,J+1,K) - EX(I,J,K)] \quad (3.22)$$

These expressions are utilised in the programs associated with this research.

3.2.3 Choice of Cell Size and Time Step

The cell size must be chosen to be considerably less than the smallest wavelength existing within the modelled structure. The Nyquist sampling theorem gives a theoretical maximum cell size of $\lambda/2$ where λ is the smallest wavelength. A cell size of $\lambda/10$ is often quoted as being acceptable, although reasonable results have been obtained with cell sizes as large as $\lambda/4$ [38]. For very accurate results, or to model certain physical features, a cell size of $\lambda/20$ or smaller may be necessary. As more powerful computers become available smaller cell sizes may be utilised with impunity.

From the foregoing it is evident that one drawback of the basic FDTD method is that the cell size must be determined from the wavelength in the most electrically dense part of the structure being modelled, which is the dielectric filling in the case of IDG. This results in smaller cells than are necessary being used to model the rest of the structure, which for IDG includes a considerable volume of free space. Equally, if it is required to model complex shapes involving fine details or curves, a small cell size must be selected. Various methods have been proposed to obviate the need to use a very small cell size for the whole structure [108, 109]. One such is considered in the next section.

Once the cell size has been selected, the time step is set by stability considerations. It must be sufficiently small that the wave cannot propagate through more than one cell during one time step, as this would contravene a basic assumption of the FDTD algorithm. The maximum time step for stability has been calculated [39] and is known as the Courant stability criterion:

$$v_{max}\Delta t \leq \left(\frac{1}{\Delta x^2} + \frac{1}{\Delta y^2} + \frac{1}{\Delta z^2}\right)^{-\frac{1}{2}} \tag{3.23}$$

where v_{max} is the maximum wave phase velocity existing within the modelled structure. For cubic cells with $v_{max} = c$ equation (3.23) becomes:

$$\frac{c\Delta t}{\delta} \leq \frac{1}{\sqrt{3}} \tag{3.24}$$

The left hand side of this equation is referred to as the stability factor, s [110]. To simplify implementation, the time stepping equations can be rewritten in terms of the stability factor. The multipliers in the update equations for the **E** and **H** components, equations (3.12) to (3.15), are $\Delta t/\epsilon\Delta l$ and $\Delta t/\mu\Delta l$ respectively. These can be expressed in terms of the characteristic impedance of free space Z_0 as sZ_0/ϵ_r and $s/\mu_r Z_0$. Thus, if **E** and **H** are normalised such that $Z_0 = 1$ then the multipliers in the time stepping equations become simply s for all components of the **H** field and for the **E** field components in free space, and s/ϵ_r for **E** field components in dielectric. The stability factor s is a program parameter that can usually be set at 0.5, but may be varied if the stability of the model is suspect.

3.2.4 Mesh Modifications

As discussed in the last section, there may be parts of a structure that are best modelled using very small cells, such as the non-uniform fields around a discontinuity or the fields inside a dense material. Such accurate modelling is usually only needed where it is the field shape, rather than the propagation constant, that is required. As a rule of thumb, it is generally considered that a 10% error in the fields leads to a 1% error in the calculated propagation constant. In uniform IDG the fields in the dielectric and around the slot edge are of primary interest and need to

be modelled accurately. In order to avoid the time and storage penalties involved in modelling the whole of the structure with this degree of accuracy, the graded mesh algorithm of Choi and Hoefer [108] has been employed in the FDTD implementations used during this project. This algorithm has been found to perform well in general.

The graded mesh algorithm modifies the basic FDTD time stepping equations by allowing each cell in the lattice to have its dimensions set according to $\Delta x = p\Delta l$, $\Delta y = q\Delta l$ and $\Delta z = r\Delta l$ where p,q and r are grading factors which can take any real positive value. The modifications to the FDTD equations are straightforward to derive. For the case of the E_y component, equation (3.8) must be modified by the grading factors as follows:

$$\begin{aligned} pr(\Delta l)^2\epsilon_0\frac{d}{dt}E_y(i,j,k) = r\Delta l\left(H_z(i+\frac{1}{2},j,k) - H_z(i-\frac{1}{2},j,k)\right) \\ +p\Delta l\left(H_x(i,j,k-\frac{1}{2}) - H_x(i,j,k+\frac{1}{2})\right) \end{aligned} \tag{3.25}$$

So that the difference equation becomes:

$$\begin{aligned} E_y^{n+1}(i,j,k) \;=\; E_y^n(i,j,k) + \frac{\Delta t}{\epsilon_0\Delta l}\left[\frac{\left\{H_z^{n+\frac{1}{2}}(i+\frac{1}{2},j,k) - H_z^{n+\frac{1}{2}}(i-\frac{1}{2},j,k)\right\}}{p}\right. \\ \left. +\frac{\left\{H_x^{n+\frac{1}{2}}(i,j,k-\frac{1}{2}) - H_x^{n+\frac{1}{2}}(i,j,k+\frac{1}{2})\right\}}{r}\right] \end{aligned} \tag{3.26}$$

The modifications to the other components follow a similar pattern. As is the case for standard FDTD, the stability factor must be set using the smallest cell dimension that exists within the structure. Even though the mesh is irregular, the

time step Δt remains constant throughout. It has been found that the interface between two regions with different grading factors can cause unwanted reflections or even instability of the model, so to ensure that this does not happen the cell size is increased or decreased gradually.

The uniform IDG FDTD algorithm as implemented uses the smallest cells in the dielectric and in the air close to the dielectric surface and slot edge; larger cells are used in the rest of the air region.

3.2.5 Fields at Dielectric Boundaries

The FDTD algorithm assumes that field components vary in a linear manner between calculation points. If an FDTD cell spans a dielectric interface then this assumption of linearity may need to be revised. When modelling IDG in FDTD, some compensation must be inserted into the algorithm for those cells falling on the air/dielectric interface.

Referring to Fig. 3.5, the lattice has been implemented such that the E_y, E_z and H_x field components lie on the interface. The H_x update equation (3.14) depends on μ, which is constant across the boundary, and on E_y and E_z which are continuous across the boundary as they are tangential to it. Equations (3.10) and (3.13) show that updates of the E_y and E_z components require special consideration, as these components depend on ϵ_r.

In [111] Zhang and Mei show that for a regular lattice, where the boundary falls mid-way between calculation points, the effect of the dielectric boundary can be catered for simply by using the average value of the permittivity in the calculation. This has been implemented in the IDG FDTD model by defining a multiplier $2s/(\epsilon_r + 1)$ to be used for the E_y and E_z updates on the air/dielectric interface.

Special techniques for handling more complex interfaces than those considered

by Zhang and Mei have been presented by Railton and McGeehan [112] and Paul *et al.* [43].

3.2.6 Symmetry

The symmetry of the IDG structure is exploited in order to save computing resources. Only one half of the structure is modelled (i.e. it is divided longitudinally) and field symmetry is enforced at the centre of the structure based on the known characteristics of the fields in deep or shallow slot IDG. The advantages of doing this are clear in terms of run times and memory requirements. However, the technique is only valid if the excitation of the structure being modelled is such that the polarisation is either LSM or LSE. For the case of dual polarisation such symmetry cannot be enforced and it would be necessary to model the complete structure.

3.2.7 Absorbing Boundary Conditions

As the inset dielectric guide is an open waveguide, the FDTD model of the structure must be bounded in some way so that it can fit within a limited computer memory. This boundary condition must be set such that outgoing waves are absorbed (i.e. allowed to pass through) so as to simulate infinite free space. Reflections from the outer boundary back into the model must be small enough so as not to greatly interfere with the required solution before it reaches steady state. More specifically, certain field components at each of the boundaries of the model need to be updated using components that fall outside the boundary. The job of the absorbing boundary condition (ABC) is to provide values for these missing field components which give the impression that the model is surrounded by free space.

There is a large amount of literature dealing with FDTD absorbing boundary conditions. It is not consistent with the objectives of this thesis to attempt a

review of this literature. In any case, an excellent discussion of the most important techniques is given in Chapter 7 of Taflove's book [104].

The FDTD models of uniform IDG and of the IDG-TSA use different ABCs. The reason for this is related to the different modes of excitation used for the two models. It is convenient to consider both methods in this section. No development work was carried out on the ABCs as part of this project, so discussions of them are kept to a minimum here.

Considering the IDG-TSA model first, where the excitation is a single frequency sinusoid. In this case the first order Mur ABC [40] is used. This method is based on the one-way wave equation theory derived by Engquist and Majda [113]. As implied by the name, one way wave equations are partial differential equations allowing wave propagation only in certain directions. An example of the update equations derived by Mur is given below, for E_z at the $y = 0$ boundary:

$$E_z^{n+1}(i,0,k+\frac{1}{2}) = E_z^n(i,1,k+\frac{1}{2}) + \frac{c\Delta t - \Delta l}{c\Delta t + \Delta l}\left(E_z^{n+1}(i,1,k+\frac{1}{2}) - E_z^n(i,0,k+\frac{1}{2})\right) \tag{3.27}$$

This equation is straightforward to implement within the existing time stepping structure. The only additional storage requirement is for the previous field value at the cell just inside the boundary. This ease of implementation coupled with its good performance make the Mur ABCs very attractive. They are still much used today, and developments of them continue to be proposed [114].

The FDTD model of the uniform IDG uses pulsed excitation in order to obtain the characteristics of the waveguide across a range of frequencies. In this situation, Mur's 1st order ABC becomes less effective [115]. This is due to the fact that the velocities of the fields within the model are different for different frequencies because of the dispersive nature of IDG. Mur's first order ABC is only an effective absorber

of waves at one phase velocity or one frequency, and at near-normal incidence. As such, it has been necessary to utilise a dispersive boundary condition for the uniform IDG FDTD. The method used is that of Zhao *et al.* [41]. This technique has been found to give accurate and stable results.

3.2.8 Special Cells in FDTD

The edges of the IDG slot cause some of the field components to exhibit singular behaviour in the immediate vicinity of the edge. This effect is discussed in Section 3.3. The CPFDTD formulation is based on the two integral approximations of equations (3.6) and (3.7). These assumptions break down around a metal edge where the fields might vary as, say, $r^{-1/3}$ (where r is the distance from the edge) rather than being linear. Errors can be introduced into the FDTD solution if the non-linearity of these fields is not taken into account.

The most straightforward way of handling singularities in FDTD is simply to decrease the cell size. This has severe penalties in terms of storage requirements and run times. The use of a graded mesh (refer to Section 3.2.4) to model the fields around the edge more carefully is a better approach. This still has the disadvantage of stretching the run time. Given that the field behaviour at an edge can be predicted using an analytical method such as that considered in the next section, the best option is to include this data in the FDTD algorithm. Such techniques reduce the errors in the calculation whilst only slightly increasing the run time.

A number of authors have suggested ways in which these special cells can be created. Aside from the early work of Mur [116], most researchers have handled the problem using contour path techniques [106, 107, 117, 118]. This approach has been adopted in the current work. Local field behaviour can easily be catered for in the CPFDTD algorithm. Only those cells next to the edge need to have their algorithm modified; the rest of the model uses standard cells.

If the field behaviour at an edge is known in advance in analytical form, then this information can be used to modify the assumptions of equations (3.6) and (3.7) with correction factors CF_s (surface integral) and CF_l (line integral) [107]:

$$\int_S \mathbf{F} \cdot d\mathbf{S} = \hat{F}\,\Delta x\,\Delta y\,CF_s \tag{3.28}$$

$$\oint_C \mathbf{F} \cdot d\mathbf{l} = \hat{F}\,\Delta l\,CF_l \tag{3.29}$$

So that:

$$CF_s = \frac{\int_S \mathbf{F} \cdot d\mathbf{S}}{\hat{F}\Delta x\Delta y} \tag{3.30}$$

$$CF_l = \frac{\oint_C \mathbf{F} \cdot d\mathbf{l}}{\hat{F}\Delta l} \tag{3.31}$$

These correction factors modify the CPFDTD time stepping equations. The E_x update equation (3.12) is given here as an example:

$$\begin{aligned} E_x^{n+1}(i,j,k) \;=\; & E_x^n(i,j,k) + \frac{\Delta t}{\epsilon_0 \delta CF_s}\Big[CF_{l1}H_z^{n+\frac{1}{2}}(i,j-\frac{1}{2},k) \\ & -CF_{l2}H_z^{n+\frac{1}{2}}(i,j+\frac{1}{2},k) + CF_{l3}H_y^{n+\frac{1}{2}}(i,j,k+\frac{1}{2}) \\ & -CF_{l4}H_y^{n+\frac{1}{2}}(i,j,k-\frac{1}{2})\Big] \end{aligned} \tag{3.32}$$

where CF_{ln} are the correction factors for each of the line integrals. As can be seen, implementation is straightforward. Only those components near to the edge that are most affected by the singularity need be treated if it is desired to keep analysis

to a minimum.

In [107] this method was applied to a microstrip filter. It was found that there was a considerable improvement in the accuracy of the model. This leads to savings in processor time and storage requirements as the desired accuracy can be achieved using a larger cell size. Similar conclusions were reached in [117] where an analysis of a coplanar line is carried out. Errors in the calculation of the characteristic impedance of the coplanar line were halved by the insertion of special cells into the CPFDTD.

Possible forms for the singular fields are discussed below. An implementation for IDG is detailed in Chapter 8.

3.3 Modelling of Singularities

3.3.1 Introduction

As noted above, certain IDG field components exhibit singular behaviour near to the slot edges. The objective of this section is to present a theory that allows this behaviour to be quantified. The motivations for considering this analysis are (a) to reduce errors in the FDTD model by incorporating it into the algorithm, (b) to allow results from non-corrected FDTD code to be assessed by comparison, and (c) to provide a description of the field behaviour that can be built into an analytical model of the IDG-TSA.

The order of the field singularity is governed by the edge condition [119] which requires the energy contained in a small volume around the edge to be finite, even if the volume contains singularities of the electromagnetic field. Early analyses, such as those of Collin [72] and Meixner [119] used this condition together with series expansions of the fields in the time varying case to obtain the orders of the

singularities. A number of subsequent authors followed the method of Meixner, extending it to more complex edge configurations [120, 121].

In [122] Andersen argued that these earlier analyses based on the time varying case are over-complex and that all the required information may be obtained from the static case. The singular behaviour of the electromagnetic field near an edge is the same as that of the static fields because very close to the edge the effects of propagation are not important as the singular behaviour is a local phenomenon. Specifically, the spatial derivatives of the fields are much larger than the time derivatives in Maxwell's equations, so the latter may be ignored [123]. The work of Andersen was extended by Van Bladel [124] to cover a variety of edge configurations. It is this latter work that will be discussed in more detail here.

3.3.2 Analysis

In addition to considering the problem to be static a further simplification may be made as the IDG edge is straight, allowing a two dimensional analysis to be performed. The geometry to be considered is shown in Fig. 3.6(a) and the co-ordinate systems to be used (rectangular and cylindrical) are shown in Fig. 3.6(b).

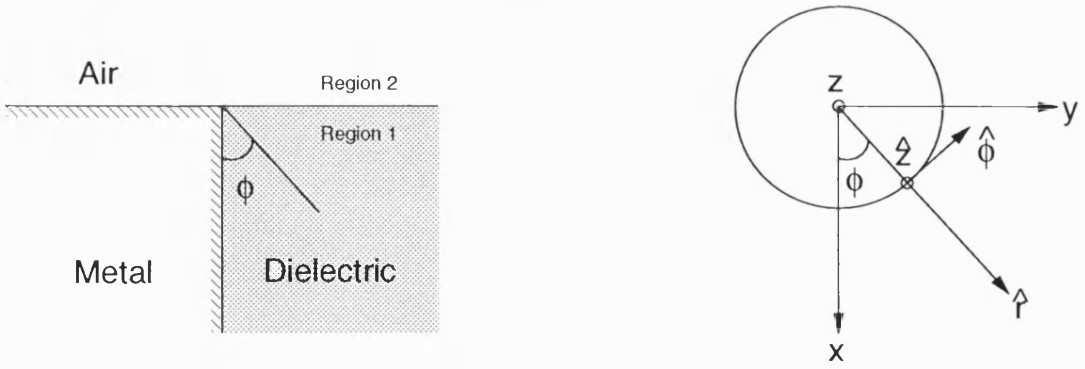

Figure 3.6: (a) IDG edge geometry, and (b) the co-ordinate system for the analysis.

From electrostatic theory, the following relationships can be recalled:

$$\mathbf{E} = -\nabla\Phi_e = -\left(\hat{\mathbf{r}}\frac{d\Phi_e}{dr} + \hat{\phi}\frac{1}{r}\frac{d\Phi_e}{d\phi}\right) \tag{3.33}$$

$$\mathbf{H} = -\nabla\Phi_m = -\left(\hat{\mathbf{r}}\frac{d\Phi_m}{dr} + \hat{\phi}\frac{1}{r}\frac{d\Phi_m}{d\phi}\right) \tag{3.34}$$

where Φ_e and Φ_m are the scalar electric and magnetic potentials respectively. The scalar potentials satisfy the Laplace equation $\nabla^2\Phi = 0$ where Φ represents either Φ_e or Φ_m. A general solution of Laplace's equation in two dimensions can be obtained by separation of variables [125] as:

$$\Phi = (Ar^{\nu} + Br^{-\nu})(C\cos\nu\phi + D\sin\nu\phi) \tag{3.35}$$

where A, B, C, D and ν are constants. Note that the small argument approximation of the Bessel function $J_\nu(r)$ has been used here. The Bessel function is selected here over other solutions to Laplace's equation as it meets the requirements of the edge condition discussed above [123].

Boundary Conditions

Before proceeding, it is useful to state the boundary conditions that apply at the metal surfaces and the dielectric boundary in Fig. 3.6(a). Assume that the circle shown in Fig. 3.6(b) is overlaid on Fig. 3.6(a) centred at the slot edge. Close to the edge (i.e. $r \rightarrow 0$) the $\hat{\mathbf{z}}$ directed field components are tangential to the edge, whilst the $\hat{\phi}$ directed components are normal to the edge. The following boundary conditions apply:

- Metal surface:
  - Tangential **E** is zero, giving $\frac{d\Phi_e}{dz} = 0$
  - Normal **H** is zero, giving $\frac{d\Phi_m}{d\phi} = 0$
- Dielectric boundary:
  - Normal **D** is continuous, requiring $\epsilon\frac{d\Phi_e}{d\phi}$ to be continuous
  - Tangential **E** is continuous, requiring Φ_e to be continuous
  - Normal **B** is continuous, requiring $\mu\frac{d\Phi_m}{d\phi}$ to be continuous
  - Tangential **H** is continuous, requiring Φ_m to be continuous

Expressions for the Potentials in Regions 1 and 2

Using the above boundary conditions together with equation (3.35), expressions for the potentials in regions 1 and 2 of Fig. 3.6(a) can be produced:

- Dielectric region (Region 1):

  Electric potential: Φ_e zero at $\phi = 0$ gives the electric potential as:

$$\Phi_{1e} = Mr^{\kappa}\sin\kappa\phi \tag{3.36}$$

  Magnetic potential: $\frac{d\Phi_m}{d\phi} = 0$ at $\phi = 0$ gives the magnetic potential as:

$$\Phi_{1m} = Nr^{\chi}\cos\chi\phi \tag{3.37}$$

  where the '1' subscripts refer to region 1.

- Air region (Region 2):

  Electric potential: Φ_e zero at $\phi = \frac{3\pi}{2}$ gives the electric potential as:

$$\Phi_{2e} = Ar^{\kappa} \sin\left(\frac{3\pi}{2} - \phi\right)\kappa$$

with A constant. A is found by enforcing continuity of Φ_e at $\phi = \frac{\pi}{2}$ to give:

$$\Phi_{2e} = Mr^{\kappa}\frac{\sin\frac{\kappa\pi}{2}}{\sin\pi\kappa}\sin\left(\frac{3\pi}{2} - \phi\right)\kappa \tag{3.38}$$

Knowing that $\epsilon\frac{d\Phi_e}{d\phi}$ is continuous at $\phi = \frac{\pi}{2}$ leads to the characteristic equation for κ:

$$\epsilon_r \tan\kappa\pi = -\tan\frac{\kappa\pi}{2} \tag{3.39}$$

Magnetic potential: $\frac{d\Phi_m}{d\phi}$ zero at $\phi = \frac{3\pi}{2}$ gives the form of the magnetic potential as:

$$\Phi_{2m} = Br^{\chi}\cos\left(\frac{3\pi}{2} - \phi\right)\chi$$

with B constant. B is found by enforcing continuity of Φ_m at $\phi = \frac{\pi}{2}$ to give:

$$\Phi_{2m} = Nr^{\chi}\frac{\cos\frac{\chi\pi}{2}}{\cos\pi\chi}\cos\left(\frac{3\pi}{2} - \phi\right)\chi \tag{3.40}$$

Applying continuity of $\mu\frac{d\Phi_m}{d\phi}$ at $\phi = \frac{\pi}{2}$ leads to the characteristic equation for χ:

$$\tan\chi\pi = -\tan\frac{\chi\pi}{2} \tag{3.41}$$

where the '2' subscripts refer to region 2.

Field Expressions

The field expressions for the transverse fields in the dielectric region (region 1) are obtained from equations (3.33) and (3.34) as:

$$\begin{aligned} E_r &= M\kappa r^{\kappa-1}\sin\kappa\phi \\ E_\phi &= M\kappa r^{\kappa-1}\cos\kappa\phi \\ H_r &= N\chi r^{\chi-1}\cos\chi\phi \\ H_\phi &= -N\chi r^{\chi-1}\sin\chi\phi \end{aligned} \tag{3.42}$$

The corresponding low frequency longitudinal fields can be derived from Maxwell's equations giving:

$$\begin{aligned} E_z &= -j\omega\mu N r^{\chi}\sin\chi\phi \\ H_z &= -j\omega\epsilon_0\epsilon_r M r^{\kappa}\cos\kappa\phi \end{aligned} \tag{3.43}$$

The above equations show how the fields transverse to the edge can become infinite due to the $r^{\nu-1}$ variation whereas those tangential to the edge remain finite with an r^{ν} variation.

The characteristic equations (3.39) and (3.41) are readily solved using a computer. In this case, a modified bisection technique was employed [126]. Throughout this work μ_r is fixed at 1, and χ is calculated as 0.6667. For an ϵ_r of 2.3, which is the nominal value of relative permittivity used in many of the structures built during this project, κ is calculated as 0.7455. Thus the transverse **E** fields vary as $r^{-0.2545}$ near to the edge whilst the transverse **H** fields vary as $r^{-0.3333}$. The variation of κ

with ϵ_r is shown in Fig. 3.7(a) and (b) which show ϵ_r ranges of 1 to 10 and 10 to 100 respectively.

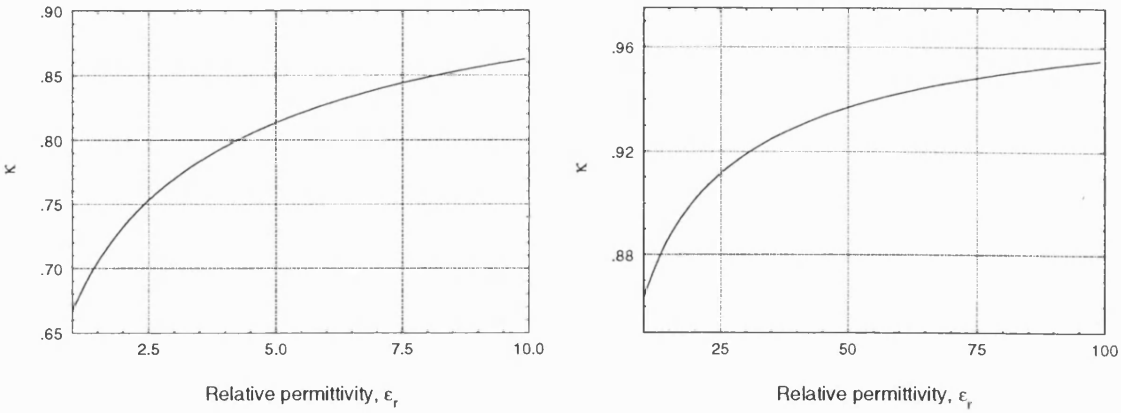

Figure 3.7: Variation of κ as ϵ_r varies from (a) 1 to 10, and (b) 10 to 100.

The results for the lower values of ϵ_r have been separated out as they are of more interest in the current work. The key point to note from the figures is the manner in which the degree of the singularity increases as ϵ_r is decreased.

3.4 Analysis of the IDG-TSA

3.4.1 Introduction

This section deals with theory relating to the analysis of the IDG-TSA that was developed prior to the current work. This material includes both non-specific theory applicable to the general class of aperture antennas, together with more specific theory that has been applied to IDG antennas in the past.

3.4.2 Radiation from an Aperture

The IDG-TSA is an aperture antenna in that the sources of the radiation are considered to be fields on the antenna surface. This is in contrast to wire-type

antennas where the analysis assumes a current distribution to be the source of the radiation. In this section, a technique for obtaining an expression for the far field radiation pattern of an aperture antenna is considered. The basis of this method is Huygen's principle, which states that any wave front can be considered as a source of secondary waves that add to produce distant wave fronts [125]. Thus, if the field distribution on an antenna aperture is known, it is logical to expect that the far fields can be uniquely determined from it. The approach used here is based on considering the fields as resulting from equivalent current sheets on the antenna surface. This requires a consideration of field equivalence principles.

Field Equivalence Principles

This theory is well known and is covered comprehensively in the literature ([127, 128, 129] for example). Only a brief summary is given here. The equivalence principle is based on the uniqueness theorem which states that a field in a lossy region is uniquely specified by the sources within the region plus the tangential components of the electric field over the boundary, or the tangential components of the magnetic field over the boundary, or the former over part if the boundary and the latter over the rest of the boundary [128].

By the field equivalence principle, the fields outside an imaginary closed surface are obtained by placing over the closed surface suitable electric and magnetic current densities that satisfy the boundary conditions. The current densities are selected so that the fields inside the closed surface are zero and outside are equal to the radiation produced by the actual sources. Thus the technique can be used to obtain the fields radiated outside a closed surface by the sources enclosed within it [27].

Consider the problem shown in 3.8(a) where some arbitrary source, represented by the current densities $\mathbf{J}_{es}$ and $\mathbf{J}_{me}$, is contained within a surface S and radiates fields $\mathbf{E}$ and $\mathbf{H}$ both inside and outside S.

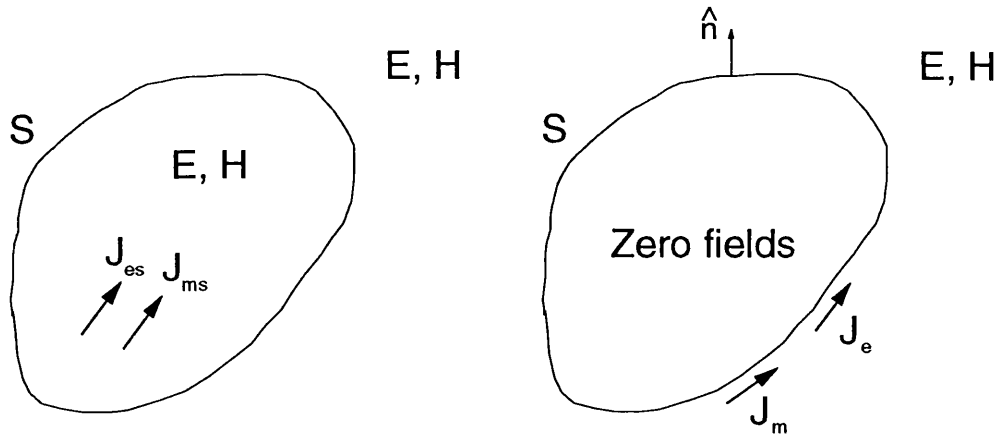

Figure 3.8: Field equivalence principle (a) Actual problem, and (b) equivalent problem.

One can set up a problem equivalent to this where the sources have been removed and there are zero fields within S. It is required that the original fields $\mathbf{E}$, $\mathbf{H}$ are maintained outside S, so electric and magnetic surface current densities $\mathbf{J}_e$ and $\mathbf{J}_m$ must exist on S in order to account for the discontinuity in the fields at S. This equivalent problem is depicted in Fig. 3.8(b).

Application of Ampere's law at the surface S shows that the discontinuity of the tangential magnetic field is equal to the surface electric current density [51]:

$$\mathbf{J}_e = \hat{\mathbf{n}} \times \mathbf{H} \tag{3.44}$$

and application of Faraday's law gives:

$$\mathbf{J}_m = -\hat{\mathbf{n}} \times \mathbf{E} \tag{3.45}$$

where $\hat{\mathbf{n}}$ is a unit vector normal to the surface of S and directed outwards from it.

This is a powerful concept. If a surface can be defined over an antenna aperture

on which the tangential fields are known, or can be estimated, then the equivalent electric and magnetic current densities can be found. Calculation of $\mathbf{J}_e$ and $\mathbf{J}_m$ is the first step in finding the far field radiation pattern of the antenna.

Fields in terms of Potentials

Maxwell's equations can be rewritten to include the magnetic charge density ρ_m and current density $\mathbf{J}_m$:

$$\begin{aligned} \nabla \times \mathbf{E} &= -\mathbf{J}_m - j\omega\mathbf{B} \\ \nabla \times \mathbf{H} &= \mathbf{J}_e + j\omega\mathbf{D} \\ \nabla \cdot \mathbf{D} &= \rho_e \\ \nabla \cdot \mathbf{B} &= \rho_m \end{aligned} \tag{3.46}$$

where an $e^{j\omega t}$ time dependence has been assumed. It can be shown that the $\mathbf{E}$ and $\mathbf{H}$ fields can be written in terms of the magnetic vector potential $\mathbf{A}$ and the electric vector potential $\mathbf{F}$ [96]:

$$\mathbf{E} = -j\omega\mathbf{A} - \frac{j\omega}{k_0^2}\nabla(\nabla \cdot \mathbf{A}) - \frac{1}{\epsilon}\nabla \times \mathbf{F} \tag{3.47}$$

$$\mathbf{H} = -j\omega\mathbf{F} - \frac{j\omega}{k_0^2}\nabla(\nabla \cdot \mathbf{F}) + \frac{1}{\mu}\nabla \times \mathbf{A} \tag{3.48}$$

where $\mathbf{A}$ and $\mathbf{F}$ are defined as:

$$\mathbf{A} = \mu \int_S \frac{\mathbf{J}_e e^{-jk_0 R}}{4\pi R}\, dS \tag{3.49}$$

$$\mathbf{F} = \epsilon \int_S \frac{\mathbf{J}_m e^{-jk_0 R}}{4\pi R} dS \tag{3.50}$$

where R is the distance from a point on the source to the observation point.

Far Field Approximations

The expressions for the vector potentials can be modified for use in the far field. In the left hand part of Fig. 3.9 consider a point $\mathbf{r}'$ on some arbitrary source where R is the distance from this point to the observation point and $\mathbf{r}$ is the distance from the origin to the observation point. Far away from the source, where $|\mathbf{r}| \gg |\mathbf{r}'|$, it can be assumed that all radiation paths from the source are parallel with each other. This assumption is incorporated into Fig. 3.9.

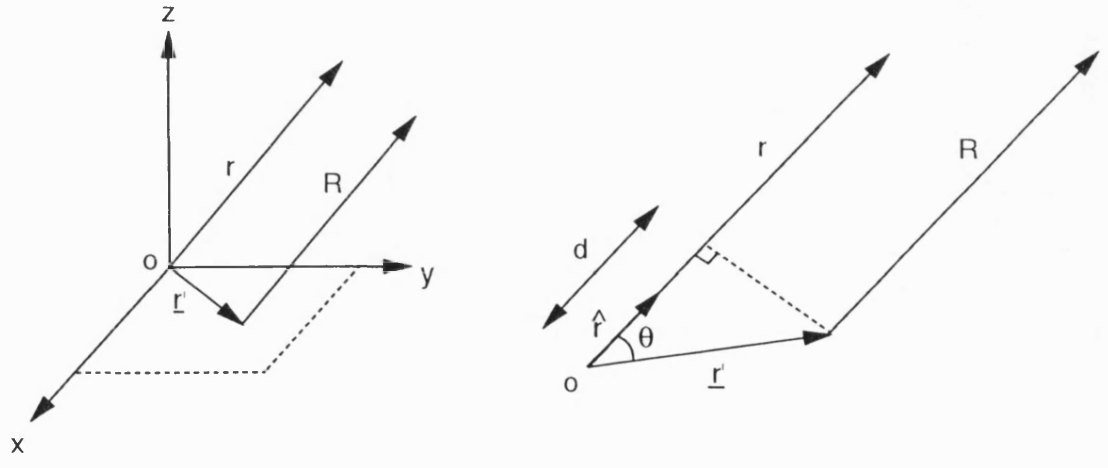

Figure 3.9: Illustrating the far field approximations.

From the right hand part of Fig. 3.9 it can be seen that:

$$d = r - R = r' \cos\theta = \hat{\mathbf{r}} \cdot \mathbf{r}' \tag{3.51}$$

where $\hat{\mathbf{r}}$ is a unit vector in the direction of r. Thus an approximation for R in the far field is:

$$R \approx r - \hat{\mathbf{r}} \cdot \mathbf{r}' \tag{3.52}$$

This approximation is used for the phase terms in equations (3.49) and (3.50). For the amplitude terms the approximation $R \approx r$ is valid. Equations (3.49) and (3.50) can therefore be written:

$$\mathbf{A} = \frac{\mu e^{-jk_0 r}}{4\pi r} \int_S \mathbf{J}_e e^{-jk_0 \hat{\mathbf{r}} \cdot \mathbf{r}'} \, dS \tag{3.53}$$

$$\mathbf{F} = \frac{\epsilon e^{-jk_0 r}}{4\pi r} \int_S \mathbf{J}_m e^{-jk_0 \hat{\mathbf{r}} \cdot \mathbf{r}'} \, dS \tag{3.54}$$

Further, in the far field the radial field components have negligible amplitude compared to the transverse components, so that $E_r = H_r = 0$. By using equations (3.47) and (3.48) to find the partial $\mathbf{H}$ fields due to $\mathbf{J}_e$ and the partial $\mathbf{E}$ fields due to $\mathbf{J}_m$ and then summing, it can be shown that [128]:

$$\begin{aligned} E_\theta &= -j\omega A_\theta - j\omega Z_0 F_\phi \\ E_\phi &= -j\omega A_\phi + j\omega Z_0 F_\theta \\ H_\theta &= -Y_0 E_\phi \\ H_\phi &= Y_0 E_\theta \end{aligned} \tag{3.55}$$

Equations (3.53) to (3.55) are sufficient to facilitate calculation of the antenna far fields assuming that the fields on the various Huygen's surfaces around the structure are known.

Far Field Radiation Expressions

The objective of this section is to develop expressions for E_θ and E_ϕ in the far field. H_θ and H_ϕ follow directly from these and are not reproduced here.

Consider an antenna aperture placed at $z = z_0$ in the xy plane of the co-ordinate system shown in Fig. 3.10.

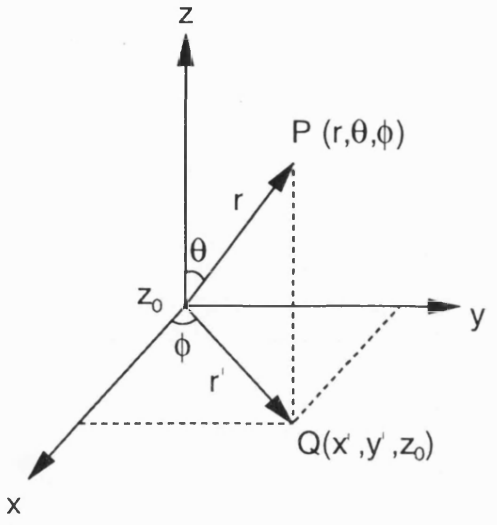

Figure 3.10: Co-ordinate system for derivation of far field radiation expressions.

A general point on the aperture is $Q(x', y', z_0)$ and P is a point in space, the observation point. For the point Q:

$$\begin{aligned} \mathbf{r}' &= x'\hat{\mathbf{x}} + y'\hat{\mathbf{y}} + z_0\hat{\mathbf{z}} \\ \hat{\mathbf{r}} &= \sin\theta\cos\phi\hat{\mathbf{x}} + \sin\theta\sin\phi\hat{\mathbf{y}} + \cos\theta\hat{\mathbf{z}} \end{aligned}$$

so that:

$$\hat{\mathbf{r}} \cdot \mathbf{r}' = x' \sin\theta \cos\phi + y' \sin\theta \sin\phi + z_0 \cos\theta \tag{3.56}$$

From equations (3.53) and (3.54) the θ and ϕ components of $\mathbf{A}$ and $\mathbf{F}$ are as follows:

$$\begin{aligned}
A_\theta &= \frac{\mu_0 e^{-jk_0 r}}{4\pi r} \int_S \left(J_{ex} \cos\theta \cos\phi + J_{ey} \cos\theta \sin\phi - J_{ez} \sin\theta\right) e^{jk_0 \hat{\mathbf{r}} \cdot \mathbf{r}'} \, d\hat{\mathbf{r}} \\
A_\phi &= \frac{\mu_0 e^{-jk_0 r}}{4\pi r} \int_S \left(-J_{ex} \sin\phi + J_{ey} \cos\phi\right) e^{jk_0 \hat{\mathbf{r}} \cdot \mathbf{r}'} \, d\hat{\mathbf{r}} \\
F_\theta &= \frac{\epsilon_0 e^{-jk_0 r}}{4\pi r} \int_S \left(J_{mx} \cos\theta \cos\phi + J_{my} \cos\theta \sin\phi - J_{mz} \sin\theta\right) e^{jk_0 \hat{\mathbf{r}} \cdot \mathbf{r}'} \, d\hat{\mathbf{r}} \\
F_\phi &= \frac{\epsilon_0 e^{-jk_0 r}}{4\pi r} \int_S \left(-J_{mx} \sin\phi + J_{my} \cos\phi\right) e^{jk_0 \hat{\mathbf{r}} \cdot \mathbf{r}'} \, d\hat{\mathbf{r}}
\end{aligned} \tag{3.57}$$

where $J_{x,y,z}$ are the Cartesian components of $\mathbf{J}$. To obtain the desired expressions for the E_θ and E_ϕ fields due to the aperture at $z = z_0$, the above are substituted into equation (3.55) and the relationships $\mathbf{J}_e = \hat{\mathbf{n}} \times \mathbf{H}$ and $\mathbf{J}_m = -\hat{\mathbf{n}} \times \mathbf{E}$ are used to convert from an equivalent current to a field notation. After some manipulation, the following relationships are obtained:

$$\begin{aligned}
E_\theta &= \frac{jk_0 e^{-jk_0 r}}{4\pi r} \left(f_x \cos\phi + f_y \sin\phi + Z_0 \cos\theta \left[g_y \cos\phi - g_x \sin\phi\right]\right) \\
E_\phi &= \frac{jk_0 e^{-jk_0 r}}{4\pi r} \left(\cos\theta \left[f_y \cos\phi - f_x \sin\phi\right] - Z_0 \left[g_y \sin\phi + g_x \cos\phi\right]\right)
\end{aligned} \tag{3.58}$$

where the terms f_x, f_y, g_x and g_y are the Fourier transforms of the tangential electric and magnetic fields over the aperture respectively. The expression for f_x is:

$$f_x = \int_{-\infty}^{\infty} \int_{-\infty}^{\infty} E_x(x', y') e^{jk_x x' + jk_y y' + jk_z z_0} \, dx' \, dy' \tag{3.59}$$

where $k_x = k_0 \sin\theta \cos\phi$, $k_y = k_0 \sin\theta \sin\phi$, and $k_z = k_0 \cos\theta$. The form of the other Fourier transform terms is similar. The notation used in equations (3.58) and (3.59) is due to Collin [129].

The above analysis relates to an infinite antenna aperture placed at $z = z_0$. It is not difficult to extend the analysis to work out the radiation from a six sided box surrounding the source, rather than just from this single aperture surface [104]. For the underside of the box at $z = -z_0$, the expressions given above may be used with the sign of z_0 reversed, and the integration limits of the expressions of the form of equation (3.59) need to be adjusted to reflect the finite size of the box ($-x_0$ to x_0 and $-y_0$ to y_0 in the x and y directions respectively).

Equation (3.56) can be rewritten for the sides of the box at $x = \pm x_0$ and $y = \pm y_0$:

$$\begin{aligned} \hat{\mathbf{r}} \cdot \mathbf{r}' &= \pm x_0 \sin\theta \cos\phi + y' \sin\theta \sin\phi + z' \cos\theta \\ \hat{\mathbf{r}} \cdot \mathbf{r}' &= x' \sin\theta \cos\phi \pm y_0 \sin\theta \sin\phi + z' \cos\theta \end{aligned} \tag{3.60}$$

Using equations (3.55) and (3.57) the E_θ expression for the sides at $x = \pm x_0$ can be derived:

$$E_\theta = \frac{jk_0 e^{-jk_0 r}}{4\pi r} \left(f_z \cos\phi + Z_0 \left[g_y \sin\theta + g_z \cos\theta \sin\phi \right] \right) \tag{3.61}$$

with the Fourier transform terms taking the form:

$$f_z = \int_{-y_0}^{y_0} \int_{-z_0}^{z_0} E_z(y', z') e^{\pm jk_x x_0 + jk_y y' + jk_z z'} \, dy' \, dz' \tag{3.62}$$

Similarly, for the sides at $y = \pm y_0$:

$$E_\theta = \frac{jk_0 e^{-jk_0 r}}{4\pi r} \left(f_z \sin\phi + Z_0 \left[g_z \cos\theta \cos\phi + g_x \sin\theta \right] \right) \tag{3.63}$$

with the Fourier transform terms taking the form:

$$f_z = \int_{-x_0}^{x_0} \int_{-z_0}^{z_0} E_z(x', z') e^{jk_x x' \pm jk_y y_0 + jk_z z'} \, dx' \, dz' \tag{3.64}$$

g_x and g_z have similar forms and k_x, k_y and k_z are as defined previously. Thus, the theoretical apparatus has been derived to find the far fields radiated by any of the six Huygen's surfaces on a box surrounding an arbitrary source. The main difficulty in applying this theory lies in finding forms for the tangential fields that are required for integration.

3.4.3 The Effect of the IDG-TSA Finite Ground Plane

Power flow in shallow slot (LSM) IDG is via the E_x and H_y field components, and via the E_y and H_x field components in deep slot (LSE) IDG (refer to Section 7.4). Therefore, a shallow slot IDG-TSA has power-carrying components that can spread out over the antenna ground plane whereas those of the deep slot IDG-TSA are zero over the ground plane. This indicates that the far field radiation pattern of the shallow slot IDG-TSA may be much affected by the currents flowing on the surface of the finite ground plane. This possibility is investigated in the later chapters of this thesis.

Applying equation (3.58) to the IDG-TSA, using the co-ordinate axes defined for IDG in Fig. 2.1, gives the following expressions for the elevation and azimuthal patterns of the LSM antenna:

$$E_\theta(\phi = 0) \propto f_z + g_y Z_0 \sin\theta \tag{3.65}$$

$$E_\theta(\theta = 0) \propto f_z \cos\phi + f_y \sin\phi \tag{3.66}$$

In these equations, and throughout the thesis, the elevation angle θ is measured from the aperture surface. The effect of the H_y component on the elevation pattern can be seen in equation (3.65), this component is finite over the ground plane as well as over the aperture. Equation (3.66) shows that the azimuthal pattern is unaffected by currents flowing on the ground plane.

In [1] Stephenson and Walter proposed an approximate analytical method for dealing with the currents flowing on the ground plane in the vertically polarised (LSM) case. The method is also discussed in the later book by Walter [51]. The problem to be overcome here is that of finding a suitable analytical form for the ground plane currents. Walter's method assumes that the electric current that is set up on the ground plane travels with a uniform amplitude and a constant phase velocity equal to the velocity of light in free space.

The amplitude of the ground plane fields relative to the aperture fields also needs to be established. Walter does this by noting that if the aperture were in an infinite ground plane, the tangential electric fields in the aperture would produce the same far fields as the tangential magnetic fields over the whole surface. If the ground plane is large it would seem reasonable to adjust the amplitude and phase of the magnetic fields relative to the electric fields such that both sources would produce the same amplitude and phase at the maximum value of their respective far field

patterns.

Walter found that adjustment of the two sources was not critical, and that good results could be obtained by letting the sources be in phase at the origin and adjusting their amplitudes so that their pattern maxima are equal. In practice, this method calculates the antenna far field pattern by summing the pattern of a line source of magnetic current along the length of the aperture and that of a line source of electric current along the length of the aperture plus the ground plane, with their amplitudes adjusted as specified.

The main effect of the ground plane current in the case of the LSM polarised antenna is to tilt the endfire beam upwards from the ground plane. The beam tilt angle θ_t is a function of both the aperture length L and the length of the ground plane extending beyond the aperture, L_g. For small values of beam tilt, Walter has shown that [51]:

$$\theta_t \approx \frac{49}{\sqrt{\frac{L+L_g}{\lambda}}} \tag{3.67}$$

Whilst reasonable results have been obtained using this method, it is clearly rather approximate, with the major assumption being that the aperture is situated in a large ground plane. It is difficult to establish limits on the validity of the method without accurate foreknowledge of the ground plane fields, obtained via some other technique.

3.4.4 Modified Walter's Method

This approximate analytical method is used by Stoiljković in [3]. It will be referred to here as modified Walter's method as it is based largely on the material in Chapter 2 of Walter's book [51]. No direct development of this method was carried out

during the course of this project, so only an outline of the technique is given here. The program code for the method is available at the University of Bath, so was used during the project for comparison purposes.

The modified Walter's method consists of two main steps [3]. In the first, the longitudinal component of the near-field electric field is calculated. In the second, the far fields radiated by the equivalent magnetic current in the slot are calculated by breaking the aperture into a number of small rectangular elements.

The tapered geometry of the IDG-TSA is approximated by a large number of small IDG sections with uniform dimensions connected end to end. To account for the step discontinuities, power continuity is enforced at each step. This criterion links the undetermined multiplicative constants in the expression for the electric field in each section, so yielding the field distribution corresponding to a forward travelling wave on the aperture.

The shape and propagation constants of the aperture fields are determined from the H-guide approximation of IDG. H-guide is considered in detail in Chapter 5. Once the aperture fields have been calculated, a Huygen's surface is defined over the aperture and the equivalent magnetic current on it is calculated. It is assumed that the aperture is situated in an infinite ground plane, allowing calculation of the far fields from electric fields only. Each of the small elements into which the antenna has been broken is considered as a constant amplitude source with linear phase excitation. The far fields of each element are calculated analytically and the results summed to give the radiation pattern of the whole structure.

In order to account for the finite size of the ground plane, the approximate method described in Section 3.4.3 is employed. A number of results obtained using the modified Walter's method are presented in Chapter 7.

3.4.5 FDTD Analysis of the IDG-TSA

The FDTD technique has already been detailed in Section 3.2. Some additions to the basic algorithm are required in order to model the IDG-TSA. Chief amongst these are a near to far field transformation and a method for modelling the tapered depth of the structure. These additions are discussed below.

Near to Far Field Transformation

A number of FDTD near to far field transformations have been proposed. These fall into two broad categories; wide band and single frequency transformation. The earliest methods to be proposed were of the single frequency type [130, 131] and are useful for situations where the antenna radiation pattern is required at only a small number of frequencies. Single frequency excitation is used and the transformation is carried out in the frequency domain. The storage requirements for single frequency transformations are not prohibitive and the FDTD calculation is not significantly slowed by the extra processing required.

If the radiation characteristics are required over a range of frequencies a wide band technique can be used [132, 133]. For this case, pulsed excitation of the structure is used so that data at multiple frequencies can be obtained from one FDTD run, and the near to far field transformation is carried out in the time domain. The storage requirements for these methods can be great, and the FDTD code can be slowed down by as much as a factor of two [57].

For the IDG-TSA, a single frequency transformation is used, due to the relative ease of implementation and to the comparatively low overhead in terms of storage requirements.

Using a single frequency excitation, the far field is found using the method detailed earlier in Section 3.4.2. Surfaces are defined on which the equivalent magnetic and

electric currents are calculated. Radiation from the top surface of the structure is obtained using equation (3.58). The integrals of the form of equation (3.59) are handled as straightforward summations.

The frequency domain fields required by the far field calculation are obtained using a running discrete Fourier transform (DFT) of the time domain fields calculated by FDTD. The DFT is an efficient way of performing this task; storage requirements are for a two dimensional complex array covering each of the Huygen's surfaces, and the overhead of running the DFTs is not great as they need only be run for a proportion of the total FDTD runtime. To illustrate this consider the DFT definition [134]:

$$H_n = \sum_{k=0}^{N-1} h_k e^{2\pi jkn/N} \tag{3.68}$$

where H_n is the DFT, h_k are samples of a function $h(t)$ taken at intervals of Δt at times $t_k = k\Delta t$ where $k = 0, 1, 2, \ldots, N-1$. The DFT of $h(t_k)$ is $H(f_n)$ where the discrete frequency values are:

$$f_n = \frac{n}{N\Delta t}$$

where $n = -\frac{N}{2}, \ldots, \frac{N}{2}$. In single frequency FDTD results are required only at $n = 1$ so that $f_1 = 1/N\Delta t$ is the operating frequency of the model. With Δt having been fixed, the number of time steps over which the DFT is to be taken is therefore defined as $N = 1/f_1\Delta t$.

As an example, consider a 3000 time step FDTD run with a minimum cell size of 0.635mm. These are typical figures [4]. With a stability factor of 0.5, the time step is approximately 1ps. At 10GHz therefore, the DFT should run for 94 time steps out of the total of 3000. Clearly, these would be the last 94 time steps when the

model should have reached a steady state.

Conformal Modelling of the IDG-TSA Taper

It is a relatively straightforward matter to modify CPFDTD to take account of the tapered depth of the IDG-TSA using the technique of Jurgens *et al.* [105]. Using this Contour Path (CP) method, cells next to the tapered surface are distorted to conform to its profile. All other cells in the model remain unchanged.

Referring to the CPFDTD cell shown earlier in Fig. 3.5 it can be seen that the H_y and H_z component updates could be affected if the cell is located on a metal surface which slopes in the z direction. The situation with respect to the H_y component is shown in Fig. 3.11.

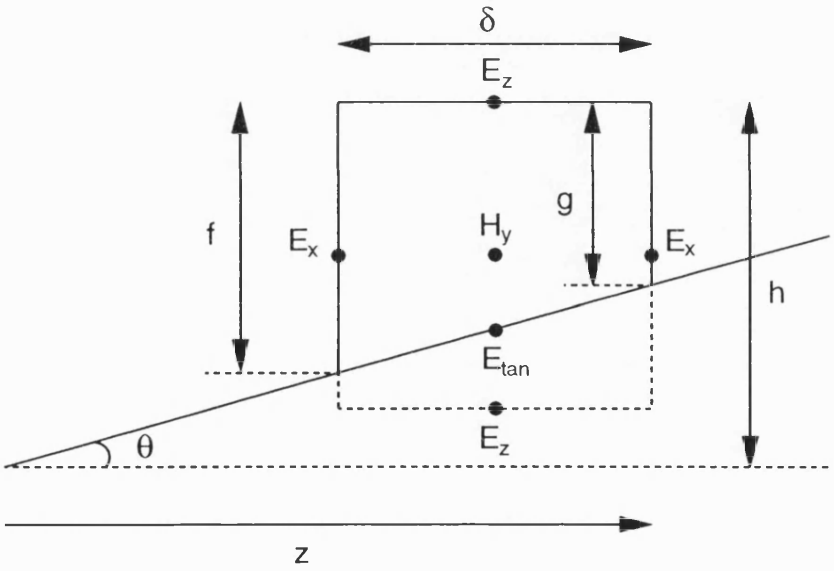

Figure 3.11: Geometry for incorporating the taper surface into the H_y FDTD update.

In the figure the sloped floor is shown cutting through the regular cell at an angle θ. The distorted cell is shown using a solid line, the original is shown dotted. The area of the distorted cell is A. Note that the lower E_z component has been distorted

to conform to the metal surface and that $E_{tan} = 0$. Bearing in mind the usual CP assumptions (equations (3.6) and (3.7)), application of Faraday's law around the contour gives:

$$H_y^{n+\frac{1}{2}}(i+\frac{1}{2},j,k+\frac{1}{2}) = H_y^{n-\frac{1}{2}}(i+\frac{1}{2},j,k+\frac{1}{2}) + \frac{\Delta t}{\mu A}\Big[E_x^n(i+\frac{1}{2},j,k)f - E_x^n(i+\frac{1}{2},j,k+1)g + E_z(i+1,j,k+\frac{1}{2})\delta\Big] \tag{3.69}$$

The formulation for the H_z component is similar, but in this case the E_x components on either side of it are distorted by the same amount because the H_z contour is located across rather than along the taper.

In the implementation of FDTD used for the IDG-TSA, the taper is first approximated by a staircase of regular cells before the lowest cells are deformed. The staircase is set up such that none of the regular cells next to the taper have a side which protrudes by less than half a cell above the taper surface. This ensures that all the E_x points in Fig. 3.11 remain calculable, and so cells are stretched rather than compressed. This avoids having to 'borrow' component values from neighbouring cells as proposed in [105].

The parameters A, f and g in equation (3.69) are easily calculated. A is the sum of the area of the rectangle (δg) and the area of the triangle ($0.5[f-g]\delta$) which works out as $0.5\delta(f+g)$. The length g is simply $h - z\tan\theta$ and f is calculated similarly. As can be seen, this technique is easily implemented, and doing so means that the cell size chosen for the model is no longer dictated by the need to produce a satisfactory staircase approximation of the taper.

Excitation

The IDG-TSA FDTD model is fed using a rectangular waveguide through which an excitation signal is supplied which has a single frequency sinusoidal time variation. The field components that are excited are E_x in the shallow slot (LSM) case and E_y in the deep slot (LSE) case.

The LSM excitation takes the form $\cos(\pi y/2W)$ where W is the guide half-width, so that there is a half wavelength sinusoidal amplitude distribution across the slot and a constant distribution in the x (depth) direction. The LSE excitation has the form $\sin(\pi x/d)$ where d is the guide depth, so that there is a half wavelength sinusoidal distribution across the guide depth and a constant distribution in the y (width) direction.

Modelling of Three Dimensional Objects

The full FDTD model of the IDG-TSA that is introduced in Chapter 8 requires the modelling of a number of objects in three dimensions; the rectangular waveguide feed and its flange, and the antenna mounting block. Care needs to be exercised when implementing the FDTD algorithm on the surfaces of such metal objects, and particularly at the corners where two surfaces meet. By examining the FDTD cell of Fig. 3.5 it is clear that when any side of the cell abuts a metal surface that modifications to the algorithm are required to cater for those field components that are shorted out by the surface. If this is not done, gaps or overlaps in the FDTD model of the structure are likely, leading to inaccuracies in the results.

The Existing IDG-TSA FDTD Model

As has been mentioned (Section 3.2.1), an FDTD model of the IDG-TSA has been built by Stoiljković *et al.* [4, 53]. The existing model includes a number of the features that have been discussed in this chapter, namely,

- a graded mesh
- symmetry
- first order Mur ABC
- conformal modelling of the taper

The far field radiation pattern is calculated from the magnetic current on the slot surface only. The finite ground plane approximation of Walter (Section 3.4.3) is then applied.

3.5 Transitions onto IDG

Two techniques have been used in the past to couple power into inset dielectric guide. These are feeding with rectangular waveguide (RWG) and probe feeding. Of the two, the former has received the most research interest.

Feeding of deep slot IDG using rectangular waveguide was proposed by Rozzi and Hedges in [6]. The depth of the slot needs to be at least one half of the broad waveguide dimension for effective coupling. This is due to the similarity of the IDG LSE mode to that existing in half an RWG operating in its fundamental mode. With a dielectric taper fitted into the feed RWG it was found that an SWR of better than 1:1.12 could be achieved in the frequency range 8 to 12GHz. Since its proposal, this type of feed has been used by various researchers [9].

RWG feeding of shallow slot guide was considered by Sewell and Rozzi in [29]. The S-parameters of the transition were predicted using a rigorous characteristic Green's function approach, and favourable comparisons were made to $|S_{11}|$ measurements. A more complete analysis of the RWG to shallow IDG transition is given by Stoiljković *et al.* [47, 48]. In these papers FDTD is used to characterise the transition and the results compared to those of Sewell and Rozzi. Both the reflection and transmission behaviour of the junction are determined experimentally using a de-embedding procedure. The salient points of this procedure are given in Section 3.5.1 below.

Probe feeding of shallow IDG has been used by Ma *et al.* [8] for feeding a linear array and by Rozzi *et al.* [12] for feeding microstrip loaded IDG. Both of these structures are fed centrally by a coaxial probe pushed up through the guide floor into the dielectric. Ma *et al.* reported an input reflection coefficient of better than -10dB over the 9.6GHz to 11GHz range using this arrangement.

3.5.1 Experimental Characterisation of Transitions

A method of obtaining the S-parameters of novel transitions is made use of in Chapter 10 of this thesis. This technique is based upon that presented by Pennock *et al.* [135]. This method requires measurements to be taken from two sets of back-to-back transitions separated by different, known, electrical lengths. If the transitions in the back-to-back arrangement are assumed to be the same, then the S-parameters of the transition can be uniquely determined from these measurements.

A block diagram of back-to-back transitions is shown in Fig. 3.12.

For the sake of the calculation the transitions, C and D, will initially be assumed to be different. The box X represents the transmission line between the junctions.

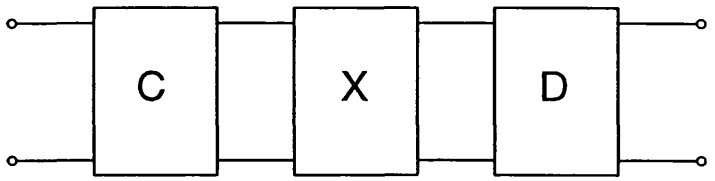

Figure 3.12: Back-to-back transitions: block diagram.

The analysis can be carried out by reference to the signal flow graph of Fig. 3.13.

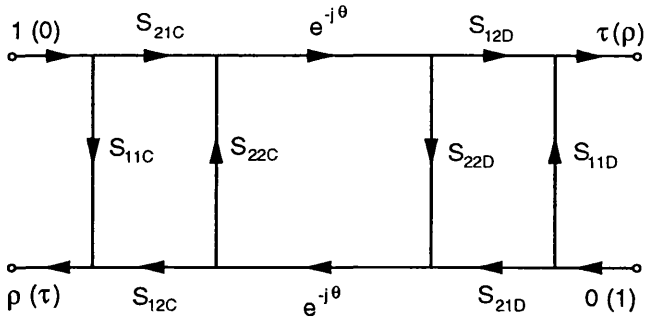

Figure 3.13: Back-to-back transitions: signal flow graph.

The electric length of the transmission line between the junctions is $\theta = \beta l$ where l is the line length and β is its propagation constant, which is assumed to be known. The bracketed symbols relate to the determination of port 2 parameters. By using Mason's rule the overall S-parameters of this arrangement are found to be as follows:

$$S_{11} = S_{11C} + \frac{S_{21C}S_{22D}S_{12C}e^{-2j\theta}}{1 - S_{22C}S_{22D}e^{-2j\theta}} \tag{3.70}$$

$$S_{22} = S_{11D} + \frac{S_{21D}S_{22C}S_{12D}e^{-2j\theta}}{1 - S_{22C}S_{22D}e^{-2j\theta}} \tag{3.71}$$

$$S_{21} = S_{12} = \frac{S_{21C}S_{12D}e^{-j\theta}}{1 - S_{22C}S_{22D}e^{-2j\theta}} \tag{3.72}$$

Writing these expressions for two sets of measurements, referred to as A and B, and performing some manipulation leads to a number of expressions relating the S-parameters of the junction to the measured values:

$$S_{11C} = S_{11A} - \frac{S_{21A}(S_{11A} - S_{11B})e^{-j\theta_A}}{S_{21A}e^{-j\theta_A} - S_{21B}e^{-j\theta_B}} \tag{3.73}$$

$$S_{11C} = S_{11B} - \frac{S_{21B}(S_{11A} - S_{11B})e^{-j\theta_B}}{S_{21A}e^{-j\theta_A} - S_{21B}e^{-j\theta_B}} \tag{3.74}$$

$$S_{11D} = S_{22A} - \frac{S_{21A}(S_{22A} - S_{22B})e^{-j\theta_A}}{S_{21A}e^{-j\theta_A} - S_{21B}e^{-j\theta_B}} \tag{3.75}$$

$$S_{11D} = S_{22B} - \frac{S_{21B}(S_{22A} - S_{22B})e^{-j\theta_B}}{S_{21A}e^{-j\theta_A} - S_{21B}e^{-j\theta_B}} \tag{3.76}$$

$$\frac{S_{22D}S_{12C}}{S_{12D}} = \frac{S_{11A} - S_{11B}}{S_{21A}e^{-j\theta_A} - S_{21B}e^{-j\theta_B}} \tag{3.77}$$

$$\frac{S_{21D}S_{22C}}{S_{21C}} = \frac{S_{22A} - S_{22B}}{S_{21A}e^{-j\theta_A} - S_{21B}e^{-j\theta_B}} \tag{3.78}$$

$$S_{21C}S_{12D} = S_{21A}(1 - S_{22C}S_{22D}e^{-2j\theta_A})e^{j\theta_A} \tag{3.79}$$

$$S_{21C}S_{12D} = S_{21B}(1 - S_{22C}S_{22D}e^{-2j\theta_B})e^{j\theta_B} \tag{3.80}$$

If the junctions are different, then these expressions are not sufficient to determine their S-parameters. If they are assumed to be the same, however, then the S_{11} of the junction is given by any of equations (3.73) to (3.76) in terms of the measured values, and S_{22} is given by equation (3.77) or (3.78). Once S_{22} has been determined then equations (3.79) and (3.80) can be used to give $S_{21}S_{12}$.

Pennock *et al.* identified limits on the difference in lengths of the two transmission lines used in the measurements. It was found that a separation difference of less than $\lambda/2$ leads to the most accurate results, with $\lambda/4$ being the optimum difference required to minimise errors due to inaccurate electrical length data.

3.6 Chapter Summary

Two methods for the analysis of IDG have been discussed; TRD and FDTD. An analytical technique for describing field behaviour close to metal edges has been introduced. Equations for the far field radiation from a source in the form of a six sided box have been developed. The foregoing theory is applied in the later chapters of this thesis.

The methods that have been used in the past for IDG-TSA analysis have been discussed; modified Walter's method and FDTD. Rather than building a complete model of the fields on the aperture and ground plane, these earlier methods model the aperture electric field components only and use an approximate method to cater for the fields on the finite ground plane.

Chapter 4

Analysis of Waveguide Discontinuities: Existing Theory

The analytical model of the IDG-TSA introduced in Section 3.4.4 uses trial and error to determine the power lost from the fundamental mode to other modes as it travels along the IDG taper. It is desirable to remove this possible source of inaccuracy from the model. As such, a method for characterising the mode coupling along the taper is considered in this chapter. Whilst the short term aim of considering this technique is to obtain an analysis of the IDG taper that is as complete as possible, in the longer term it may be desirable to use the experience and knowledge so gained to develop a simple approximation that can be inserted into analytical IDG-TSA models without significant impact on the run times

Before considering the technique, a section concerning the modes of dielectric slab waveguide is included, defining the terminology and the theoretical framework utilised in the subsequent sections. Following this is a brief section considering the choice of method from those introduced in Section 2.3.

4.1 The Modes of Dielectric Slab Waveguide

Consider the dielectric slab shown in Fig. 4.1.

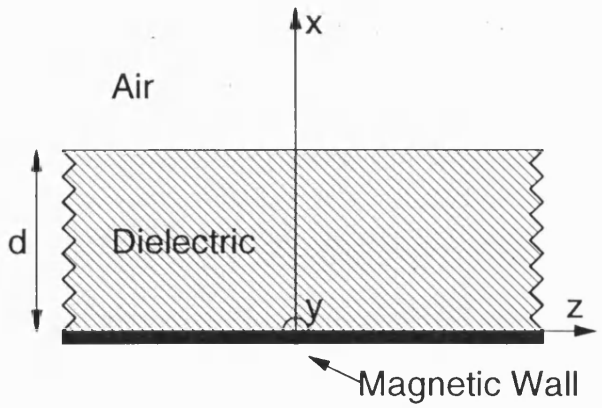

Figure 4.1: Infinite dielectric slab waveguide geometry.

Propagation is assumed to be in the z direction and the structure is of infinite extent in the y direction, and the time dependence is assumed to be of the form $exp(j\omega t)$. The slab can support TE modes ($E_z = 0$) and TM modes ($H_z = 0$). Only even TE modes are considered here; the other modes can be treated similarly. Applying Maxwell's equations in this case gives:

$$\begin{aligned} \gamma_z E_y &= -j\omega\mu H_x \\ \frac{\partial E_y}{\partial x} &= -j\omega\mu H_z \\ \frac{\partial H_z}{\partial x} &= \left(\frac{\gamma_z^2}{j\omega\mu} - j\omega\epsilon\right) E_y \end{aligned} \tag{4.1}$$

where the longitudinal propagation constant is $\gamma_z = j\beta$ and $\epsilon = \epsilon_0\epsilon_r$. Rearranging this equation gives the following wave equation and propagation constant relationship [75]:

$$\frac{\partial^2 E_y}{\partial x^2} + k_x^2 E_y = 0 \tag{4.2}$$

$$k_x^2 = \omega^2 \mu \epsilon + \gamma_z^2 \tag{4.3}$$

Considering even modes only, solution of equation (4.2) and application of boundary conditions as dictated by Fig. 4.1 leads to fields of the form:

$$\begin{aligned} Slab: \quad E_y &= A\cos(k_{xd}x) \\ Air: \quad E_y &= A\cos(k_{xd}d)e^{-\gamma_{xa}(x-d)} \end{aligned}$$

where A is a constant.

4.1.1 Origin of the Continuum

Rewriting the propagation constant relationship equation (4.3) in the air and in the slab, and letting $\gamma_{xa} = jk_{xa}$ gives:

$$\begin{aligned} Air: \quad \beta^2 &= k_0^2 - k_{xa}^2 \\ Slab: \quad \beta^2 &= \epsilon_r k_0^2 - k_{xd}^2 \end{aligned} \tag{4.4}$$

Consider the conditions leading to real values of β:

- In air, β is real if $0 \leq k_{xa}^2 \leq k_0^2$. This leads to values of β in the range $0 \leq \beta^2 \leq k_0^2$.
- In the slab, β is real if $0 \leq k_{xd}^2 \leq \epsilon_r k_0^2$, leading to values of β in the range $0 \leq \beta^2 \leq \epsilon_r k_0^2$.

The range of β for which the waves are bound to the slab is therefore:

$$k_0^2 \leq \beta^2 \leq \epsilon_r k_0^2$$

Substituting this range of β values back into equation (4.4) above gives the range of x directed propagation constants corresponding to the bound modes:

- In air: $0 \leq k_{xa}^2 \leq (1 - \epsilon_r)k_0^2$, giving k_{xa} imaginary for bound modes, i.e. $k_{xa} = j\gamma_{xa}$.
- In the slab: $0 \leq k_{xd}^2 \leq (\epsilon_r - 1)k_0^2$

The above defines the range that should be used for the root finding routine when the transcendental equations are being solved for the propagation constants of the guided modes. For these ranges, there will be a few discrete solutions.

For $0 \leq \beta^2 \leq k_0^2$, β is real in the air but not in the slab. This range corresponds to a continuum of radiation modes, for which $0 \leq k_{xa}^2 \leq k_0^2$ and $(\epsilon_r - 1)k_0^2 \leq k_{xd}^2 \leq \epsilon_r k_0^2$

Consider now conditions leading to imaginary β:

- In air $k_{xa}^2 > k_0^2$ for $\beta^2 < 0$.
- In the slab $k_{xd}^2 > \epsilon_r k_0^2$ for $\beta^2 < 0$.

These modes are reactive, being attenuated in the direction of propagation. They represent energy stored close to the slab. In terms of k_{xa}^2, the situation can be represented as shown by Fig. 4.2 below.

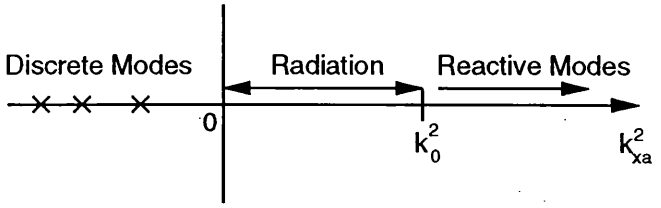

Figure 4.2: Illustration of mode spectrum of dielectric slab guide.

4.1.2 Modes of the Continuum

The wave equation (4.2) can be solved for the radiation modes, i.e. with $0 \leq k_{xa}^2 \leq k_0^2$, to give (in the slab):

$$E_y = B \cos \sigma x$$

where B is a constant and σ represents a continuous set of values defined by $\sigma^2 = \epsilon_r k_0^2 - \beta^2$. In the air, the solution is:

$$E_y = Ce^{j\rho(x-d)} + De^{-j\rho(x-d)}$$

where $\rho^2 = k_0^2 - \beta^2$. By equating tangential field components at the interface, it can be shown that $D = C^*$ and that [75]:

$$C = \frac{B}{2}\left(\cos \sigma d + j\frac{\sigma}{\rho} \sin \sigma d\right)$$

So that in the air:

$$E_y = Ce^{j\rho(x-d)} + C^*e^{-j\rho(x-d)}$$

For both the guided and radiation modes, the other field expressions can be found from equation (4.1).

The foregoing has demonstrated the existence of the three parts of the spectrum of infinite slab guide; the discrete, radiative, and reactive modes. This theory applies equally to the H-guide structure considered in Chapters 5 and 6, but with the additional complication of the bounding in the y direction.

4.2 Choice of Method for Taper Analysis

Various methods for analysing waveguide discontinuities were introduced in Section 2.3. Most of the differential equation techniques lead to similar sets of equations. In these approaches, the fields of a non-uniform waveguide at a point are expressed as a sum of the fields of the uniform waveguide whose dimensions are defined by the cross section of the taper at that point. These are so-called local normal modes [90, 96]. In the expansion in terms of local normal modes performed by Marcuse [90], the transverse fields in the non-uniform guide are expressed as a summation of the guided and radiation mode amplitudes of the local uniform guide:

$$\begin{aligned} \mathbf{E}_t &= \sum_{\nu=1}^{N} a_\nu \mathcal{E}_{\nu t} + \int_0^\infty a_\rho \mathcal{E}_{\rho t}\, d\rho \\ \mathbf{H}_t &= \sum_{\nu=1}^{N} b_\nu \mathcal{H}_{\nu t} + \int_0^\infty b_\rho \mathcal{H}_{\rho t}\, d\rho \end{aligned} \tag{4.5}$$

The script letters are the fields of the local normal modes, a and b are amplitude coefficients and N is the number of guided modes supported by the uniform guide. Equation (4.5) can be written in compact form as:

$$\begin{aligned} \mathbf{E_t} &= \sum_{\nu} a_\nu \mathcal{E}_{\nu t} \\ \mathbf{H_t} &= \sum_{\nu} b_\nu \mathcal{H}_{\nu t} \end{aligned} \tag{4.6}$$

Based on these equations, Marcuse derived a set of coupled mode equations for the forward and backward travelling waves (denoted by '+' and '-' superscripts):

$$\begin{aligned} \frac{da_\mu^+}{dz} + j\beta_\mu a_\mu^+ &= -\frac{1}{2}\sum_{\nu=1}^{N} a_\nu^+[R_{\mu\nu} + S_{\mu\nu}] + \frac{1}{2}\sum_{\nu=1}^{N} a_\nu^-[R_{\mu\nu} - S_{\mu\nu}] \\ \frac{da_\mu^-}{dz} - j\beta_\mu a_\mu^- &= \frac{1}{2}\sum_{\nu=1}^{N} a_\nu^+[R_{\mu\nu} - S_{\mu\nu}] - \frac{1}{2}\sum_{\nu=1}^{N} a_\nu^-[R_{\mu\nu} + S_{\mu\nu}] \end{aligned} \tag{4.7}$$

with coupling coefficients defined by:

$$\begin{aligned} R_{\mu\nu} &= \int_{-\infty}^{\infty}\int_{-\infty}^{\infty} \mathcal{E}_{\mu t}^* \times \frac{d\mathcal{H}_{\nu t}}{dz} \cdot \hat{\mathbf{z}}\, dx\, dy \\ S_{\mu\nu} &= \int_{-\infty}^{\infty}\int_{-\infty}^{\infty} \frac{d\mathcal{E}_{\nu t}}{dz} \times \mathcal{H}_{\mu t}^* \cdot \hat{\mathbf{z}}\, dx\, dy \end{aligned} \tag{4.8}$$

The difficulty in implementing these equations for a taper lies in the existence of the infinite integrals over the radiation spectrum. Various methods of solution have been proposed for specific geometries [94, 78, 95]. It was considered that application of equations (4.7) and (4.8) to the IDG taper would be a difficult task. Instead, it was decided to bypass the problem of dealing with the integrals across

the radiation spectrum by investigating the use of a mode matching technique based on a bounded structure.

4.3 The Bounded Mode Matching Method: Existing Theory

The bounded mode matching (BMM) method was introduced in Section 2.3. It is a method for the analysis of single abrupt discontinuities in planar dielectric waveguides. The technique was introduced by Brooke and Kharadly in [84] and given a more complete exposure in [85].

In this section the basics of the method are discussed and some intermediate results presented before consideration is given to applying the technique to H-guide steps and tapers in Chapter 6.

4.3.1 Basic Theory

As has been seen, open waveguiding structures require the continuum of radiative and reactive modes to be taken into account as well as the finite number of guided modes. When trying to analyse discontinuities in open waveguide one inevitably generates expressions containing infinite integrals across the continuum such as those involved in the coupled mode equations (4.5) and (4.7). These integrals are difficult to deal with. The bounded mode matching method seeks to solve this problem by bounding the open waveguide discontinuity with either a perfect electric conductor (PEC) or perfect magnetic conductor (PMC). Such an arrangement is shown in Fig 4.3.

It can be shown that there is a correspondence between the bounded and un-

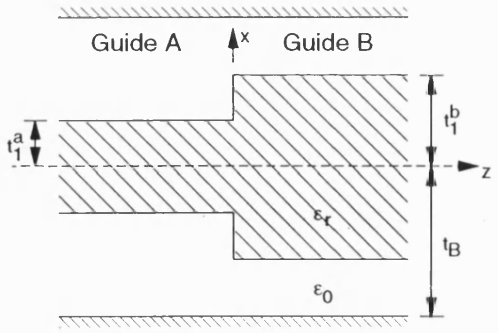

Figure 4.3: Bounded step discontinuity in dielectric slab.

bounded structures which allows an approximate solution to the original open problem to be generated. Mathematically the BMM method is much more straightforward than, say, the rigorous Ritz-Galerkin (RG) approach of Rozzi [80].

The three parts of the spectrum in the open waveguide are surface waves, radiation, and attenuated (reactive) radiation. The equivalent modes in the bounded case are referred to as slow, fast, and evanescent modes respectively. In [85] it is shown that there is a one-to-one correspondence between the mode spectra of the bounded and unbounded guides. Specifically, the analysis shows that the fast and evanescent modes are functionally identical to the radiative spectrum of the open case, but at discrete values of the propagation constant. The slow modes and surface modes become functionally identical as the bounding is moved towards infinity, although in reality the bounding need only be a small number of free space wavelengths away from the waveguide for the modes to be virtually identical.

The correspondence between the open and closed configurations is considered in more detail later, though the formal analysis has not been included here as it is presented in full in [85]. The analysis holds equally for H-guide; the bounding in the y direction does not affect the substance of the argument.

The method proceeds by applying a standard mode matching technique such as that proposed by Clarricoats and Slinn [74] to the closed guide of Fig. 4.3. In

the figure, a mode of unit amplitude is assumed to be incident from waveguide A. Mode matching at the interface between the guides A and B gives:

$$\mathbf{e}_i^a + \sum_{n=1}^{\infty} a_n \mathbf{e}_n^a = \sum_{m=1}^{\infty} b_m \mathbf{e}_m^b \tag{4.9}$$

$$\mathbf{h}_i^a - \sum_{n=1}^{\infty} a_n \mathbf{h}_n^a = \sum_{m=1}^{\infty} b_m \mathbf{h}_m^b \tag{4.10}$$

where $\mathbf{e}$ and $\mathbf{h}$ are the transverse fields. The subscript i refers to the incident mode, the superscripts a and b refer to modes in the A and B guides respectively, and n and m are mode labels. a and b are the unknown reflected and transmitted mode amplitudes.

The summations in the above mode matching equations can be truncated so that N modes are considered to exist on each side of the discontinuity. Clarricoats and Slinn proposed solution of the mode matching equations by application of the orthogonality conditions:

$$\begin{aligned} \int_0^{t_B} \mathbf{e}_k^a \times \mathbf{h}_i^a \cdot \hat{\mathbf{z}}\, dx &= \delta_{ki} P_k^a \\ \int_0^{t_B} \mathbf{e}_k^b \times \mathbf{h}_i^b \cdot \hat{\mathbf{z}}\, dx &= \delta_{ki} P_k^b \end{aligned} \tag{4.11}$$

where t_B is the separation between the centre of the waveguide and the bounding.

By integrating equation (4.9) and taking the vector cross product with $\mathbf{h}_k^a$, application of orthogonality leads to:

$$\delta_{ki} P_i^a + a_k P_k^a = \sum_{m=1}^{N} b_m P_{mk}^{ba} \tag{4.12}$$

where:

$$P_{mk}^{ba} = \int_0^{t_B} \mathbf{e}_m^b \times \mathbf{h}_k^a \cdot \hat{\mathbf{z}}\, dx \tag{4.13}$$

Now by integrating equation (4.10) and crossing with $\mathbf{e}_k^a$, application of orthogonality leads to:

$$a_k = \delta_{ki} - \sum_{m=1}^{N} \frac{b_m P_{km}^{ab}}{P_k^a} \tag{4.14}$$

where $k = 1, \cdots, N$ and:

$$P_{km}^{ab} = \int_0^{t_B} \mathbf{e}_k^a \times \mathbf{h}_m^b \cdot \hat{\mathbf{z}}\, dx \tag{4.15}$$

Adding equations (4.12) and (4.14) leads to

$$\sum_{m=1}^{N} b_m (P_{mk}^{ba} + P_{km}^{ab}) = 2\delta_{ki} P_i^a \tag{4.16}$$

Solution of this set of simultaneous equations leads to values for the amplitude coefficients b_m. The coefficients a_k are then obtained from equation (4.14) by substitution.

Brooke and Kharadly followed Clarricoats [70] in defining a set of normalised mode coefficients as follows:

$$\bar{a}_n = a_n \left(\frac{P_n^a}{P_i^a} \right)^{\frac{1}{2}}$$

$$\bar{b}_m = b_m \left(\frac{P_n^b}{P_i^b} \right)^{\frac{1}{2}}$$

for $m, n = 1, \cdots, N$. By doing this, a check on power conservation can be carried out by defining the power error P_e as:

$$P_e = 1 - \sum_{n=1}^{N_p^a} |\bar{a}_n|^2 - \sum_{m=1}^{N_p^b} |\bar{b}_m|^2 \tag{4.17}$$

where N_p^a and N_p^b are the numbers of propagating modes in guides A and B. Similarly, an approximate value for the power radiated by the discontinuity can be obtained by summing the power in the modes with β between zero and k_0:

$$P_r = \sum_{n=N_s^a+1}^{N_p^a} |\bar{a}_n|^2 + \sum_{m=N_s^b+1}^{N_p^b} |\bar{b}_m|^2$$

where N_s^a and N_s^b are the numbers of slow modes propagating in guides A and B, i.e. modes with $\beta > k_0$.

Brooke and Kharadly derived expressions for the orthogonality terms P_k^a and P_k^b and the inter-waveguide orthogonality terms P_{mk}^{ba} and P_{km}^{ab} for the even TE and TM infinite dielectric slab guide. These are not reproduced here. However, expressions for the H-guide are considered in Chapter 6.

4.3.2 The Mode Spectra

In this section the correspondence of the surface and slow modes of the open and closed slab guides is considered, together with the form of the fast mode spectrum.

Fig. 4.4 is a comparison of the closed and open configurations, showing the ratio of

the slow mode to surface mode propagation constant. The results are for even TE modes with PMC bounding, and t_1 and t_B are the slab thickness and distance from the slab centre to the bounding. It is clear that once $(t_B - t_1)$ is increased above about $1.5\lambda_0$ the propagation constants for the slow and surface modes are virtually identical. Brooke and Kharadly noted that bounding of the TE case with a PEC is less satisfactory than bounding with a PMC as the ratio of β values displays cut-off behaviour. This is not necessarily a problem if the user of the method is aware of the cut-off value, but given a free choice PMC bounding for TE modes seems the wisest choice.

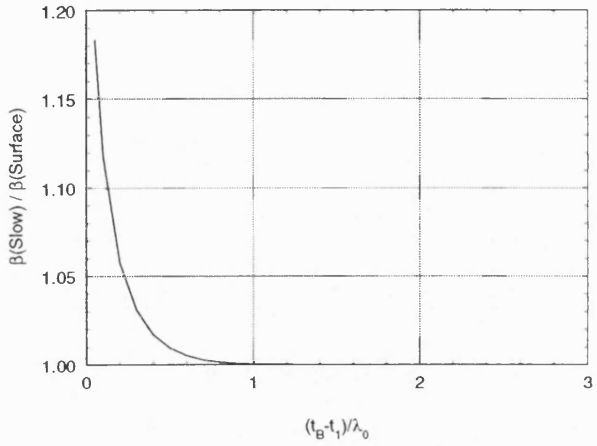

Figure 4.4: Ratio of the propagation constant of the slow mode to that of the surface wave for the grounded slab.

Fig. 4.5 shows the variation of the fast mode propagation constants as $t_{B0} = t_B/\lambda_0$ is varied for an odd TE guide with PMC bounding. The variation of β with t_{B0} can be seen to be great, especially for the lower part of the fast mode range. The figure shows that by bounding the structure, the continuum of modes in the range $0 \leq \beta/k_0 \leq 1$ has been reduced to a number of discrete modes. The distribution of the fast modes over this range is uneven, however, and this has a significant effect on the mode matching solution. This is demonstrated in Section 4.3.4 where the effect of varying the distance to the boundary is investigated.

Another point to note from Fig. 4.5 is that modes transfer from the evanescent region into the fast mode region at regular intervals of t_{B0} of about 0.5. Therefore,

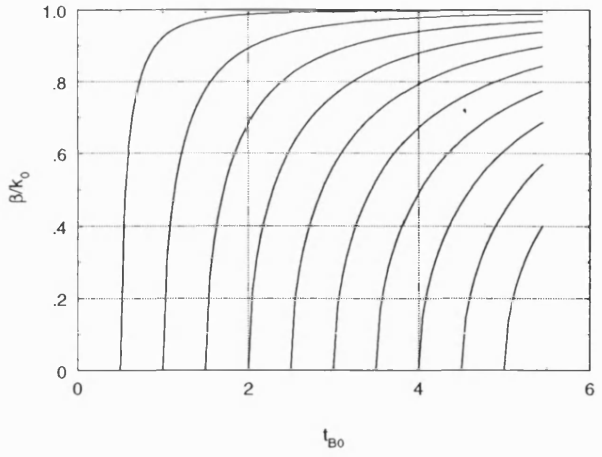

Figure 4.5: Variation of fast mode propagation constants with t_{B0} for a grounded slab guide.

each time the bounding distance is increased by $\lambda_0/2$ a new mode is added to the fast mode spectrum.

4.3.3 Validation of the Current Implementation

The method outlined in Section 4.3.1 has been implemented as part of the current work. Before continuing it is necessary to demonstrate correct operation of the implementation by comparison to existing results.

Results have been obtained for an even TE slab guide step where $\epsilon_r = 5.0$, $t_1^a = 0.07\lambda_0$ and $t_1^b = 0.35\lambda_0$. The second slow mode of guide B was considered as the incident mode. The magnitude and argument of the input reflection coefficient b_2 was monitored for two values of $t_{B0} = t_B/\lambda_0$ and a range of values of N, where N is the number of modes considered to exist on either side of the discontinuity, as defined in Section 4.3.1. The power error P_e for each case was calculated, where P_e is as defined in equation (4.17). The results are presented in Tables 4.1 and 4.2. Values generated by the current implementation are shown against those given by Brooke and Kharadly in [85].

	Reference [85]			Current Work		
N	$\|b_2\|$	Arg(b_2)	P_e	$\|b_2\|$	Arg(b_2)	P_e
5	0.4237	0	0.5974	0.4237	0	0.5974
10	0.4050	0.5164	0.0136	0.4050	0.5164	0.0136
15	0.4081	0.5490	0.0013	0.4081	0.5497	0.0013
20	0.4081	0.5537	0.0002	0.4081	0.5537	0.0002
25	0.4081	0.5541	2e-5	0.4082	0.5541	8.4e-5
30	0.4082	0.5545	2e-5	0.4082	0.5545	2.6e-5
40	0.4082	0.5546	1e-5	0.4082	0.5546	1.1e-5

Table 4.1: Results for $t_{B0} = 2.0$.

	Reference [85]			Current Work		
N	$\|b_2\|$	Arg(b_2)	P_e	$\|b_2\|$	Arg(b_2)	P_e
5	0.2203	0	8.58	0.2203	0	8.58
10	0.4444	0.2678	0.2330	0.4444	0.2678	0.2330
15	0.4299	0.5490	0.0132	0.4299	0.5492	0.0132
20	0.4265	0.5604	0.0130	0.4265	0.5604	0.0130
25	0.4286	0.5770	0.0061	0.4286	0.5770	0.0061
30	0.4294	0.5934	0.0009	0.4294	0.5934	0.0009
40	0.4294	0.5961	0.0001	0.4294	0.5961	0.0001

Table 4.2: Results for $t_{B0} = 4.0$.

The tables show extremely close agreement between the sets of results. Further comparisons are made in the following sections.

4.3.4 Features of the Results

The results presented in Tables 4.1 and 4.2 demonstrate a dependence both on the truncation value N and on the boundary distance t_{B0}. The tables show that the solutions converge as N is increased, but that convergence is faster for smaller values of the boundary distance. This is illustrated graphically in Fig. 4.6 where the power error P_e is plotted against N for three values of t_{B0}. These results indicate that higher order modes are more readily excited as t_{B0} is increased, as more modes

are needed for convergence for the higher bounding distances. An explanation of this behaviour is given in [85].

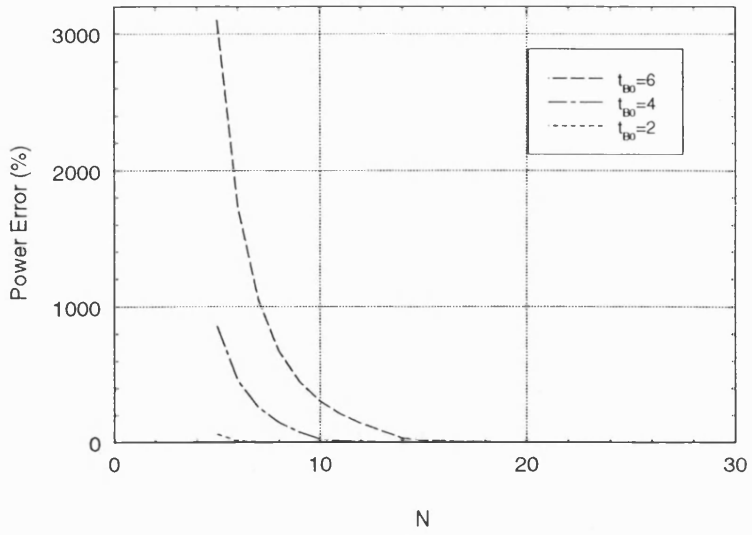

Figure 4.6: Variation of power error with N for dielectric slab.

Again considering Tables 4.1 and 4.2, it can be seen that the solution converges on different values of b_2 for the two values of t_{B0}. To investigate this characteristic, consider an even TE slab step with $\epsilon_r = 5.0$, $t_1^a = 0.2t_1^b$ and $t_1^b = 0.35\lambda_0$ with the second slow mode from guide B incident on the junction. Fig. 4.7 shows the reflection coefficient b_2 for a range of t_{B0}. The truncation value N was fixed at 40 to keep the power error low.

The results from the current implementation are the solid line in this figure, whilst the values used to create the dotted line have been transcribed from a plot given in [85]. The agreement is good in terms of the period and peak values of the oscillation, but the shapes are somewhat different with the Brooke and Kharadly results being more sinusoidal. It is not known how many t_{B0} points were taken to generate the Brooke and Kharadly results. However, if only a moderate number of points were taken, and a curve fitting routine was used to construct the characteristic, then these results would not seem to be inconsistent with the results of the current work, for which 816 points were taken.

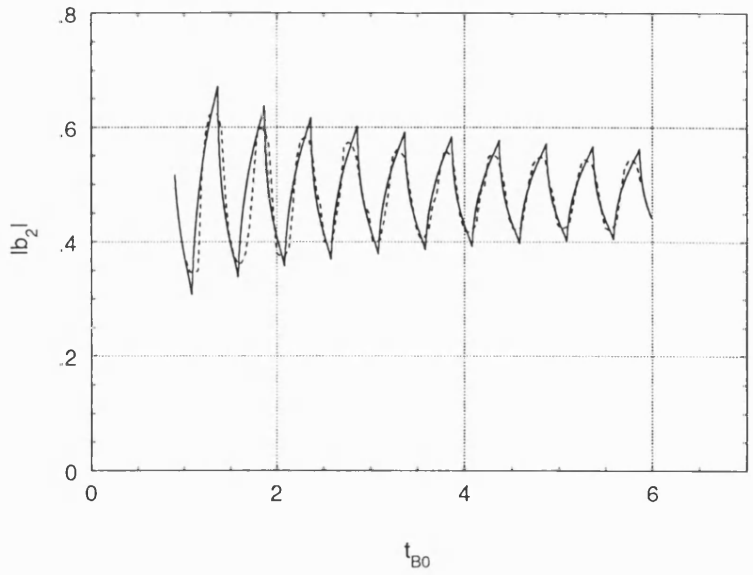

Figure 4.7: Variation of $|b_2|$ with t_{B0}. Current work: ——, Brooke and Kharadly: – – –.

The results show a significant and oscillatory variation in the reflection coefficient as t_{B0} is varied. Some qualitative explanation for the shape of the curve can be attempted. The oscillations can be attributed to the variable density of the fast modes across the range $0 \leq \beta \leq k_0$ as shown in Fig. 4.5. As the modes vary with t_{B0} their contributions to the mode matching solution vary.

It can be seen that the period of the oscillation is approximately $0.5\lambda_0$. This can be related to the transition of a mode from the evanescent mode region to the fast mode region of the spectrum every $0.5\lambda_0$ as discussed above. Whilst the fast modes are very dispersive with t_{B0}, Fig. 4.4 shows that the slow modes are little affected by changes in t_{B0}. Thus the contribution of the slow modes to the mode matching solution is constant, and it is to this that the reasonably constant mean in the curve of Fig. 4.7 can be attributed. The slow convergence of the solution can be explained by the slow increase in the density of the fast modes in the lower part of the spectrum visible in Fig. 4.5.

The magnitude of the scattering coefficient oscillations depends on the degree to which the lower part of the fast mode spectrum is excited. For some discontinuities

these modes are not greatly excited and the method is accurate. However, it is clear that the accuracy of the method is compromised when significant power is scattered into this part of the spectrum. Ideally, t_{B0} should be increased so that coverage is improved but the slow convergence with t_{B0} means that a large N is required for a satisfactory solution - it has already been shown that convergence is slower for large t_{B0}. Limited computer resources prevent N being increased indefinitely, so using a large value of t_{B0} may be impractical. A simple extension to the bounded mode matching approach provides a way around this problem. This is referred to as the variable bounded mode matching (VBMM) method. [85].

4.3.5 The Variable Bounded Mode Matching Method

As has been noted, the oscillation shown in Fig. 4.7 is about a reasonably constant mean value. According to Brooke and Kharadly the assumption that the oscillations are about a fixed mean value seems to be valid for sufficiently large values of t_{B0}. Thus, averaging the scattering coefficients over a range of t_{B0} values should give a good estimate of the mean value.

For the example considered in the last section, Table 4.3 lists some averaged results for various ranges of t_{B0} (where each range is referred to as Δt_{B0}), using an averaging interval of $0.1t_{B0}$. These results were obtained using the current implementation, which are again very close to Brooke and Kharadly's results (not reproduced here). Rozzi's results [80] for the same configuration have also been included, for both six and ten term Laguerre polynomial expansions. Comparison with Rozzi's results shows good agreement. Hence it is shown that the assumption that the mean value of the scattering coefficient oscillation approximates to the required solution is valid.

A full characterisation of a slab guide step provides further comparison with Rozzi's results. For a step with $\epsilon_r = 5.0$, $t_1^a = 0.2t_1^b$ and $t_1^b = 0.159\lambda_0$ the following

	Δt_{B0}	$\|a_1\|$	$\|b_1\|$	$\|b_2\|$
VBMM	0.9 - 1.4	0.3258	0.1765	0.4728
	1.9 - 2.4	0.3262	0.1795	0.4790
	3.9 - 4.4	0.3265	0.1808	0.4814
Rozzi	R_6	0.3282	0.1834	0.4940
	R_{10}	0.3272	0.1814	0.4820

Table 4.3: Comparison of scattering coefficients calculated using the variable bound method and Rozzi's method with six and ten terms in the expansion (R_6 and R_{10}).

	Rozzi	VBMM
$\|\Gamma_1\|$%	20.40	20.39
Arg(Γ_1)-π rad	-0.0860	-0.0843
$\|T\|$%	94.16	94.13
Arg(T) rad	-0.0075	-0.0069
$\|\Gamma_2\|$%	24.79	24.83
Arg(Γ_2) rad	0.0764	0.0739
Forward Rad. Loss	7.18	7.21

Table 4.4: Characterisation of a dielectric waveguide step: comparison of variable bound to Rozzi's results.

parameters were used in the calculation: $N = 40$, $t_{B0} = 1$ to 3 made up from 40 steps of 0.05. Table 4.4 shows the results obtained when the step was characterised. The table uses Rozzi's nomenclature for input and output reflection coefficients (Γ_1 and Γ_2) and transmission coefficient (T).

Rozzi's results quoted in Table 4.4 are for 20 polynomial expansion terms. Good agreement between the results can be seen. This agreement with Rozzi's results demonstrates that the bounded approach is effectively a method of performing a numerical integration over the continuous spectrum of the original problem.

4.3.6 Analysis of a Dielectric Slab Waveguide Step

As an example of the application of the method, the scattering and radiation properties of a step in slab guide (see Fig. 4.3) were analysed using the variable bound approach. A range of slab thicknesses t_1^b were considered. Other parameters were as follows: $\epsilon_r = 5.0$, $t_1^a = 0.2t_1^b$, $N = 40$, $t_{B0} = 0.9$ to 1.4 in steps of 0.1.

Guide A supports one slow mode, whilst guide B supports three. The slow mode in guide A is labelled as mode 1, those in guide B are labelled as modes 2, 3, and 4 respectively.

Fig. 4.8 shows the normalised TE slow mode scattering coefficients for a range of t_1^b/λ_0. Note that $|S_{ij}|$ refers to the reflection coefficient of the jth mode with respect to the ith incident mode. Fig. 4.9 shows the total radiated power for the configuration, where curve A_1 relates to incidence of mode 1, and curves B_1, B_2 and B_3 relate to incidence of modes 2, 3, and 4.

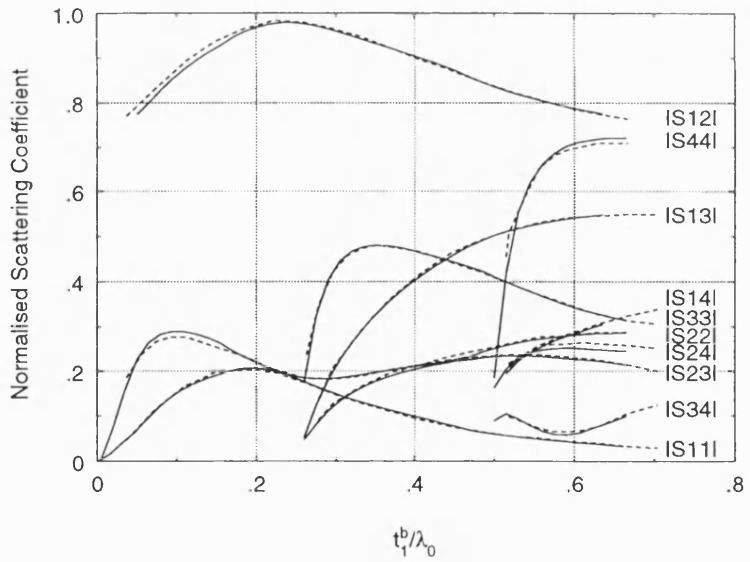

Figure 4.8: Normalised TE slow mode scattering coefficients for a range of t_1^b/λ_0. Current work: ——, Brooke and Kharadly: – – –.

The solid lines in Figures 4.8 and 4.9 are results from the current implementation, the dotted lines are Brooke and Kharadly's results. These were transcribed by

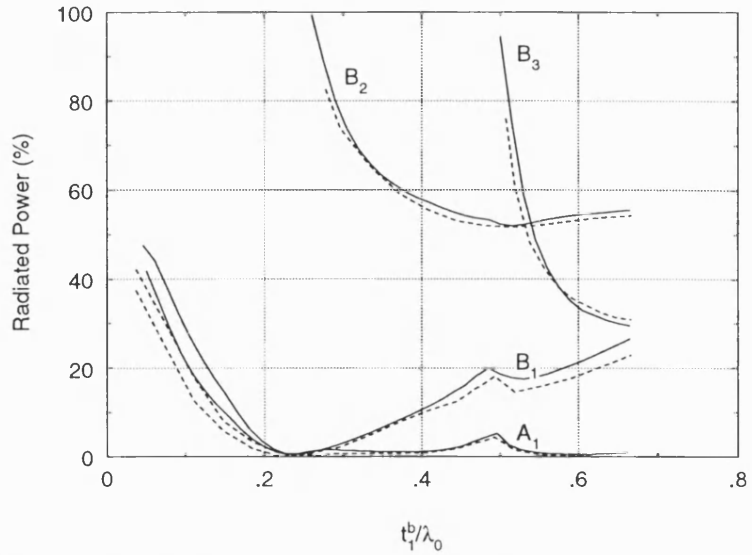

Figure 4.9: Normalised radiated power. Current work: ——, Brooke and Kharadly: – – –.

hand from [85], so some degree of error must be expected due to this. Even so, the results show very good agreement. The Brooke and Kharadly results are, in turn, favourably compared to Rozzi's results in the paper.

4.3.7 Verification of the Results Against Simple Theory

Results for the analysis of a small step using the variable-bound approach are presented in this section and are verified using the simple theoretical method used by Rozzi [80].

For a small step in a slab guide (where the ratio of the guide depths is between approximately 0.4 and 1), the main effect of the step is a change in impedance. This results in the simple equivalent circuit shown in Fig 4.10 below.

In this case, the moduli of the reflection coefficients for incidence from the left (Γ_1) and incidence from the right (Γ_2) are almost identical. For the TE case, for example, where $Z_1 = \frac{\omega\mu}{\beta_1}$ and $Z_2 = \frac{\omega\mu}{\beta_2}$:

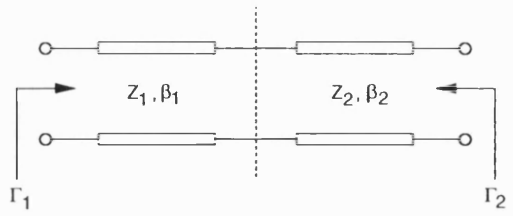

Figure 4.10: Simple equivalent circuit of step.

$$\Gamma_2 = -\Gamma_1 = \frac{Z_1 - Z_2}{Z_1 + Z_2} = \frac{\beta_2 - \beta_1}{\beta_2 + \beta_1} \tag{4.18}$$

As a numerical example consider a step with $\epsilon_r = 5.0$, $t_1^a = 0.159\lambda_0$ and $t_1^b = 0.1272t_1^a$ (i.e. $t_1^b/t_1^a = 0.8$). The parameters used in the VBMM calculation are $N = 40$ with $t_{B0} = 1$ to 3 in steps of 0.05. The VBMM results are $|\Gamma_1| = 0.0214$ and $|\Gamma_2| = 0.0216$.

Knowing that $\beta_a = 398.4$ and $\beta_b = 415.90$, the simple theory gives:

$$\Gamma_2 = -\Gamma_1 = \frac{\beta_b - \beta_a}{\beta_b + \beta_a} = 0.0215$$

The variable-bound method results are therefore in agreement with those of the simple analytical method.

4.4 Chapter Summary

The variable bounded mode matching (VBMM) method for analysis of transverse steps in open dielectric slab waveguide has been discussed in detail. The method has been implemented as part of the current work, and this implementation has been validated by comparison with existing results.

Comparison to results from an earlier theoretical method shows that VBMM effectively discretises the continuous spectrum and so provides a way of dealing with the infinite integrals across the continuum that appear in the analysis. Having demonstrated the effectiveness both of the technique and of the current implementation, the method can now be extended for application to the IDG taper. This is considered in Chapter 6.

Chapter 5

Development of the Theory: Inset Dielectric Guide

The H-guide model of Inset Dielectric Guide was introduced in Chapter 2 as a straightforward analytical alternative to some of the more rigorous, time consuming methods that have been applied to IDG in the past. In the first part of this chapter, the H-guide analysis is developed in detail. The second part of the chapter consists of a study of the fields of IDG in which the validity of the H-guide model is tested.

5.1 The Modelling of IDG as H-Guide

In this section, expressions for the LSE and LSM modes of the H-guide are developed and the longitudinal propagation constant is calculated.

The H-guide is introduced in Section 2.1.4. It consists of a dielectric slab sandwiched between infinite metal plates as shown in Fig. 2.2(a). As the fields decay away from the slab in an exponential manner it is reasonable to apply the analysis with infinite plates to the case of finite plates. The analysis presented here is

limited to those H-guide modes that exist in the open trough guide depicted below in Fig. 5.1. As shown in Fig. 2.2(b), folding down the side plates of this structure results in IDG. The assumption being made here is that it is realistic to apply the H-guide analysis to this trough guide with the side plates folded down. The validity of this assumption is investigated in Section 5.2 by comparison to results from the more accurate TRD and FDTD methods.

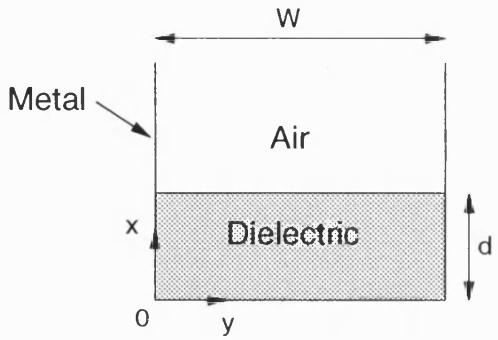

Figure 5.1: Intermediate structure in H-guide analysis.

5.1.1 H-Guide Field Expressions

The field expressions for the H-Guide are derived in this section. The H-Guide is able to support two types of mode:

- LSM modes, with $H_x = 0$. These modes can be thought of as TM modes with respect to the x direction.
- LSE modes, with $E_x = 0$, or TE modes with respect to the x direction.

The above modes correspond to those of the shallow and deep slot IDG, as discussed in Section 2.1.2.

Method of Analysis

The H-Guide fields are derived from the Hertzian vector potentials:

$$\mathbf{\Pi}_e = \hat{\mathbf{x}}\psi_e(x,y)e^{-j\beta z} \tag{5.1}$$

$$\mathbf{\Pi}_h = \hat{\mathbf{x}}\psi_h(x,y)e^{-j\beta z} \tag{5.2}$$

where β is the propagation constant in the longitudinal (z) direction, and $\hat{\mathbf{x}}$ is a unit vector in the x direction.

The fields can be expressed in terms of the Hertzian vector potentials as follows [96]:

$$\begin{aligned} \mathbf{E} &= k^2\mathbf{\Pi}_e + \nabla\nabla\cdot\mathbf{\Pi}_e - j\omega\mu\nabla\times\mathbf{\Pi}_h \\ \mathbf{H} &= j\omega\epsilon\nabla\times\mathbf{\Pi}_e + k^2\mathbf{\Pi}_h + \nabla\nabla\cdot\mathbf{\Pi}_h \end{aligned} \tag{5.3}$$

The scalar potentials satisfy the wave equation:

$$\nabla_t^2\psi_{e,h}(x,y) + (\epsilon_r k_0^2 - \beta^2)\psi_{e,h}(x,y) = 0 \tag{5.4}$$

where k_0 is the free space propagation constant and ϵ_r is the relative permittivity of the dielectric material.

Solution of the Scalar Wave Equation

Solution of equation (5.4) is performed by separation of variables [125, chapter 7]. In the dielectric region, this leads to the following scalar potential and propagation

constant relationships:

$$\psi_{e,h} = (A\cos k_x x + B\sin k_x x)(C\cos k_y y + D\sin k_y y) \tag{5.5}$$

$$k_y^2 + k_{xd}^2 = \epsilon_r k_0^2 - \beta^2 \tag{5.6}$$

In the air region, separation of variables gives:

$$\psi_{e,h} = [A\exp\gamma_x(x-d) + B\exp -\gamma_x(x-d)][C\cos k_y y + D\sin k_y y] \tag{5.7}$$

$$k_y^2 - \gamma_x^2 = k_0^2 - \beta^2 \tag{5.8}$$

In the above equations, k_{xd} is the propagation constant in the x direction in the dielectric, $k_{xa} = j\gamma_x$ is the propagation constant in the x direction in the air region, k_y is the propagation constant across the slot (in the y direction), and A, B, C and D are constants.

Field Expressions

LSM Mode Fields The LSM fields are obtained by considering the case where $\psi_h = 0$. Equation (5.3) thus becomes [123]:

$$\begin{aligned} \mathbf{E} &= k^2\mathbf{\Pi}_e + \nabla\nabla\cdot\mathbf{\Pi}_e = \nabla\times\nabla\times\mathbf{\Pi}_e \\ \mathbf{H} &= j\omega\epsilon\nabla\times\mathbf{\Pi}_e \end{aligned}$$

Substituting equation (5.1) into the above yields expressions for the fields:

$$\begin{aligned} E_x &= -\frac{\partial^2\psi_e(x,y)}{\partial y^2} - \gamma^2\psi_e(x,y) \\ E_y &= \frac{\partial^2\psi_e(x,y)}{\partial x \partial y} \\ E_z &= -\gamma\frac{\partial\psi_e(x,y)}{\partial x} \\ H_x &= 0 \\ H_y &= -j\omega\epsilon_0\epsilon_r\gamma\psi_e(x,y) \\ H_z &= -j\omega\epsilon_0\epsilon_r\frac{\partial\psi_e(x,y)}{\partial y} \end{aligned} \tag{5.9}$$

where $\gamma = j\beta$. Note that the z dependence $e^{-j\beta z}$ introduced in equations (5.1) and (5.2) has been dropped from the above equations. This also applies to all the field expressions given below.

The boundary conditions to be applied to the wave equation solutions (5.5) and (5.7) are:

- $E_z = E_y = 0$ at $x = 0$
- $E_x = E_z = 0$ at $y = 0$ and $y = W$
- Fields must decay away from the dielectric slab surface

Application of these conditions gives the following expressions for the fields in the slab:

$$\begin{aligned} E_x &= A_d(k_y^2 + \beta^2)\cos k_{xd}x \sin k_y y \\ E_y &= -A_d k_{xd} k_y \sin k_{xd}x \cos k_y y \\ E_z &= jA_d\beta k_{xd} \sin k_{xd}x \sin k_y y \end{aligned}$$

$$\begin{aligned} H_x &= 0 \\ H_y &= A_d \omega \epsilon_0 \epsilon_r \beta \cos k_{xd} x \sin k_y y \\ H_z &= -j A_d \omega \epsilon_0 \epsilon_r k_y \cos k_{xd} x \cos k_y y \end{aligned} \tag{5.10}$$

and the fields in the air:

$$\begin{aligned} E_x &= A_a (k_y^2 + \beta^2) e^{-\gamma_x (x-d)} \sin k_y y \\ E_y &= -A_a \gamma_x k_y e^{-\gamma_x (x-d)} \cos k_y y \\ E_z &= A_a \gamma_x \gamma e^{-\gamma_x (x-d)} \sin k_y y \\ H_x &= 0 \\ H_y &= A_a \omega \epsilon_0 \beta e^{-\gamma_x (x-d)} \sin k_y y \\ H_z &= -j A_a k_y \omega \epsilon_0 e^{-\gamma_x (x-d)} \cos k_y y \end{aligned} \tag{5.11}$$

where $k_y = \frac{n\pi}{W}$, and A_a and A_d are constants for the air and dielectric regions respectively.

LSE Mode Fields The LSE fields are obtained by considering the case where $\psi_e = 0$. Equation (5.3) thus becomes [123]:

$$\begin{aligned} \mathbf{E} &= -j\omega\mu_0 \nabla \times \mathbf{\Pi}_h \\ \mathbf{H} &= k^2 \mathbf{\Pi}_h + \nabla\nabla \cdot \mathbf{\Pi}_h = \nabla \times \nabla \times \mathbf{\Pi}_h \end{aligned}$$

Substituting equation (5.2) into the above yields expressions for the fields:

$$E_x = 0$$

$$
\begin{aligned}
E_y &= j\omega\mu_0\gamma\psi_h(x,y) \\
E_z &= j\omega\mu_0\frac{\partial\psi_h(x,y)}{\partial y} \\
H_x &= -\frac{\partial^2\psi_h(x,y)}{\partial y^2} - \gamma^2\psi_h(x,y) \\
H_y &= \frac{\partial^2\psi_h(x,y)}{\partial x\partial y} \\
H_z &= -\gamma\frac{\partial\psi_h(x,y)}{\partial x}
\end{aligned}
\tag{5.12}
$$

Applying the boundary conditions as for the LSM case to the wave equation solutions (5.5) and (5.7) gives the following expressions for the fields in the slab:

$$
\begin{aligned}
E_x &= 0 \\
E_y &= -A_d\omega\mu_0\beta\sin k_{xd}x\cos k_y y \\
E_z &= -jA_d\omega\mu_0 k_y\sin k_{xd}x\sin k_y y \\
H_x &= A_d(k_y^2+\beta^2)\sin k_{xd}x\cos k_y y \\
H_y &= -A_d k_{xd}k_y\cos k_{xd}x\sin k_y y \\
H_z &= -jA_d\beta k_{xd}\cos k_{xd}x\cos k_y y
\end{aligned}
\tag{5.13}
$$

and the fields in the air:

$$
\begin{aligned}
E_x &= 0 \\
E_y &= -A_a\omega\mu_0\beta e^{-\gamma_x(x-d)}\cos k_y y \\
E_z &= -jA_a\omega\mu_0 k_y e^{-\gamma_x(x-d)}\sin k_y y \\
H_x &= A_a(k_y^2+\beta^2)e^{-\gamma_x(x-d)}\cos k_y y \\
H_y &= A_a\gamma_x k_y e^{-\gamma_x(x-d)}\sin k_y y \\
H_z &= jA_a\beta\gamma_x e^{-\gamma_x(x-d)}\cos k_y y
\end{aligned}
\tag{5.14}
$$

where $k_y = \frac{n\pi}{W}$.

5.1.2 Calculation of the Propagation Constants

The propagation constants for the guide can be calculated either using the transverse resonance method [123] or by equating tangential field components at the air/dielectric interface. For the single-dielectric structure considered here neither method has a particular advantage over the other, so the method of equating tangential field components is applied below. However, for a layered dielectric system transverse resonance would be the method of choice, as the equivalent circuit representation used in this method allows the characteristic equation to be derived more efficiently than by equating fields at each interface.

From the previous section (equations (5.6) and (5.8)), the propagation constants satisfy the following conditions in the dielectric and air respectively:

$$\begin{aligned} k_{xd}^2 + k_y^2 + \beta^2 &= \epsilon_r k_0^2 \\ k_{xa}^2 + k_y^2 + \beta^2 &= k_0^2 \end{aligned}$$

Subtracting these two equations gives:

$$k_{xd}^2 + \gamma_x^2 = (\epsilon_r - 1)k_0^2 \tag{5.15}$$

For the LSM case: Equating E_y and H_z components respectively at $x = d$ gives:

$$\begin{aligned} A_a\gamma_x &= A_d k_{xd} \sin k_{xd} d \\ A_a &= \epsilon_r A_d \cos k_{xd} d \end{aligned}$$

Combining these two equations leads to:

$$\epsilon_r \gamma_x = k_{xd} \tan k_{xd} d \tag{5.16}$$

Equations (5.15) and (5.16) can be solved for the propagation constants. Combining these equations yields the equation to be solved for k_{xd} as:

$$\epsilon_r^2 u^2 \cos^2 u + u^2 \sin^2 u = v^2 \epsilon_r^2 \cos^2 u \tag{5.17}$$

where $u = k_{xd} d$ and $v = \sqrt{(\epsilon_r - l) k_0^2 d^2}$. Once k_{xd} has been found, γ_x follows from equation (5.16).

For the LSE case: Equating E_y and H_z components respectively at $x = d$ gives:

$$\begin{aligned} A_a &= A_d \sin k_{xd} d \\ A_a\gamma_x &= -k_{xd} A_d \cos k_{xd} d \end{aligned}$$

Combining these two equations leads to:

$$-\gamma_x = k_{xd} \cot k_{xd} d \tag{5.18}$$

Equations (5.15) and (5.18) can be solved for the propagation constants. Combining these equations yields the equation to be solved for k_{xd} as:

$$u^2 - v^2 \sin^2 u = 0 \tag{5.19}$$

where $u = k_{xd}d$ and $v = \sqrt{(\epsilon_r - l)k_0^2 d^2}$. Once k_{xd} has been found, γ_x follows from equation (5.18).

The characteristic equations (5.16) and (5.18) are the same as those for modes of the infinite dielectric slab waveguide [96]. In the x direction:

- LSM H-Guide modes are equivalent to even TM slab waveguide modes.
- LSE H-Guide modes are equivalent to odd TE slab waveguide modes.

5.1.3 Solution of the Characteristic Equations

Equations (5.17) and (5.19) must be solved either graphically or numerically. Graphical methods are only of any real use for fault finding and for gaining additional insight into the problem.

There are a number of numerical methods that can be used for root finding (see [134] for example). The method chosen for use here is a modified bisection method [126]. This method makes possible the simultaneous search for several roots, and can be applied to a wide variety of functions. No conditions are placed on the function other than that it be continuous within the interval of interest.

In order to apply a root finding routine, it is necessary to know the interval over which the routine is to work. In this application, this range is dictated by the fact that the roots of interest are those leading to real values of the longitudinal propa-

gation constant β. The range of k_{xd} which gives real β is discussed in Section 4.1.1 and is as follows:

$$0 \leq k_{xd} \leq k_0\sqrt{\epsilon_r - 1}$$

5.1.4 Fundamental Modes of H-Guide

LSM: Using the results of Section 5.1.1, and recognising that $k_y = 0$ is not a valid solution, the H-Guide field expressions for the fundamental mode are, in the slab:

$$\begin{aligned}
E_x &= A_{d1}\left(\left(\frac{\pi}{W}\right)^2 + \beta_1^2\right)\cos k_{xd1}x \sin\frac{\pi}{W}y \\
E_y &= -A_{d1}k_{xd1}\frac{\pi}{W}\sin k_{xd1}x \cos\frac{\pi}{W}y \\
E_z &= jA_{d1}\beta_1 k_{xd1}\sin k_{xd1}x \sin\frac{\pi}{W}y \\
H_x &= 0 \\
H_y &= A_{d1}\omega\epsilon_0\epsilon_r\beta_1 \cos k_{xd1}x \sin\frac{\pi}{W}y \\
H_z &= -jA_{d1}\omega\epsilon_0\epsilon_r\frac{\pi}{W}\cos k_{xd1}x \cos\frac{\pi}{W}y
\end{aligned} \tag{5.20}$$

and the fields in the air:

$$\begin{aligned}
E_x &= A_{a1}\left(\left(\frac{\pi}{W}\right)^2 + \beta_1^2\right)e^{-\gamma_{x1}(x-d)}\sin\frac{\pi}{W}y \\
E_y &= -A_{a1}\gamma_{x1}\frac{\pi}{W}e^{-\gamma_{x1}(x-d)}\cos\frac{\pi}{W}y \\
E_z &= A_{a1}\gamma_{x1}\gamma e^{-\gamma_{x1}(x-d)}\sin\frac{\pi}{W}y \\
H_x &= 0 \\
H_y &= A_{a1}\omega\epsilon_0\beta_1 e^{-\gamma_{x1}(x-d)}\sin\frac{\pi}{W}y \\
H_z &= -jA_{a1}\frac{\pi}{W}\omega\epsilon_0 e^{-\gamma_{x1}(x-d)}\cos\frac{\pi}{W}y
\end{aligned} \tag{5.21}$$

where the quantities marked with the additional '1' subscript relate to the first LSM mode, and $A_{a1} = \epsilon_r A_{d1} \cos k_{xd1} d$.

LSE: In this case k_y is permissible, so that the H-Guide field expressions for this mode are, in the slab:

$$\begin{aligned} E_x &= 0 \\ E_y &= -A_{d1}\omega\mu_0\beta_1 \sin k_{xd1} x \\ E_z &= 0 \\ H_x &= A_{d1}\beta_1^2 \sin k_{xd1} x \\ H_y &= 0 \\ H_z &= -jA_{d1}\beta_1 k_{xd1} \cos k_{xd1} x \end{aligned} \tag{5.22}$$

and the fields in the air:

$$\begin{aligned} E_x &= 0 \\ E_y &= -A_{a1}\omega\mu_0\beta_1 e^{-\gamma_{x1}(x-d)} \\ E_z &= 0 \\ H_x &= A_{a1}\beta_1^2 e^{-\gamma_{x1}(x-d)} \\ H_y &= 0 \\ H_z &= jA_{a1}\beta_1\gamma_{x1} e^{-\gamma_{x1}(x-d)} \end{aligned} \tag{5.23}$$

where the quantities marked with the additional '1' subscript relate to the first LSE mode, and $A_{a1} = A_{d1} \sin k_{xd1} d$.

5.2 Study of the Fields of IDG

This section has two objectives: to study the fields of IDG and to assess the validity and accuracy of the H-guide model of IDG as developed in the foregoing sections. These objectives are achieved firstly by a consideration of the longitudinal propagation constant of IDG and secondly by an examination of its fields.

5.2.1 Longitudinal Propagation Constant

Fig. 5.2 shows the normalised fundamental propagation constant β/k_0 for LSM H-guide for three guide widths, W. As expected, the propagation constant drops as guide depth d is decreased. As the width is decreased, $k_y = \pi/W$ is increased and the characteristic is pulled down. Notice how $\beta < k_0$ becomes increasingly likely as the depth and width of the guide are decreased.

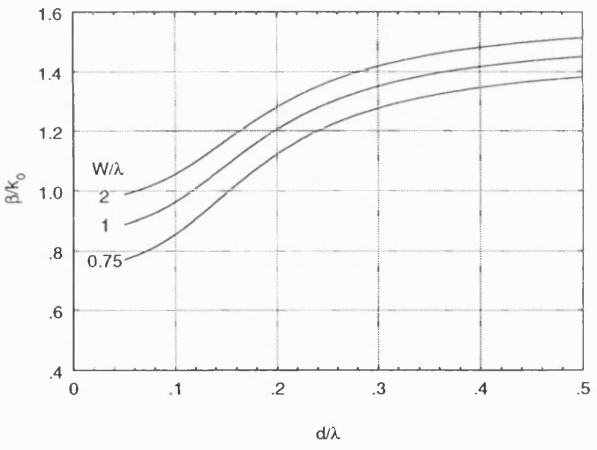

Figure 5.2: LSM H-guide propagation constant for various guide dimensions, $\epsilon_r = 2.56$.

In Figures 5.3 and 5.4 H-guide results are compared against experiment and results from two other theoretical methods, TRD and FDTD. The figures show results for the fundamental mode. One shallow slot (LSM) and two deep slot (LSE) geometries are considered. In the shallow slot case it can be seen that the H-guide results match

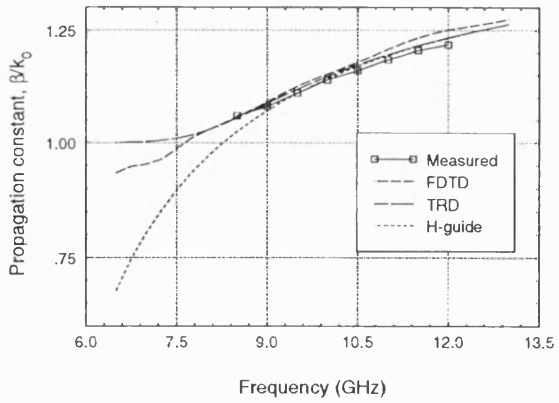

Figure 5.3: Propagation constant of shallow slot (LSM) IDG with $\epsilon_r = 2.08$. Guide is 22.86mm wide and 10.16mm deep.

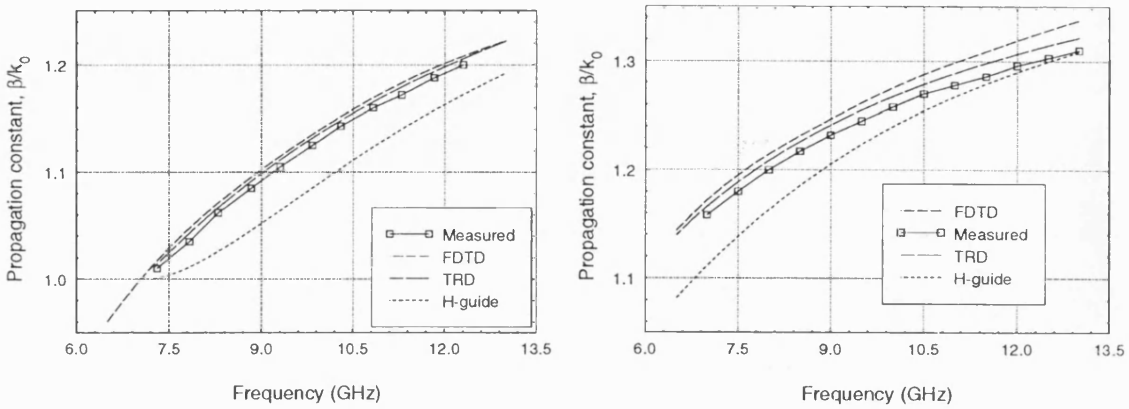

Figure 5.4: Propagation constant of deep slot (LSE) IDG with $\epsilon_r = 2.08$. Guide dimensions are (a) 10.16mm wide by 10.16mm deep, and (b) 10.16mm wide by 15.24mm deep.

the other theoretical and the measured results very closely above 9GHz. Below this frequency the H-guide results drop off too rapidly and agreement is poor. For the deep guides, FDTD and TRD are close to the measured values. The H-guide values show a reasonable match but are not as close as was observed for the shallow slot above 9GHz.

In Figures 5.5 and 5.6 H-guide and TRD results are compared for different values of the dielectric constant. FDTD results have been omitted here for clarity; the close agreement between TRD and FDTD has already been established. As might be expected given the previous results, agreement between H-guide and TRD for

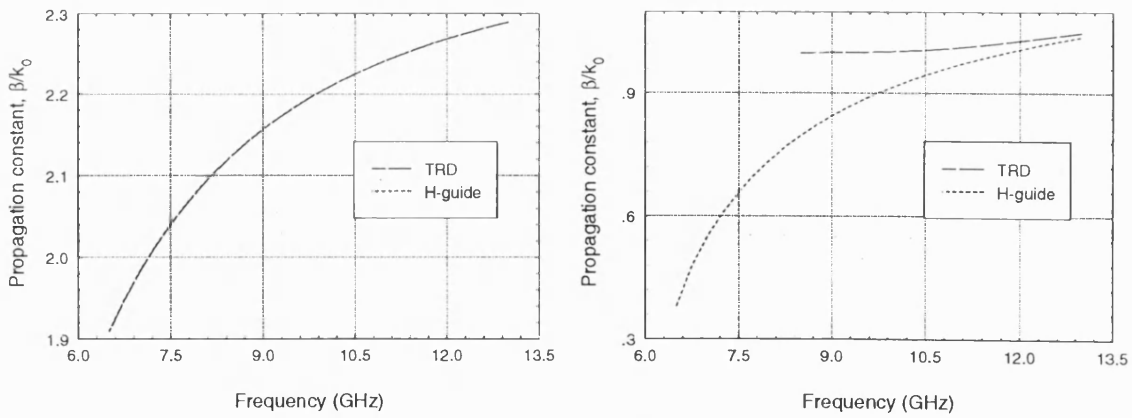

Figure 5.5: Propagation constant of shallow slot (LSM) IDG, 22.86mm wide and 10.16mm deep, with (a) $\epsilon_r = 5.8$, and (b) $\epsilon_r = 1.5$.

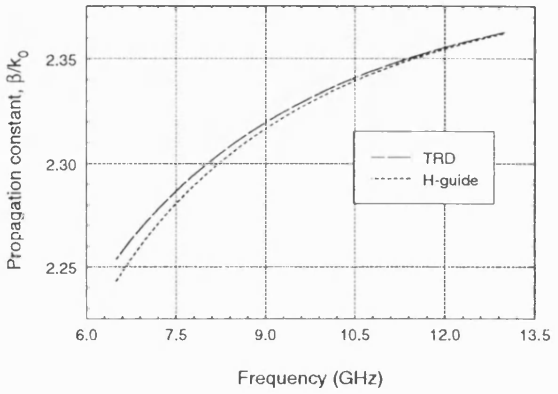

Figure 5.6: Propagation constant of deep slot (LSE) IDG with $\epsilon_r = 5.8$. Guide is 10.16mm wide and 22.86mm deep.

higher ϵ_r is good for both deep and shallow slots. Very poor agreement is shown for low ϵ_r where the TRD β/k_0 is close to 1 over the whole frequency range.

Consider now the behaviour of the H-guide and TRD propagation constants along a taper where the guide width is held constant but the depth is varied. Results at two frequencies are given for both the shallow and deep slot cases in Fig. 5.7, where the guide widths are 22.86mm and 10.16mm respectively. For the shallow slot the TRD and H-guide results are close until β/k_0 drops to around 1.1 at which point significant deviation begins to occur. Agreement is better in the deep slot case where the H-guide has $k_y = 0$ so that the excessive lowering of β/k_0 that occurs in the shallow slot case for low β/k_0 does not happen.

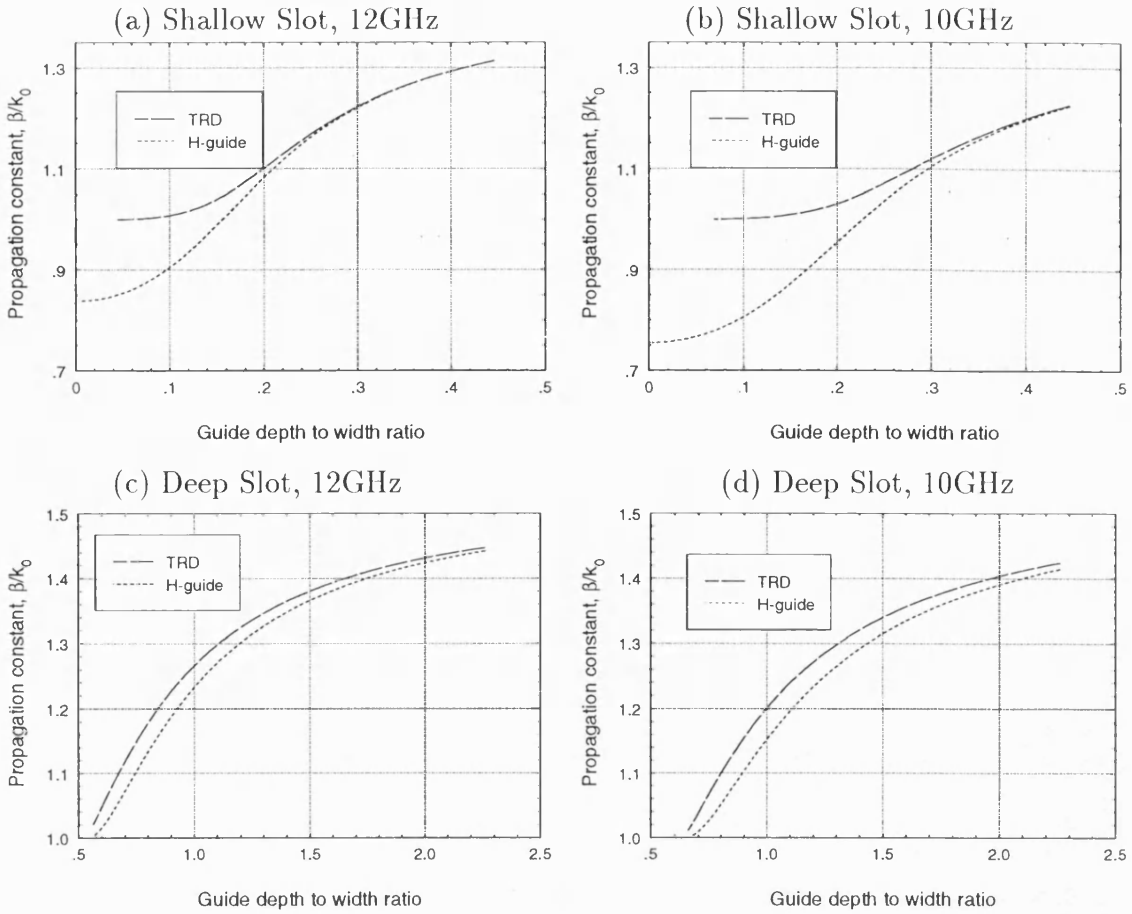

Figure 5.7: Propagation constant along IDG tapers, $\epsilon_r = 2.3$.

The above results show that the H-guide model of IDG provides quite accurate values of the propagation constant both for deep slots and for shallow slots where the TRD value is greater than a threshold value (around $1.1k_0$ in the above results). This inaccuracy in the LSM case for low β/k_0 is troublesome as the antenna structures with which this work is concerned include sections of IDG with this characteristic, particularly towards the end of the tapered slot. As such, for guides with β approaching k_0 it is prudent to derive values of β using TRD rather than the H-guide model. There is a time penalty involved in doing this, but it is unavoidable if accuracy is to be maintained. As a guide, approximate run times for the three theoretical models are as follows: FDTD 57 minutes, TRD 1 minute 10 seconds, H-guide 0.1 seconds. These timings were taken on the same machine, an HP712 workstation, and relate to the results given in Fig. 5.4(b).

5.2.2 Field Distribution

In this section plots are presented showing the field distributions at transverse cross sections of shallow and deep slot IDG. Accurate FDTD results are presented first followed by the H-guide approximations to them. Fig. 5.8 shows the six FDTD components of the field in a shallow slot, 22.86mm wide and 10.16mm deep with a dielectric constant of 2.3. The space cell size used is 0.635mm ($\lambda_0/47$ at 10GHz) so that the number of cells in the slot is 16 (x) by 36 (y).

In each figure the horizontal axis represents displacement across the slot, with the metal walls falling at $\pm$0.011m. A further 0.006m of space on each side of the slot is shown. The vertical axis shows the displacement up through the slot, with the floor of the slot at zero and the surface of the slot at 0.01m, together with an additional 0.006m of space above the guide to show the field behaviour in the air. The black rectangles in the lower corners of the plots represent a slice through the perfect electric conductor in which the dielectric is set. The guide floor is not shown. Note that each figure is normalised to the maximum of the particular field component depicted. No information regarding the relative field magnitudes can be derived from these figures; it is the field shapes rather than their absolute values that are of interest here.

Before commenting on the FDTD results it is useful to reproduce the H-guide approximations of these same field components. These are depicted in Fig. 5.9. Note that there are only five components in this case as the LSM analysis has $H_x = 0$. In these results, data is given for the 0.006m of air above the dielectric but no data is given outside the $\pm$0.011m slot width; the field outside these bounds is zero in the H-guide analysis. Otherwise, however, these results are directly comparable with those of FDTD.

In comparing the two sets of results the effect on the field distributions of the 90° metal edges, modelled by FDTD but not by H-guide, is clear. Local field peaks can

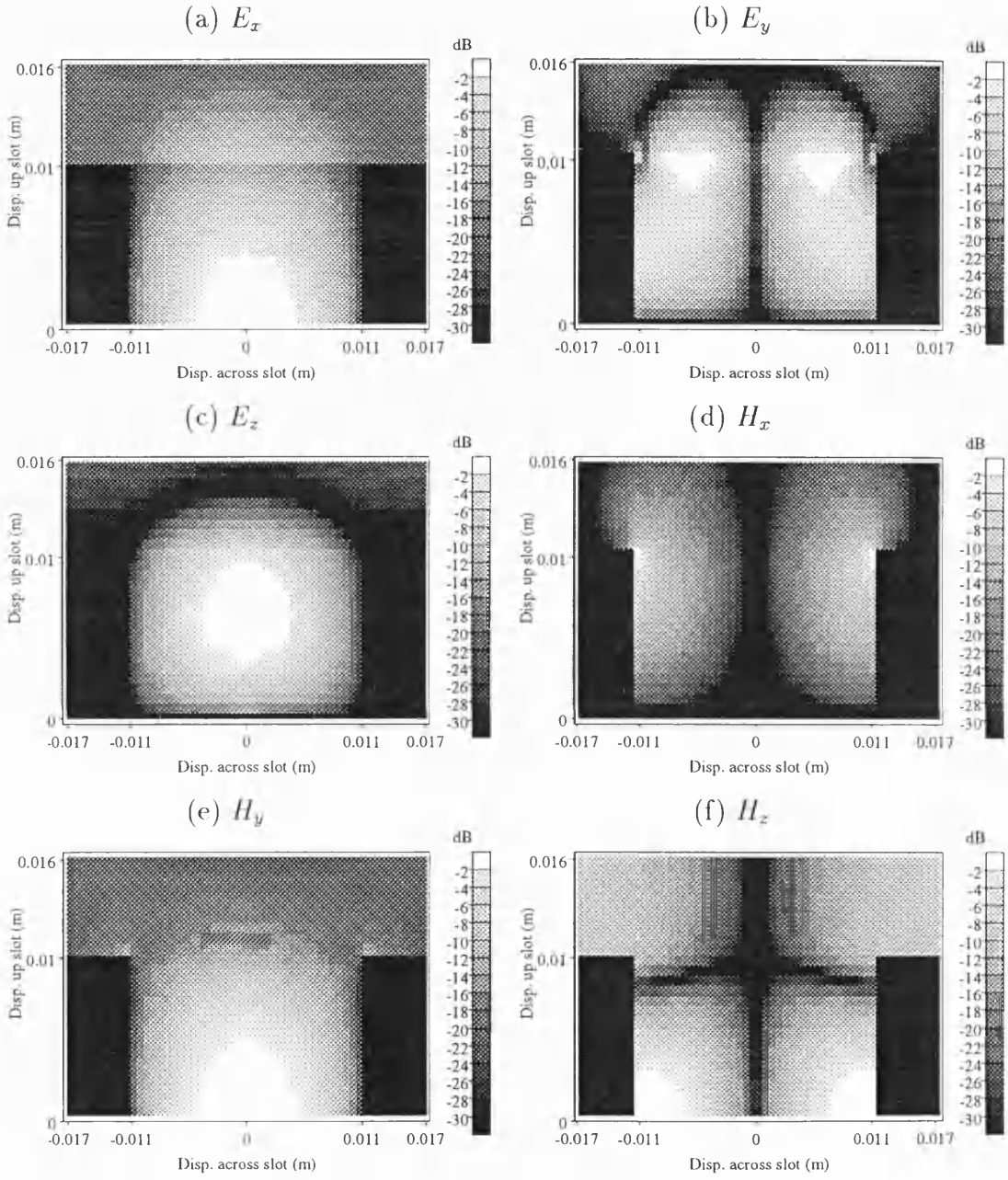

Figure 5.8: Shallow IDG field components at a cross section by FDTD.

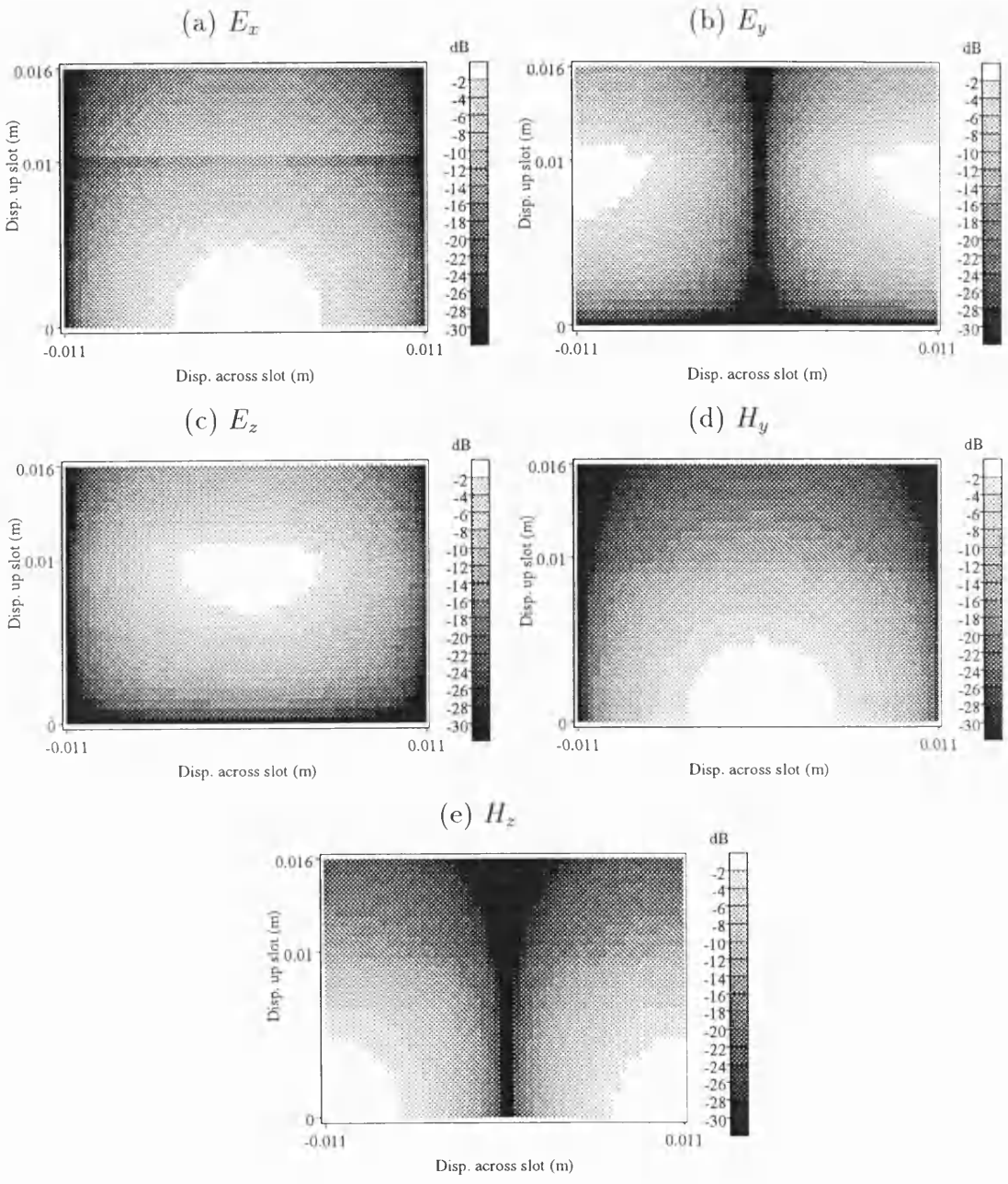

Figure 5.9: LSM H-guide field components at a cross section.

be seen around the metal edges for the FDTD E_y, H_x and H_y components. In the FDTD results, the H_x component, zero in the H-guide analysis, is dominated by the presence of the corners. Indeed, the fact that this component consists merely of two singular peaks centred on the edges justifies the five component LSM approximation used in both the TRD and H-guide analyses.

Comparing the FDTD and H-guide E_y components, the maxima have been shifted in the FDTD results by the edge effects. Similar effects can be seen in the E_z and H_z cases. In general, though, the H-guide fields are similar to those derived by the accurate FDTD analysis, particularly lower down in the slot where the influence of the edges is reduced.

A similar comparison can be made for an LSE guide, 10.16mm wide and 22.86mm deep in this case. Again, a 0.635mm space cell size is used, giving 36 (x) by 16 (y) cells in the slot. Fig. 5.10 shows the six components derived by FDTD. The fundamental LSE H-guide mode has only three non-zero components, and these are shown in Fig. 5.11.

Here, the three zero components in the H-guide analysis (E_x, E_z and H_y) are shown by FDTD to consist purely of reactions to the existence of the metal corners, and the assumption that $E_x = 0$ in the five component LSE approximation can be seen to be reasonable. In addition to these components, local field maxima can also be observed around the edges in the E_y and H_x components calculated by FDTD. However, there is good agreement in terms of the general field shape between the FDTD and H-guide representations. It is interesting to note that within the slot, away from the influence of the edges, FDTD shows the fields to be invariant with displacement across the slot as predicted by the H-guide analysis.

It is also of interest to examine the variation of the field components on the air/dielectric interface in one dimension. Fig. 5.12 depicts the shallow slot components in this format, and Fig. 5.13 shows the deep slot components, all calculated

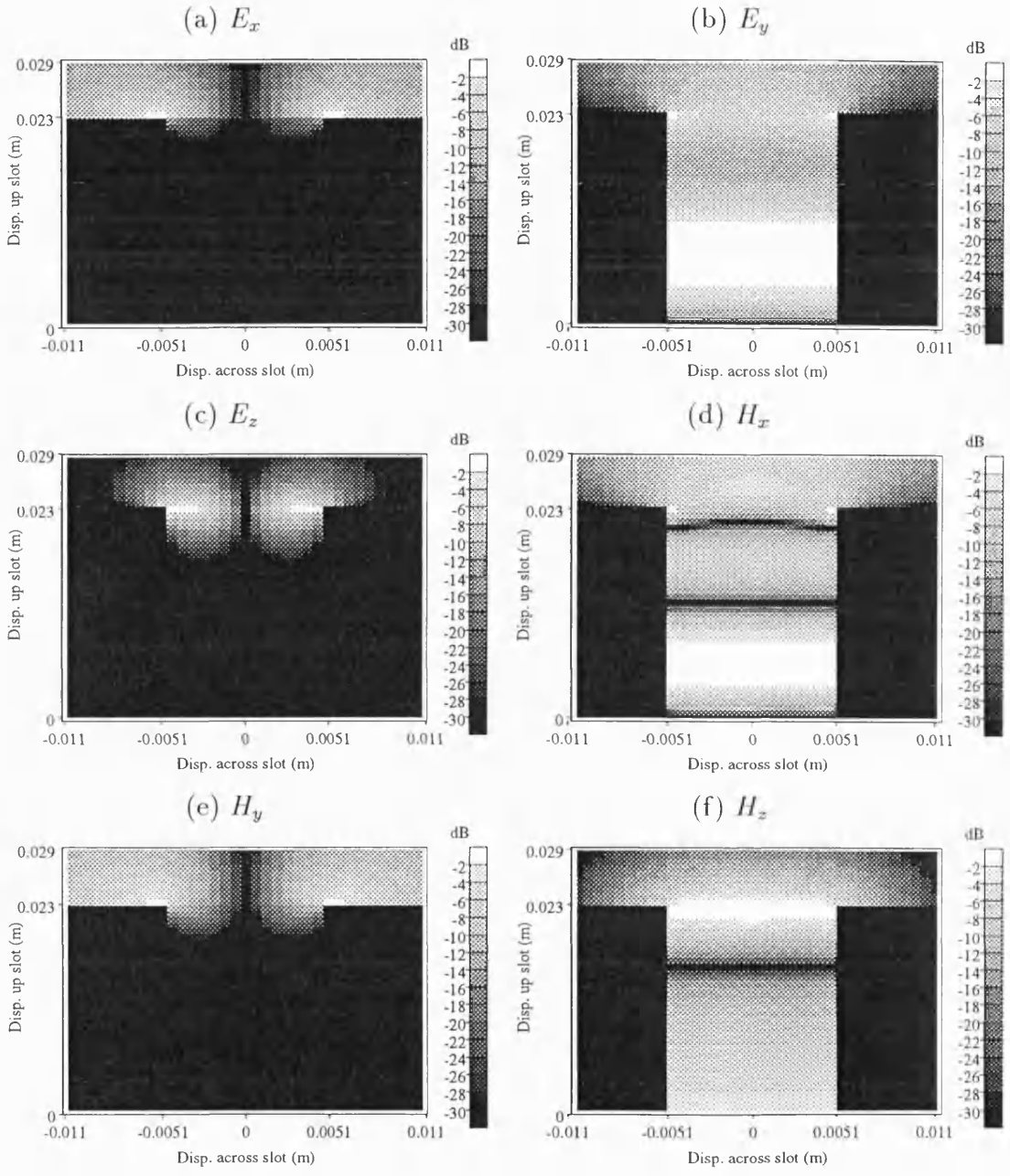

Figure 5.10: Deep IDG field components at a cross section by FDTD.

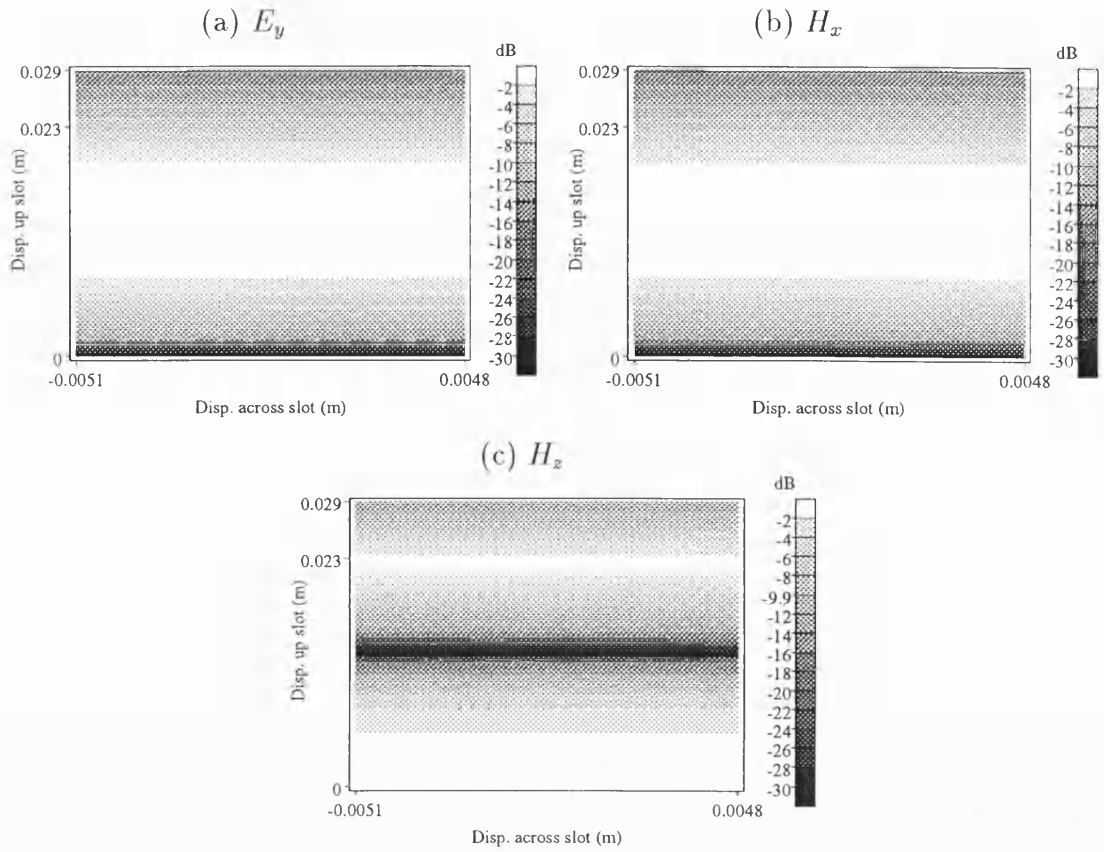

Figure 5.11: LSE H-guide field components at a cross section.

by FDTD. The shallow slot is 22.86mm wide and the deep slot is 10.16mm wide. Clearly, the general features shown here are the same as in the two-dimensional results, but this format allows the detail to be seen more easily. In these results, no normalisation of the field magnitudes has been carried out. Thus, the field magnitudes shown are those calculated by FDTD based on the parameters of the model, i.e. the excitation and the number of time steps. The relative magnitudes of the field components are therefore shown by these results. However, it should be noted that the FDTD calculation is carried out such that $Z_0 = 1$. As well as showing the peaks around the slot edges, these plots show the extent to which certain of the field components spread onto the ground plane surface.

The results of Figures 5.12 and 5.13 were generated at 9GHz using an FDTD model

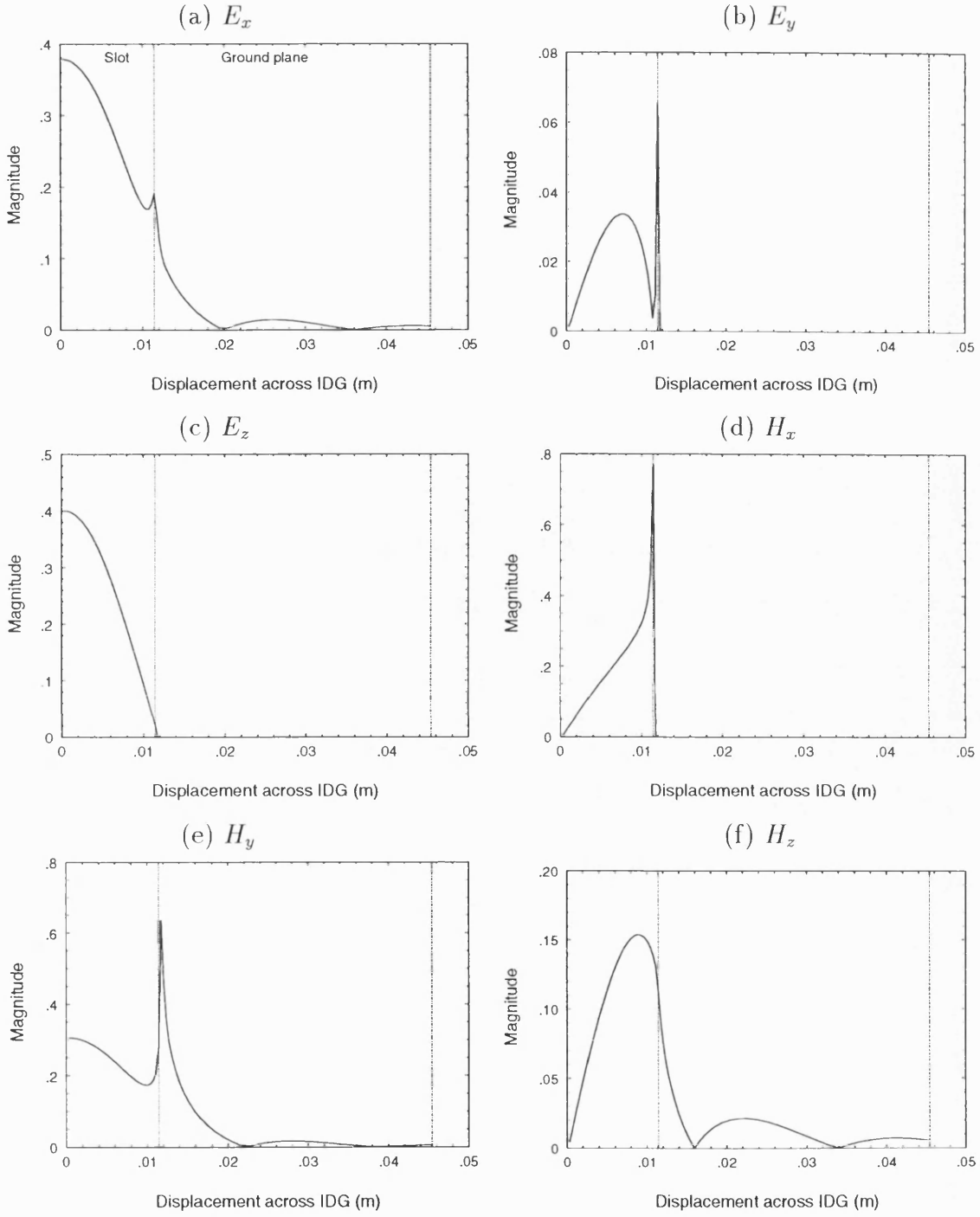

Figure 5.12: Shallow IDG fields across air/dielectric interface and ground plane.

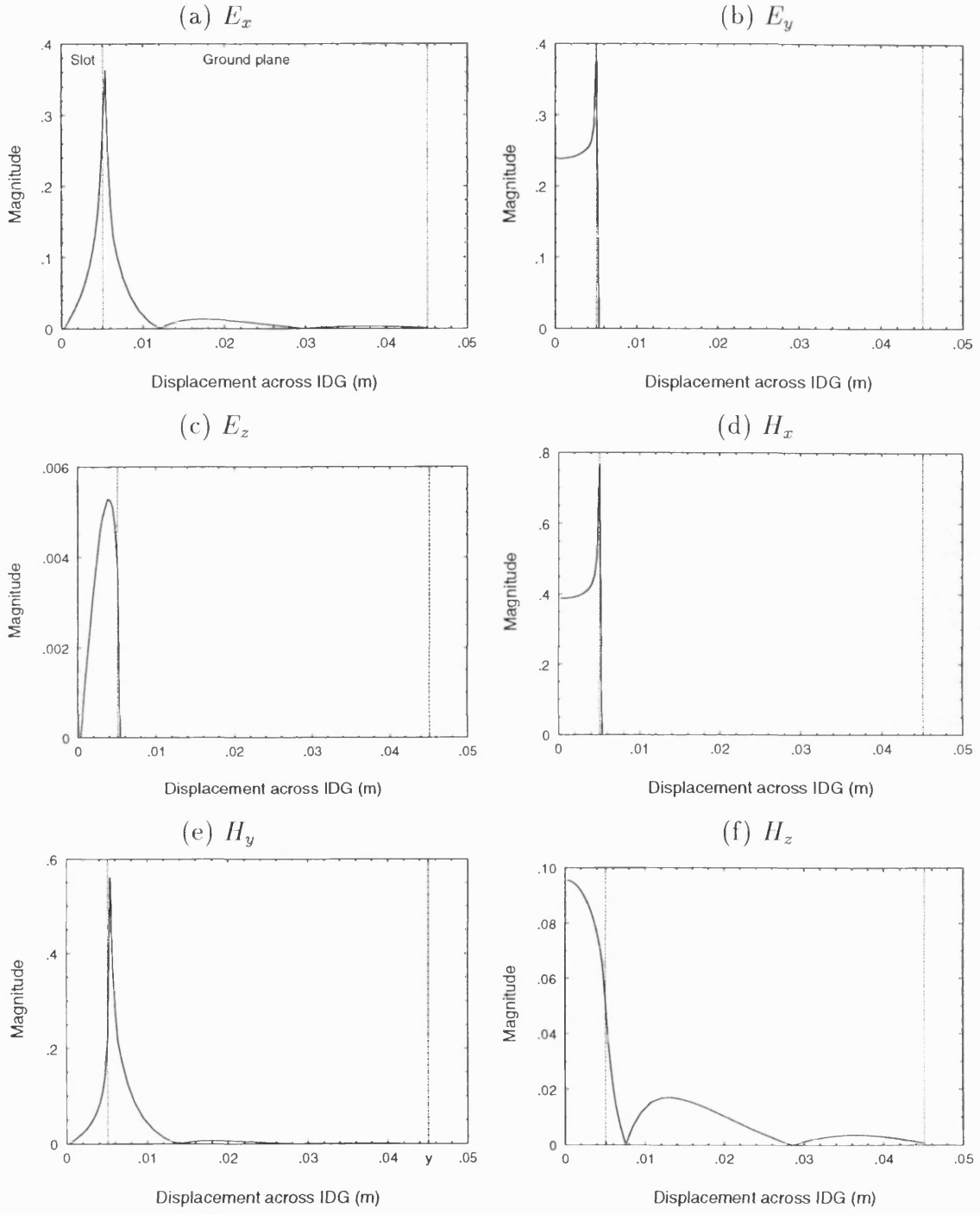

Figure 5.13: Deep IDG fields across air/dielectric interface and ground plane.

with a time step of 0.53ps, a space step of 0.3175mm, and a stability factor of 0.5. The shallow slot model has 32 (x) by 36 (y) cells in the half-slot and 71 (x) by 71 (y) cells in the air above the half-slot. The deep IDG model has 72 (x) by 16 (y) cells in the half-slot and 93 (x) by 52 (y) cells in the air above it.

The foregoing indicates that agreement between the H-guide and the FDTD, and thus the actual, field distribution is in general good. However, the 90° metal edges of the structure cause significant disturbance to the distribution which is not modelled by the H-guide analysis. The H-guide results are most accurate lower down in the dielectric, away from the edges. For the antenna analysis, however, it is the tangential surface fields that are of primary interest. It is unfortunately the case that the largest discrepancies between the H-guide and FDTD field distributions occur on the plane of greatest interest in the IDG-TSA analysis. This problem is given further consideration in Chapter 7.

5.3 Chapter Summary

The analysis of the H-guide has been developed and the degree to which the H-guide propagation constant and fields match those of IDG has been investigated.

The H-guide propagation constant compares well to measured data and values calculated by FDTD and TRD for most guide geometries. However, considerable deviation is seen when the IDG value approaches k_0.

The H-guide fields at a transverse cross section are generally similar to the IDG fields calculated by FDTD. For IDG-TSA analysis, however, it is the surface fields that are of primary interest and in this there are significant differences between the two representations.

Chapter 6

The Analysis of the H-Guide Taper

In Chapter 4 it was shown that the variable bounded mode matching (VBMM) approach can be used to provide an accurate analysis of scattering at a step in infinite even symmetry TE or TM dielectric slab waveguide. The objective of this chapter is to apply the technique firstly to H-guide steps and then to an H-guide taper, with the eventual aim of determining the power loss suffered by the first surface mode as it travels along the taper.

Two types of H-guide step are considered. In the first, the discontinuity appears in the dielectric, whilst in the second it is in the ground plane. Both LSE and LSM H-guide steps are analysed for each step type. As was noted in Chapter 5, the LSE H-guide fields exhibit no y dependence so the structure reduces to an odd TE slab. In the x direction the LSM H-guide is equivalent to an even TM slab, but the y dependence must be taken into account also.

The first section of this chapter presents expressions for the field components of bounded LSE and LSM H-guide. Mode matching expressions for H-guide step-

in-dielectric discontinuities are then given. The mode matching method used by Brooke and Kharadly [85] is unsuitable for the step-in-ground plane discontinuity. A different formulation is introduced in this chapter to handle these configurations. After having verified the VBMM method for each step type, the characteristics of H-guide steps with various dielectric thicknesses are investigated. Finally, results are presented for the power losses on the H-guide taper and comparisons with FDTD results are made.

6.1 Bounded H-Guide Field Expressions

Before generating the orthogonality and inter-waveguide orthogonality expressions it is necessary to produce the field expressions for the bounded H-guide whose structure is shown in Fig. 6.1 (a) and (b) in both longitudinal and transverse cross section. Note that the bounding in the y direction is the same on both sides of the steps considered in this chapter - only the guide depth varies.

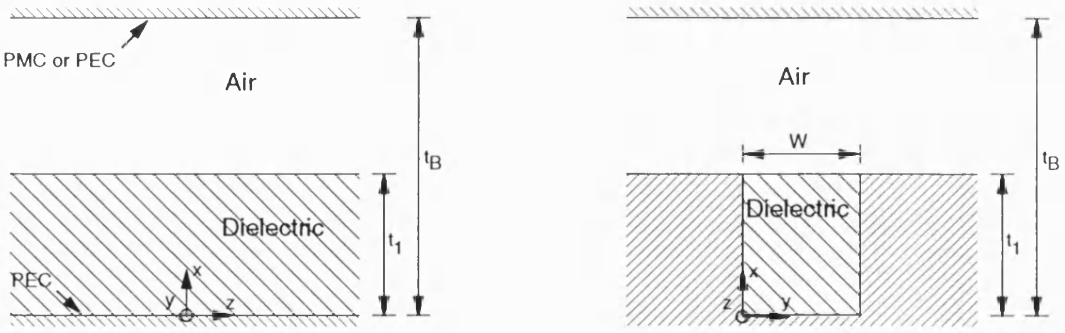

Figure 6.1: Bounded H-guide (a) Longitudinal section, and (b) Transverse section.

6.1.1 LSE H-Guide

It was noted in Section 4.3.2 that PMC bounding is most appropriate for TE slabs, so only this type of bounding is considered here. The modes of LSE H-guide are

derived in Section 5.1. The field expressions for the nth mode in the slab are the same as for the open case (equation (5.22)) although A_d has been set to 1 for convenience and the expressions have been divided by $-\omega\mu_0\beta$:

$$\begin{aligned} E_{yn} &= \sin(k_{dn}x) \\ H_{xn} &= -\frac{\beta_n}{\omega\mu_0}\sin(k_{dn}x) \\ H_{zn} &= \frac{jk_{dn}}{\omega\mu_0}\cos(k_{dn}x) \end{aligned} \tag{6.1}$$

Bearing in mind the solution to the scalar wave equation (Section 5.1.1) and knowing that tangential **H** field components must be zero at $x = t_B$, the fields in the air are derived from the potential $\varphi_{hn} = A_{an}\cos[k_{an}(x - t_B)]$:

$$\begin{aligned} E_{yn} &= A_{an}\cos[k_{an}(x - t_B)] \\ H_{xn} &= -\frac{A_{an}\beta_n}{\omega\mu_0}\cos[k_{an}(x - t_B)] \\ H_{zn} &= -\frac{jA_{an}k_{dn}}{\omega\mu_0}\sin[k_{an}(x - t_B)] \end{aligned} \tag{6.2}$$

where A_{an} is a constant, β_n is the longitudinal propagation constant, and k_{an} and k_{dn} are the x directed propagation constants in the air and dielectric respectively.

Equating tangential field components at $x = t_1$ leads to expressions for A_{an} and the characteristic equation:

$$A_{an} = \frac{\sin(k_{dn}t_1)}{\cos[k_{an}(t_1 - t_B)]} \tag{6.3}$$

$$k_{dn}\cot(k_{dn}t_1) + k_{an}\tan[k_{an}(t_1 - t_B)] = 0 \tag{6.4}$$

Rewriting equation (5.15):

$$k_{dn}^2 - k_{an}^2 = (\epsilon_r - 1)k_0^2 \tag{6.5}$$

Equations (6.4) and (6.5) can be solved by elimination of one of the unknowns and by then applying a root finding computer routine such as the modified bisection method [126]. Equation (6.4) holds for the fast and evanescent modes as k_{an} is real for these modes (refer to Section 4.1.1). For the slow modes k_{an} is imaginary, i.e. $k_{an} = j\gamma_{an}$. For solution, the equations are rearranged to split the tangent terms. Thus the equations for solution for the slow and fast modes respectively are:

$$\begin{aligned} k_{dn}\cos(k_{dn}t_1)\cosh[\gamma_{an}(t_1 - t_B)] - \gamma_{an}\sinh[\gamma_{an}(t_1 - t_B)]\sin(k_{dn}t_1) &= 0 \\ k_{dn}\cos(k_{dn}t_1)\cos[k_{an}(t_1 - t_B)] + k_{an}\sin[k_{an}(t_1 - t_B)]\sin(k_{dn}t_1) &= 0 \end{aligned} \tag{6.6}$$

These equations are further rearranged for computer solution. Details of this are given in Appendix B.

The above expressions hold for the co-ordinate system shown in Fig. 6.1, i.e. with $x = 0$ defined as being at the base of the structure. This arrangement is used for the analysis of the step-in-dielectric discontinuity. For the step-in-ground plane discontinuity it is convenient to define $x = 0$ as being at the air/dielectric interface so that the ground plane is at $x = -t_1$ and the bounding at $x = t_B$. This shift in reference plane modifies some of the above expressions slightly: in equation (6.1) 'x' is replaced by '$x + t_1$' and the sign after the first term in equation (6.4) becomes a minus. Additionally, the expressions for A_{an} and the characteristic equation use 't_B' in place of '$t_1 - t_B$'.

The correspondence between the first slow mode of the PMC bound LSE H-guide and the first surface mode of the open guide is demonstrated in Fig. 6.2. These results are for a 22.86mm deep guide at 10GHz with an ϵ_r of 2.3. The correspondence is very close; the greatest deviation between the propagation constants is 4%. The error becomes negligible (<0.01%) if the bounding is placed more than 0.5 free space wavelengths from the guide.

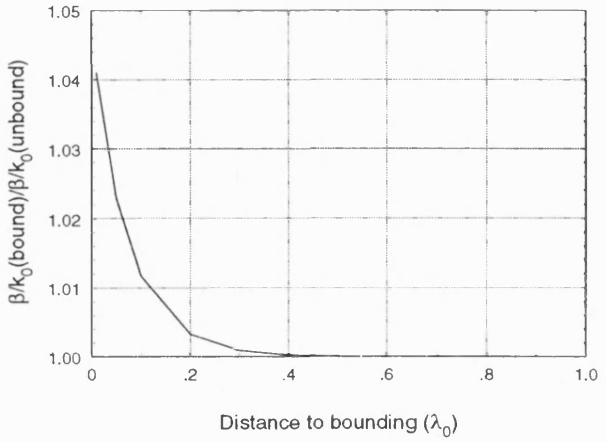

Figure 6.2: Correspondence of bounded to unbounded discrete LSE mode.

6.1.2 LSM H-Guide

The performance of both PEC and PMC bounding of the LSM H-guide needs to be investigated as this guide structure has not been considered in previous work.

PEC Bounding

The LSM field components for the open H-guide are derived in Section 5.1. The fields for the nth mode in the slab are as per the open case, i.e. equation (5.20), although for convenience A_d has been set to 1:

$$E_{xn} = (k_y^2 + \beta_n^2)\cos(k_{dn}x)\sin(k_y y)$$

$$\begin{aligned} E_{yn} &= -k_{dn}k_y \sin(k_{dn}x)\cos(k_y y) \\ E_{zn} &= j\beta_n k_{dn} \sin(k_{dn}x)\sin(k_y y) \\ H_{xn} &= 0 \\ H_{yn} &= \omega\epsilon_0\epsilon_r\beta_n \cos(k_{dn}x)\sin(k_y y) \\ H_{zn} &= -j\omega\epsilon_0\epsilon_r k_y \cos(k_{dn}x)\cos(k_y y) \end{aligned} \tag{6.7}$$

Bearing in mind the solution to the scalar wave equation and knowing that tangential **E** field components must be zero at $x = t_B$, the field components in the air are derived from the potential $\varphi_{en} = A_{an}\cos[k_{an}(x - t_B)]\sin(k_y y)$:

$$\begin{aligned} E_{xn} &= A_{an}(k_y^2 + \beta_n^2)\cos[k_{an}(x - t_B)]\sin(k_y y) \\ E_{yn} &= -k_{an}k_y A_{an}\sin[k_{an}(x - t_B)]\cos(k_y y) \\ E_{zn} &= j\beta_n k_{an} A_{an}\sin[k_{an}(x - t_B)]\sin(k_y y) \\ H_{xn} &= 0 \\ H_{yn} &= \omega\epsilon_0\beta_n A_{an}\cos[k_{an}(x - t_B)]\sin(k_y y) \\ H_{zn} &= -j\omega\epsilon_0 k_y A_{an}\cos[k_{an}(x - t_B)]\cos(k_y y) \end{aligned} \tag{6.8}$$

Equating tangential field components at the air/dielectric interface $x = t_1$ leads to expressions for A_{an} and the characteristic equation:

$$A_{an} = \epsilon_r \frac{\cos(k_{dn}t_1)}{\cos[k_{an}(t_1 - t_B)]} \tag{6.9}$$

$$k_{dn}\tan(k_{dn}t_1) - \epsilon_r k_{an}\tan[k_{an}(t_1 - t_B)] = 0 \tag{6.10}$$

The characteristic equations for the slow and fast modes respectively are:

$$\begin{aligned} k_{dn}\sin(k_{dn}t_1)\cosh[\gamma_{an}(t_1-t_B)] + \epsilon_r\gamma_{an}\sinh[\gamma_{an}(t_1-t_B)]\cos(k_{dn}t_1) &= 0 \\ k_{dn}\sin(k_{dn}t_1)\cos[k_{an}(t_1-t_B)] - \epsilon_r k_{an}\sin[k_{an}(t_1-t_B)]\cos(k_{dn}t_1) &= 0 \end{aligned} \tag{6.11}$$

Appendix B describes how these equations are rearranged for computer solution.

Again, the above expressions are modified slightly if $x = 0$ is shifted to the air/dielectric interface. The slab mode expressions use '$x + t_1$' in place of 'x' and the expressions for A_{an} and the characteristic equations use 't_B' in place of '$t_1 - t_B$'. Additionally, the sign after the first term in (6.10) is reversed.

PMC Bounding

The slab modes are the same as for the PEC case above, but the air modes are subject to the boundary condition that tangential **H** fields are zero at $t = t_B$. The potential is thus $\varphi_{en} = A_{an}\sin[k_{an}(x-t_B)]\sin(k_y y)$ and the air field components are:

$$\begin{aligned} E_{xn} &= A_{an}(k_y^2+\beta_n^2)\sin[k_{an}(x-t_B)]\sin(k_y y) \\ E_{yn} &= k_{an}k_y A_{an}\cos[k_{an}(x-t_B)]\cos(k_y y) \\ E_{zn} &= -j\beta_n k_{an}A_{an}\cos[k_{an}(x-t_B)]\sin(k_y y) \\ H_{xn} &= 0 \\ H_{yn} &= \omega\epsilon_0\beta_n A_{an}\sin[k_{an}(x-t_B)]\sin(k_y y) \\ H_{zn} &= -j\omega\epsilon_0 k_y A_{an}\sin[k_{an}(x-t_B)]\cos(k_y y) \end{aligned} \tag{6.12}$$

$$A_{an} = \epsilon_r \frac{\cos(k_{dn} t_1)}{\sin[k_{an}(t_1 - t_B)]} \tag{6.13}$$

The characteristic equations for the slow and fast modes respectively are:

$$\begin{aligned} k_{dn} \sin(k_{dn} t_1) \sinh[\gamma_{an}(t_1 - t_B)] + \epsilon_r \gamma_{an} \cosh[\gamma_{an}(t_1 - t_B)] \cos(k_{dn} t_1) &= 0 \\ k_{dn} \sin(k_{dn} t_1) \sin[k_{an}(t_1 - t_B)] + \epsilon_r k_{an} \cos[k_{an}(t_1 - t_B)] \cos(k_{dn} t_1) &= 0 \end{aligned} \tag{6.14}$$

Appendix B describes how these equations are rearranged for computer solution.

The correspondence between the first slow modes of both PMC and PEC bound LSM H-guide and the first surface mode of the open configuration is shown in Fig. 6.3.

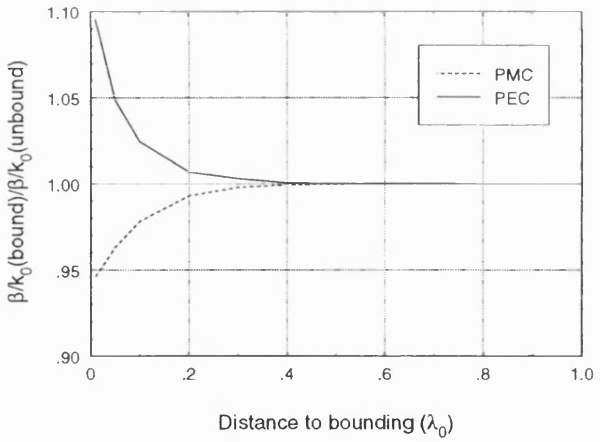

Figure 6.3: Correspondence of PMC/PEC bounded to unbounded discrete LSM mode.

The results are taken at 10GHz for a guide with a dielectric constant of 2.3, a depth of 10.16mm and a width of 22.86mm. Note that the PMC bound LSM H-guide does not display the cut-off characteristics that Brooke and Kharadly identified in [85] with respect to the TM slab, to which the LSM H-guide is related. Although the

deviation is greater for PEC bounding for the smallest values of bounding distance, the error is reduced to around 0.02% in both cases for bounding distances of greater than $0.5\lambda_0$. As such, the choice of which boundary type to use is arbitrary. For the rest of this chapter, PEC bounding will be used in conjunction with LSM H-guide.

Fig. 6.4 shows the variation of the fast mode propagation constants as the bounding distance is varied for a guide with the same characteristics as that considered in Fig. 6.3. These results demonstrate similar properties to those obtained for the TE slab in Section 4.3.2, i.e. an apparent discretisation of the radiative part of the spectrum but with an uneven distribution of modes across the range of interest and considerable variation with bounding distance. In this case however, the propagation constant values do not converge on $\beta = k_0$. This is due to the modification to the propagation constant relationships introduced by k_y, the propagation constant across the H-guide width.

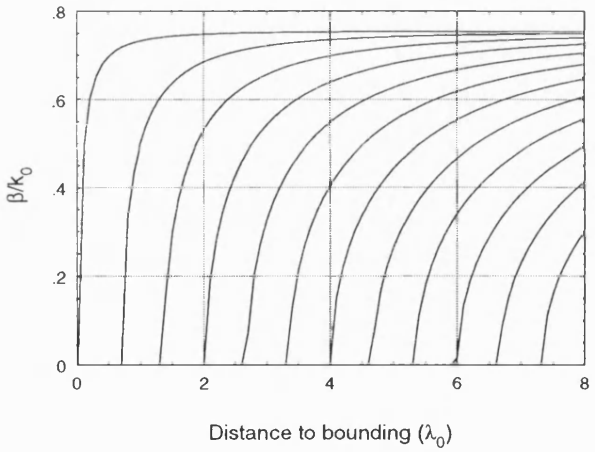

Figure 6.4: Fast mode propagation constants for PEC bounded LSM H-guide.

With $k_y = 0$, the analysis of Section 4.1.1 indicates that slow modes exist in the range $k_0^2 \leq \beta^2 \leq \epsilon_r k_0^2$ and that fast modes exist in the range $0 \leq \beta^2 \leq k_0^2$. With finite k_y these relationships are modified to $k_0^2 \leq \beta^2 + k_y^2 \leq \epsilon_r k_0^2$ and $0 \leq \beta^2 + k_y^2 \leq k_0^2$ respectively. The boundary between the slow and fast modes is thus shifted. 'Slow' modes may be found with propagation constants as low as $\sqrt{\epsilon_r k_0^2 - k_y^2}$ and the top end of the fast mode region is reduced to $\sqrt{k_0^2 - k_y^2}$ which equates to a β of $0.755k_0$

in the current example (Fig. 6.4).

The fact that the β of the discrete H-guide modes can drop below k_0 has already been identified as a major difference between H-guide and IDG (Section 5.2.1). With $\beta < k_0$ these H-guide modes must be considered as leaky, or radiative, but in the IDG with equivalent dimensions β will be greater than k_0 (assuming that cut-off has not occurred) and the mode is still bound to the dielectric to some extent. This difference between H-guide and IDG presents a problem. Further consideration is given to this later on in Sections 6.5 and 6.6.

6.2 H-Guide Step-in-Dielectric Bounded Mode Matching

Given the transverse fields it is possible to derive the bounded mode matching (BMM) orthogonality and inter-waveguide orthogonality expressions defined in equations (4.11), (4.13) and (4.15). The following sections relate to the structure shown in Fig. 6.5.

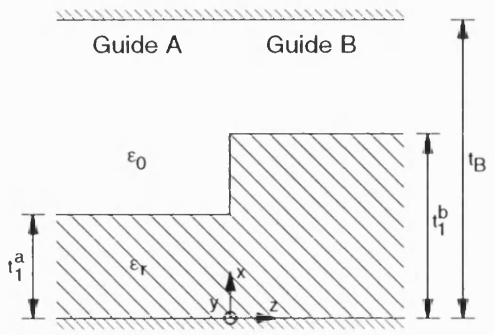

Figure 6.5: Step-in-dielectric discontinuity.

6.2.1 LSE H-Guide BMM Expressions

PMC bounding is used in this case.

$\mathbf{P_n}$: These expressions are the same for each waveguide, so the 'a' and 'b' superscripts are omitted below. P_n is defined in equation (4.11) and in the case of the LSE bounded H-guide is given by:

$$P_n = \int_0^{t_B} -E_{ny} \cdot H_{nx}\, dx$$

The result of performing this integral, using the field expressions given in Section 6.1.1, is:

$$P_n = \frac{\beta_n}{2\omega\mu}\left[t_1\left(1 - S\{2k_{dn}t_1\}\right) - A_{an}^2(t_1 - t_B)\left(1 + S\{2k_{an}[t_1 - t_B]\}\right)\right]$$

where $S\{x\}$ is shorthand for $\sin\{x\}/x$

$\mathbf{P_{nm}^{ab}}$: From equation (4.15) this is given by:

$$P_{nm}^{ab} = \int_0^{t_B} -E_{ny}^a \cdot H_{mx}^b\, dx$$

which results in the following expression:

$$P_{nm}^{ab} = \frac{\beta_m^b}{2\omega\mu_0}\left[T_1 + A_{an}^a T_2 + A_{an}^a A_{am}^b T_3\right]$$

where:

$$T_1 = t_1^a \left[S\{(k_{dn}^a - k_{dm}^b)t_1^a\} - S\{(k_{dn}^a + k_{dm}^b)t_1^a\} \right]$$

$$T_2 = \left[\frac{\cos A_1 - \cos A_2}{k_{an}^a + k_{am}^b} + \frac{\cos A_3 - \cos A_4}{k_{an}^a - k_{am}^b} \right]$$

$$T_3 = -(t_1^b - t_B) \left[S\{(k_{an}^a + k_{am}^b)(t_1^b - t_B)\} + S\{(k_{an}^a - k_{am}^b)(t_1^b - t_B)\} \right]$$

and:

$$\begin{aligned} A_1 &= (k_{an}^a + k_{dm}^b)t_1^a - k_{an}^a t_B \\ A_2 &= (k_{an}^a + k_{dm}^b)t_1^b - k_{an}^a t_B \\ A_3 &= (k_{an}^a - k_{dm}^b)t_1^b - k_{an}^a t_B \\ A_4 &= (k_{an}^a - k_{dm}^b)t_1^a - k_{an}^a t_B \end{aligned}$$

$\mathbf{P_{mn}^{ba}}$: From equation (4.13) this is given by:

$$P_{mn}^{ba} = \int_0^{t_B} -E_{my}^b \cdot H_{nx}^a \, dx$$

Evaluation of this integral reveals that P_{mn}^{ba} can be written in terms of P_{nm}^{ab} as:

$$P_{mn}^{ba} = \frac{\beta_n^a}{\beta_m^b} P_{nm}^{ab} \tag{6.15}$$

6.2.2 LSE H-Guide BMM Results

In this section, a small number of BMM results using the above expressions are presented. These results are intended to demonstrate the properties of the method as applied to this particular type of step, and indicate whether the extension to variable BMM is possible.

Firstly, it is necessary to check the convergence of the technique. Fig. 6.6 shows the variation of the slow mode reflection coefficient as the number of modes in the summation, N, is increased. The results are for a step where $t_1^a = 1.1t_1^b$, $t_1^b = 0.4\lambda_0$ and $\epsilon_r = 2.3$. It is clear that the results converge very rapidly, with as few as 10 modes being required to obtain convergence to six decimal places.

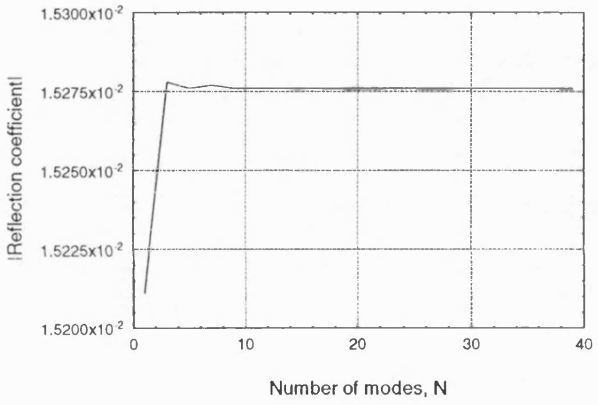

Figure 6.6: LSE H-guide step-in-dielectric convergence of reflection coefficient magnitude with N.

The remainder of the results considered in this section concern a step-down where $t_1^a = 2t_1^b$ and $t_1^b = 0.3\lambda_0$, $\epsilon_r = 2.3$ and the frequency is 10GHz (i.e. t_1^a=18mm and t_1^b=9mm). Both slabs are monomode with $\beta_a = 1.36k_0$ and $\beta_b = 1.10k_0$.

An important factor in determining whether BMM is operating satisfactorily is the power error, P_e, as defined in equation (4.17). P_e is a measure of the amount of power that is added to or subtracted from the closed system in the course of the mode matching calculations. Clearly, P_e should ideally be zero. Fig. 6.7 shows the variation in P_e as N is increased for the step defined above. It can be seen that a

very small power error can be achieved by including only 10 modes on either side of the junction. With $N = 100$, the power error is negligible (0.06ppm).

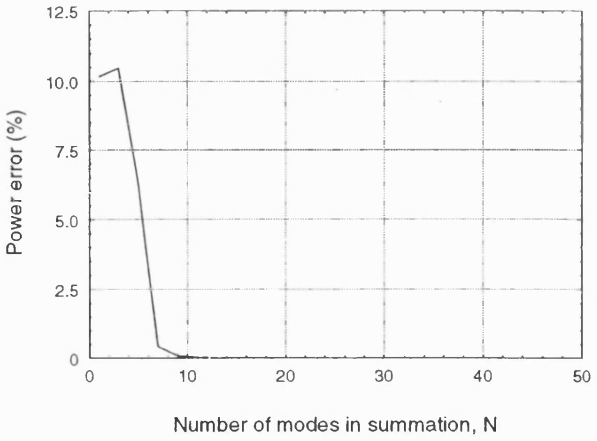

Figure 6.7: LSE H-guide step-in-dielectric variation of power error, P_e, with N. The bounding is $1.5\lambda_0$ from the guide.

Fig. 6.8 shows the manner in which power is spread across the transmitted and reflected modes at the junction. Approximately 91% of the power incident on the left hand side of the junction goes into the first, and only, slow mode (mode 1) on the right hand side. A relatively small amount of power is scattered into the other modes - logarithmic scales have been used in Fig. 6.8 in order to bring out this detail. For these results, 500 modes were considered on both sides of the junction and the bounding was placed far away from the guide ($10\lambda_0$). Modes 2 to 21 in each guide are fast modes and modes 22 upwards are reactive.

Considering the higher order modes, the figure shows that the scattered power peaks at mode 21 on both sides of the discontinuity, the boundary between the fast and reactive sections of the spectrum. Negligible power is scattered into the reactive spectrum beyond mode 60.

Fig. 6.9 shows the variation of the slow mode transmission and reflection coefficient as the distance to the boundary is varied. These results are similar to those presented for the even TE slab in Section 4.3.4. The average values of the scattering coefficient variations can be seen to be approximately constant, so that this type

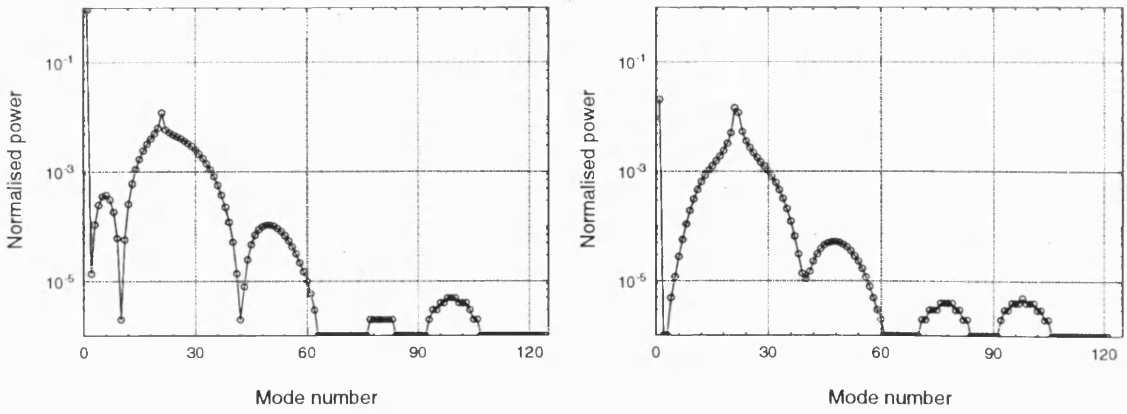

Figure 6.8: LSE H-guide step-in-dielectric spread of power across (a) transmitted modes, and (b) reflected modes.

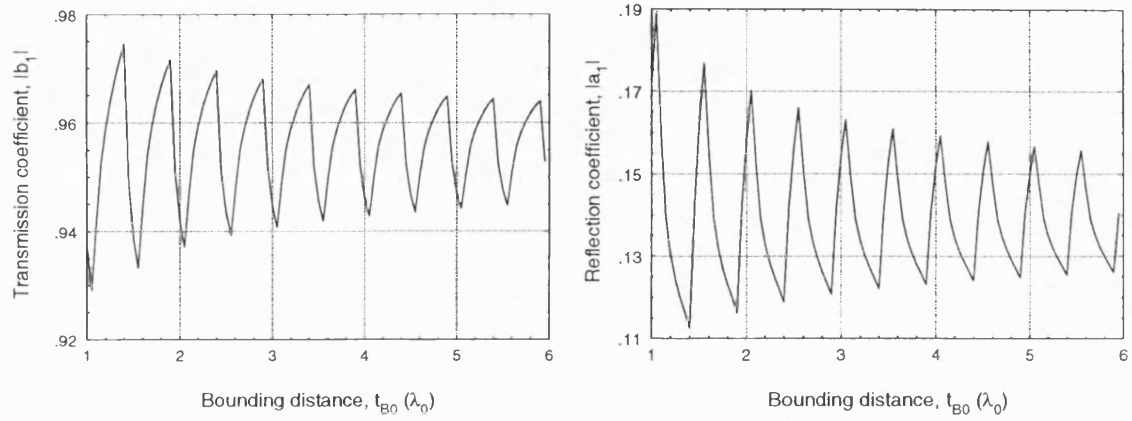

Figure 6.9: LSE H-guide step-in-dielectric scattering coefficient variation with bounding distance: (a) transmission coefficient, and (b) reflection coefficient.

of junction is amenable to the application of VBMM.

6.2.3 LSM H-Guide BMM Expressions

PEC bounding is used in this case.

P_n: This is given by the following expression:

$$P_n = \int_0^W \int_0^{t_B} E_{xn} H_{yn} \, dx \, dy$$

	$t_1^a > t_1^b$		$t_1^a < t_1^b$	
	P_{nm}^{ab}	P_{mn}^{ba}	P_{nm}^{ab}	P_{mn}^{ba}
B_1	β_m^b	β_n^a	β_m^b	β_n^a
B_2	β_n^a	β_m^b	β_n^a	β_m^b
E	1	ϵ_r	ϵ_r	1

Table 6.1: Variables for LSM H-guide step-in-dielectric mode matching expressions.

The result of performing this integral using the field expressions given in Section 6.1.2 is:

$$P_n = \frac{\omega\epsilon_0\beta_n}{4}(k_y^2+\beta_n^2)W\left[\epsilon_r t_1(1+S\{2k_{dn}t_1\}) - A_{an}^2(t_1-t_B)(1+S\{2k_{an}(t_1-t_B)\}\right]$$

$\mathbf{P_{nm}}$: For the LSM H-guide, equations (4.15) and (4.13) give these terms as:

$$P_{nm}^{ab} = \int_0^W \int_0^{t_B} E_{xn}^a H_{ym}^b \, dx\, dy$$

$$P_{mn}^{ba} = \int_0^W \int_0^{t_B} E_{xm}^b H_{yn}^a \, dx\, dy$$

These terms are slightly different for a step-up ($t_1^a < t_1^b$) than for a step-down ($t_1^a > t_1^b$). All of the values are calculated from:

$$P = \frac{\omega\epsilon_0 B_1 W}{4}(k_y^2+B_2^2)\left[\epsilon_r T_1 + E T_2 + A_{an}^a A_{am}^b T_3\right] \tag{6.16}$$

The values of the terms B_1, B_2, and E are given in Table 6.1.

For $t_1^a > t_1^b$ the terms T_1, T_2, and T_3 are:

$$T_1 = t_1^b \left[S\{(k_{dn}^a + k_{dm}^b)t_1^b\} + S\{(k_{dn}^a - k_{dm}^b)t_1^b\} \right] \tag{6.17}$$

$$T_2 = A_{am}^b \left[\frac{\sin A_1 - \sin A_2}{(k_{dn}^a + k_{am}^b)} + \frac{\sin A_3 - \sin A_4}{(k_{dn}^a - k_{am}^b)} \right] \tag{6.18}$$

$$T_3 = -(t_1^a - t_B) \left[S\{(k_{an}^a + k_{am}^b)(t_1^a - t_B)\} + S\{(k_{an}^a - k_{am}^b)(t_1^a - t_B)\} \right] \tag{6.19}$$

$$\begin{aligned} A_1 &= (k_{dn}^a + k_{am}^b)t_1^a - k_{am}^b t_B \\ A_2 &= (k_{dn}^a + k_{am}^b)t_1^b - k_{am}^b t_B \\ A_3 &= (k_{dn}^a - k_{am}^b)t_1^a + k_{am}^b t_B \\ A_4 &= (k_{dn}^a - k_{am}^b)t_1^b + k_{am}^b t_B \end{aligned} \tag{6.20}$$

For $t_1^a < t_1^b$, T_1 and T_3 are obtained from equations (6.17) and (6.19) by switching t_1^a and t_1^b. For this step geometry, T_2 is given by:

$$T_2 = A_{an}^a \left[\frac{\sin A_1 - \sin A_2}{(k_{dm}^b + k_{an}^a)} + \frac{\sin A_3 - \sin A_4}{(k_{dm}^b - k_{an}^a)} \right] \tag{6.21}$$

$$\begin{aligned} A_1 &= (k_{dm}^b + k_{an}^a)t_1^b - k_{an}^a t_B \\ A_2 &= (k_{dm}^b + k_{an}^a)t_1^a - k_{an}^a t_B \\ A_3 &= (k_{dm}^b - k_{an}^a)t_1^b + k_{an}^a t_B \end{aligned}$$

$$A_4 = (k^b_{dm} - k^a_{an})t^a_1 + k^a_{an}t_B \tag{6.22}$$

6.2.4 LSM H-Guide BMM Results

The convergence of the method is shown in Fig. 6.10 for a step with $t^a_1 = 1.1t^b_1$, $t^b_1 = 0.25\lambda_0$, $\epsilon_r = 2.3$ and a width of $0.7625\lambda_0$. Convergence can be seen to be considerably slower that that demonstrated in the LSE case. An explanation for this is considered below.

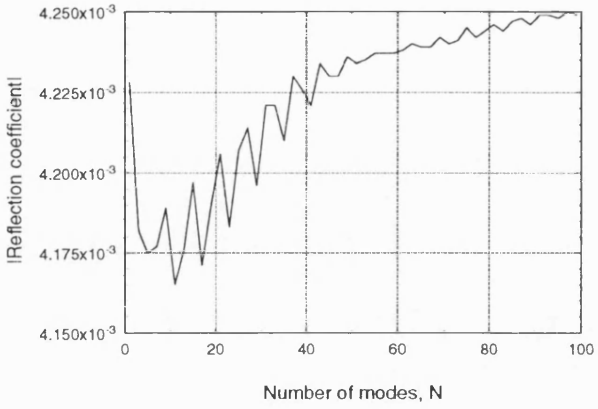

Figure 6.10: LSM H-guide step-in-dielectric convergence of reflection coefficient magnitude with N.

Most of the remaining results presented in this section concern a step-down discontinuity where $t^a_1 = 1.1t^b_1$ and $t^b_1 = 0.30809\lambda_0$, the guide width is $0.76253\lambda_0$, $\epsilon_r = 2.3$ and the frequency is 10GHz. Thus, guide A depth is 10.16mm, guide B depth is 9.24mm and the guide width either side of the step is 22.86mm. Both guides are monomode, with $\beta_a = 1.223k_0$ and $\beta_b = 1.199k_0$.

Fig. 6.11 shows the power error variation as the number of modes in the summation is increased. Although the power error here is small in all cases, more modes are required than in the LSE case for the oscillations to die away and for P_e to become negligible.

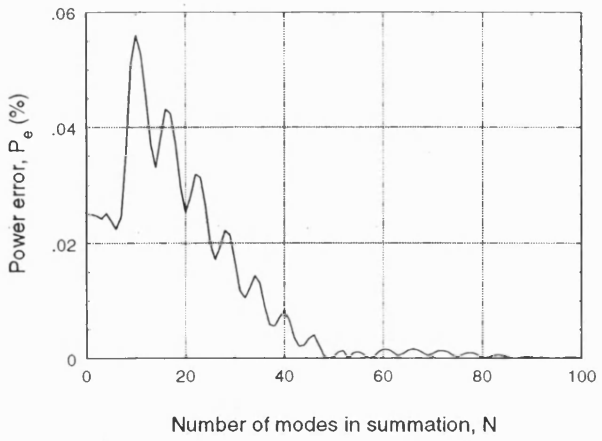

Figure 6.11: LSM H-guide step-in-dielectric variation of power error with N. The bounding distance is $1.5\lambda_0$.

Fig. 6.12 shows the distribution of power across the transmitted and reflected modes. 500 modes and a bounding distance of $10\lambda_0$ have been used to generate these results. Mode 1 on either side of the junction is slow, modes 2 to 11 are fast, and the rest are reactive. Again, most of the power resides in the transmitted slow mode. However, in comparison with the LSE case many more modes need to be used in the summations in order to include all the power scattered into the high order reactive modes.

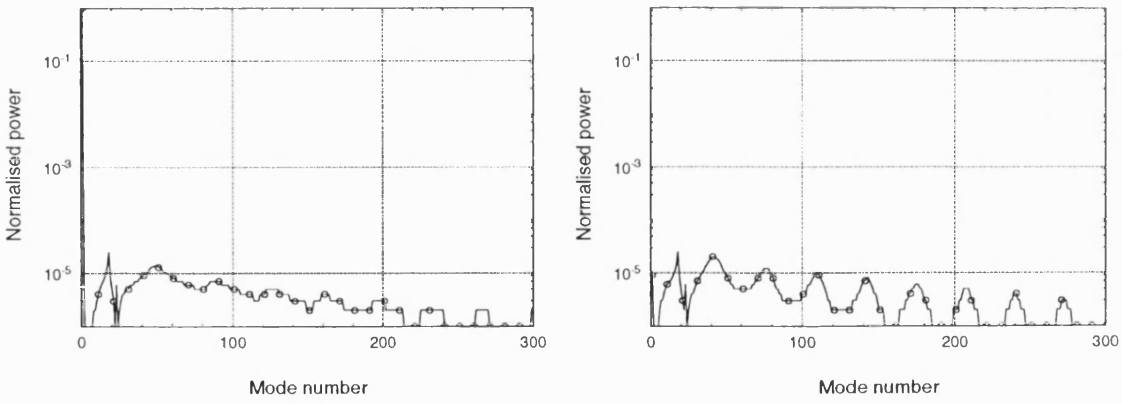

Figure 6.12: LSM H-guide step-in-dielectric spread of power across (a) transmitted modes, and (b) reflected modes.

One possible cause for the slower convergence in the LSM case and the spreading of power into many more higher order modes than in the LSE case is the existence of singularities in the transverse fields. The LSE mode matching uses the E_y and

H_x field components whereas LSM uses E_x and H_y. The y components are parallel to the edge so remain finite close to it. The x components are normal to the edge, so the possibility of singularities exists. Theory states that only the electric field components are subject to singular behaviour in the presence of a dielectric wedge, magnetic field components are unaffected by the change in ϵ_r as long as μ_r remains constant [123, 124]. Thus no singularities need to be taken account of in the LSE case, so rapid convergence may be expected. Singularities exist in the LSM field; the mode matching system needs many modes to try to model these.

Fig. 6.13 shows the slow mode scattering coefficient variation with bounding distance for the step considered above. Fig. 6.14 shows a similar plot for a step-up discontinuity where $t_1^a = 0.75t_1^b$ and $t_1^b = 0.3389\lambda_0$.

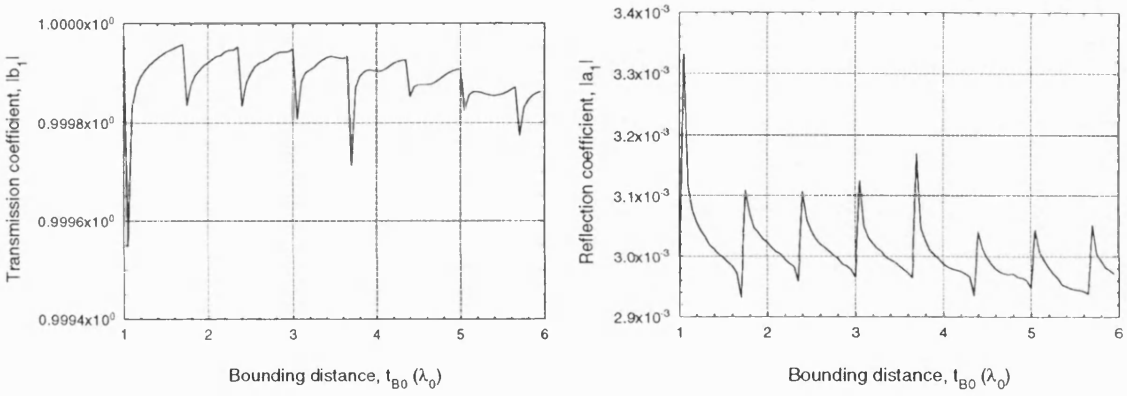

Figure 6.13: LSM H-guide step-in-dielectric ($t_1^a = 1.1t_1^b$) scattering coefficient variation with bounding distance: (a) transmission coefficient, and (b) reflection coefficient.

In both cases, the variations display similar features to those presented in Section 4.3.4 for the TE slab, but are rather more irregularly shaped. Convergence is also very slow. However, in the examples shown, the amplitude of the oscillations is not large nor erratic enough to call the validity of the method into question. Additionally, the variations appear to be around a reasonably constant mean so that taking the mean value to be the value of the scattering coefficient is not unreasonable. For instance, in the latter figure the range of the oscillations of the transmission coefficient is approximately -0.0043±0.0017 dB, whilst that of the

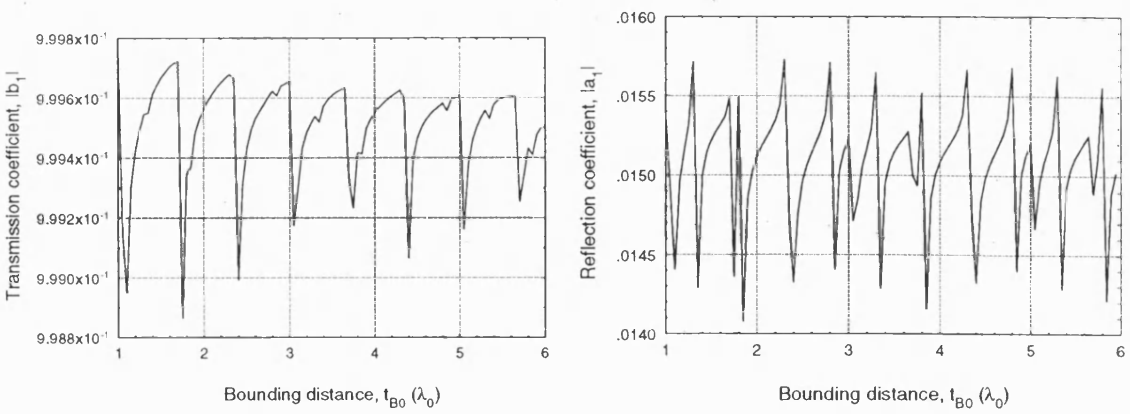

Figure 6.14: LSM H-guide step-in-dielectric ($t_1^a = 0.75t_1^b$) scattering coefficient variation with bounding distance: (a) transmission coefficient, and (b) reflection coefficient.

reflection coefficient is approximately -36.5±0.3 dB.

The increased variation and irregularity in Figures 6.13 and 6.14 can be explained in part by the $(k_y^2 + \beta^2)$ terms that exist in the LSM H-guide mode matching expressions. As the bounding distance, t_{B0}, is changed and reactive modes 'move' through the spectrum, there are values of t_{B0} for which β^2 and k_y^2 are approximately equal and opposite. This leads certain coefficients in the system of mode matching equations to go to zero, causing sharp peaks and troughs in the power in some of the modes. Such behaviour has not been seen previously as BMM has not been applied to this type of structure, with variation in two planes.

6.3 H-Guide Step-in-Ground Plane Bounded Mode Matching

The step-in-ground plane discontinuity is shown in Fig. 6.15 in cross section.

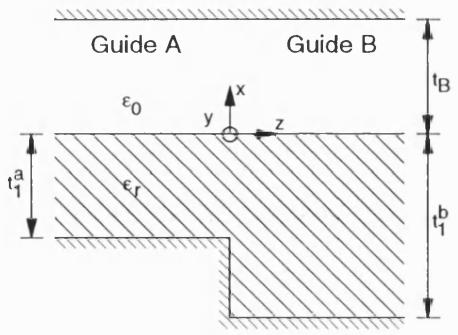

Figure 6.15: Step-in-ground-plane discontinuity.

6.3.1 Modification to the Mode Matching

The mode matching method presented by Brooke and Kharadly in [85] cannot be used for a structure where the external cross section of the waveguide changes [70]. Brooke and Kharadly apply the orthogonality condition on the same side (waveguide A) to both equation (4.9) and (4.10). This does not make any change in the waveguide cross section explicit - it is assumed to be constant. By applying orthogonality on both sides of the junction a formulation suitable for use with the stepped ground plane H-guide structure can be obtained.

The method proceeds by vector post-multiplying equation (4.9) by $\mathbf{h}_k^b$ and integrating across the cross section of waveguide A, S_A:

$$\int_{S_A} \mathbf{e}_i^a \times \mathbf{h}_k^b \, dS + \sum_{n=1}^{\infty} a_n \int_{S_A} \mathbf{e}_n^a \times \mathbf{h}_k^b \, dS = \sum_{m=1}^{\infty} b_m \int_{S_A} \mathbf{e}_m^b \times \mathbf{h}_k^b \, dS \tag{6.23}$$

The integral on the right hand side of this equation can be extended across S_B, the cross section of waveguide B, by adding the following term [70]:

$$\sum_{m=1}^{\infty} b_m \int_{S_B - S_A} \mathbf{e}_m^b \times \mathbf{h}_k^b \, dS$$

This term is equal to zero as the tangential electric field on the metal face of the discontinuity is zero. Rearrangement of equation (6.23) and truncation of the summation to N modes gives:

$$\sum_{n=1}^{N} a_n P_{nk}^{ab} - b_k P_k^b = -P_{ik}^{ab} \tag{6.24}$$

where:

$$\begin{aligned} P_k^b &= \int_{S_B} \mathbf{e}_k^b \times \mathbf{h}_k^b \, dS \\ P_{nk}^{ab} &= \int_{S_A} \mathbf{e}_n^a \times \mathbf{h}_k^b \, dS \end{aligned} \tag{6.25}$$

Equation (4.10) is treated by pre-multiplying by $\mathbf{e}_k^a$ and integrating across S_A. Rearrangement and truncation to N modes leads to:

$$a_k P_k^a + \sum_{m=1}^{\infty} b_m P_{km}^{ab} = \delta_{ki} P_k^a \tag{6.26}$$

$$P_k^a = \int_{S_A} \mathbf{e}_k^a \times \mathbf{h}_k^a \, dS \tag{6.27}$$

Equations (6.24) and (6.26) can be combined as a matrix equation of the form $[A][X] = [B]$ and solved using a computer.

6.3.2 LSE H-Guide BMM Expressions

PMC bounding is used in this case.

$\mathbf{P_n}$: The integration is carried out as for the step-in-dielectric case and results in:

$$P_n = \frac{\beta_n}{2\omega\mu_0}\left[t_1(1 - S\{2k_{dn}t_1\}) + A_{an}^2 t_B(1 + S\{2k_{an}t_B\})\right] \tag{6.28}$$

$\mathbf{P_{nm}^{ab}}$: The result of the integration in this case is:

$$P_{nm}^{ab} = \frac{\beta_m^b}{2\omega\mu_0}\left[T_1 + A_{an}^a A_{am}^b t_B T_2\right]$$

where:

$$T_1 = \left[\frac{\sin A_1 - \sin A_2}{k_{dn}^a - k_{dm}^b} + \frac{\sin A_3 - \sin A_4}{k_{dn}^a + k_{dm}^b}\right]$$

$$T_2 = \left[S\{[k_{an}^a + k_{am}^b]t_B\} + S\{[k_{an}^a - k_{am}^b]t_B\}\right]$$

$$\begin{aligned} A_1 &= k_{dn}^a t_1^a - k_{dm}^b t_1^b \\ A_2 &= k_{dm}^b (t_1^a - t_1^b) \\ A_3 &= k_{dm}^b (t_1^b - t_1^a) \\ A_4 &= k_{dn}^a t_1^a + k_{dm}^b t_1^b \end{aligned} \tag{6.29}$$

The above holds for the case where $t_1^a < t_1^b$. For $t_1^a > t_1^b$ the terms A_2 and A_3 change:

$$A_2 = A_3 = k_{dn}^a (t_1^a - t_1^b)$$

6.3.3 LSE H-guide BMM Results

Similar results are presented here as for the LSE guide step-in-dielectric. In fact, the step geometry used is the same. For the monomode step-in-ground plane configuration it is found that the power error, P_e is negligible under all the test conditions that were applied.

Fig. 6.16 shows the variation of the reflection coefficient as N is increased for two values of bounding distance. It can be seen that convergence in this case is noticeably slower than that seen in the step-in-dielectric results.

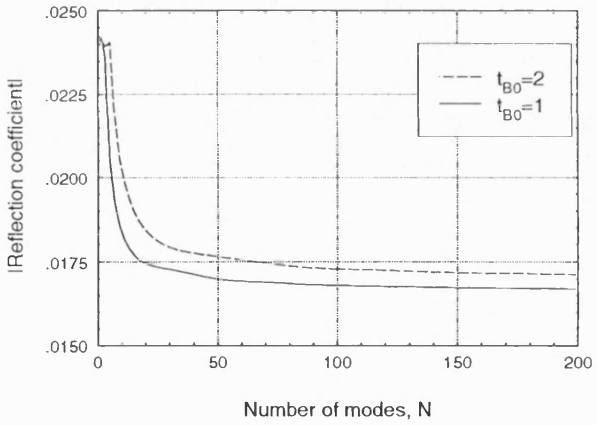

Figure 6.16: LSE H-guide step-in-ground plane convergence of reflection coefficient magnitude with N.

The spread of power across the transmitted and reflected modes is given in Fig. 6.17 for the case where $N = 300$ and the bounding distance is $10\lambda_0$. The fast modes for this configuration are numbered 2 to 22. Whilst most of the power, approximately 71%, resides in the transmitted and reflected slow modes it is clear that significant power has also been scattered into a large number of higher order modes. The

decay of power as N is increased is very slow when compared to that seen in the step-in-dielectric case, and many more than 300 modes would be needed to see the peak of the reflected mode power oscillations drop below 10^{-5}. This was achieved using 60 modes in the step-in-dielectric case. However, the use of $N = 100$ in the current case takes into account all modes with a normalised power of greater than 0.001. This degree of accuracy is sufficient for the problem in hand.

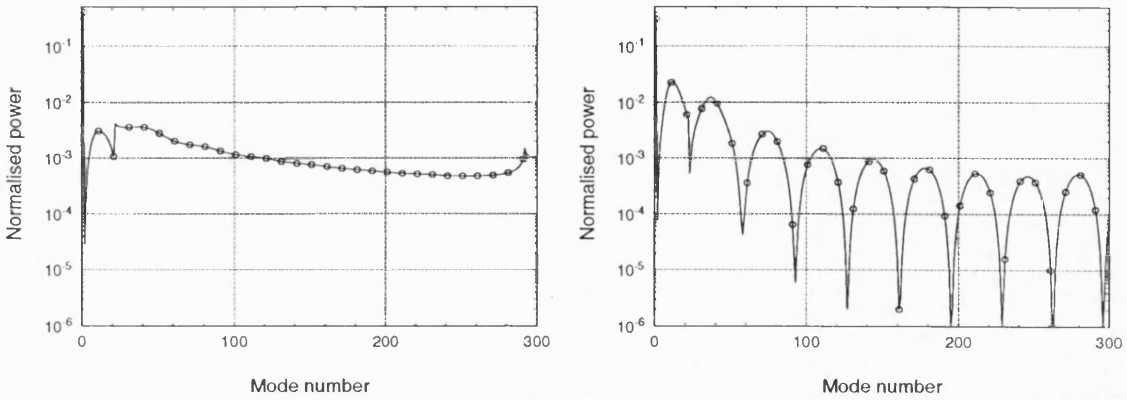

Figure 6.17: LSE H-guide step-in-ground plane spread of power across (a) transmitted modes, and (b) reflected modes. Bounding distance is $10\lambda_0$.

The slower convergence and increased amount of power being scattered into the reactive modes is due at least in part to the existence of singularities in the transverse fields. It is known that for a conducting corner the normal components of both the **E** and **H** fields can become singular close to the edge [123]. In the step-in-dielectric LSE discontinuity there were no singularities, whilst in the present case each of the transverse fields involved in the mode matching is subject to this behaviour.

Fig. 6.18 shows the scattering coefficient variations as the bounding distance is increased. The behaviour shown is similar to that seen in the cases considered earlier.

6.3.4 LSM H-Guide BMM Expressions

PEC bounding is used in this case.

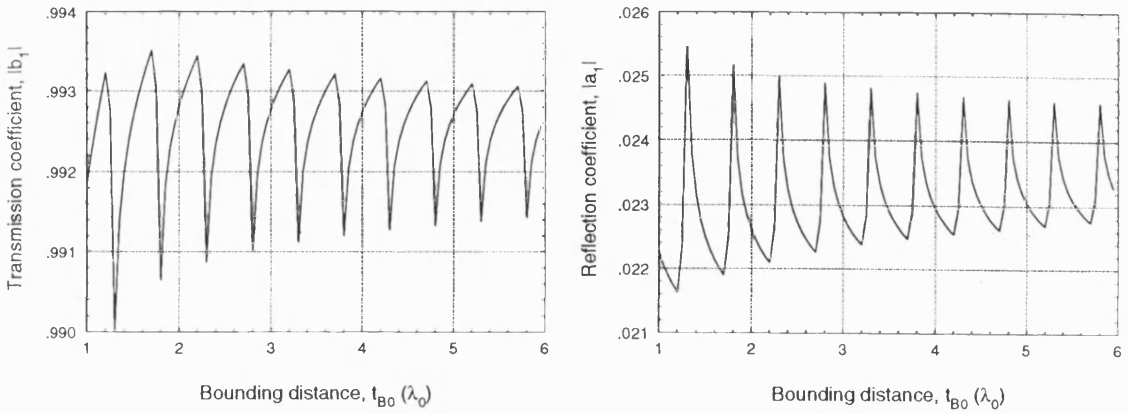

Figure 6.18: LSE H-guide step-in-ground plane scattering coefficient variation with bounding distance: (a) transmission coefficient, and (b) reflection coefficient.

The following results are obtained for $t_1^a < t_1^b$:

$$P_n = \frac{\omega\epsilon_0\beta_n(k_y^2+\beta_n^2)W}{4}\left[\epsilon_r t_1(1+S\{2k_{dn}t_1\}) + A_{an}^2 t_B(1+S\{2k_{an}t_B\})\right] \qquad (6.30)$$

$$P_{nm}^{ab} = \frac{\omega\epsilon_0\beta_m^b(k_y^2+(\beta_n^a)^2)W}{4}\left[\epsilon_r T_1 + A_{an}^a A_{am}^b t_B T_2\right]$$

where:

$$T_1 = \left[\frac{\sin A_1 - \sin A_2}{k_{dn}^a - k_{dm}^b} + \frac{\sin A_3 - \sin A_4}{k_{dn}^a + k_{dm}^b}\right]$$

$$T_2 = \left[S\{(k_{an}^a + k_{am}^b)t_B\} + S\{(k_{an}^a - k_{am}^b)t_B\}\right]$$

$$\begin{aligned} A_1 &= k_{dn}^a t_1^a - k_{dm}^b t_1^b \\ A_2 &= k_{dm}^b (t_1^a - t_1^b) \\ A_3 &= k_{dn}^a t_1^a + k_{dm}^b t_1^b \\ A_4 &= k_{dm}^b (t_1^b - t_1^a) \end{aligned} \tag{6.31}$$

For the reverse step ($t_1^a > t_1^b$) the above expressions remain valid except for those for A_2 and A_4 which become:

$$A_2 = A_4 = k_{dn}^a (t_1^a - t_1^b)$$

6.3.5 LSM H-Guide BMM Results

The results given in this section use the same step details as for the LSM H-guide step-in-dielectric discontinuity. As for the LSE step-in-ground plane case, the power error has been found to be negligible for all the configurations tested.

Reflection coefficient variation with N is depicted in Fig. 6.19 and convergence again proves to be much slower than for the step-in-dielectric discontinuities.

Fig. 6.20 shows the power spread on either side of the junction for $N = 300$ and a $10\lambda_0$ bounding distance. The characteristics of these results are similar to those of the LSE step-in-ground plane case; again, all field components normal to the metal edges are subject to singularities.

Fig. 6.21 shows the scattering coefficient variation with bounding distance. The features of these results are as observed for the step-in-dielectric case in Section 6.2.4. In this case, the range of the variation of the transmission coefficient is approxi-

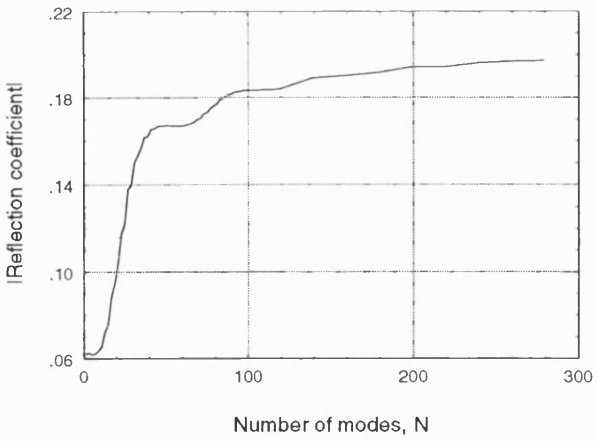

Figure 6.19: LSM H-guide step-in-ground plane convergence of reflection coefficient magnitude with N.

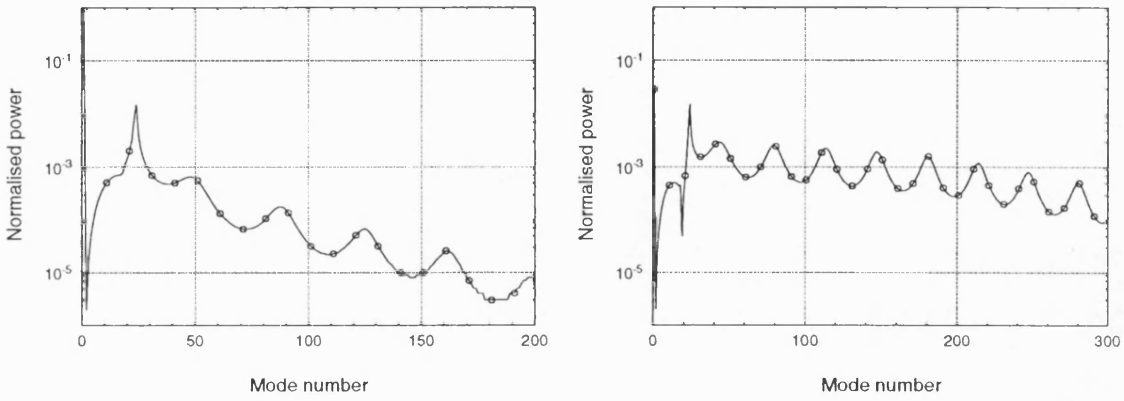

Figure 6.20: LSM H-guide step-in-ground plane spread of power across (a) transmitted modes, and (b) reflected modes. $N = 300$, $t_{B0} = 10\lambda_0$.

mately -0.31±0.22 dB and for the reflection coefficient is -15±4 dB.

6.4 Choice of Step for Taper Approximation

Having ascertained that both the step-in-dielectric and step-in-ground plane H-guide discontinuities can be analysed using VBMM it was decided that, on balance, further work should concentrate on the step-in-ground plane discontinuity. In terms of the operation of the BMM there is little to choose between the two configurations; the step-in-ground plane discontinuities show lower power error than the step-in-

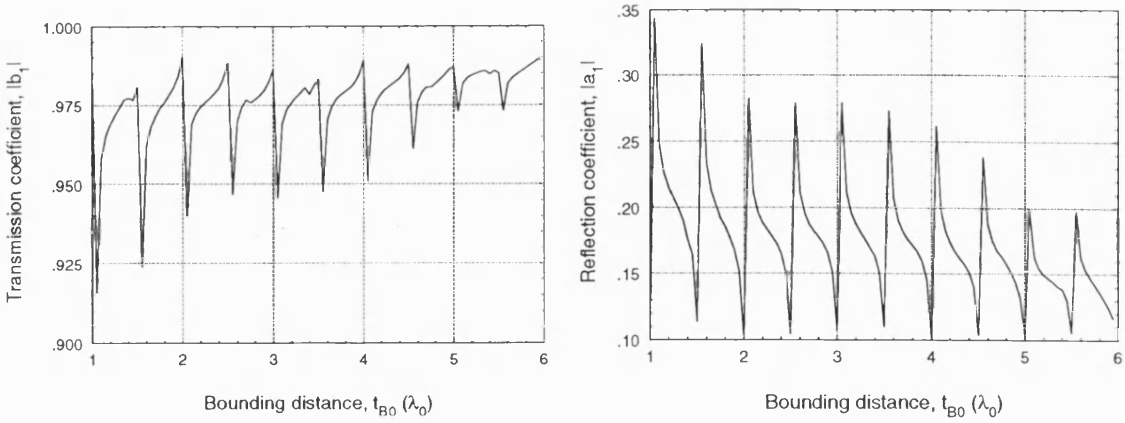

Figure 6.21: LSM H-guide step-in-ground plane scattering coefficient variation with bounding distance: (a) transmission coefficient, and (b) reflection coefficient.

dielectric, but convergence is slower. Both types of step include field singularities that do not exist in the real taper. However, a series of ground plane steps seems better suited to modelling a tapered IDG antenna than does a series of steps in the dielectric surface.

6.5 VBMM Characterisation of H-Guide Steps

The aim of this section is to present VBMM results for the slow mode transmission and reflection coefficients, and the total radiated power from H-guide steps with a range of guide thicknesses. The following is concerned with steps in the ground plane only.

6.5.1 LSE

The results in this section relate to guides with an ϵ_r of 2.3, and the frequency is fixed at 10GHz. Guide A thickness is $1.1t_1^b$ and t_1^b is varied between $0.22\lambda_0$ and $0.65\lambda_0$. The lower limit here represents the slow mode cut-off and the upper limit is the thickest monomode slab. 40 modes are used in the mode matching summations

and the boundary distance is varied from 1 to 3 free space wavelengths. Fig. 6.22 shows the variation of the slow mode transmission and reflection coefficients as the guide B thickness, t_1^b, is varied.

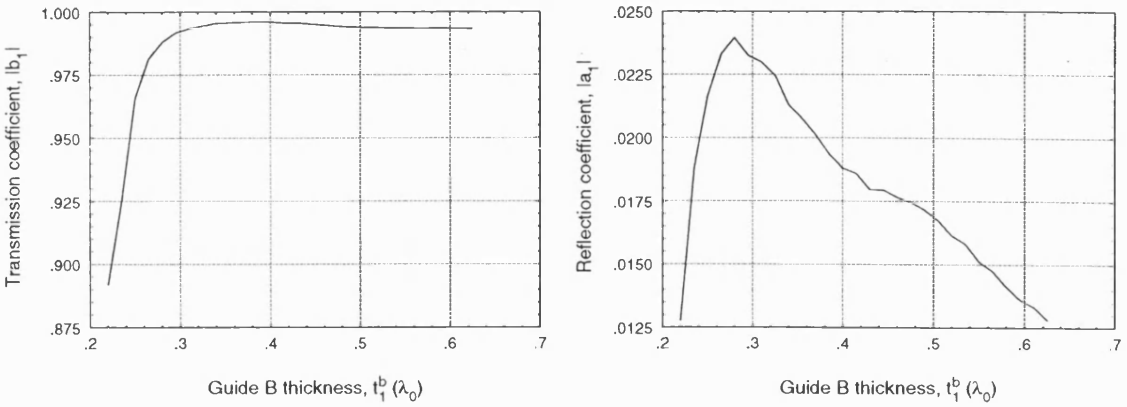

Figure 6.22: LSE H-guide step-in-ground plane scattering coefficient variation with guide B thickness: (a) transmission coefficient, and (b) reflection coefficient.

Fig. 6.23(a) shows the total radiated power for the same range of guide B thickness. The radiated power is calculated by summing the power in the forward and backward travelling fast modes.

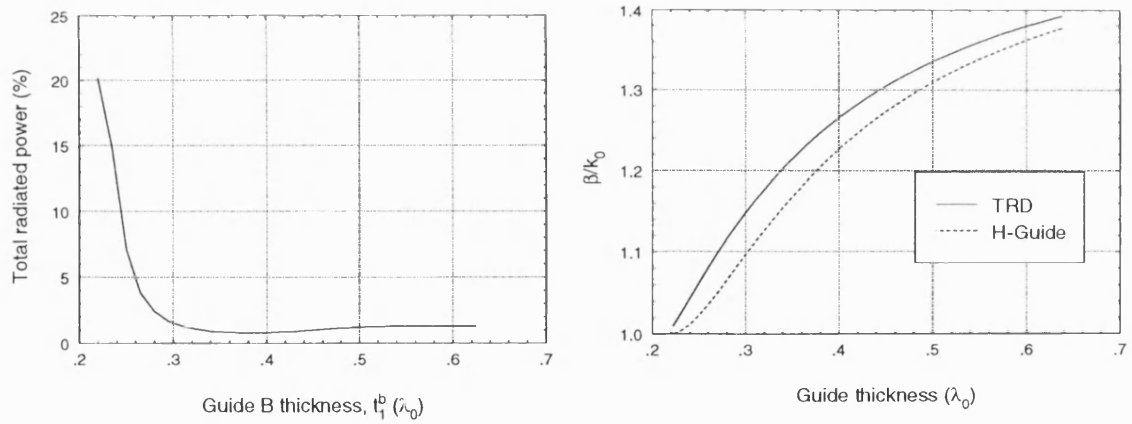

Figure 6.23: (a) LSE H-guide step-in-ground plane variation in total radiated power with guide B thickness. (b) LSE H-guide and TRD propagation constants.

It is helpful to view these figures in conjunction with Fig. 6.23(b) which depicts the longitudinal propagation constant, β, for the same range of guide thickness. Both H-guide and transverse resonance diffraction (TRD) [6] β values are shown.

Fig. 6.22(a) shows that the transmission across the discontinuity is close to 1 for

steps thicker than approximately $0.3\lambda_0$. As the guide thickness drops below this value and β drops below $1.1k_0$, the transmission drops significantly and the radiation from the step increases. This behaviour can be explained by considering the extent to which the slow mode is bound to the dielectric. A distance t_C can be defined as the height above the guide surface in which 99.99% of the power of the slow mode is contained. The expressions developed for BMM can be used to calculate t_C and some results are shown in Fig. 6.24.

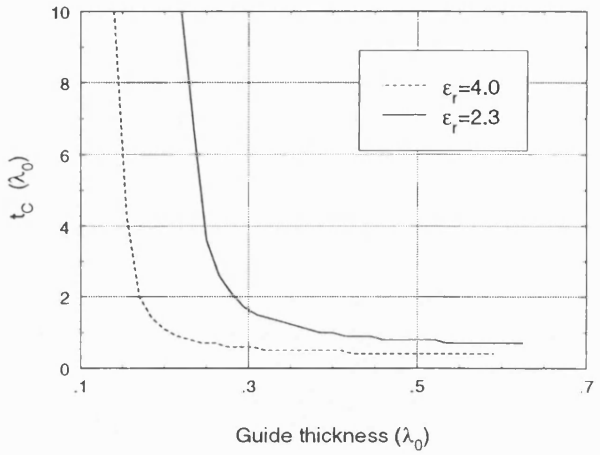

Figure 6.24: LSE H-guide: first slow mode power concentration.

A curve for the same step with a higher value of dielectric constant has also been included in Fig. 6.24 in order to illustrate the increased concentration of the slow mode power in the dielectric. For an ϵ_r of 2.3, it is clear from the figure that for guides thinner than $0.3\lambda_0$ the power in the mode is very loosely bound to the dielectric. When the power is spread like this into the air, the slow mode becomes less orthogonal with the fast modes and coupling to the fast mode spectrum is more likely to occur.

6.5.2 LSM

In this section a discontinuity with $t_1^a = 1.1t_1^b$ is considered, and t_1^b is varied between $0.015\lambda_0$ and $0.435\lambda_0$ which corresponds approximately to the monomode range of

H-guide. 40 modes are used in the summations and the bounding distance is varied between 1 and 3 free space wavelengths. The guide width is $0.7625\lambda_0$, ϵ_r is 2.3 and the frequency is 10GHz. Slow mode transmission and reflection coefficients, and the total radiation from the step as guide B thickness is varied are shown in Figures 6.25 and 6.26(a). The plots show a gradual decrease in the transmission and increase in the radiation as the step thickness increases. The effect of the irregular variation of the scattering coefficients discussed in Section 6.2.4 can be observed in these results in the form of sharp peaks and troughs.

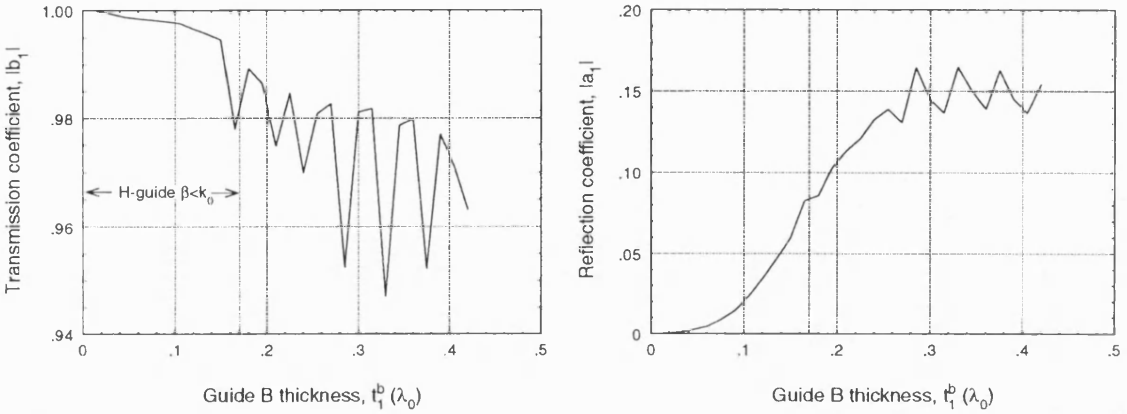

Figure 6.25: LSM H-guide step-in-ground plane scattering coefficient variation with guide B thickness: (a) transmission coefficient, and (b) reflection coefficient.

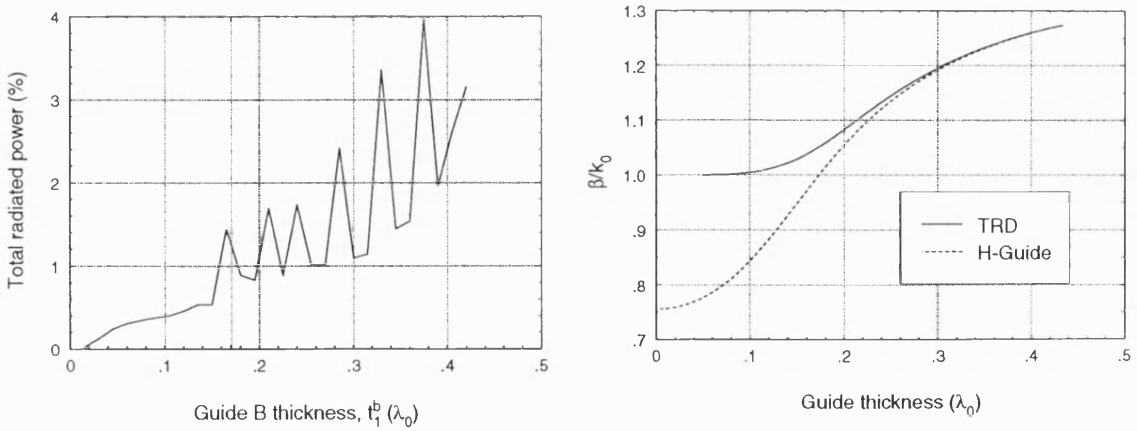

Figure 6.26: (a) LSM H-guide step-in-ground plane variation in total radiated power with guide B thickness. (b) LSM H-guide and TRD propagation constants.

These figures can only be meaningfully viewed in conjunction with the β plot in Fig. 6.26(b). When the guide thickness is less than $0.17\lambda_0$ the H-guide β is below

k_0 due to the effect of the finite guide width. In Fig. 6.26(a) this mode has been treated as if it had $\beta > k_0$ so it is not included as radiation - in actuality, once the $0.17\lambda_0$ threshold is passed all the modes in the system are radiative. This point has been marked on Figures 6.25 and 6.26(a) - to the left of the threshold the results must be considered as invalid.

Attempting to characterise the radiation loss for H-guide less than $0.17\lambda_0$ thick is not necessarily very helpful to the problem in hand. Fig. 6.26(b) shows that for this range of geometries the H-guide β values are so far removed from the accurate TRD values as to be of little use for modelling purposes. To make the VBMM model more realistic for those geometries where the H-guide and TRD propagation constants diverge significantly, the TRD values can be inserted into the mode matching equations. Tests have confirmed that this can be done without having any obvious deleterious effect on the power error or convergence characteristics of the calculation.

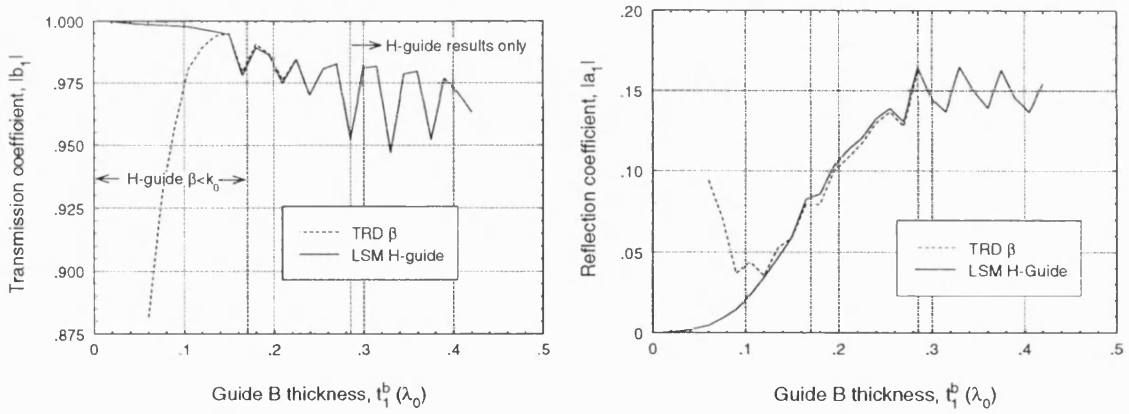

Figure 6.27: LSM step-in-ground plane configuration using H-guide and TRD β: scattering coefficient variation with guide B thickness: (a) transmission coefficient, and (b) reflection coefficient. TRD results exist only for $t_1^b < 0.285\lambda_0$.

Figures 6.27 and 6.28 repeat the previous results but include in addition results based on TRD β values for guide thicknesses of less than $0.285\lambda_0$, at which point the TRD and H-guide β values are within 0.05% of each other. The figures show that the TRD results track the H-guide results closely until the guide is about $0.14\lambda_0$ thick, where the difference in the β values has increased to 10%. After this

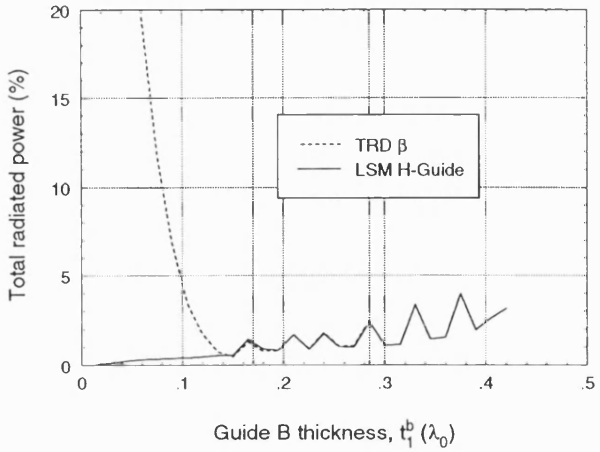

Figure 6.28: LSM step-in-ground plane configuration using H-guide and TRD β: variation in total radiated power with guide B thickness. TRD results exist only for $t_1^b < 0.285\lambda_0$.

point the step behaviour calculated using TRD is very much as was seen for the LSE step, with decreasing transmission and increasing radiation as the guide depth reduces. Note that no TRD solution exists for guides with a thickness of less than $0.05\lambda_0$.

Finally, it is of interest to look at the extent to which the slow mode power is bound to the LSM guide, as was done for the LSE case. Fig. 6.29(a) shows the value of t_C for two values of ϵ_r, and Fig. 6.29(b) compares t_C for LSM and LSE H-guides of the same geometry with an ϵ_r of 2.3. The first of these figures shows the increased binding of the power to the dielectric in the case of the higher dielectric constant, as expected. The second figure shows that the LSM mode is more closely tied to the dielectric than the mode in the comparable LSE guide.

6.6 Modelling of the Complete IDG Taper

A model of the IDG taper is to be built from a number of H-guide step-in-ground plane discontinuities. It is clear that TRD propagation constants must be used if the conditions on the taper are to be accurately represented.

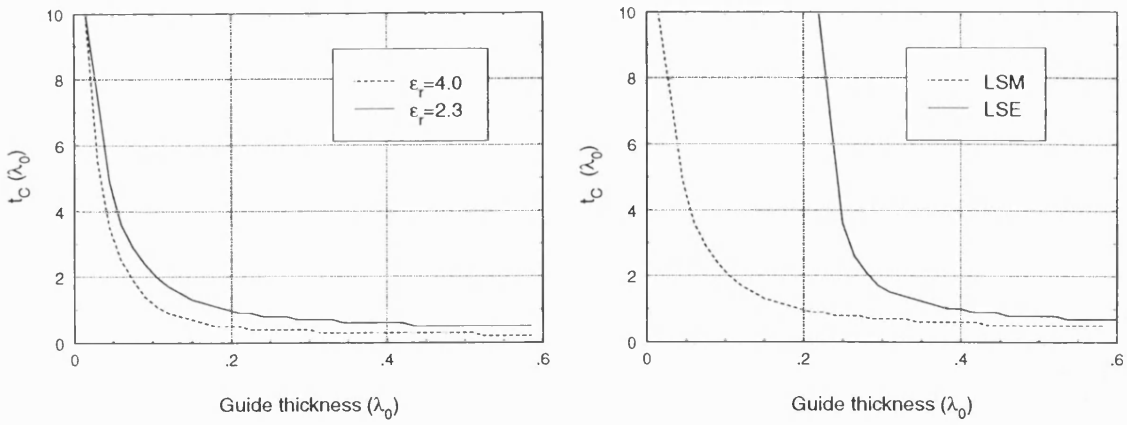

Figure 6.29: First slow mode power concentration: (a) LSM H-guide, and (b) LSM and LSE H-guides.

The model of the taper used here is straightforward; only the first bound mode is of interest, so only this mode is modelled. Firstly, the taper is broken up into a number of step discontinuities. This is done in such a manner as to make each step approximately the same size. A 10% step is aimed for, whereby the depth of the thinner guide in any given step discontinuity is not less than 90% of the depth of the thicker guide. This leads to an uneven distribution of discontinuities along the taper - more at the end than at the beginning. The bound mode propagation constants are then calculated for each guide geometry by TRD. VBMM is used to generate the scattering (S) parameter matrix for the bound mode for each of these discontinuities. Clearly, this involves running VBMM twice for each step to account for incidence from both sides. The S-parameter matrices are converted to ABCD matrices and inserted into a transmission line model of the taper. This model is described in detail in Section 7.3. It is then possible to calculate the power loss suffered by the fundamental mode on the taper.

In both the LSM and LSE cases, no TRD solution exists once the taper thickness drops below a certain value. It is not obvious how this should be handled in the transmission line model. In reality power ceases to be bound to the dielectric at this point. As such, one option is simply to terminate the transmission line here. Alternatively, the last valid values of TRD β and VBMM S-parameter matrix

may be repeatedly applied to the small number of steps for which no solution is available. In the results that follow the first of these two options has been used, so that no numerical values are given for the sections of the taper where no solution is available. The effect of doing this is most noticeable in the LSE results where cut-off occurs further from the end of the taper than in the LSM case.

6.6.1 Results for LSM Tapers

Fig. 6.30 shows the first mode power loss for an LSM taper at four frequencies. The tapers considered in this section are all 300mm long, 22.86mm wide and 10.16mm deep at the start. The depth tapers down to zero at the end of the structure. The dielectric constant is 2.3, and TRD propagation constants have been used. As expected, the results show that the first mode is more tightly bound to the dielectric at the higher frequencies. Note that these calculations take no account of dielectric losses.

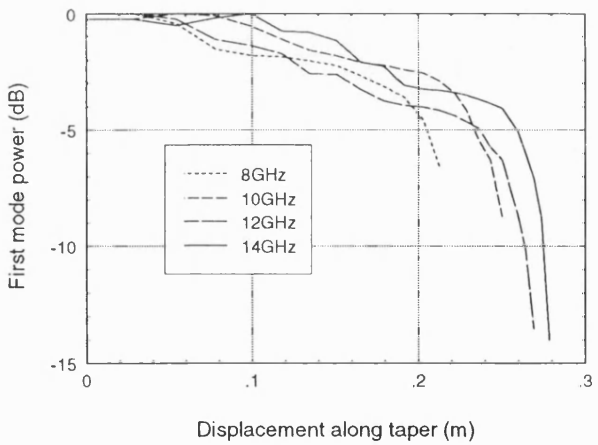

Figure 6.30: Fundamental mode power along an LSM H-guide taper by VBMM at various frequencies.

The results of Fig. 6.30 also indicate that losses from the first third of the taper are small, less than 2dB. Thus, this first section of the taper is doing little more than carrying power to the more radiative section of the taper; it is acting as a transmission line rather than as an antenna. This has implications for the design

of the IDG-TSA. The irregular variation already observed in the results for single LSM H-guide step-in-ground plane discontinuities can be seen here in the 'stepped' nature of these results.

The validity of the above results can be tested to some extent by comparison with results from FDTD. The power flowing along the taper can be calculated by:

$$P = \frac{1}{2} Re \left(\int_S \mathbf{E}_t \times \mathbf{H}_t^* dS \right) \tag{6.32}$$

where $\mathbf{E}_t$ and $\mathbf{H}_t$ are the transverse fields. When applied to the discretised structure modelled in FDTD this becomes:

$$P \approx \frac{1}{2} Re \left(\sum_{i=1}^{N_x} \sum_{j=1}^{N_y} [E_x(i,j) H_y^*(i,j) - E_y(i,j) H_x^*(i,j)] \Delta x \, \Delta y \right) \tag{6.33}$$

where Δx and Δy are the lengths of the cell sides in the x and y directions, and N_x and N_y are the number of cells in the x and y directions respectively. Fig. 6.31 shows comparisons between VBMM and FDTD results at three frequencies. It should be noted that these figures do not compare like with like. FDTD includes all propagating modes in the power calculation whereas VBMM includes only the fundamental mode, both in the slab and in the air. Two FDTD results are shown in each of the figures; one represents the power flow in the slab alone whilst the other represents the power flow in the slab plus that in the air above the slab (to a height of 6.35mm). The latter results encompass some of the power carried by the fundamental mode in the air, but will also include a contribution from radiative modes. Thus, these comparisons must be considered as a guide only.

Agreement between FDTD and VBMM can be seen to be reasonable, especially for the higher frequencies. The FDTD results exhibit a certain amount of 'stepping' which is due to the staircase approximation of the taper depth; the power calcula-

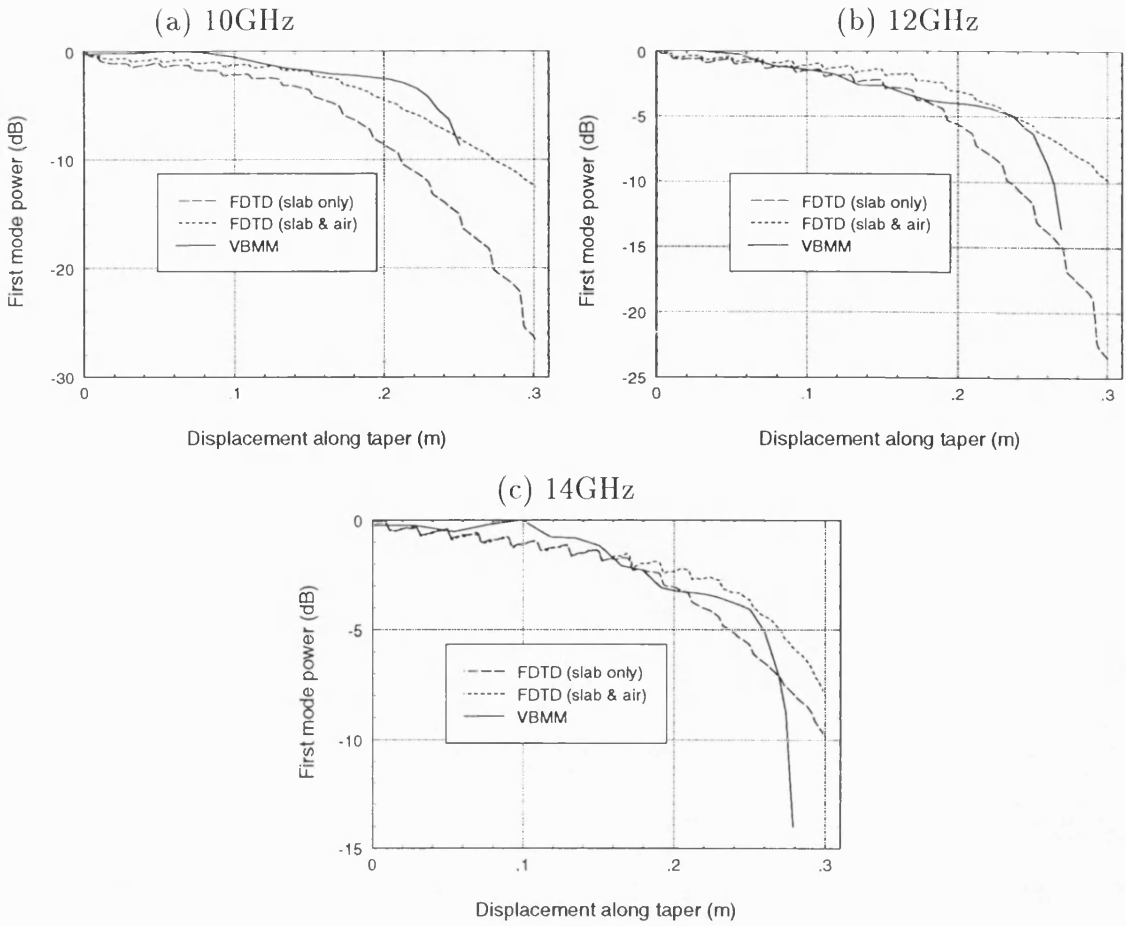

Figure 6.31: Fundamental mode power along an LSM taper by VBMM and FDTD.

tions do not use the contour path model of the taper but rather use whole regular cells instead.

Performing VBMM for a complete taper is time consuming. For example, consider a 300mm long LSM taper at 10GHz. The section of the taper for which TRD solutions for the propagation constant exist is broken into 17 junctions, which need 34 runs of VBMM to characterise them. Taking 100 modes for each guide and varying the bounding distance between 1 and $3\lambda_0$ in 20 steps leads to a total run time of 2 hours 19 minutes on a Silicon Graphics Origin 2000 machine. This is approximately 8 minutes for each junction.

6.6.2 Results for LSE Tapers

Similar results are presented here as were given for the LSM taper above. In this case the 300mm long tapers are 10.16mm wide and 22.86mm deep at the start, with the depth tapering to zero at the end of the structure. Fig. 6.32 shows the first mode power loss for two frequencies.

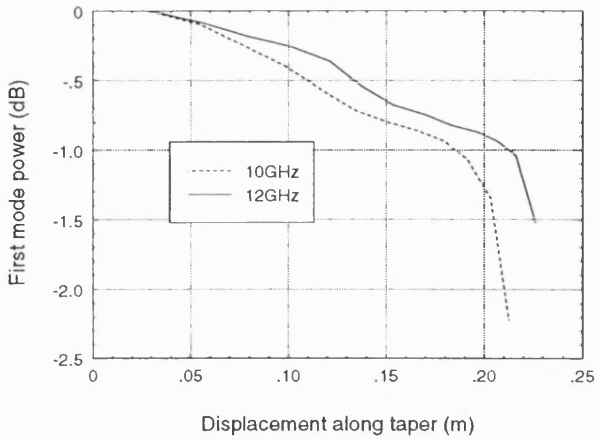

Figure 6.32: Fundamental mode power along an LSE H-guide taper by VBMM at two frequencies.

The results show similar characteristics to the LSM case, although the loss is much smaller. Comparisons with FDTD are shown in Fig. 6.33. These results are repeated in Fig. 6.34 for the first 80% of the taper only, i.e. for the section of the taper where the mode has not cut off. This allows a comparison to be made more easily.

The VBMM results can be seen to be very close to those FDTD results which include a section of the air region in the calculation.

6.7 Chapter Summary

The field expressions and characteristic equations of bounded H-guides have been derived, and bounded mode matching has been applied to step-in-dielectric discon-

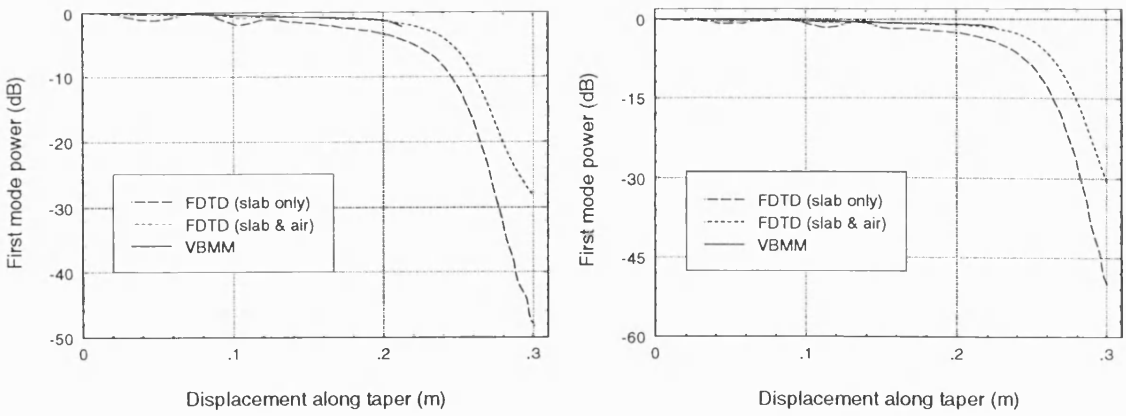

Figure 6.33: Fundamental mode power along an LSE taper by VBMM and FDTD at (a) 10GHz, and (b) 12GHz.

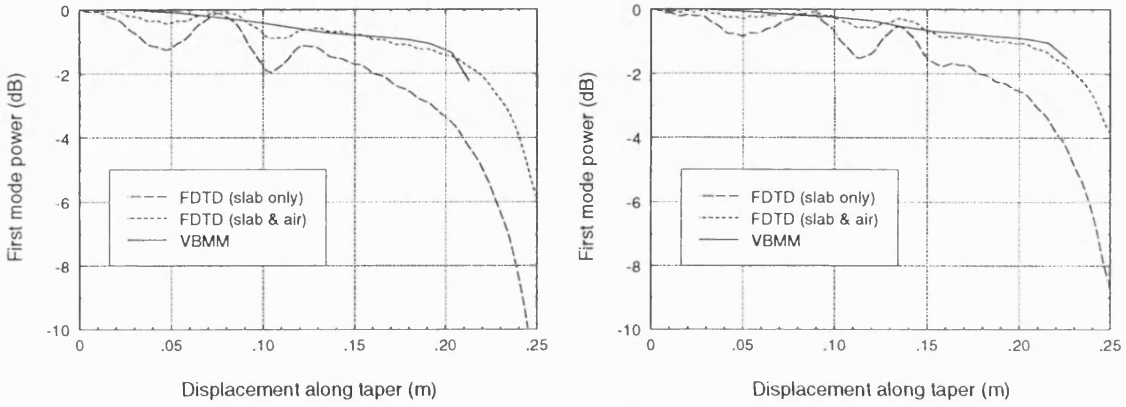

Figure 6.34: Fundamental mode power along an LSE taper by VBMM and FDTD at (a) 10GHz, and (b) 12GHz. Reduced ranges on displacement axes.

tinuities. A modification to the theory has allowed the method to be successfully applied to step-in-ground plane discontinuities. As the H-guide thickness reduces along a taper its propagation constant becomes increasingly inaccurate. To overcome this problem, TRD values are used in the mode matching equations.

A transmission line model of the H-guide taper has been built into which transmission matrices derived by variable BMM are inserted. The power loss characteristics of the first mode have been derived from this, and the results show good agreement with FDTD. The results for the tapers studied indicate that only a small amount of radiation occurs from the first section of the structure, which does little more than carry power to the main radiating section.

Chapter 7

Development of an Analytical Method

7.1 Review and Introduction

In Chapter 3, the state of the art in the analysis of the IDG-TSA was delineated. The only analytical method developed to date is the modified Walter's method. This has shown itself able to provide results which are reasonably accurate when compared to measured values [3]. A more accurate analysis using FDTD has also been developed [4], but this too has the disadvantage of using Walter's approximate method for taking account of the finite ground plane, as described in Section 3.4.3. A further drawback with the FDTD analysis is that it takes a long time to run.

It was with the above in mind that the objectives of the work described in the current chapter were formulated. These aims are to produce an analytical technique for characterising the IDG-TSA that can rival FDTD in terms of accuracy but that runs much more rapidly. In addition to this, it was considered desirable to remove the least justifiable approximations used by the previous analytical method; namely

the use of Walter's approximation for the effect of the finite ground plane, and the empirical estimation of the fundamental mode losses on the aperture. The aperture losses are considered separately in Chapter 6, but the development of the rest of the method is considered in the present chapter.

The following sections describe the development of the new analytical method. Various intermediate results have been included in order to validate the method and to illuminate certain characteristics of the IDG-TSA. The following stages in the construction of the model are discussed:

- The calculation of the longitudinal phase variation of the aperture fields.
- The construction of a simple method to obtain the far field radiation pattern of a line source with this longitudinal field dependence.
- The addition to this model of Walter's approximate technique to handle the finite ground plane. The effect of doing this is assessed.
- The extension of the model to two dimensions to encompass both the slot and the finite ground plane and thus the removal of Walter's approximate technique. This necessitates the modelling of the fields on the ground plane. Various forms for these fields are considered.
- The development of a more accurate analysis which provides an analytical link between the fields on the slot surface and those on the ground plane surface. This model is the most complete model of the IDG-TSA yet developed. It is this final version of the method that is used to generate the theoretical results presented in Chapter 9.

Name	Type	Feed Width x depth	Aperture	Ground Plane	Uniform IDG
Long shallow	LSM	22.86 x 10.16	300	108	n/a
Long deep	LSE	10.16 x 22.86	300	105	n/a
Short shallow	LSM	22.86 x 10.16	30	10	n/a
Short deep	LSE	10.16 x 22.86	30	10	n/a
Long plastic	LSM	22.86 x 10.16	300	115	95
Medium plastic	LSM	22.86 x 10.16	30	30	30

Table 7.1: Antenna details. All dimensions are in millimetres.

7.2 Antenna Dimensions

The dimensions of the most important antennas that were constructed as part of this work are listed in Table 7.1. Where it is necessary to make reference to one of the structures in this chapter and those that follow, the name given in the first column of the table is used. By this method, needless repetition of the antenna details is avoided. The table lists the dimensions of the feed, the length of the aperture and the length of the ground plane extending beyond it, as well as the length of uniform IDG incorporated at the feed.

The following features are common to all of the structures:

- The dielectric constant of the guide filling is 2.3.
- The total width of the block in which the antenna is set is 90mm.
- The slot width remains constant along the length of the aperture whilst the depth tapers to zero at the end of the aperture.
- Aluminium construction is used except where noted.

Note that details of the dual polarised structure have been omitted; these are considered separately in Section 10.7.

A note on the plastic antennas: The possibility of constructing IDG-TSAs from plastic sheeting has been investigated. After construction the sheeting is covered with aluminium foil before dielectric material is cast into the slot. The resulting structure is extremely light, low cost, and is still satisfactorily robust. For prototyping purposes this type of construction offers a cheap, quick alternative to the machining of an aluminium block.

However, it is challenging to maintain high dimensional accuracy when building the antennas by hand like this, and achieving a good connection at the feed has proved difficult. Build would become very awkward for smaller antennas designed for higher frequency use. In addition to these difficulties, the foiled metalisation does not provide the quality of surface finish seen on the metal antennas.

The plastic structures listed in the table have sections of uniform IDG incorporated at the feed end to ease manufacture. The metal antennas do not include this feature.

7.3 The Longitudinal Phase Variation of the Aperture Fields

The phase variation of the aperture fields in the longitudinal (z) direction is obtained by breaking the tapered IDG into a number of short lengths of uniform IDG connected in cascade. Each of these elemental lengths is considered as a length of transmission line whose longitudinal propagation constant, β, is calculated using the H-guide approximation of IDG discussed in Chapter 5. Only the fundamental propagating mode is considered. A transmission (ABCD) matrix can be worked out for each element. Assuming that the line is lossless, this is:

$$\begin{bmatrix} A & B \\ C & D \end{bmatrix} = \begin{bmatrix} cos\theta & jZ_0 sin\theta \\ jY_0 sin\theta & cos\theta \end{bmatrix}$$

where $\theta = \beta l$ is the electric length of the element, l is its physical length and $Z_0 = 1/Y_0$ is the characteristic impedance.

By multiplying together the transmission matrices of all the elements and applying source and load conditions, the phase variation of the aperture fields can be calculated. Consider an arrangement whereby the IDG taper has been divided into T cascaded longitudinal elements. By multiplying together the elemental ABCD matrices and assuming a source voltage V_s, a source impedance Z_s, and a termination impedance Z_L, the voltage and current at the input to any element n on the line can be shown to be:

$$V_n = \frac{Z_{in} V_s}{(Z_s + Z_{in})} \frac{(A_n Z_L + B_n)}{(A_T Z_L + B_T)}$$

$$I_n = \frac{V_s}{(Z_s + Z_{in})} \frac{(C_n Z_L + D_n)}{(C_T Z_L + C_T)}$$

where:

$$Z_{in} = \frac{A_T Z_L + B_T}{C_T Z_L + D_T}$$

is the input impedance of the terminated cascade of elements as seen from the source. The elements A_T, B_T, C_T and D_T are elements of the transmission matrix of the total structure. The elements A_n, B_n, C_n and D_n relate to the transmission matrix for n cascaded elements only, where $n < T$.

Using the foregoing, a picture of the behaviour of the voltage and current variations on the equivalent transmission line can be built up. In general, Z_s is set to equal the characteristic impedance of the first transmission line element. The load impedance Z_L is chosen as the impedance of free space, which is a reasonable assumption for a section of IDG whose thickness tapers down to zero.

7.4 A Note on IDG-TSA Polarisation

It has been noted previously (Section 2.1.2) that inset dielectric guide can be made to exhibit nearly pure polarisation properties by the selection of certain guide geometries. The fields in shallow slots can be described using the LSM approximation whilst the fields in deep slots can be described using the LSE approximation. It is difficult to lay down general rules as to what constitutes a 'shallow' or 'deep' slot as a number of parameters are involved in this decision. FDTD and TRD analyses can be used to reveal whether a particular slot geometry is predominantly of one type or the other. As an example, for IDG with $\epsilon_r = 2.3$ at X-band frequencies, a 10.16mm deep, 22.86mm wide guide (2.25:1 width:depth) is predominantly LSM polarised whereas a 22.86mm deep, 10.16mm wide guide (0.44:1 width:depth) is predominantly LSE polarised.

The majority of the antennas considered in this thesis are nominally single polarisation types, either LSM or LSE; measurements given in Section 10.6 indicate the extent to which the polarisations are in fact pure.

In Chapter 5 the field expressions of the H-guide were developed as an approximate representation of the fields of IDG. From this analysis, the principal power carrying field components for the LSM and LSE cases can be identified. These are shown in Fig. 7.1 in which a transverse cross section of each type of guide is depicted.

The polarisation of the IDG-TSA far field is dictated by the components shown in

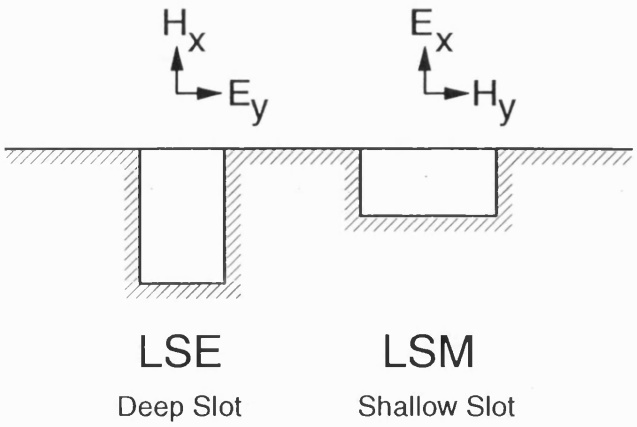

Figure 7.1: Illustrating the polarisation properties of deep and shallow slot IDG.

the figure. LSM antennas give vertically polarised radiation whilst LSE antennas give horizontally polarised radiation.

If the cross sections shown in Fig. 7.1 are considered as part of an IDG-TSA aperture sited in a ground plane, it is clear that the power carrying components in the LSM case (E_x, H_y) can spread onto the ground plane, whilst the H_x and E_y components in the LSE case are shorted out by the ground plane. These characteristics will be seen to have some bearing on the radiation properties of the LSM and LSE polarised IDG-TSA.

7.5 Line Source Method for Obtaining the Radiation Pattern

As a first step, a simple one-dimensional method was developed in order to obtain the elevation plane radiation pattern of the IDG-TSA. Not only does this provide a useful reference point for techniques developed subsequently, but it also allows the efficacy of Walter's approximate method for the effect of the finite ground plane to be tested.

In this section the aperture is considered to be a line source and the elevation plane pattern is derived from the tangential fields on the aperture only, with the ground plane being ignored. By comparing results from this line source method to measured results, the extent of the effect of ground plane fields on the overall antenna performance can be qualitatively judged.

The elevation plane radiation patterns are given by equation (3.58) written for the IDG co-ordinate axes defined in Fig. 2.1 with $\phi = 0°$. The elevation angle θ is measured from the aperture surface. For the vertically polarised LSM case:

$$E_\theta \propto f_z + g_y Z_0 \sin\theta \tag{7.1}$$

and for the horizontally polarised LSE case:

$$E_\phi \propto f_y \sin\theta - g_z Z_0 \tag{7.2}$$

The constant multipliers in equation (3.58), which depend on the frequency and the observation distance, have been omitted in these equations.

7.5.1 LSM Antenna

Considering first the LSM case, it is the E_z and H_y field components that are of interest. Using equation (5.20), the H-guide representations of these components, assuming no variation in the y direction, are:

$$E_z(z) \;=\; j\beta(z)k_x(z)\sin\left[k_x(z)d(z)\right]$$

$$H_y(z) = \omega\epsilon_0\epsilon_r\beta(z)\cos\left[k_x(z)d(z)\right] \tag{7.3}$$

where $d(z)$ is the guide depth. These characteristics are multiplied by the transmission line phase variation as discussed above. The long shallow antenna is used as an example here. The real parts of the calculated E_z and H_y fields are shown in Fig. 7.2. For calculation, the taper has been broken up into 128 elements, and a loss envelope has been imposed on these fields. The power loss of the fundamental mode along the taper was considered in the previous chapter, but the method developed therein has a long run time, over two hours for a typical taper. Inclusion of this technique in the methods developed in this chapter would put an unacceptable overhead on the run times. For instance, the method described in this section takes only a few seconds to run, whilst the complete method introduced at the end of this chapter generally runs in just over a minute. As such, the methods presented in this chapter include a simple loss envelope whose shape is based on the results of Chapter 6.

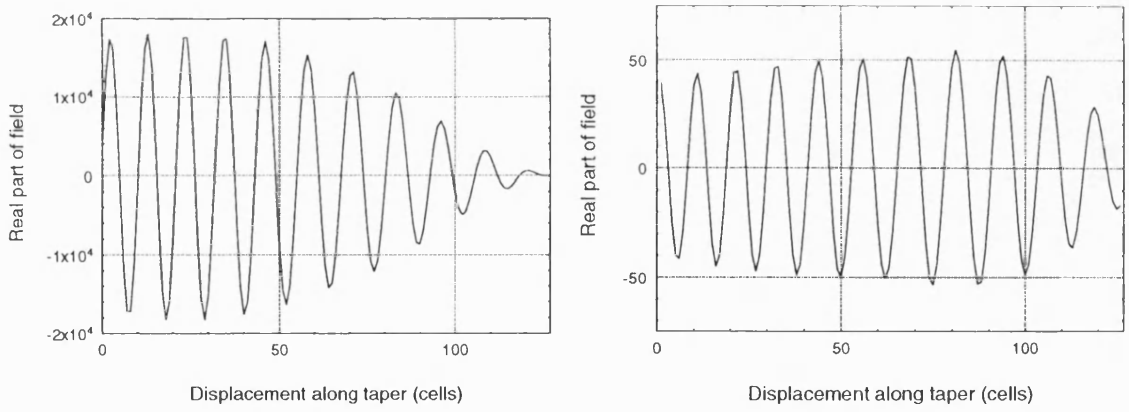

Figure 7.2: Aperture fields along a 300mm LSM H-guide antenna at 10GHz: (a) E_z, and (b) H_y.

The individual contributions of the E_z and H_y field components to the overall pattern, f_z and $g_y Z_0 \sin\theta$ respectively, together with the total pattern are shown in Fig. 7.3.

It can be seen from this figure that the E_z contribution dominates the overall

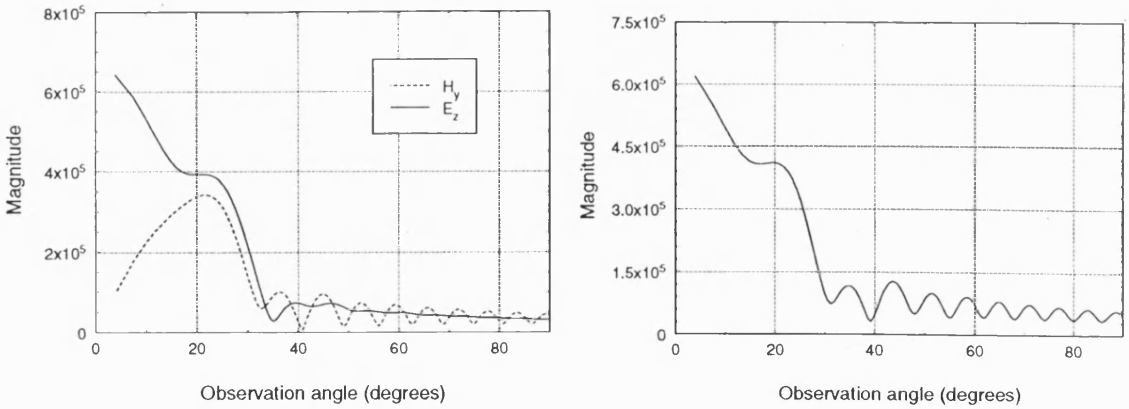

Figure 7.3: (a) E_z versus H_y contributions to the calculated radiation pattern for an LSM antenna at 10GHz, and (b) the total pattern.

radiation from the aperture at this frequency. This is generally true for this structure, as evidenced by the plots in Fig. 7.4 which show the individual E_z and H_y contributions at 7GHz and 14GHz.

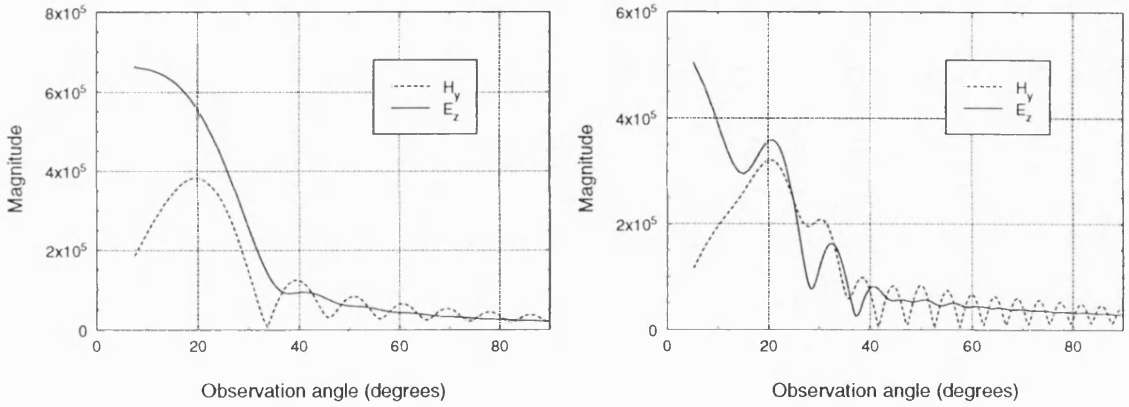

Figure 7.4: Aperture E_z versus H_y contributions to the calculated radiation pattern for an LSM antenna at (a) 7GHz, and (b) 14GHz.

In Fig. 7.5 the total theoretical radiation pattern is compared to measured data. The comparison is not favourable; the position of the main beam is incorrectly predicted, as is the number and position of the sidelobes although the general level of the radiation is reasonably well predicted.

One likely cause for the mismatch between the theoretical and experimental data, besides the possibility that the H-guide representation of the fields on the aperture

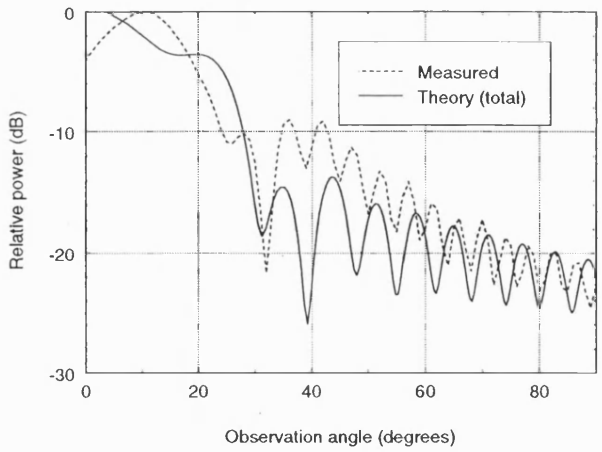

Figure 7.5: Aperture-only total calculated radiation pattern for LSM antenna at 10GHz against measured data.

is poor, is that there are fields on the ground plane which are contributing to the total pattern to such an extent that they cannot be neglected. A straightforward way of testing this hypothesis using the above method is to allow the H_y component to continue after the end of the aperture up to the end of the ground plane. There is after all no reason why the H_y field should not behave in this manner if it has not been entirely attenuated on its passage along the aperture. It is assumed in the results that follow that the field has a propagation constant of k_0 over the ground plane and that its initial amplitude is dictated by that which exists at the end of the aperture. The loss envelope that is applied to the slot fields is also applied to the ground plane fields.

Fig. 7.6(a) shows the calculated E_z and H_y contributions to the total pattern for the antenna geometry considered above with H_y allowed to continue onto the ground plane. The total pattern is also shown in part (b) of the figure against measured data. These results, which are taken at 10GHz should be contrasted with those given above in Fig. 7.3(a) and Fig. 7.5.

Note the increase in the number of sidelobes, as expected, plus the change in the relative magnitudes of the two components of the total calculated pattern; the E_z contribution has been diminished in relation to the H_y contribution. The

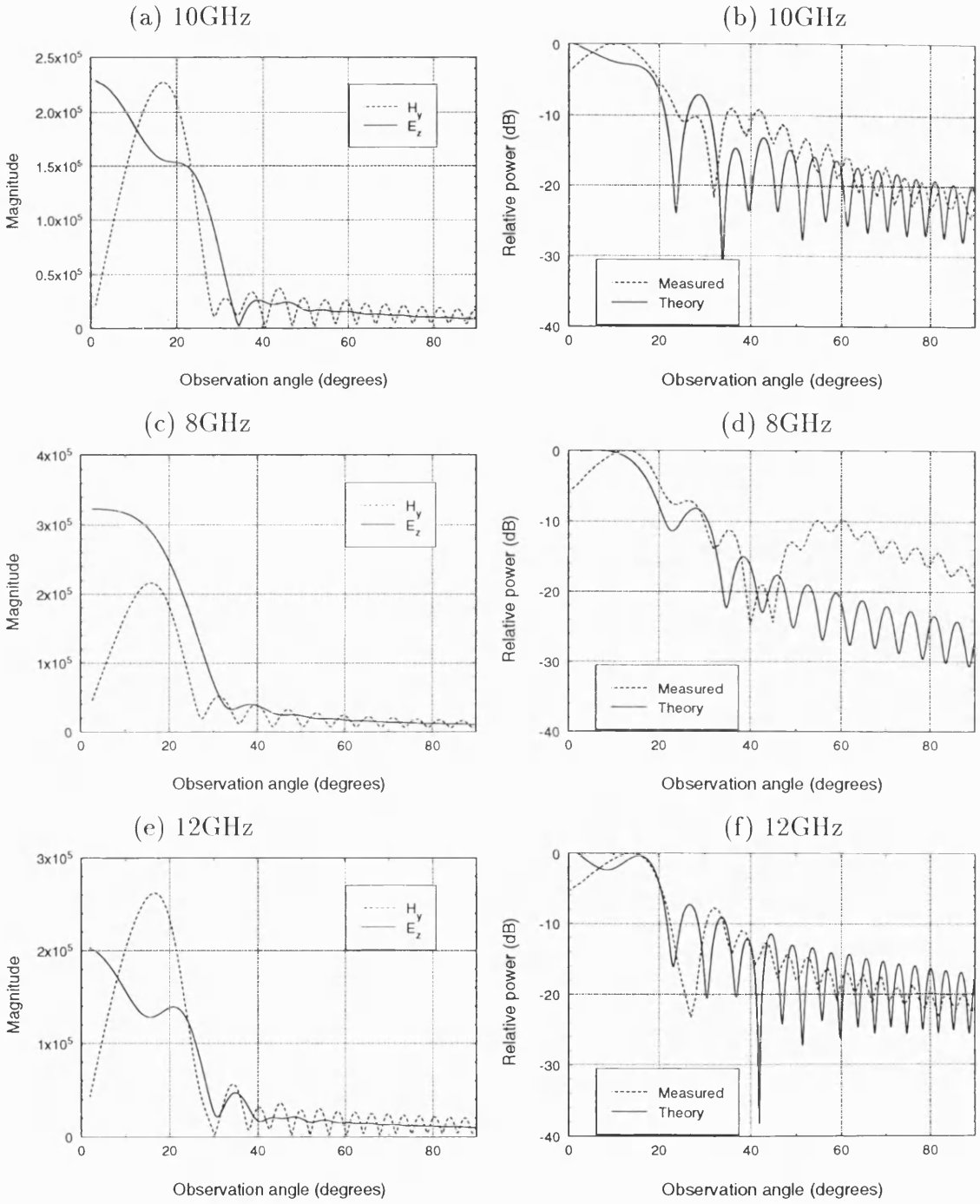

Figure 7.6: (a), (c), (e): E_z versus H_y contributions to the calculated radiation pattern for an LSM antenna. (b), (d), (f): The total pattern. Calculation includes 116mm ground plane extending beyond the aperture

comparison to measured data is now more favourable, with the number and level of the predicted sidelobes being closer to reality. The main beam is still not predicted well, though is more satisfying than that generated by the previous method.

Fig. 7.6(c)-(f) show results at 8GHz and 12GHz calculated using this method. In both cases the degree of agreement to measured results is at least passable, and this method certainly represents an improvement on the aperture-only calculation.

Before moving on, it is interesting to look at the radiation pattern from an H_y field component running the length of the antenna structure (aperture plus ground plane) with a propagation constant of k_0 and without the imposition of the H-guide field expressions. Such a pattern is shown in Fig. 7.7 at 10GHz. The agreement with measured data (i.e. measured from the complete IDG-TSA detailed earlier in this section) is good and implies that the contribution to the total elevation pattern from the H_y field on the ground plane is very significant.

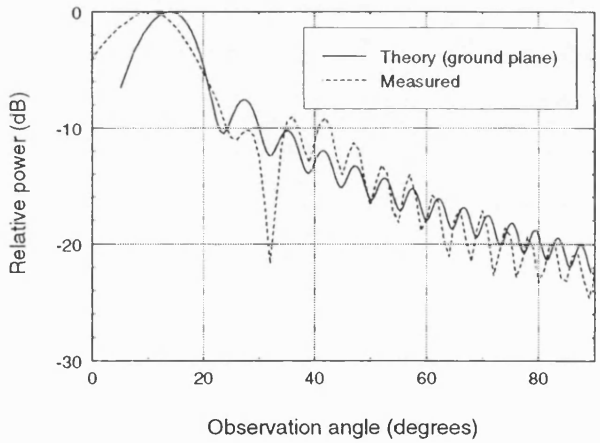

Figure 7.7: Radiation from a line source running the length of the aperture plus ground plane with $\beta = k_0$.

7.5.2 LSE Antenna

In this case it is the E_y and H_z components that are of interest when constructing the elevation plane radiation pattern. Using equation (5.22), the H-guide represen-

tation of these components is:

$$\begin{aligned} E_y &= -\omega\mu_0\beta(z)\sin\left[k_x(z)d(z)\right] \\ H_z &= -j\beta(z)k_x(z)\cos\left[k_x(z)d(z)\right] \end{aligned} \tag{7.4}$$

In this section, the long deep antenna geometry is used as an example. The real parts of the calculated fields on the surface of this structure are shown in Fig. 7.8. In these figures the antenna aperture has been broken up into 128 elements. After element 97 there is no solution to the H-guide propagation constant equations; the mode has cut off. The aperture fields have been allowed to go to zero after this point.

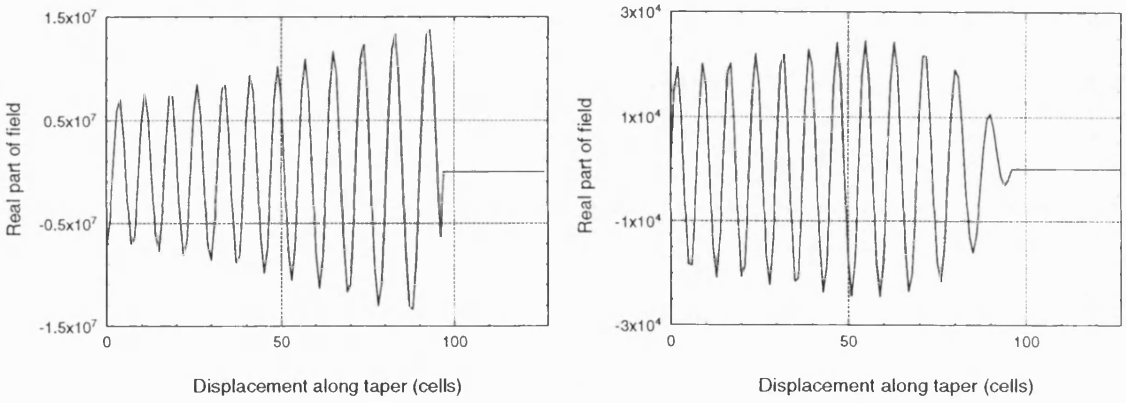

Figure 7.8: Aperture fields along a 300mm LSE H-guide antenna at 10GHz: (a) E_y, and (b) H_z.

The individual contributions at 12GHz of the E_y and H_z fields to the total calculated pattern, $f_y \sin\theta$ and $g_z Z_0$ respectively, are shown in Fig. 7.9(a) and the total calculated pattern is shown in part (b) of the figure.

In this case, the individual contributions to the total calculated pattern are approximately equal in magnitude and of similar shape. The total theoretical pattern is plotted against measured results in Fig. 7.10.

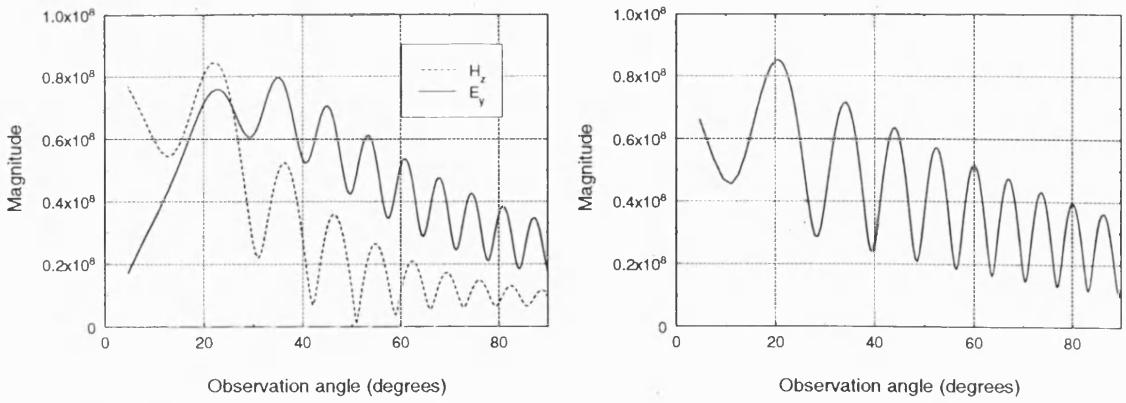

Figure 7.9: (a) E_y versus H_z contributions to the calculated radiation pattern for an LSE antenna at 12GHz, and (b) the total pattern.

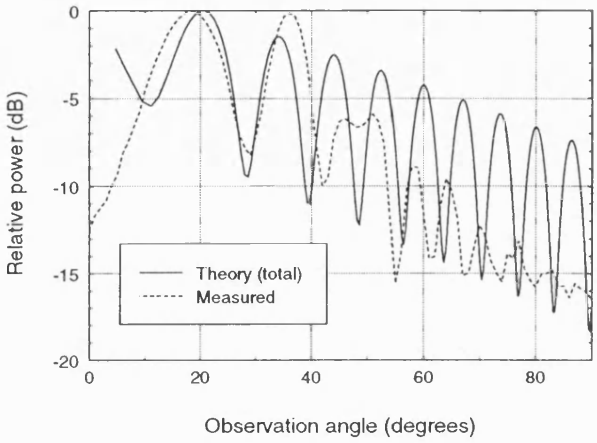

Figure 7.10: Aperture only total calculated radiation pattern for LSE antenna at 12GHz against measured data.

The agreement between measured and theoretical values is reasonable, better than that observed when this method was applied to the LSM structure. Certainly, the predicted number of sidelobes does not differ from those measured so greatly as for the LSM case. The implication is, therefore, that the ground plane fields play a less pronounced role for the LSE IDG-TSA than for the LSM structure. This ties in with the observation made in Section 7.4 that the main power carrying field components have the potential to spread onto the ground plane for LSM polarised antennas but not for those which are LSE polarised.

For the LSM structure, the above method was modified by extending the **H** field

component over the ground plane. This option is not available here as the H_z component has been allowed to go to zero before the end of the aperture due to cut-off of the mode.

7.6 Walter's Approximation for the Finite Ground Plane

It is convenient at this point to examine the effect of incorporating Walter's approximation for the finite size of the ground plane into the model described in the last section. This approximation is discussed in Section 3.4.3.

Practically, implementation of the method requires that the **H** components in equations (7.1) and (7.2) be allowed to propagate along the total length of the antenna structure, aperture plus ground plane, with a propagation constant β equal to k_0. The individual calculated contributions from the **E** and **H** field components are then modified in the far field such that their maximum magnitudes are the same before being combined. Strictly speaking, these far field components are only equal for the case where the antenna is in an infinite ground plane [129]. The results presented below provide some indication of the validity of assuming this to be true for antennas in finite ground planes. In Section 8.7, FDTD is used to investigate this assumption further.

7.6.1 Results for LSM Antenna

The results presented in this section relate to the long shallow antenna. Fig. 7.11 shows theoretical predictions made using the line source method incorporating Walter's ground plane method at six frequencies. Measured data and predictions made using modified Walter's method [3] are also included.

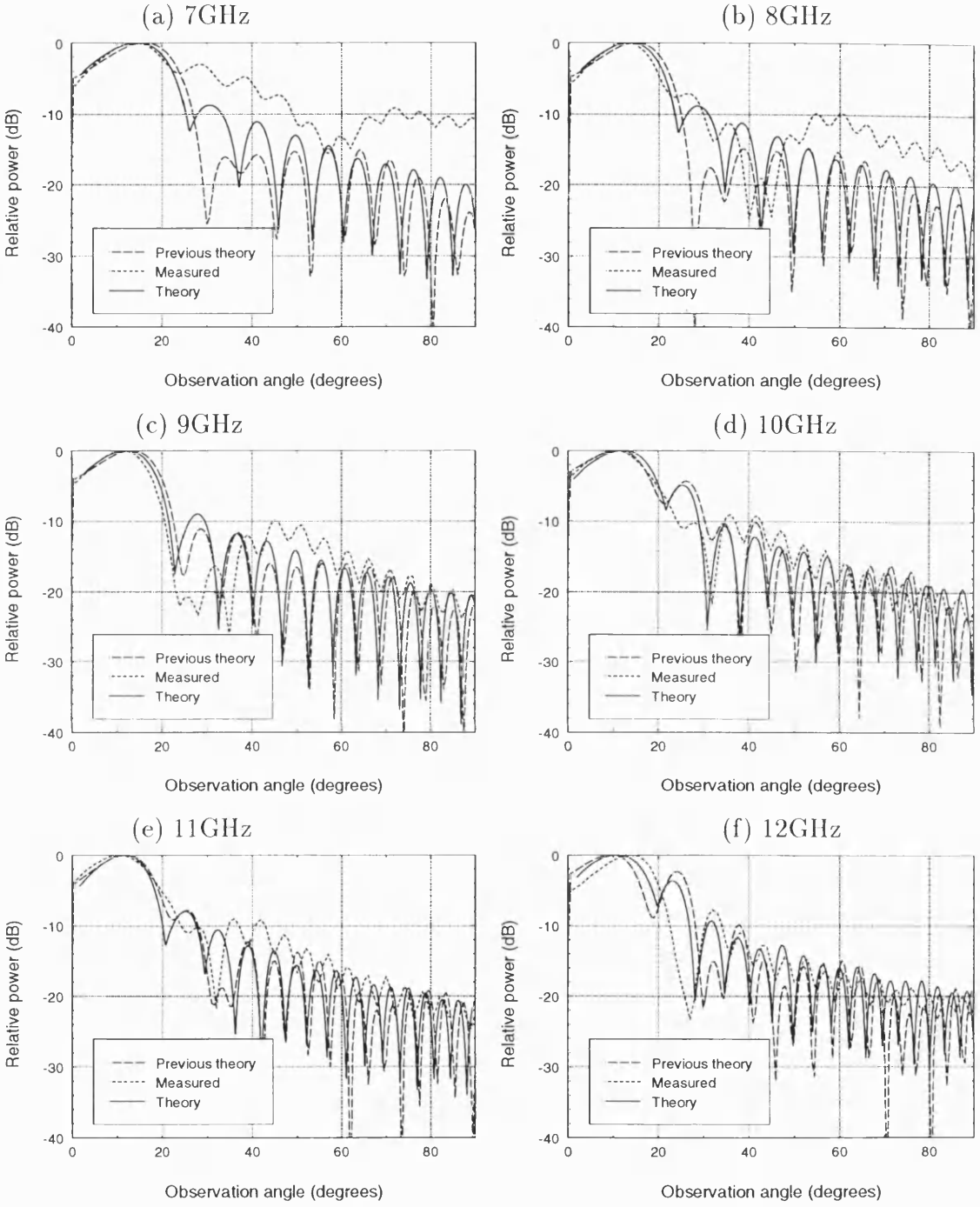

Figure 7.11: Line source method with Walter's approximation for the finite ground plane for an LSM antenna. Comparison to measurements and previous theory.

Considering first the agreement shown between the measured results and the line source method, it is clear that the assumptions made in the analysis are not unreasonable. The theory predicts the position of the main near-endfire beam accurately, and the number and positions of the sidelobes are reasonably well predicted. However, for the lower frequencies shown, 7 and 8GHz, considerable discrepancies can be seen between the theoretical and measured sidelobe level.

It is clear that the previous analytical method [3] produces broadly similar results to the line source method. For the lower frequencies, however, the line source method produces better predictions for the first sidelobes. This improvement can only be due to improved modelling of the aperture fields using the transmission line model.

7.6.2 Results for LSE Antenna

The discussion in Section 7.5 indicated that the LSE structure is less suitable for the application of Walter's ground plane method than the LSM structure. This is backed up by the results shown in Fig. 7.12 which relate to the long deep antenna. When compared to measured data, the agreement can be seen to be quite poor. Although some of the details of the measured data are picked out by the theory there is much deviation, and predictions of the positions of the main beam are particularly inaccurate.

No comparison to an earlier theoretical method is possible in this case as LSE antennas have not previously been analysed.

In considering the reasons for the differences between the predicted and measured results, it is helpful to look at the individual calculated E_y and H_z contributions in the above results and compare them to the experimental values obtained from the complete antenna structure. These comparisons are shown in Fig. 7.13 at 8,

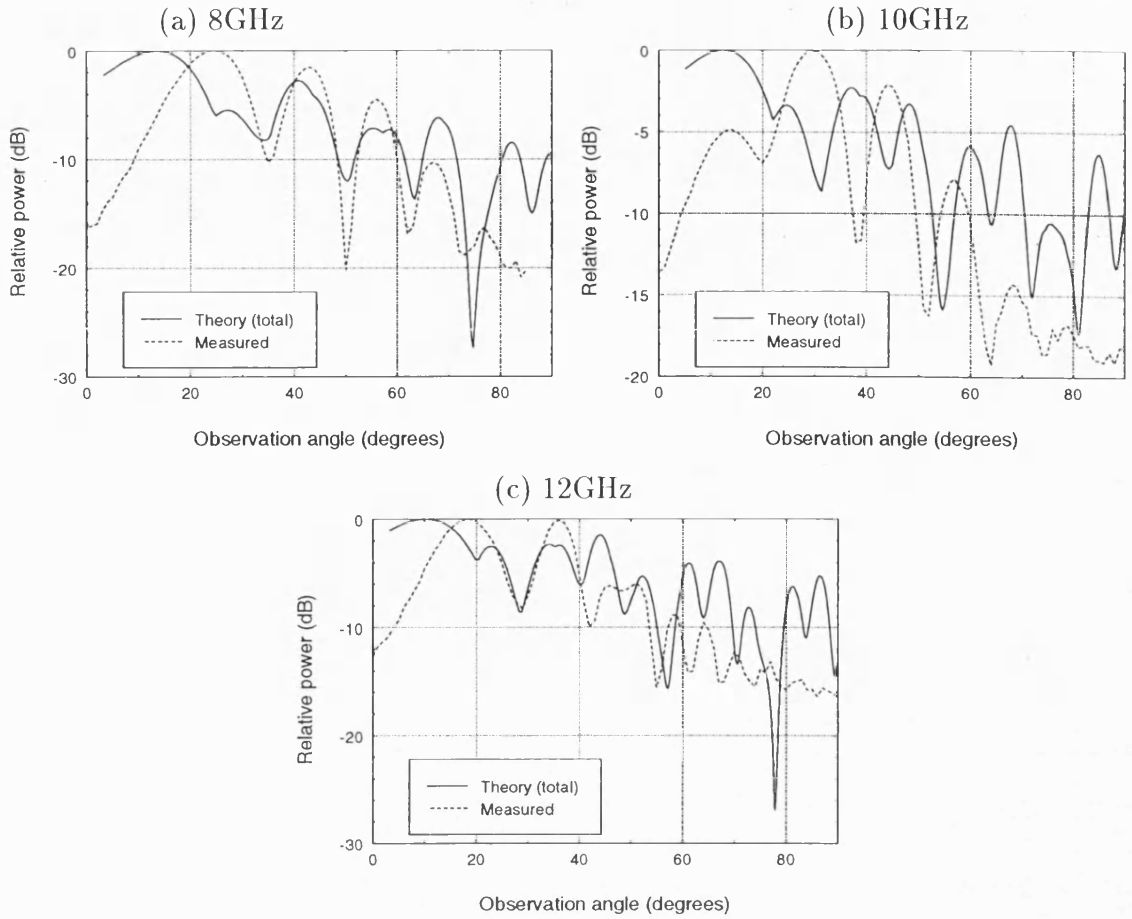

Figure 7.12: Line source method with Walter's approximation for the finite ground plane for a long LSE antenna.

10, and 12GHz.

It is clear that the pattern from the E_y component alone is much closer to the measured data than the combined patterns presented in the previous set of figures. There is no clear correlation between the H_z component pattern and the measured data. It appears, therefore, that the contribution of the H_z field to the overall pattern is being overestimated by Walter's ground plane method.

The conclusions that can be drawn from the above results are that Walter's ground plane method is reasonably effective for the LSM case but of little value for LSE structures. In the latter case, more accurate results can be obtained by considering only the aperture fields rather than the fields on both the aperture and the ground

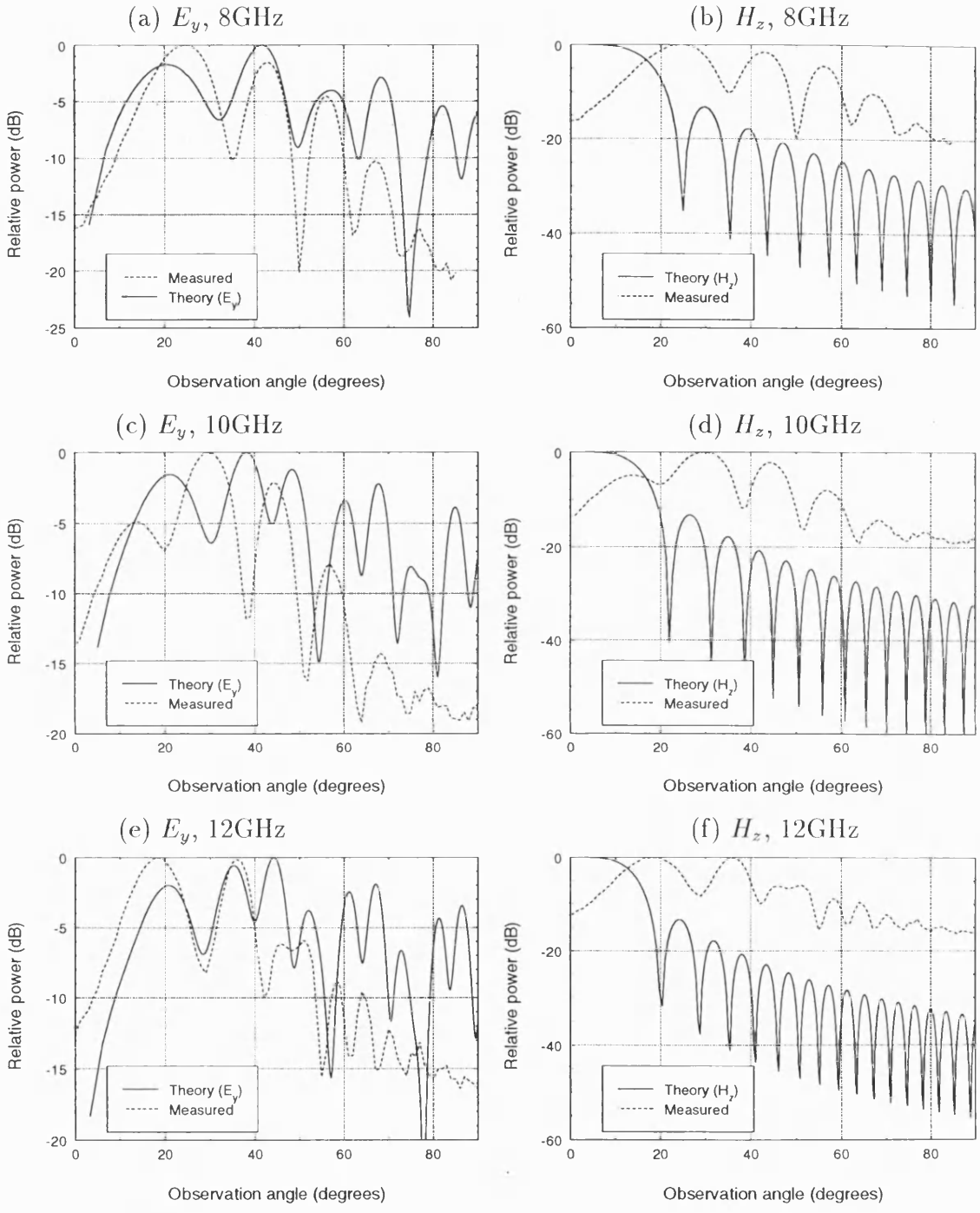

Figure 7.13: Line source method with Walter's approximation for the finite ground plane for an LSE antenna. Individual calculated contributions.

plane. This is not to say that ground plane fields do not play a role in the LSE radiation pattern, but using this approximate method it is not possible to accurately estimate the relative contributions that these fields make. These conclusions are in line with the comments made in Section 7.4.

7.7 Extension of the Model to Two Dimensions

In the light of the foregoing conclusions it was decided to extend the line source model into two dimensions to model the surface fields on both the aperture and the finite ground plane. The aim is to produce radiation pattern predictions for the IDG-TSA without recourse to Walter's approximation. Although this approximation can provide reasonable results for the LSM case, it is based on an assumption that is not universally valid, and it is certainly not satisfactory from the physical point of view as it makes no attempt to model the field variations that occur on the ground plane. It is not suitable for calculating the far field radiation over a broad range of elevation angles, i.e. away from the principal planes. In addition, Walter's approximation cannot be used in the LSE case, so some other technique must be found to take account of the fields on the ground plane for this type of structure.

Producing an analytical model of the IDG-TSA ground plane fields is not straightforward; the manner in which the slot fields act as the source for the ground plane fields is unclear. In the following section various options for the transverse variation of the ground plane fields are considered in order to establish their principal features. At this stage, some of the parameters of these field variations are set empirically. The results of this investigation are subsequently used to inform the consideration of an analytical procedure for linking the ground plane fields to those in the slot.

It was shown in the previous section that the LSM antenna radiation pattern is much more affected by ground plane fields than the LSE pattern. As such, the following sections focus on the LSM structure. The LSE structure is reintroduced in Chapter 9 once the complete model of the antenna has been developed.

7.7.1 Empirical Models of the Ground Plane Fields

For the LSM antenna, three models of the ground plane fields are tested in this section. In each case it was found that the best results were obtained when plane wave propagation is assumed along the antenna (i.e. $e^{-jk_0 z}$); cylindrical propagation was tried also but in general this caused a deterioration in the results.

Model 1: Fields constant with y

As a first approximation, it is assumed that the tangential ground plane fields (i.e. H_y and H_z) do not vary in magnitude in the transverse (y) direction and vary as $e^{-jk_0 z}$ in the longitudinal direction. An initial approximation of the magnitude of the H_z component on the ground plane is not difficult to decide upon; the H-guide field expression is finite, at a maximum, at the slot edge. This value can be extended onto the ground plane along the slot, with the final value at the end of the slot being allowed to continue onto the section of ground plane that extends beyond the end of the slot. A plot of the magnitude of the H_z component on the slot and the ground plane surface of an IDG-TSA, built using this approximation, is shown in Fig. 7.14.

In the figure, only the right hand half of the structure is depicted, as the left hand half is simply a reflection of this. The half-width of the slot is 11.43mm and it is 300mm long with 120mm of ground plane continuing beyond the end of the slot. The half-width of the complete structure, including the side plates, is 45mm. Note the invariance with y of the ground plane fields.

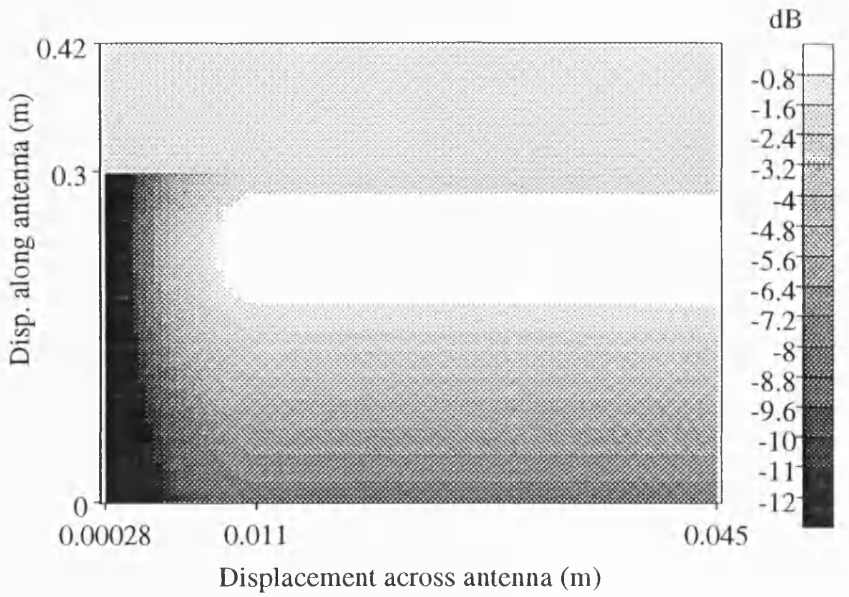

Figure 7.14: Magnitude of H_z component on antenna surface at 10GHz, calculated using H-guide fields with ground plane fields assumed to be invariant with y.

The handling of the H_y component is more difficult but accurate modelling of this is critical to the success of the method. Indeed, simulation has shown that small changes to the H_y model can have a considerable impact on the predicted radiation patterns in the principal planes, whereas the H_z model can be altered significantly with little discernible effect on these results.

A plot of the H_y component with magnitude constant in the y direction is shown in Fig. 7.15. This relates to the same structure as the H_z plot above. On the ground plane a constant magnitude, empirically determined, is set and then modified with a loss characteristic similar to that implemented within the slot. This representation of the component runs the full length of the structure.

Results at four frequencies for the long LSM antenna using the above model are shown in Figures 7.16 and 7.17. Both elevation plane and azimuthal plane results are shown. The azimuthal plane results are taken at the elevation angle corresponding to the elevation plane pattern maximum, rather than at zero elevation angle as might be expected. The agreement between theoretical and measured data

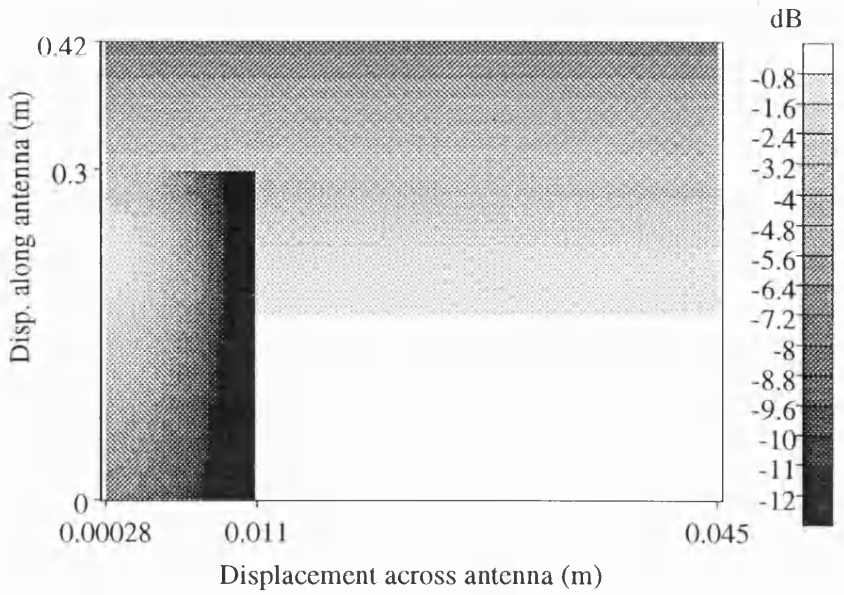

Figure 7.15: Magnitude of H_y component on antenna surface at 10GHz, calculated using H-guide fields with ground plane fields assumed to be invariant with y.

in the elevation plane is good, with the position of the main beam being correctly predicted. Sidelobes are generally well predicted, with some of the sharp troughs in the experimental data being picked out by the theory.

Agreement in the azimuthal plane is quite poor, except at 9GHz, with the beams being too narrow at all frequencies. In the figures, comparison is also made to the results of modified Walter's method [3] at 10GHz and 12GHz. There is little to choose between the two methods in the elevation plane in terms of agreement with measured results. In the azimuthal plane, the modified Walter's method results are generally closer to measurements.

It is clear from the above that the model chosen is reasonably accurate in the longitudinal direction but the invariance in the transverse y direction is unrealistic, leading to the excessively narrow azimuthal plane beams.

Model 2: Exponential decay with y

The natural response to the above results is to reduce the effective aperture in

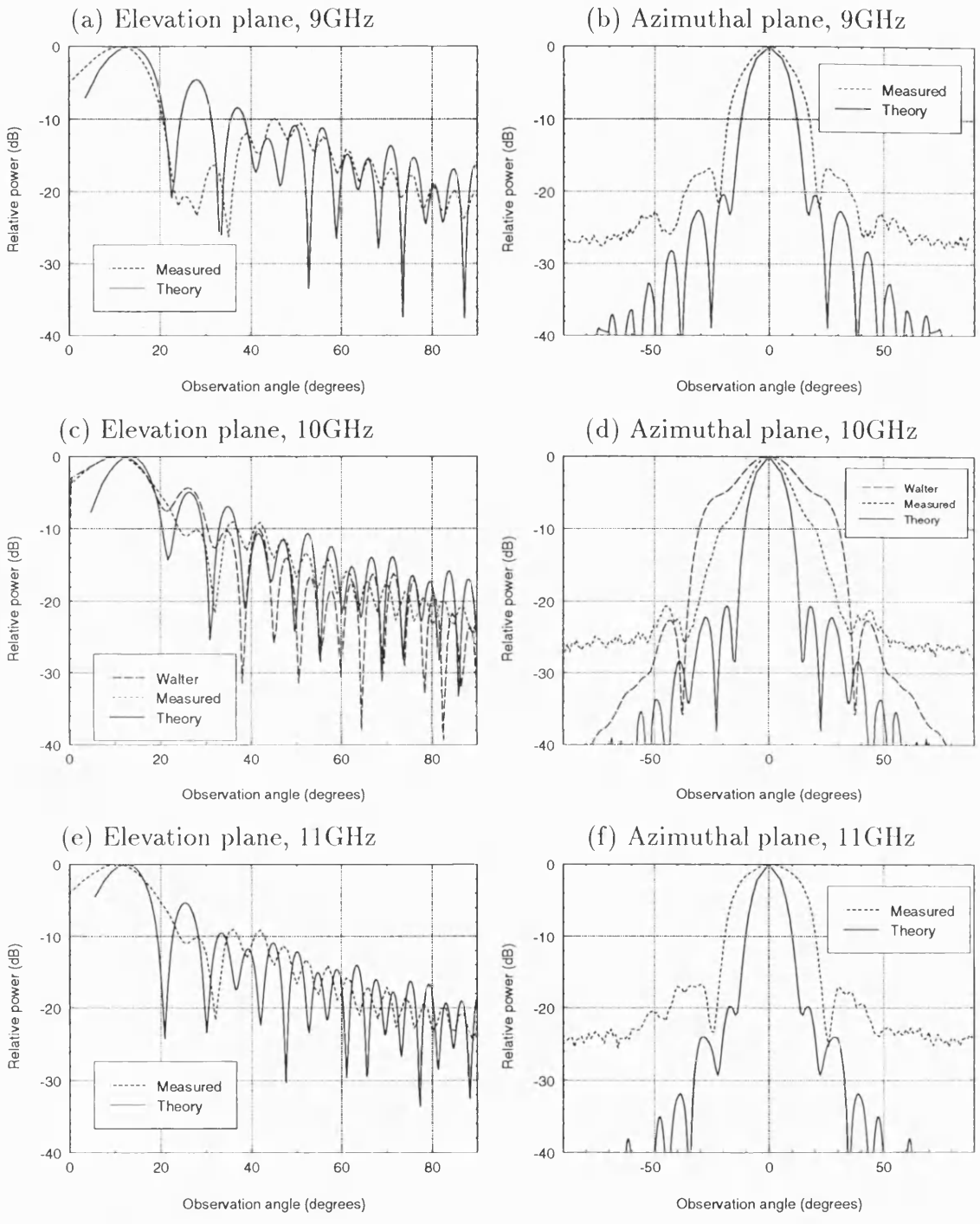

Figure 7.16: Two dimensional H-guide method. Ground plane fields are constant in the y direction.

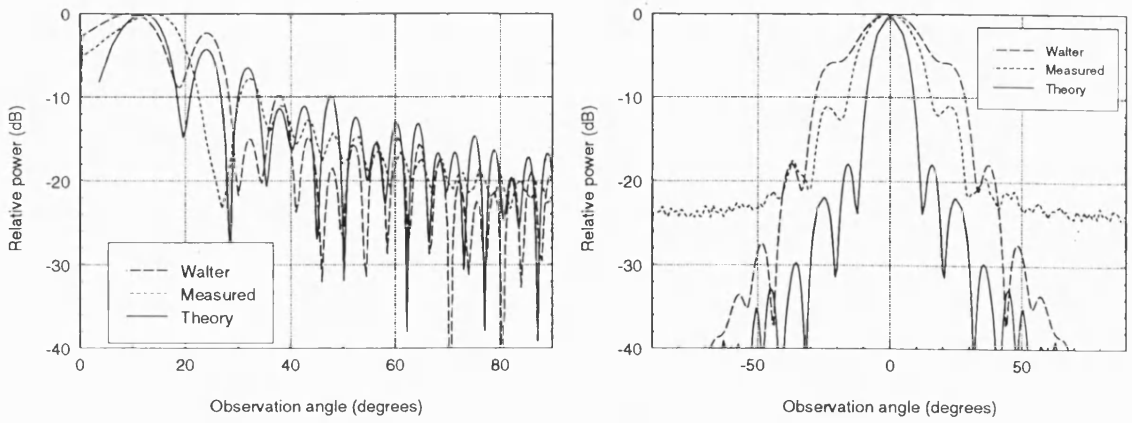

Figure 7.17: Two dimensional H-guide method at 12GHz. Ground plane fields are constant in the y direction. (a) elevation plane, and (b) azimuthal plane radiation.

the y direction whilst leaving the model unchanged in the longitudinal direction. Thus, leaving the models of E_y and E_z unchanged, the H_y and H_z components are allowed to drop off exponentially with y over the ground plane. Fig. 7.18 shows the H_y component in the case of a rapid and slow decay with y. In practice a rapid decay is found to give the most accurate results.

Figures 7.19 and 7.20 show results obtained using this model at four frequencies. In the azimuthal plane comparison to the y-invariant model has been included at 9GHz and 12GHz. The elevation plane patterns are little different from those produced using the previous model, but it is clear that in the azimuthal plane the beam has widened to give an improved match to the measured results.

Model 3: Bessel function decay with y

Model 2 gives reasonable results, but the form of the H_y field component on the ground plane is determined by purely empirical means. In this section, the shape of this component is linked to theory.

In Section 3.3 electrostatic theory is used to examine the behaviour of a field at a metal/dielectric interface. The general solution of Laplace's equation given in equation (3.35) is expressed in terms of the small argument approximation of the

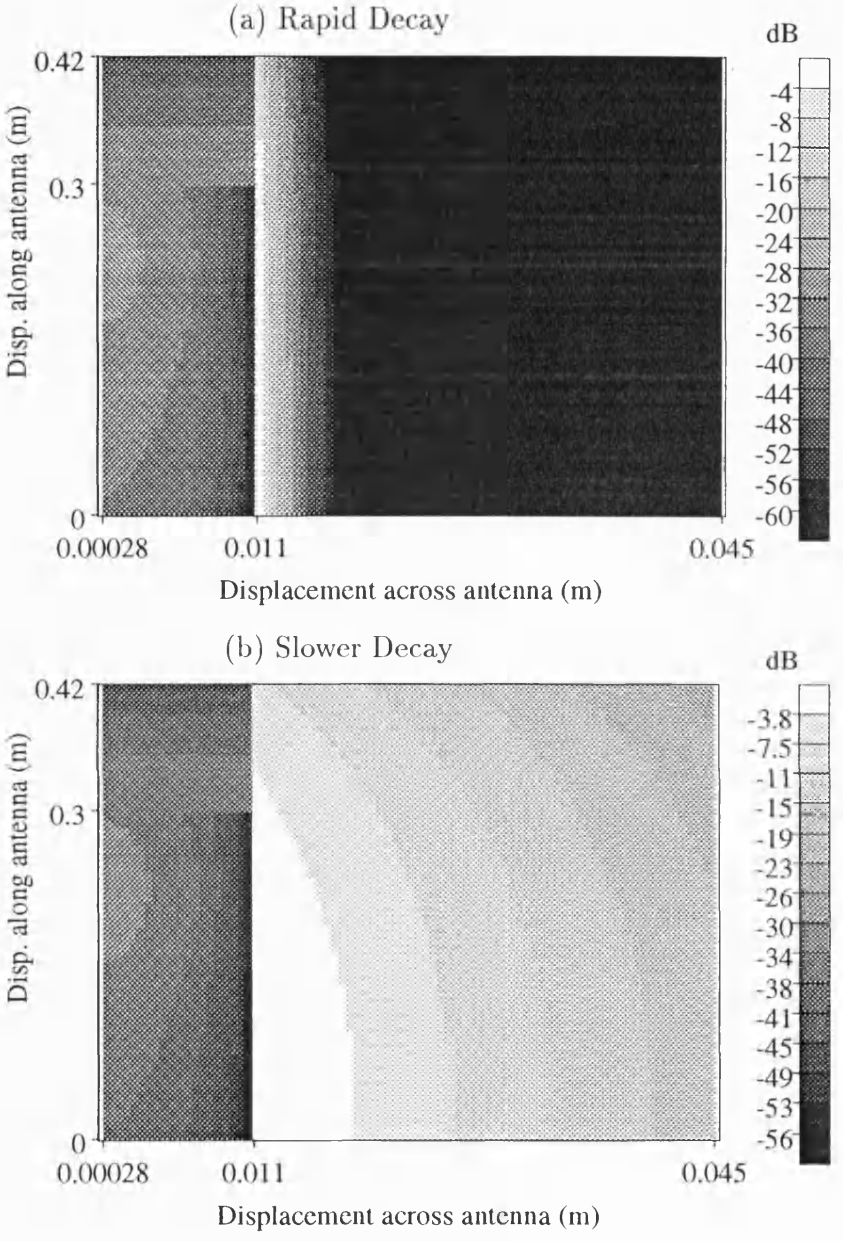

Figure 7.18: Magnitude of H_y component on antenna surface at 10GHz, calculated using H-guide fields with ground plane fields assumed to decay exponentially with y.

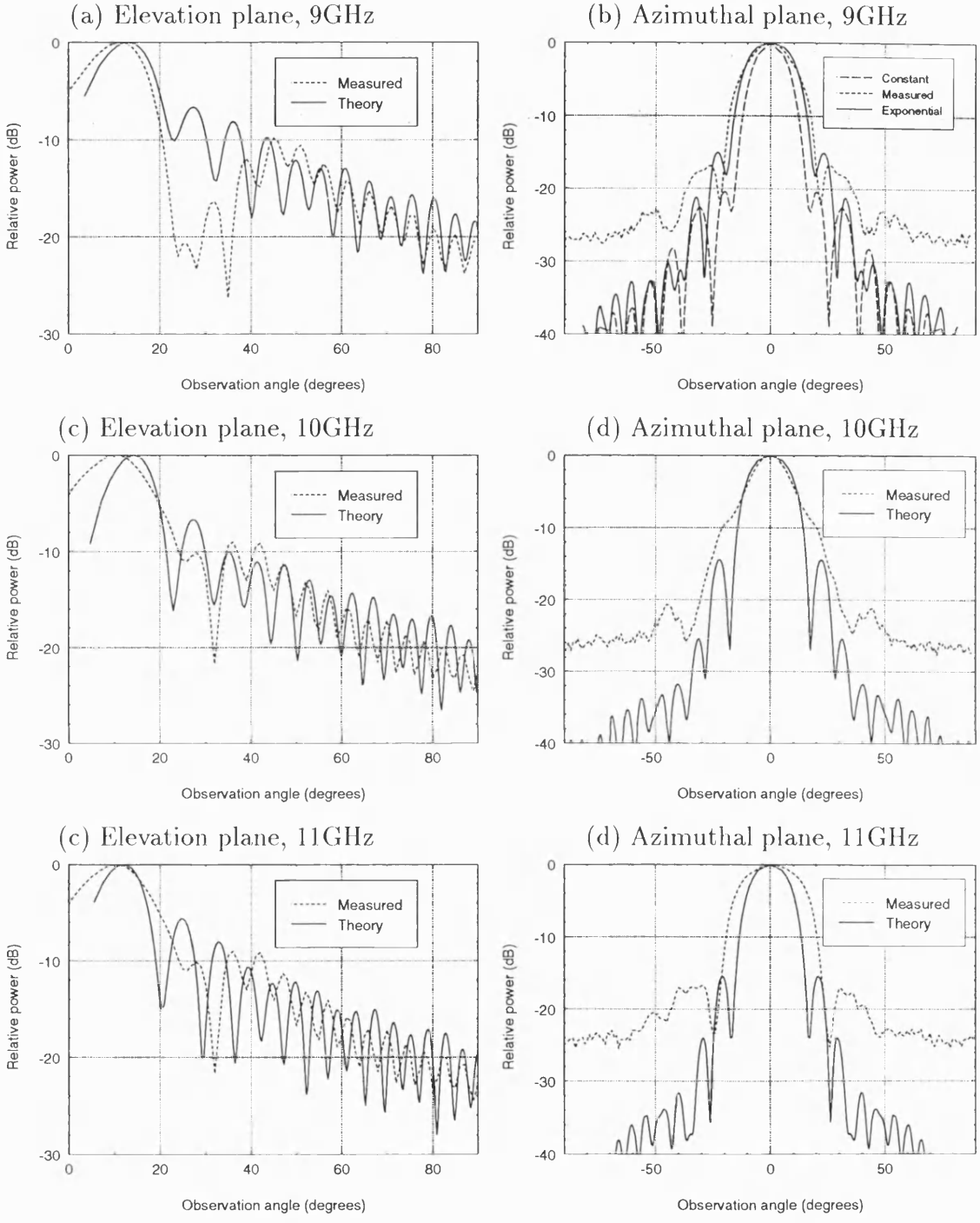

Figure 7.19: Two dimensional H-guide method. Ground plane fields decay exponentially in the y direction.

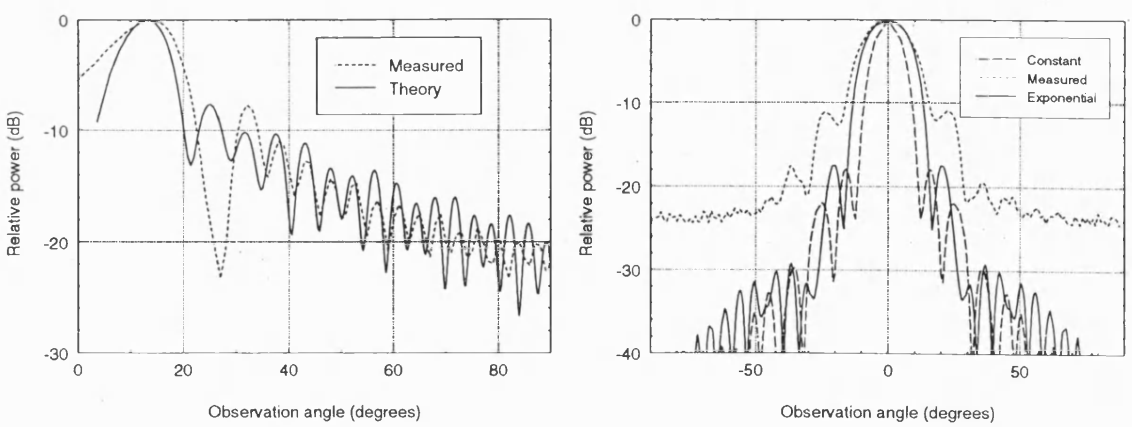

Figure 7.20: Two dimensional H-guide method at 12GHz. Ground plane fields decay exponentially in the y direction. (a) elevation plane, and (b) azimuthal plane radiation.

Bessel function $J_v(k_0 r)$ where r is the radial distance from the slot edge. From equation (3.40), the magnetic potential on the ground plane surface (where $\phi = 3\pi/2$) expressed in Bessel function form is:

$$\Phi_{2m} = AJ_\chi(k_0 r) \tag{7.5}$$

where A and χ are constants. Equation (3.34) leads to the following expression for H_y close to the slot edge on the ground plane surface:

$$H_y = B\frac{dJ_\chi(k_0 r)}{dr} \tag{7.6}$$

where B is a constant. In Section 3.3.2 the value of χ is given as 0.6667. If this form of the fields is used instead of the exponential decay employed in the previous model, the H_y component appears as shown in Fig. 7.21.

Strictly, equation (7.6) is only valid close to the edge, but for the purposes of the model it has been allowed to continue beyond this. Again, the magnitude of this component on the ground plane can only be set by experiment.

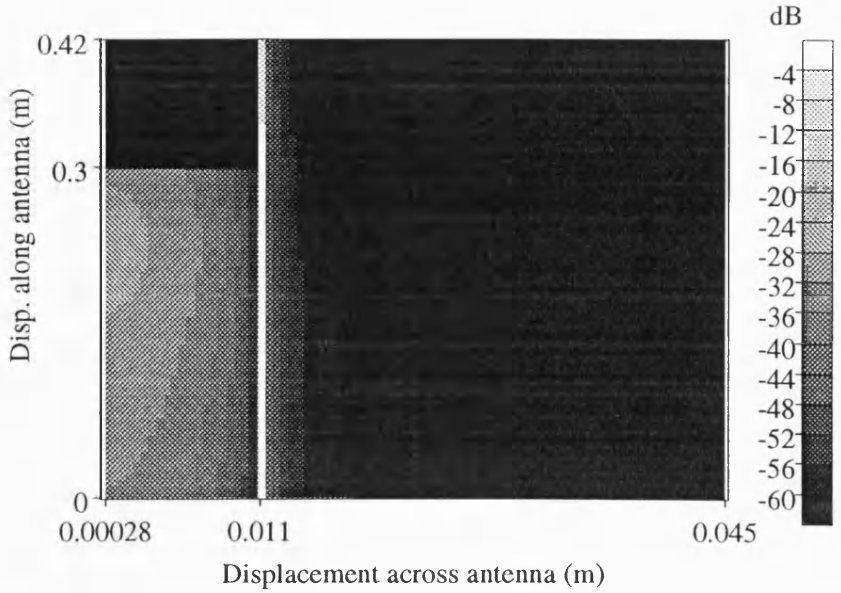

Figure 7.21: Magnitude of H_y component on antenna surface at 10GHz, calculated using H-guide fields with ground plane fields assumed to vary as a Bessel function with y.

Figures 7.22 and 7.23 show results obtained using this model. It is not easy to judge whether agreement with experiment is better for this model or Model 2; they are both reasonably effective, but the link to theory leads the present model to be more satisfying from the physical point of view. The comparisons to modified Walter's method [3] at 10GHz and 12GHz show the new model to be generally superior, especially in the azimuthal plane.

To summarise, a new method for analysis of the IDG-TSA has been developed which includes a model of the fields on the ground plane. Results obtained using this method show good agreement to measured values and show some improvements upon results generated by the previous analytical method. The new method has dispensed with Walter's approximation for the finite ground plane and has replaced it with a more realistic model of the fields.

Whilst the form of the ground plane fields identified above seems to be reasonable, it is necessary to set the magnitude of these fields empirically, with the magnitude

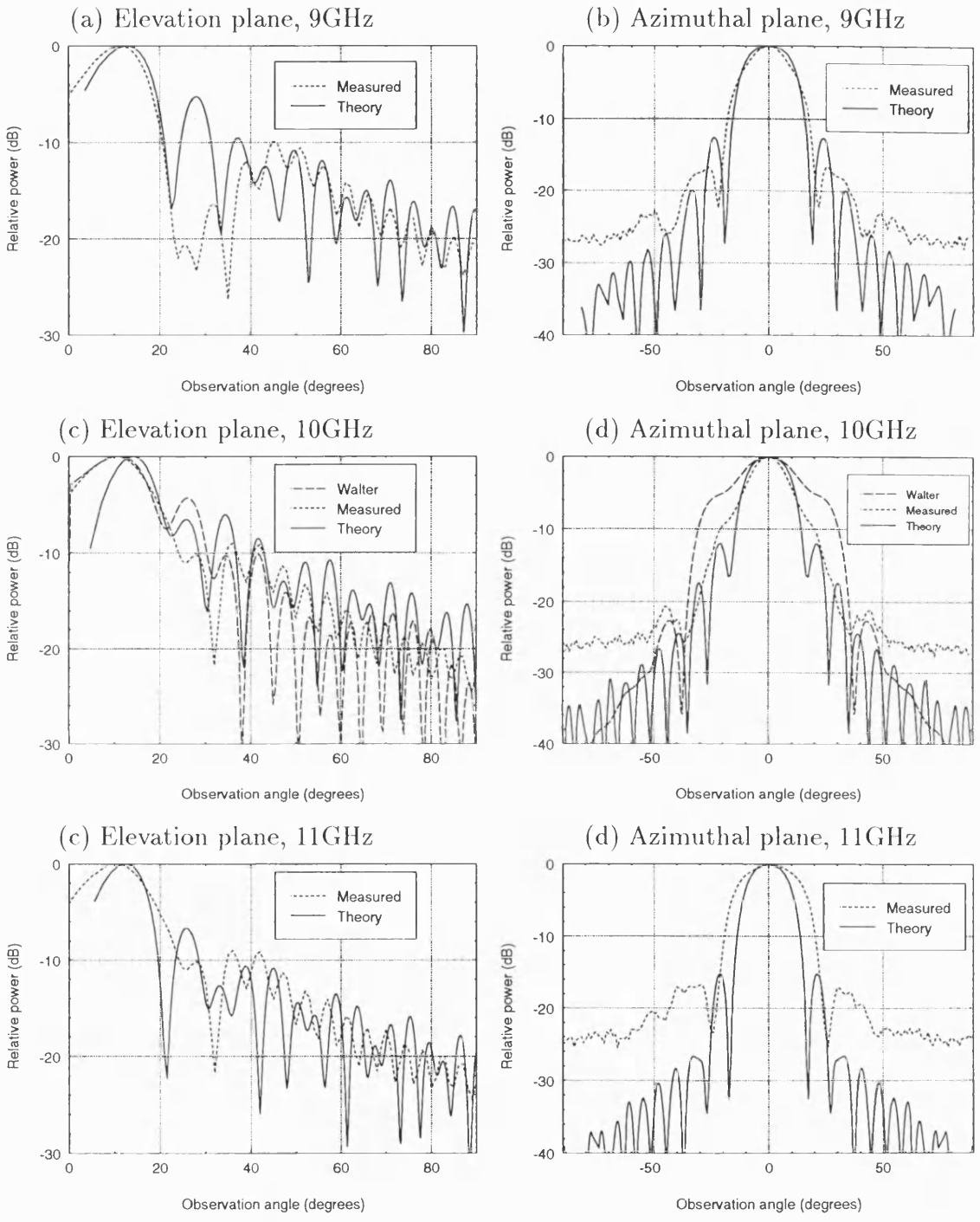

Figure 7.22: Two dimensional H-guide method. Ground plane fields decay as a Bessel function in the y direction.

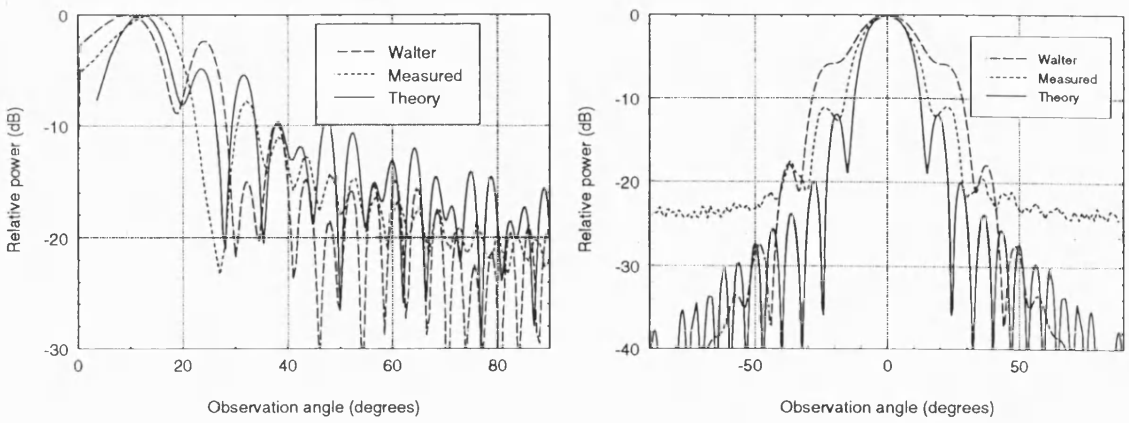

Figure 7.23: Two dimensional H-guide method at 12GHz. Ground plane fields decay as a Bessel function in the y direction. (a) elevation plane, and (b) azimuthal plane radiation.

of the fields in the slot as a guide. This is clearly not entirely satisfactory for prediction purposes. As such, consideration is given below to a new method which creates an analytical link between the ground plane fields and those on the slot surface.

7.8 More Accurate Modelling of Singularities

7.8.1 Introduction

The theory introduced in Section 3.3 can be used to develop a more accurate model of the IDG field singularities for insertion into the IDG-TSA models. Using this method, an analytical link between the fields on the slot surface and those on the ground plane surface can be made. By driving them from the known slot fields this method does away with the need to determine the magnitude of the ground plane fields empirically.

The method used here consists of deriving expressions, in rectangular co-ordinates, for the fields near to the IDG edge on the slot surface and on the ground plane

surface. The great advantage of this theory is that it is applicable on either side of the slot boundary, thus providing for the first time information about the field behaviour over the ground plane.

7.8.2 Fields in Air

Referring back to Fig. 3.6 and utilising the nomenclature and methodology introduced in Section 3.3 expressions for the fields in the air close to the edge can be derived:

$$\begin{aligned}
E_r &= M\kappa r^{\kappa-1}\frac{\sin\frac{\kappa\pi}{2}}{\sin\kappa\pi}\sin\left(\frac{3\pi}{2}-\phi\right)\kappa \\
E_\phi &= -M\kappa r^{\kappa-1}\frac{\sin\frac{\kappa\pi}{2}}{\sin\kappa\pi}\cos\left(\frac{3\pi}{2}-\phi\right)\kappa \\
E_z &= j\omega\mu_0 N r^{\chi}\frac{\cos\frac{\chi\pi}{2}}{\cos\chi\pi}\sin\left(\frac{3\pi}{2}-\phi\right)\chi \\
H_r &= N\chi r^{\chi-1}\frac{\cos\frac{\chi\pi}{2}}{\cos\chi\pi}\cos\left(\frac{3\pi}{2}-\phi\right)\chi \\
H_\phi &= N\chi r^{\chi-1}\frac{\cos\frac{\chi\pi}{2}}{\cos\chi\pi}\sin\left(\frac{3\pi}{2}-\phi\right)\chi \\
H_z &= j\omega\epsilon_0 M r^{\kappa}\frac{\sin\frac{\kappa\pi}{2}}{\sin\kappa\pi}\cos\left(\frac{3\pi}{2}-\phi\right)\kappa
\end{aligned} \tag{7.7}$$

The above equations apply generally in the air region. From these, the fields on the slot surface close to the edge (at $\phi = \frac{\pi}{2}$) can be written down:

$$\begin{aligned}
E_r &= M\kappa r^{\kappa-1}\sin\frac{\kappa\pi}{2} \\
E_\phi &= -M\kappa r^{\kappa-1}\sin\frac{\kappa\pi}{2}\cot\kappa\pi \\
E_z &= j\omega\mu_0 N r^{\chi}\cos\frac{\chi\pi}{2}\tan\chi\pi \\
H_r &= N\chi r^{\chi-1}\cos\frac{\chi\pi}{2}
\end{aligned}$$

$$\begin{aligned} H_\phi &= N\chi r^{\chi-1}\cos\frac{\chi\pi}{2}\tan\chi\pi \\ H_z &= j\omega\epsilon_0 M r^{\kappa}\sin\frac{\kappa\pi}{2}\cot\kappa\pi \end{aligned} \tag{7.8}$$

Similarly, the fields on the ground plane surface close to the edge (at $\phi = \frac{3\pi}{2}$) are:

$$\begin{aligned} E_r &= 0 \\ E_\phi &= -M\kappa r^{\kappa-1}\frac{\sin\frac{\kappa\pi}{2}}{\sin\kappa\pi} \\ E_z &= 0 \\ H_r &= N\chi r^{\chi-1}\frac{\cos\frac{\chi\pi}{2}}{\cos\chi\pi} \\ H_\phi &= 0 \\ H_z &= j\omega\epsilon_0 M r^{\kappa}\frac{\sin\frac{\kappa\pi}{2}}{\sin\kappa\pi} \end{aligned} \tag{7.9}$$

To be of practical use in the IDG-TSA model, equations (7.8) and (7.9) need to be converted to rectangular co-ordinates. Thus, on the slot surface:

$$\begin{aligned} E_x &= M\kappa r^{\kappa-1}\sin\frac{\kappa\pi}{2}\cot\kappa\pi \\ E_y &= M\kappa r^{\kappa-1}\sin\frac{\kappa\pi}{2} \\ E_z &= j\omega\mu_0 N r^{\chi}\cos\frac{\chi\pi}{2}\tan\chi\pi \\ H_x &= -N\chi r^{\chi-1}\cos\frac{\chi\pi}{2}\tan\chi\pi \\ H_y &= N\chi r^{\chi-1}\cos\frac{\chi\pi}{2} \\ H_z &= j\omega\epsilon_0 M r^{\kappa}\sin\frac{\kappa\pi}{2}\cot\kappa\pi \end{aligned} \tag{7.10}$$

and on the ground plane surface:

$$
\begin{aligned}
E_x &= -M\kappa r^{\kappa-1}\frac{\sin\frac{\kappa\pi}{2}}{\sin\kappa\pi} \\
E_y &= 0 \\
E_z &= 0 \\
H_x &= 0 \\
H_y &= -N\chi r^{\chi-1}\frac{\cos\frac{\chi\pi}{2}}{\cos\chi\pi} \\
H_z &= j\omega\epsilon_0 M r^{\kappa}\frac{\sin\frac{\kappa\pi}{2}}{\sin\kappa\pi}
\end{aligned}
\tag{7.11}
$$

Equations (7.10) and (7.11) are the required results characterising the field behaviour around the slot edge on the antenna surface.

7.8.3 Example

As an example, consider an IDG edge with $\epsilon_r = 2.3$. In this case χ is 0.6667 and κ is 0.7455, and equation (7.10) for the fields on the slot surface becomes:

$$
\begin{aligned}
E_x &= -0.69Mr^{-0.255} \\
E_y &= 0.69Mr^{-0.255} \\
E_z &= Kr^{0.667} \\
H_x &= \frac{N}{\sqrt{3}}r^{-0.333} \\
H_y &= \frac{N}{3}r^{-0.333} \\
H_z &= -0.92Lr^{0.75}
\end{aligned}
\tag{7.12}
$$

and equation (7.11) for the fields on the ground plane surface becomes:

$$\begin{aligned} E_x &= -0.98Mr^{-0.255} \\ E_y &= 0 \\ E_z &= 0 \\ H_x &= 0 \\ H_y &= \frac{2N}{3}r^{-0.333} \\ H_z &= 1.31Lr^{0.75} \end{aligned} \tag{7.13}$$

where K and L are constants. In Fig. 7.24 the above relationships are displayed for the transverse field components. The fields 5mm (i.e. $\lambda_0/10$ at 10GHz) either side of an IDG edge on the guide surface are shown. Zero displacement coincides with the edge. Fields on the ground plane are shown on the right hand side of each graph, whilst the fields on the slot surface are shown on the left hand side.

Although the fields in the plane of the air/dielectric interface depicted in these figures are the main concern of this work, it is of interest to use the above analysis to look at the field behaviour in the wider air region rather than just on a horizontal cut through it. Fig. 7.25 shows this behaviour, and indicate very clearly the extent of the effect of the edge. This data was generated using the Cartesian form of equation (7.7), which is reproduced later in the thesis as equation (8.1).

In these figures the IDG surface coincides with the lower horizontal axis, the centre of which is the location of the edge. The left hand half of each figure shows the field in the air over the dielectric, the right hand half shows that over the ground plane. Data is given for the area 'close' to the edge, this being 3mm along each of the Cartesian axes so that the most distant points depicted are 4.24mm from the edge.

As a check on the validity of the method, comparisons can be made to predictions

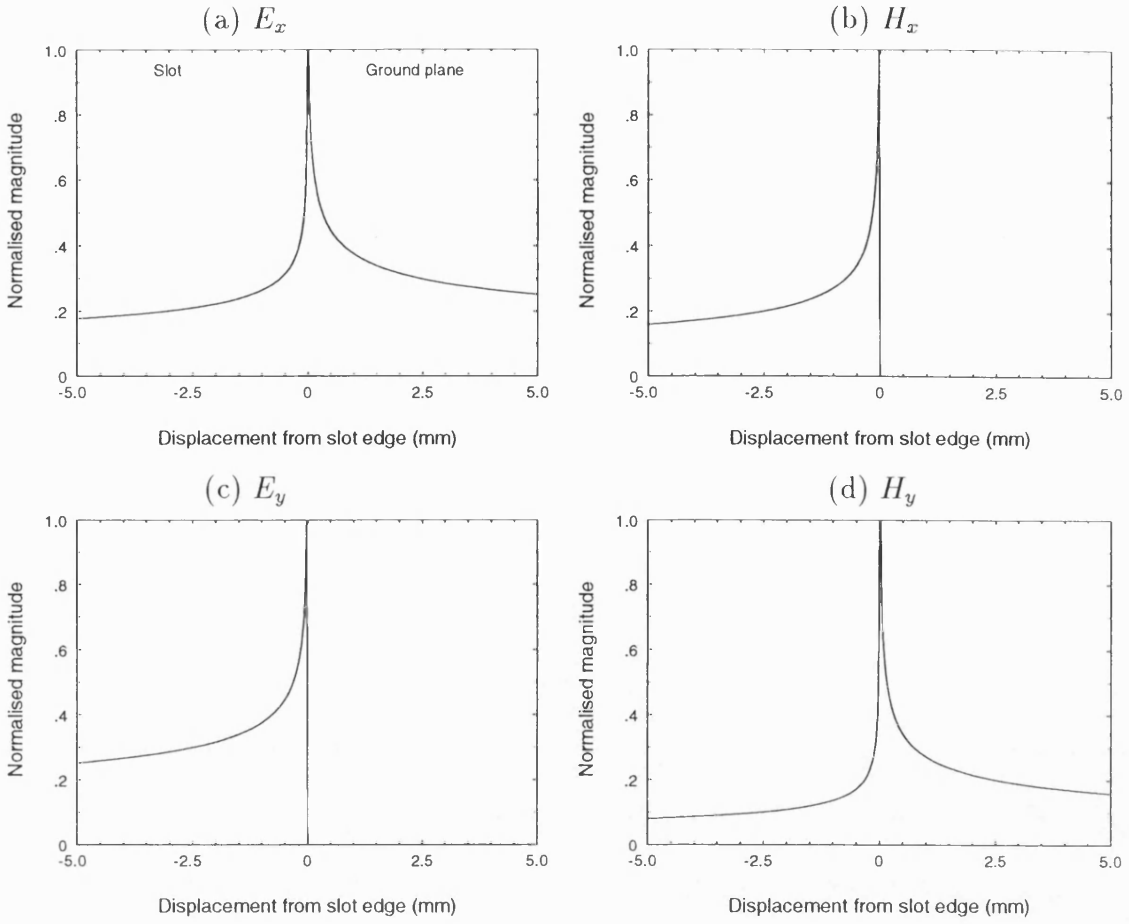

Figure 7.24: Behaviour of the x and y directed field components on IDG surface near to an edge.

of the field behaviour produced by FDTD. Fig. 7.26 gives results for shallow slot (LSM) IDG whilst Fig. 7.27 gives results for deep slot (LSE) IDG.

Again, the fields depicted are those in the plane of the air/dielectric interface, with the centre of the IDG coinciding with the zero of the horizontal scale. The half-width of the shallow slot guide is 11.43mm, that of the deep slot is 5.08mm. It is not intended that these plots be used to compare theory and FDTD across the full range of the horizontal axis. Instead, comparison should be made in the immediate vicinity of the edge. It can be seen that the general shape of the fields on either side of the edge is captured by the static theory. That the peaks of the static theory results are generally higher than those of FDTD can be attributed to the smaller

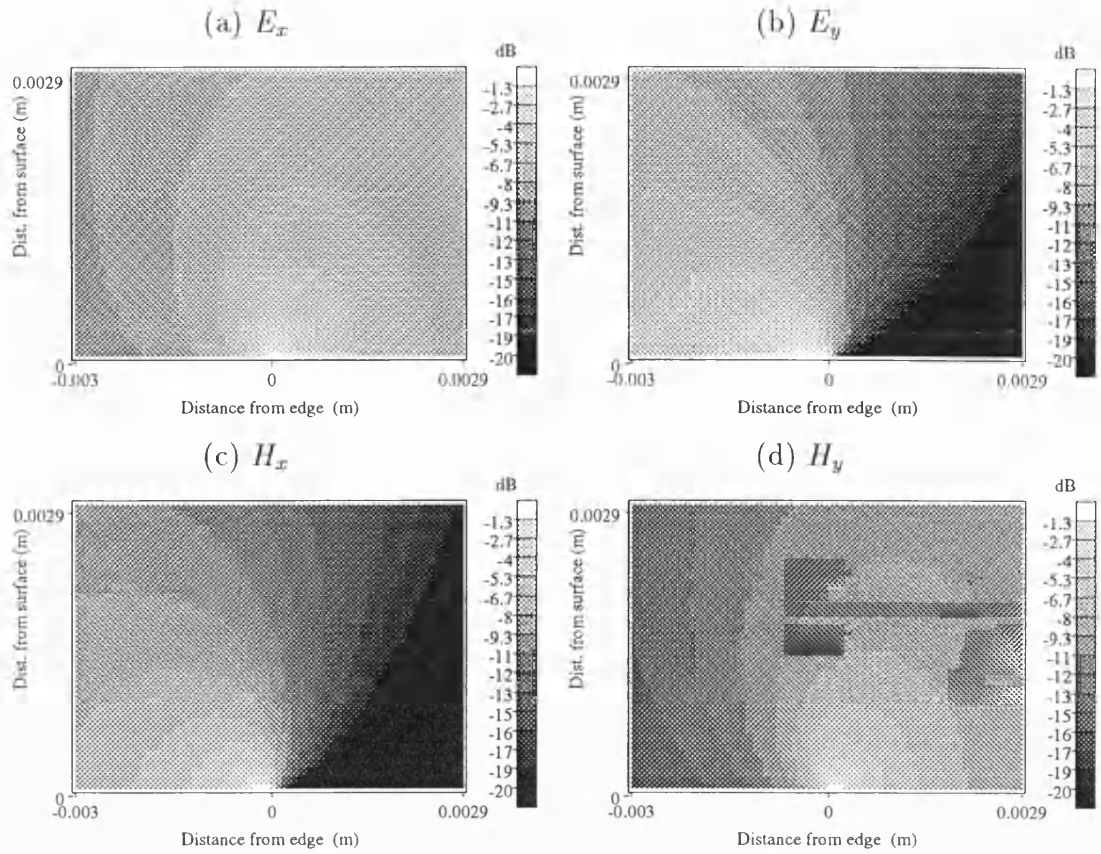

Figure 7.25: Distribution of the x and y directed field components in air by static theory.

sampling period used in the generation of the former results. It should be noted that the positions on the displacement axes of the field peaks of the static theory results in these figures have been adjusted to obtain the best fit with FDTD results, where the peaks do not coincide with the IDG edge due to the comparatively small number of samples taken across the structure.

7.9 Improved 2D IDG-TSA Model

In this section the IDG-TSA model considered in Section 7.7 is extended by the incorporation of the improved singularity modelling described in the foregoing sec-

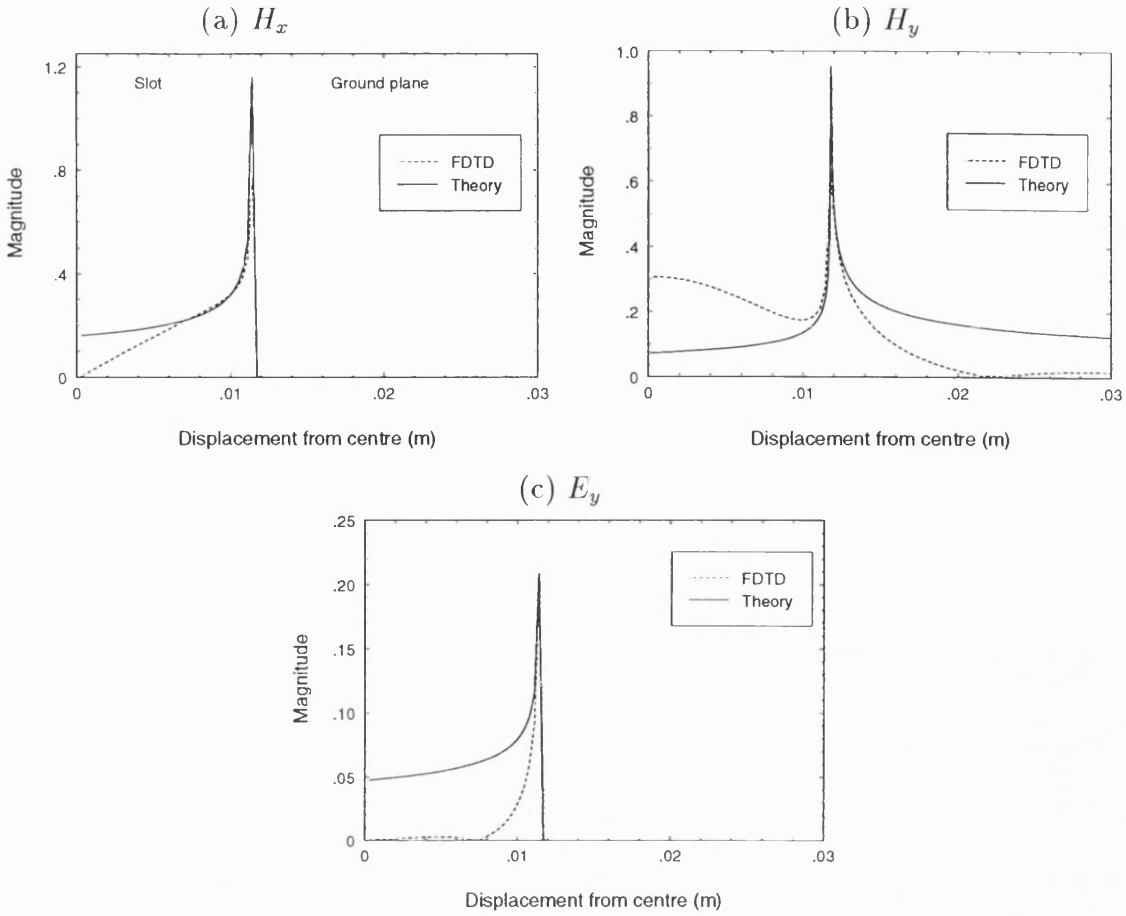

Figure 7.26: Shallow slot field components in the plane of the air/dielectric interface by static theory and FDTD.

tion. In order to judge the accuracy of this new model, it is necessary first to introduce an FDTD result, Fig. 7.28, showing the distribution of the H_y field component across the slot and ground plane of a shallow slot antenna. The FDTD model used to generate this result is described in Chapter 8, so no details of this are given here. Further such results are given in Chapter 9.

Considering then Fig. 7.28; the H_y field component in the plane of the air/dielectric interface is shown. Only the right hand half of the structure is depicted, so that the left hand vertical axis of the plot coincides with the longitudinal (z) axis of the antenna along the centre of the slot. Moving along this vertical axis; the RWG feed runs from $z = 0$ to $z = 0.11m$, the slot ends at $z = 0.41m$, and the ground

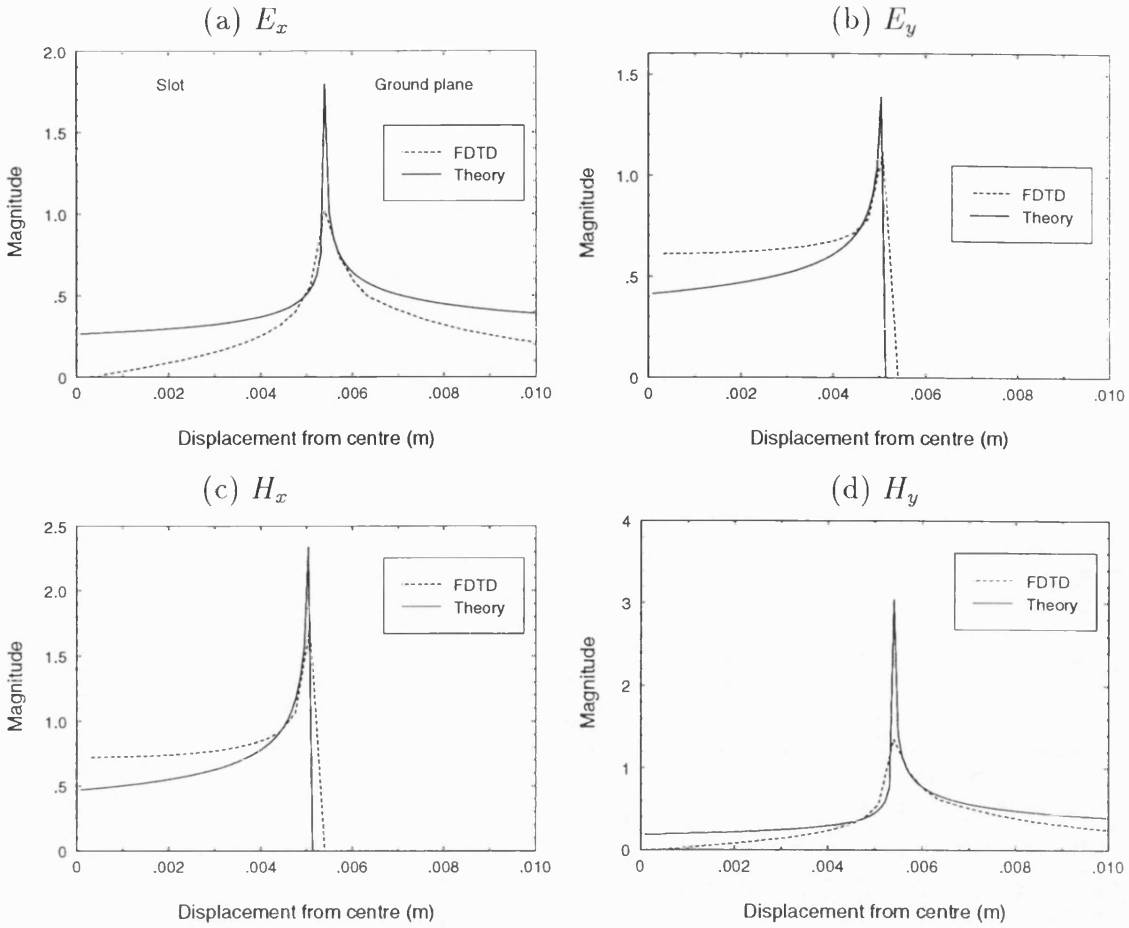

Figure 7.27: Deep slot field components in the plane of the air/dielectric interface by static theory and FDTD.

plane ends at $z = 0.54m$. On the horizontal (y) axis, the half width of the slot is 0.012m and the edge of the ground plane is at $y = 0.044m$. The free space around the structure is also modelled ($z > 0.54m$ or $y > 0.044m$).

In this figure, the field peaks at the slot edge ($y = 0.012m$) are clearly visible. A similar, though much less pronounced effect, can be seen at the edge of the ground plane ($y = 0.044m$).

Fig. 7.29 shows a first attempt at including the more accurate singularity modelling in the IDG-TSA model. The antenna depicted here is the same as that considered in the previous figure. Note that the analytical model does not include the feed RWG or the ground plane edges. The air region around the antenna structure is

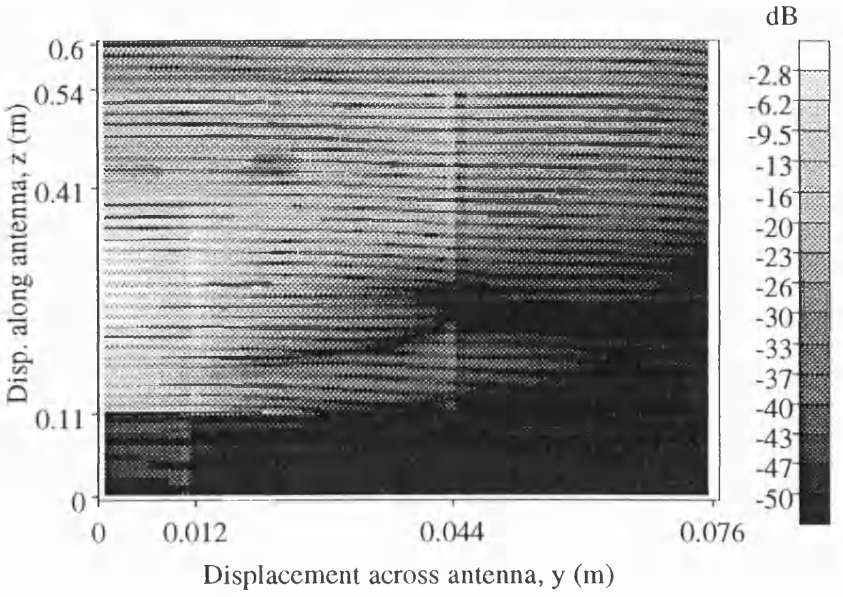

Figure 7.28: H_y component on surface of long LSM antenna calculated by FDTD. Frequency is 10GHz and $\epsilon_r = 2.3$.

therefore not shown in this figure. The real part of the H_y component is shown.

In the figure, the H-guide field expression is used to model the variation of the field within the slot. Close to the slot edge over the dielectric the H-guide field is linked to the relevant expression for the singularity. This description is then used to characterise the field across the edge itself to a point close to the edge over the ground plane. At this point, use of the static field description of the singularity is ended and the field is allowed to decay as $1/\sqrt{y}$ across the ground plane towards the edge of the structure. Comparisons with the surface fields predicted by FDTD in Chapter 8, and with the measured fields presented in Section 10.9 indicate that the $1/\sqrt{y}$ description is not unreasonable.

In the foregoing, the phrase 'close to the edge' is used but is not defined. For the purposes of the computer model it is clear that a real distance must be defined within which the static field equations are applied on either side of the slot. In this work, a distance of the order of $\lambda_0/10$ or $\lambda_0/20$ is used. These values were decided upon after studying a number of results from the FDTD model of the IDG-TSA.

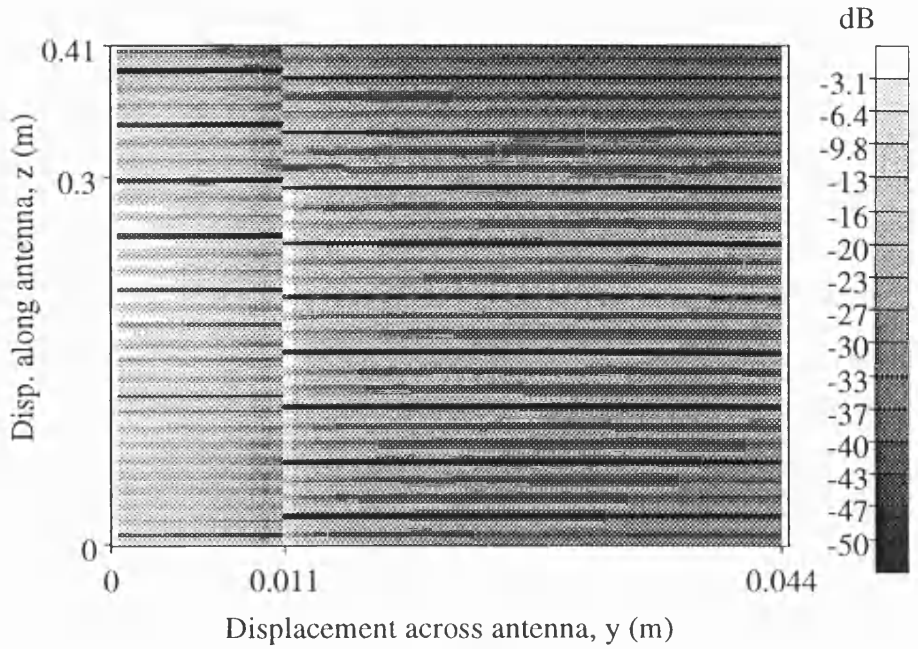

Figure 7.29: H_y component on surface of long LSM antenna calculated using the new theory. The propagation constant on the ground plane is k_0.

The author is not aware of a method by which this limit might be calculated.

The field magnitude existing along the end of the slot is used as the source for the distribution on the section of the ground plane extending beyond the slot. Following the earlier two dimensional model (Section 7.7) the fields on the ground plane in Fig. 7.29 are allowed to propagate at k_0 rad/m. Comparing this figure to the FDTD result of Fig. 7.28, it is clear that the analytical model has picked out some of the key features predicted by FDTD. For instance, the field peak at the centre and towards the end of the slot is visible, as is the effect of the slot edge.

However, a problem with this representation of the fields is evident at the slot edge where the propagation constant is switched from that of IDG to that of free space. If two different propagation constants are to be used in this manner then it is inevitable that some phase shift will exist between the slot and ground plane fields. However, the discontinuity in this case is unnecessarily large. In general, at the end of the aperture the slot propagation constant has reduced to k_0. It makes

sense therefore to adjust the phase of the ground plane fields at this point to be the same as the slot fields. The phase discontinuity is thereby minimised. The result of doing this in the case of the example considered in the foregoing figures is shown in Fig. 7.30.

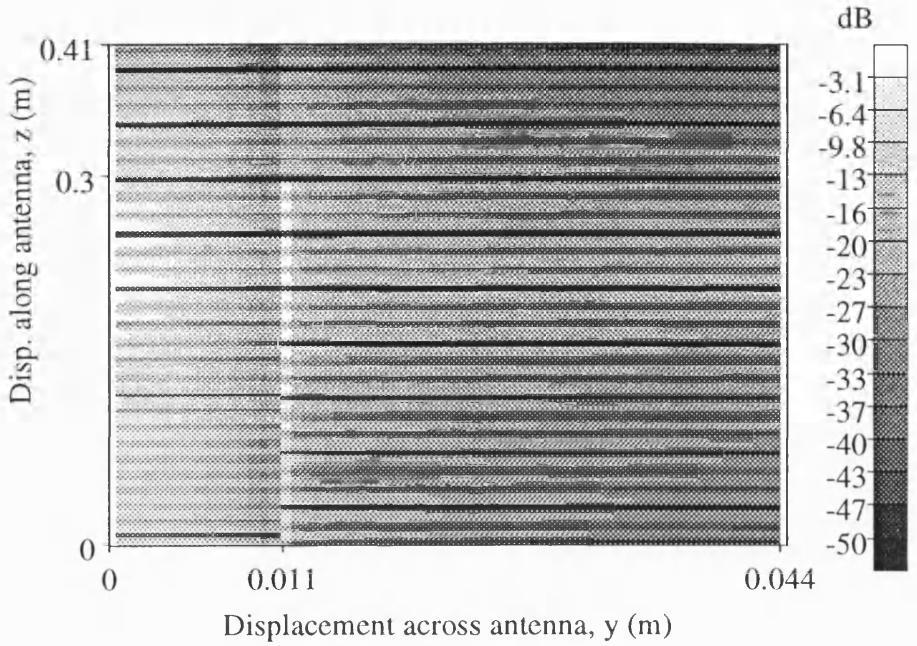

Figure 7.30: H_y component on surface of long LSM antenna calculated using the new theory. The propagation constant on the ground plane is k_0, phase shifted.

In this figure the slot and ground plane fields are in phase, or nearly in phase, from approximately half way along the slot to the end of the ground plane. The effect of performing this phase shift on the radiated far fields obtained from the model is considered later in this section.

Whilst the model of Fig. 7.30 appears more satisfying than that of Fig. 7.29 there is still a phase discontinuity across the slot edge for the first section of the slot. The FDTD results of Fig. 7.28 indicate constant phase fronts across the edge along the whole length of the antenna structure. This feature is studied in more detail in Fig. 7.31.

The figure depicts the H_y component, calculated by FDTD, on four longitudinal

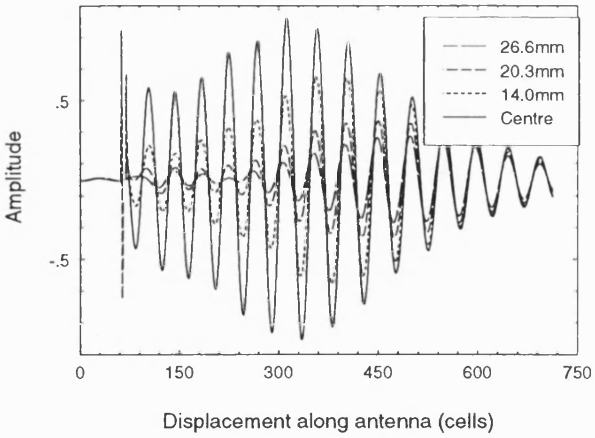

Figure 7.31: H_y field component along antenna surface calculated by FDTD.

cuts taken in the plane of the air/dielectric interface. The cuts are taken along the centre of the structure, 14mm offset from the centre (i.e. just outside the aperture, whose half-width is 11.4mm) and at 20.3mm and 26.7mm from the centre. The plots encompass the full length of the structure from the start of the feed to the end of the ground plane. It is clear from these results that the phase shift between the first two traces (centre and 14mm) is very small, and increases only slightly as the distance from the centre is increased through 20.3mm and 26.7mm. A third variation on the analytical model can thus be proposed, as shown in Fig. 7.32, where the slot propagation constant is used on the ground plane also.

This plot compares well with the FDTD result of Fig. 7.28 although some of the irregular features of the latter result located around the ground plane edges approximately half way along the structure have not been reproduced. These features exist in a region where the field has decayed to a low level, so it is not considered that their exclusion from the analytical model is an important omission.

Thus, three variations of this model of the ground plane fields have been established with (a) the slot propagation constant used on the ground plane, (b) k_0 used on the ground plane, and (c) k_0 used on the ground plane plus a phase shift. The effect on the radiation pattern of these variations is shown in Fig. 7.33.

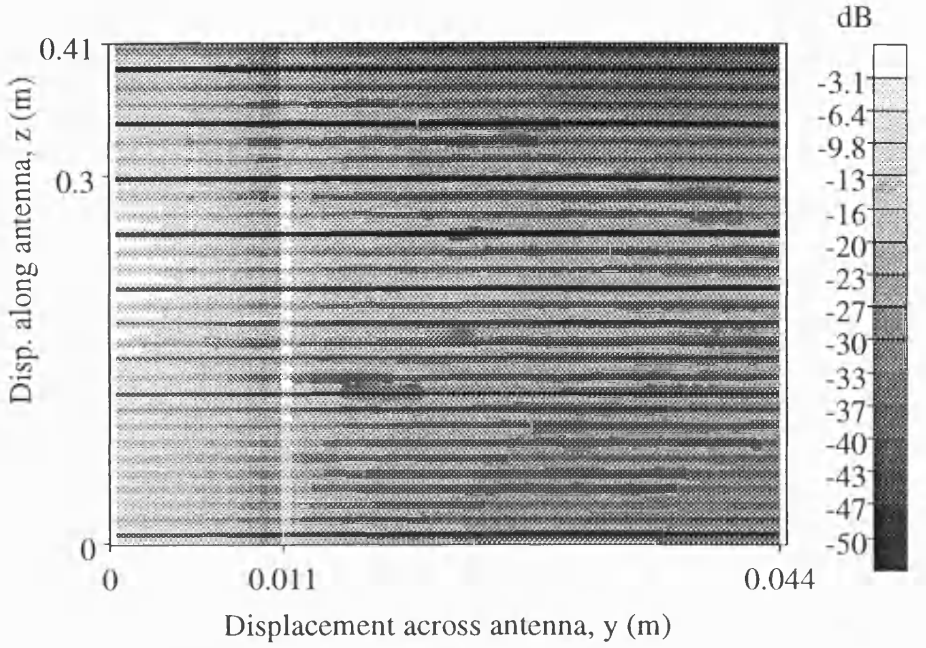

Figure 7.32: H_y component on surface of long LSM antenna calculated using the new theory. The propagation constant on the ground plane is the same as that on the slot.

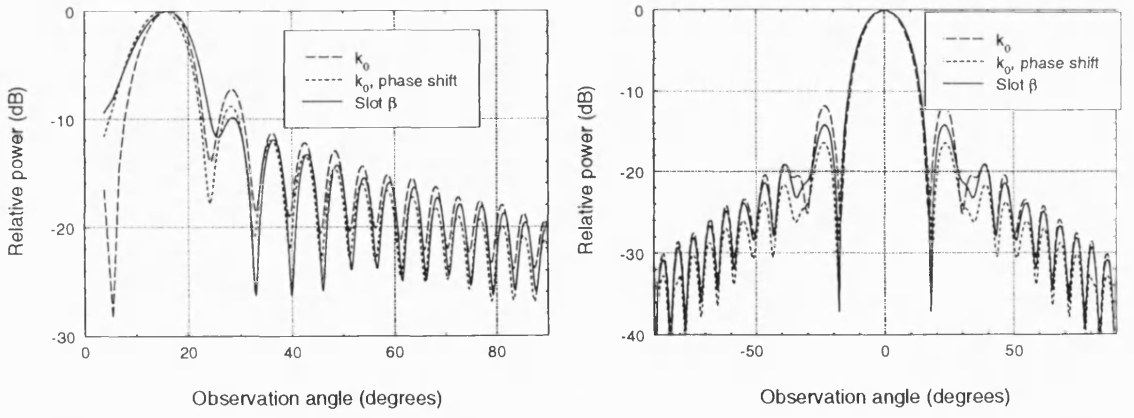

Figure 7.33: The result of varying the ground plane field model. Long LSM antenna at 10GHz. (a) Elevation plane, and (b) azimuthal plane.

The results given by the by all three versions of the model are similar. However, variation (b) gives a narrower elevation plane beam and higher first sidelobes in both the elevation and the azimuthal planes. Comparison with measured data indicates that these are undesirable features. That this is the least satisfactory of the three variations is not unexpected if one considers the previously observed discrepancies with the FDTD aperture distribution. This variation of the model will therefore be discarded.

As for the remaining two variations on the model, Fig. 7.34 shows elevation plane patterns for the long shallow antenna at 10GHz compared to measured data. The azimuthal plane patterns for both variations are plotted against measured values in Fig. 7.35. In both cases, good agreement between the new theory and measurement can be seen. There is little to choose between the two variations of the model, although experience has shown that using k_0 as the ground plane propagation constant generally gives slightly better results. The latter model is thus used to generate the results presented in the remainder of this chapter.

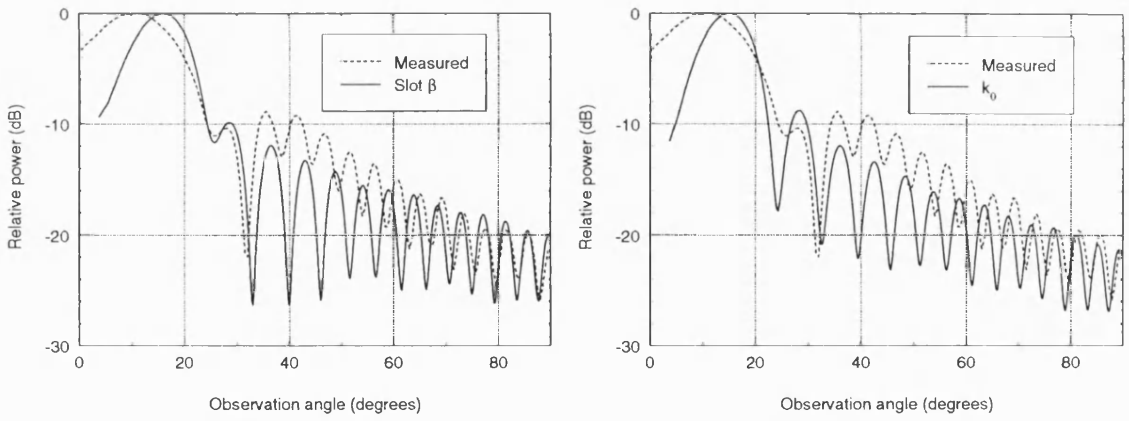

Figure 7.34: The result of varying the ground plane field model: comparison to measured data (a) Slot β on ground plane, and (b) phase shifted k_0 on ground plane.

Fig. 7.36 shows results obtained using the new theory at two frequencies compared to those generated by modified Walter's method [3] and to measured results.

It can be observed that the more realistic modelling of the ground plane fields

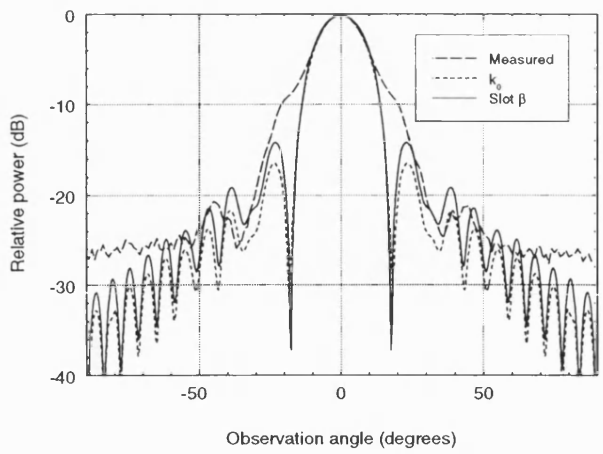

Figure 7.35: The result of varying the ground plane field model: comparison to measured data in the azimuthal plane.

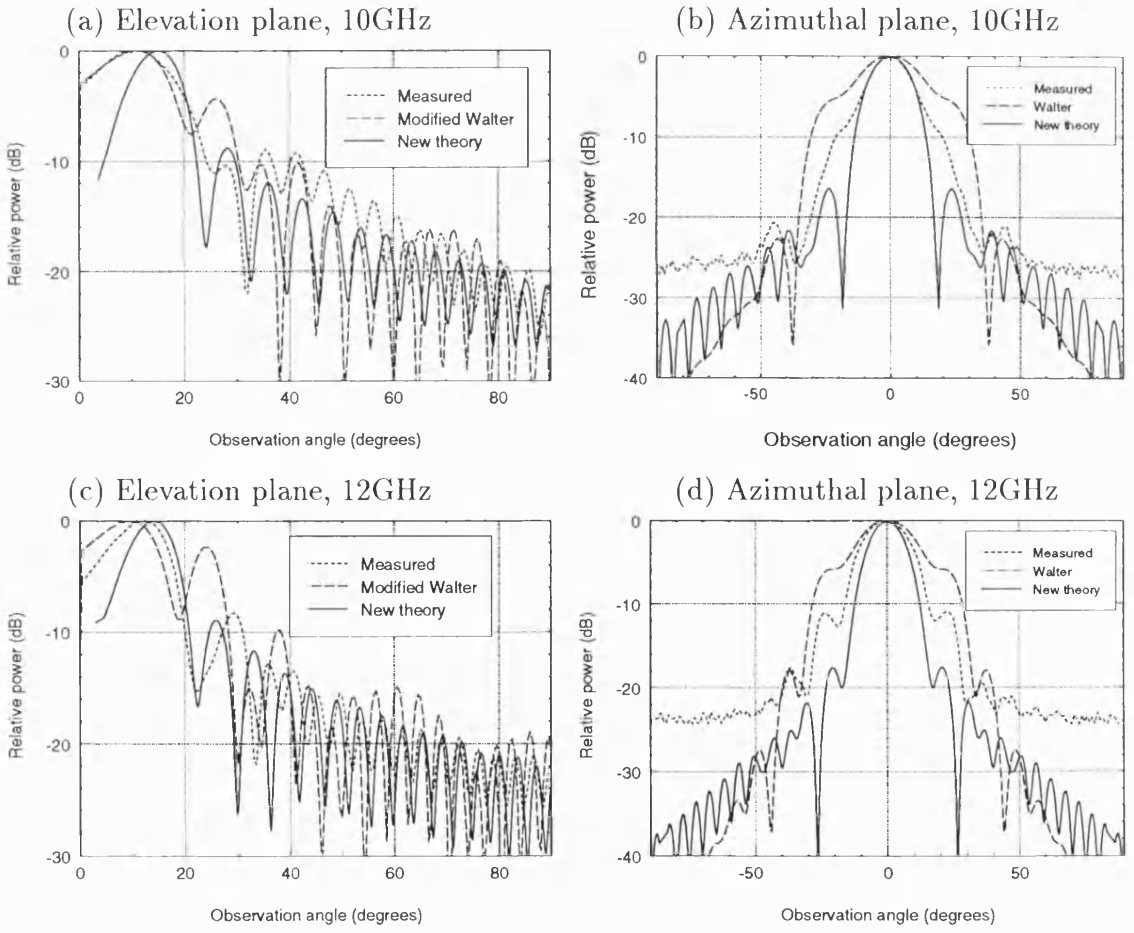

Figure 7.36: New theory against modified Walter's method and measurement.

has paid dividends in terms of improved agreement to measurement compared to that achieved by either modified Walter's method or the method presented in Section 7.7. In the elevation plane the new theory and Walter's method give broadly similar results but with the new theory giving improved prediction of the level of the first sidelobe. The new theory is considerably better than Walter's method in the azimuthal plane; the earlier technique only takes the slot E-field components into account when calculating this pattern.

The full H-guide model runs reasonably rapidly. A typical run takes a little over a minute on a Silicon Graphics Origin 2000 machine. If results at a large number of angles are demanded, the run time can be extended to approximately seven minutes. In comparison, modified Walter's method [3] and the line source method considered earlier in this chapter take approximately five seconds to run on the same machine.

The theoretical method introduced in this section is the most complete analytical IDG-TSA model developed to date. As such, the method is used to generate the results given in Chapter 9. Besides presenting results for both LSE and LSM antennas of various geometries, this later chapter considers possible reasons for the discrepancies that still exist between prediction and measurement.

7.10 Chapter Summary

The development of a new method for IDG-TSA analysis has been presented. The method includes for the first time a full model of the slot and ground plane fields, having dispensed with the approximation used by the earlier analytical technique. A theory has been derived to link the fields on the ground plane to those within the slot. Results generated using the new method compare well to theory and show improvements over predictions made using the earlier technique.

Chapter 8

FDTD Analysis of the IDG-TSA

8.1 Introduction

The FDTD model of the IDG-TSA that was developed prior to the current work [4] is described in Section 3.4.5. It will be recalled that this model generated the far field radiation pattern using only the slot electric field components. The effect of the slot and ground plane magnetic field components was then accounted for using Walter's ground plane approximation (Section 3.4.3). It is assumed that this arrangement was used in order to minimise the memory and time requirements of the computation. However, as has been pointed out in earlier sections, Walter's ground plane approximation does not produce a realistic model of the fields on the antenna, and is of little use where the far fields across a range of elevation and azimuth angles are required.

Thus, to produce an improved model of the antenna which will allow greater insight into its operation a new FDTD implementation has been developed, using the original code of Stoiljković *et al.* [4] as a starting point. The following modifications have been incorporated:

1. The scope of the calculation has been increased to cover the full extent of the real ground plane. The code implementing Walter's ground plane method has been removed and replaced by an implementation of equation (3.58) which calculates the far fields based on all four tangential surface field components.

2. Modifications have been made to allow the calculation to cope with LSE polarised structures.

3. In order to investigate the effect of the edges of the metal block in which the antenna is set, and the possible contribution made to the total radiation from the structure by the end and side faces of this block, a complete model of the structure has been created. This consists of the metal block modelled as a six-sided structure surrounded by air. The feed waveguide is also modelled. This model, which will be referred to as the full FDTD model, is in contrast to that described in point (1) above where the absorbing boundaries are placed at the extremes of the ground plane on the top side of the block. There is no air gap between the extremities of the ground plane and the ABCs. As such, this earlier model is not 'aware' of the discontinuity at the ground plane edges and will therefore be referred to as the intermediate FDTD model indicating its position between the old (Stoiljković) model and the full model.

   The full model uses the theory of Section 3.4.2 to generate the far field radiation from the top, end, and sides of the antenna structure.

4. A further modification to the full FDTD model is the addition of the flange of the feeding rectangular waveguide.

Having introduced the extensions that have been incorporated into the existing FDTD code, the effects of these changes are now investigated through a series of graphical results. The physical parameters of the antennas considered in this chapter are given in Section 7.2.

8.2 The Intermediate FDTD Model

In this model, Walter's ground plane approximation has been eliminated and the complete ground plane is modelled. Equation (3.58) is used to generate the far field pattern, and the ABCs are placed where in reality the ground plane edges are located. Fig. 8.1 shows results comparing the intermediate model to the Stoiljković [4] ('old') model at two frequencies.

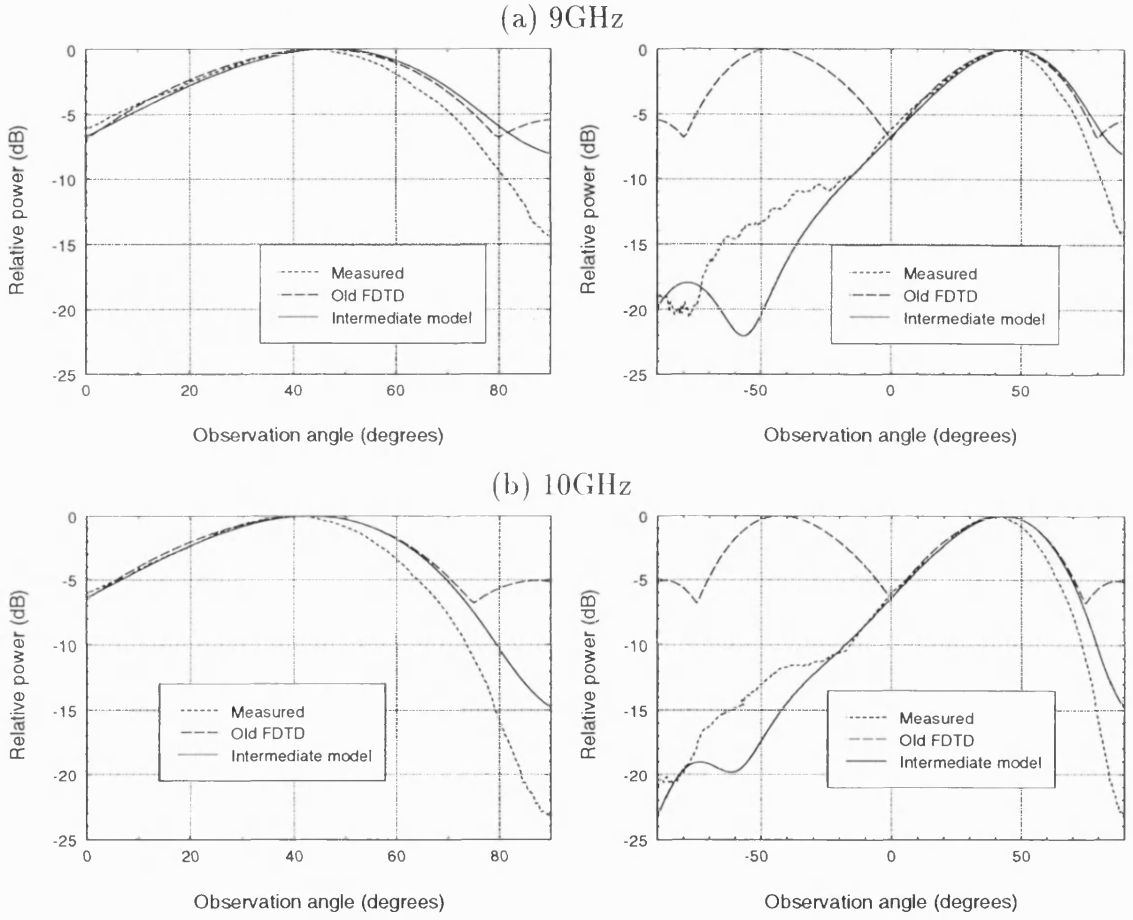

Figure 8.1: Short shallow antenna elevation plane pattern. Intermediate FDTD against old model and experiment. Two angular ranges at each frequency.

The figures reproduce the elevation plane data twice with different angular ranges. The 0° to 90° range is the usual range of interest, where 0° coincides with the aperture surface, as this is where the main beam and major sidelobes are located. However, the -90° to 0° range is also interesting and is studied further in Chapter 9.

This radiation is directed below the plane in which the aperture lies.

Considering the figures, it can be seen that the old FDTD model does not produce valid results in this downward range; it predicts a peak at around -40° which is not apparent in the measured data. This discrepancy is due to the use of Walter's ground plane approximation which uses an analytical form, $I_0 \exp(-jk_0 z)$, for the magnetic fields on the slot and ground plane. The radiation pattern of this element is superimposed on that of the slot electric fields after equalisation of the magnitudes of the two patterns. This mirroring about the 0° axis is indeed the radiation behaviour of a travelling wave antenna carrying an $I_0 \exp(-jk_0 z)$ distribution, but it is unfortunately not the behaviour of the IDG-TSA.

The ground plane of the IDG-TSA ensures that the structure cannot radiate equally both upwards and downwards. Even in the absence of a ground plane, the tapering of the slot leads to a peak in the 0° to 90° range. By using both the electric and magnetic field components calculated by FDTD to find the far field, the new FDTD model allows this behaviour to be predicted more accurately. However, there is still a discrepancy between measurement and the new FDTD model results for angles less than -20°.

The new FDTD model also shows improvement over the old in the upward direction, between 0° and 90° elevation. Both methods match measurement well up to the peak but deviate from it for angles higher than this. However, the old method predicts a non-existent sidelobe just below 90°. This is due to inaccurate handling of the ground plane fields by Walter's approximation.

The same configuration is used for both of the above FDTD models, as follows: the computational space is 63 cells long by 71 wide by 71 high. In the slot the cells are 0.635mm ($\lambda_0/47$ at 10GHz) in the transverse directions and 1.27mm ($\lambda_0/24$ at 10GHz) in the longitudinal direction. The total width of the structure modelled is 44.5mm and there is 44.5mm of space above the aperture surface. The model runs

for 3500 time steps of duration 0.847ps with a stability factor of 0.4. Note that the cell size is chosen so that the feed dimensions can be modelled by an integer number of cells (16 and 18 in the x and y directions respectively).

Both the old and intermediate models take approximately 20 minutes to run on a Silicon Graphics Origin 2000 machine. In fact, the old model can be made to run rather faster than this by reducing the width of the structure. It is not necessary to model the full width of the ground plane, as is done here, as the fields on it are not used.

Before closing this subsection two further sets of results are presented which examine the longitudinal and transverse time domain fields in the plane of the air/dielectric interface. These results relate to the long shallow antenna and are generated using the new FDTD model discussed above, which is 365 cells long in the z direction. Fig. 8.2 shows the fields along the centre of the slot and ground plane. The results show travelling wave patterns as expected with a reduction in amplitude towards the end of the slot due to power being radiated. Note that this calculation was carried out with Z_0 set to unity. It is interesting to observe that the H_y component continues onto the ground plane without apparently being affected by the discontinuity at the end of the slot. The H_z component also continues onto the ground plane, but in a much less significant manner.

Fig. 8.3 shows the fields across the structure (i.e. in the transverse plane) in the plane of the air/dielectric interface at three positions along the antenna; 10 cells in front of the feed (solid line), mid-way along the slot (dotted line), and 50 cells before the end of the slot (dashed line). Only half the structure is shown, so that the zero on the horizontal axes coincides with the centre of the slot. The half width of the slot is 11.43mm and that of the ground plane is 45mm. The effect of the slot edge is highly visible in these plots, and the degree to which the fields spread onto the ground plane can be seen to be significant. It is also apparent that the fields on the ground plane 'build up' towards the end of the slot. These plots are intended

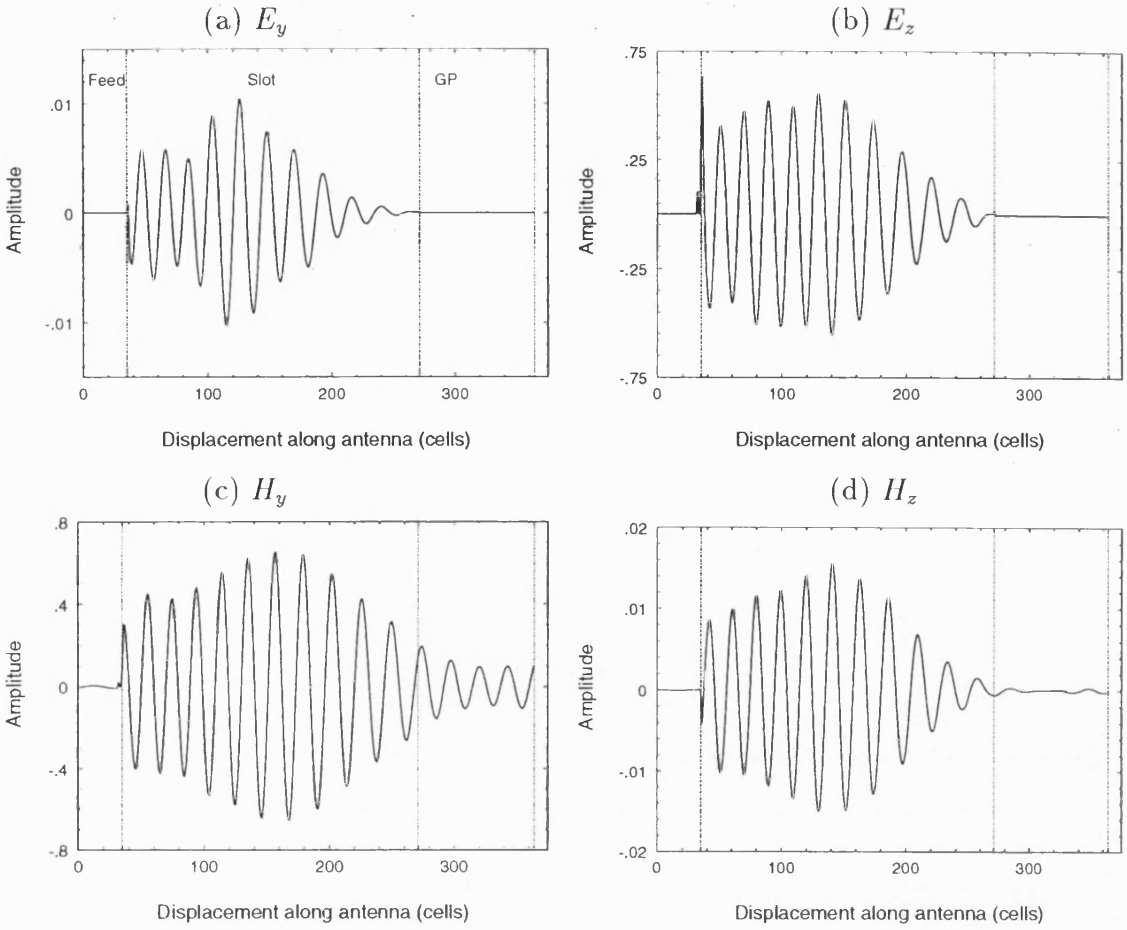

Figure 8.2: Time domain fields along the centre of the air/dielectric interface and ground plane.

for comparison with those generated by the full FDTD model in Section 8.4 below.

8.3 LSE Structures

The intermediate FDTD model described above needs only minor modification to enable it to calculate the far fields of LSE polarised antennas. These include changes to the excitation as outlined in Section 3.4.5, changes to the type of symmetry enforced at the guide centre and an extension of the far field calculation routine to include E_ϕ as well as E_θ. Fig. 8.4(a) to (c) show FDTD elevation plane patterns for the long deep antenna at three frequencies compared to measured

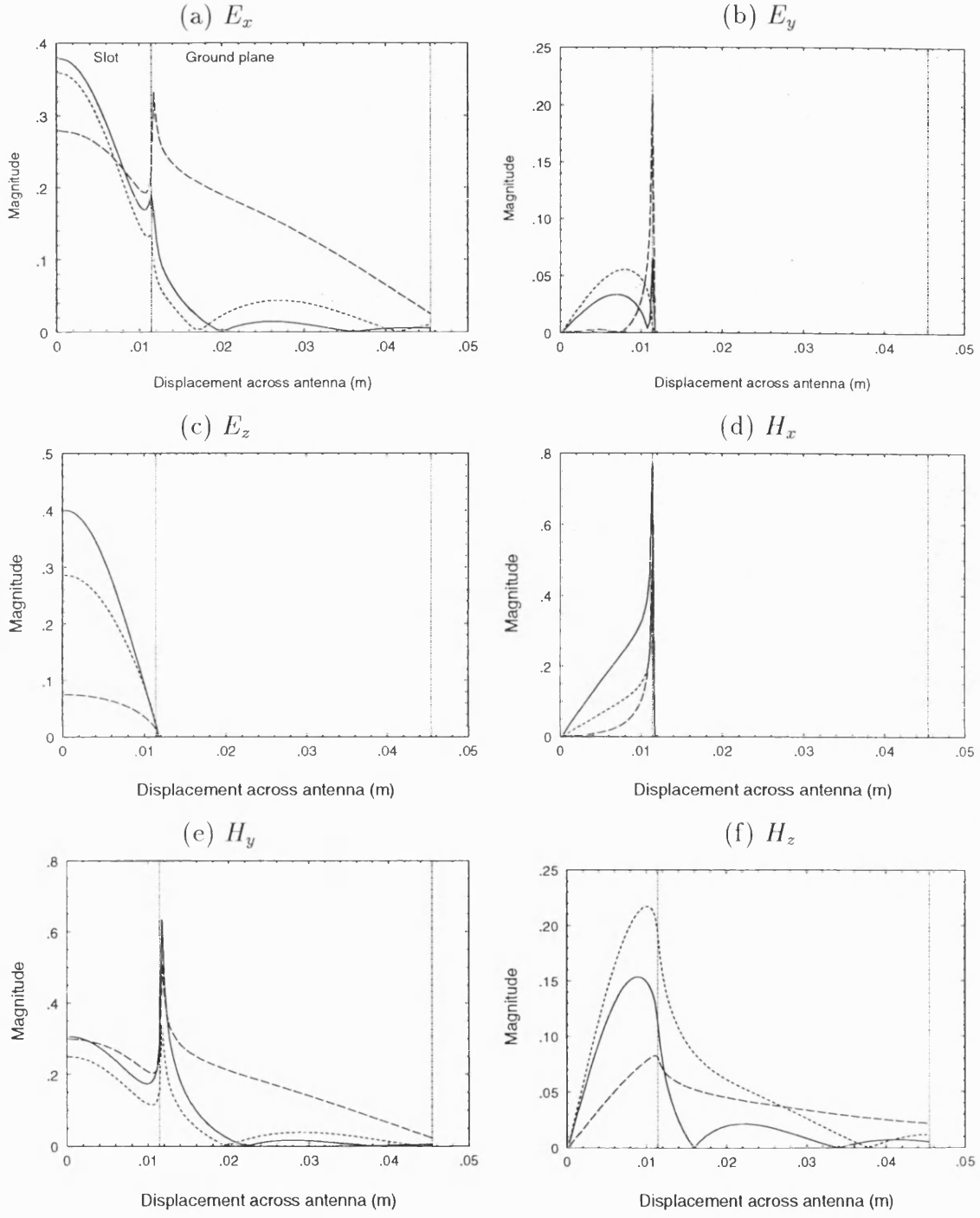

Figure 8.3: Shallow IDG-TSA time domain fields across air/dielectric interface and ground plane.

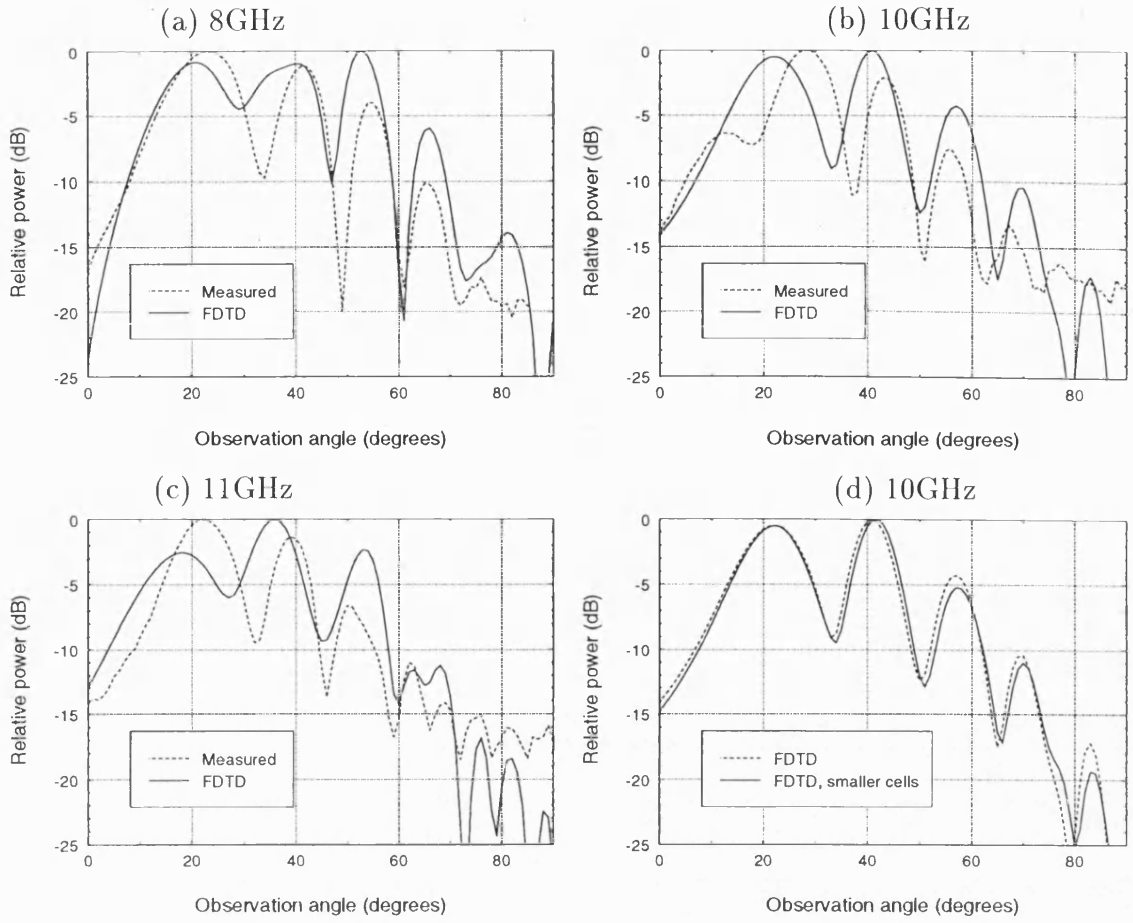

Figure 8.4: Long deep slot (LSE) antenna elevation plane radiation patterns by FDTD. Part (d) shows the effect of reducing the transverse cell size.

results. Agreement between theory and experiment is reasonable in all cases.

Fig. 8.4(d) shows the effect at 10GHz of halving the cell size in the transverse (x and y) directions to 0.3175mm ($\lambda_0/94$ at 10GHz) whilst maintaining the longitudinal cell dimension at 1.27mm. It is clear that little, if anything, has been gained by doing this in terms of improved agreement to measured data. The run-time, however, increases from around 3 hours to nearly 28 hours.

8.4 The Full FDTD Model

As has been seen in Section 8.2, the intermediate FDTD model provides predicted radiation patterns that show improved agreement to measurement when compared to the old model. However, there are still discrepancies. One possible cause of inaccuracy in the intermediate model lies in its lack of modelling of the ground plane edges. The plots of the fields across the antenna in Fig. 8.3 indicate that the field spread onto the ground plane is significant enough for there to be finite field at the model edges. On the real structure this field will interact with the edge in some way. Similarly the longitudinal field plot of Fig. 8.2(c) shows that there is a significant H_y component at the end of the structure.

Another possible area of inaccuracy is the omission of any radiation that might occur from the end face or side faces of the antenna mounting block. The FDTD model has thus been upgraded in order that these possibilities can be investigated.

These modifications are significant, requiring the addition of the five sides of the mounting block that were not previously modelled as well as the additional three sides of the feed RWG. The model also includes a volume of the air surrounding the antenna. Having established this model it can be used to provide various insights into the operation of the antenna. In addition to those given below, a number of such results are included in Chapter 9.

Fig. 8.5 depicts the structure modelled by the full FDTD code. The figure additionally shows the flange of the rectangular waveguide which is considered in Section 8.5. The various surfaces referred to in this section and the subsequent two sections are labelled in this figure.

An elevation plane result produced using the full model is shown in Fig. 8.6. Comparison is made to both the old FDTD model and to experiment. This figure can be directly compared with Fig. 8.1(b).

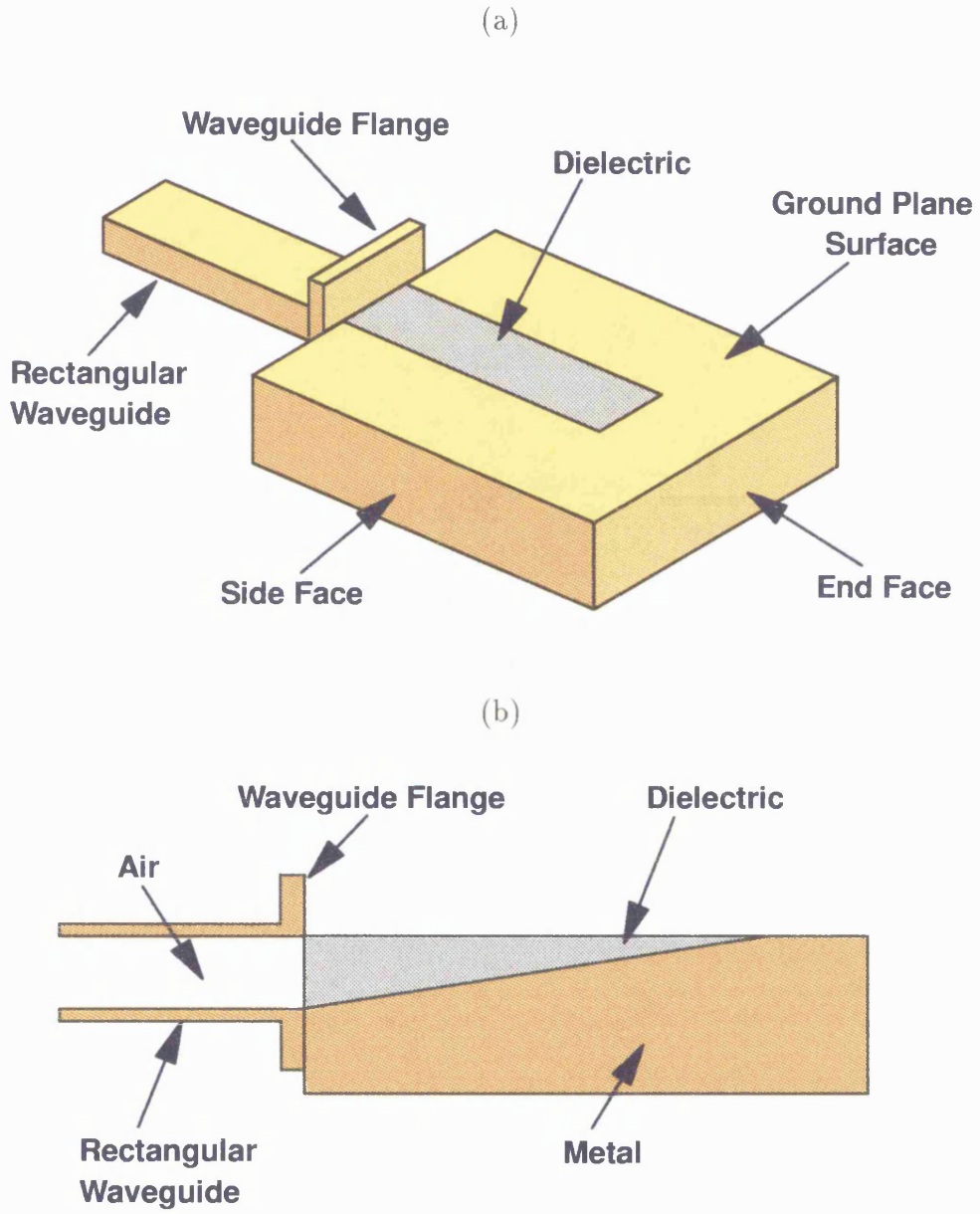

Figure 8.5: The structure modelled by the full FDTD code: (a) top view, and (b) side view.

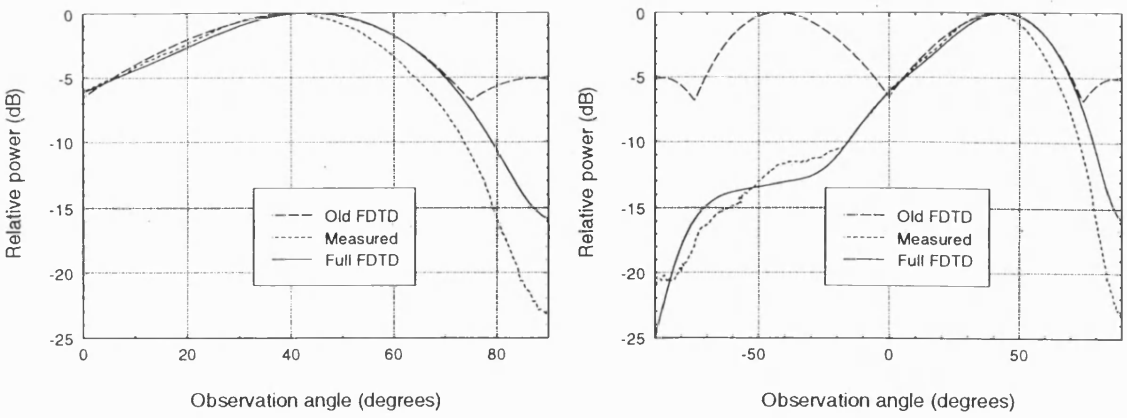

Figure 8.6: Short shallow antenna elevation plane radiation pattern at 10GHz. Full FDTD model against old model and experiment. Two angular ranges.

Whilst the agreement to measurement is still not perfect, there has been an improvement; the main beam predicted by the full model is now very slightly closer to measurement, but the largest improvement is in the downward radiation which is now in very close agreement to the measured data. These improvements can be seen more clearly in Fig. 8.7(a) which compares the intermediate model with the full model directly. Part (b) of the figure shows the effect of the radiation from the end and side faces. It is clear that without the inclusion of these surfaces that the top face radiation predicted by the full model would only be slightly different from that predicted by the intermediate model. It is the inclusion of the additional surfaces that is the main contributor to the improvement.

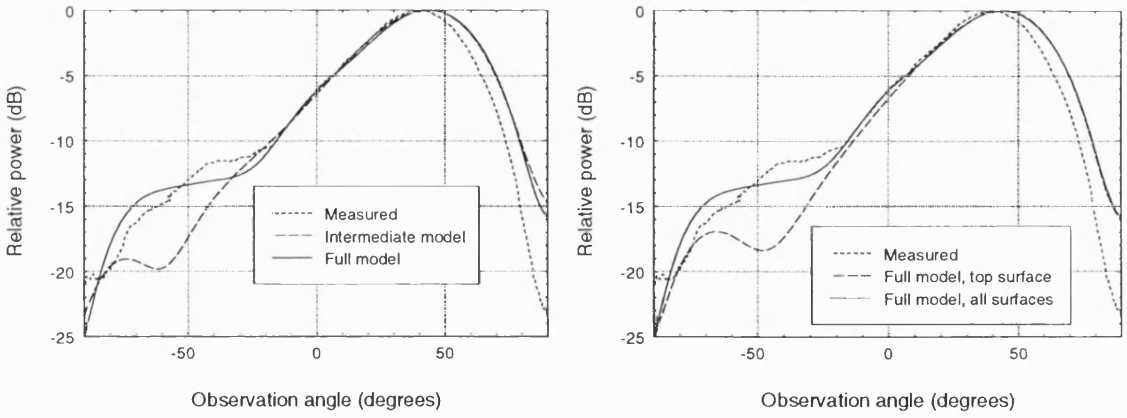

Figure 8.7: Short shallow antenna elevation plane radiation pattern at 10GHz. (a) Full FDTD model against intermediate model and experiment, and (b) The effect of the end and side face radiation.

For the structure modelled above, the full model has a comparatively long run time, 1 hour 20 minutes. The model is large, being 100 (z) by 157 (x) by 120 (y) cells and running for 3000 time steps of 0.74ps with a stability factor of 0.35. No attempt has been made to speed this particular model up by using larger cells or a graded mesh.

The FDTD model considered here consists of an antenna with a 30mm long aperture with 10mm of ground plane extending beyond it. There is 48mm of air between the end of the ground plane and the absorbing boundary. The aperture has a half-width of 11.43mm. The mounting block has a half-width of 45mm and there is a further 31mm between the ground plane edge and the absorbing boundary. The mounting block is 37mm deep, with 18mm of air between the underside of the block and the absorbing boundary. Above the antenna surface, an air space of 44mm has been modelled.

The effect of the side edges of the ground plane is clearly apparent in Fig. 8.8 which shows the fields across the surface of the structure. This figure may be compared to Fig. 8.3 although in the present case the displacement axes are extended to 76.2mm to include the air around the structure. The ground plane edges can be observed to be having a significant effect on the fields, with local peaks existing around the edges and some resultant modification of the field distribution on the ground plane itself. As with the earlier figures, three positions along the antenna are considered; 10 cells in front of the feed (solid line), mid-way along the slot (dotted line), and 50 cells before the end of the slot (dashed line).

8.5 RWG Flange

Another factor that potentially influences the distribution of the fields on the IDG-TSA surface is the flange of the feeding rectangular waveguide. In the shallow slot

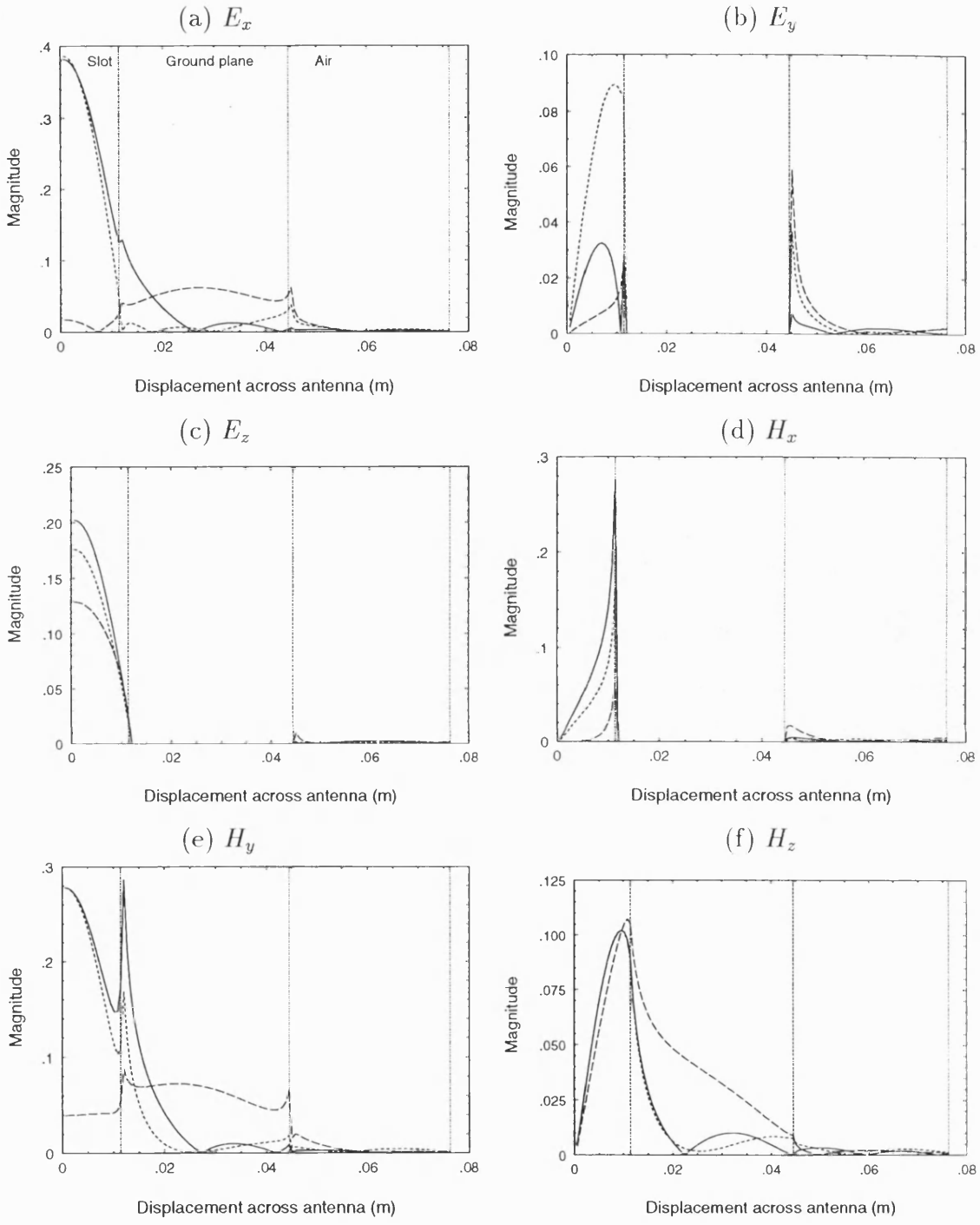

Figure 8.8: Shallow IDG-TSA fields by full FDTD model across the plane of the air/dielectric interface.

case this projects 15mm above the aperture surface, is 41mm wide and 4mm deep. This has been added to the full FDTD model as a solid metal box placed before the start of the dielectric section of the antenna. The run time of the model is extended slightly (approximately 2.5%) by the inclusion of the flange due to the increased number of surfaces to be processed and the resultant segmentation of the air region above the antenna.

Fig. 8.9 shows the tangential aperture fields in the frequency domain along the centre of the structure both with and without the inclusion of the RWG flange model. As might be expected, the flange reduces the spread of field backward from the RWG/antenna interface. This has consequences for the field distributions on the aperture, all of which are considerably modified, with the exception of the E_z component which unlike the E_y component is not shorted out by the flange. A further point to note here is the considerable spread onto the ground plane and into the air at the end of the structure of the magnetic field, particularly H_y.

The effect of the RWG flange on the far field radiation pattern is shown in Figures 8.10 and 8.11. The first of these figures is concerned with radiation from the top surface only. Whilst there is some modification to the downward radiation the most noticeable change is for observation angles greater than that of peak radiation. The existence of the flange has narrowed the main beams to give much better agreement to measurement. The result is confirmed in the second figure, showing the total radiation pattern, where an extremely good match to measurement can now be observed.

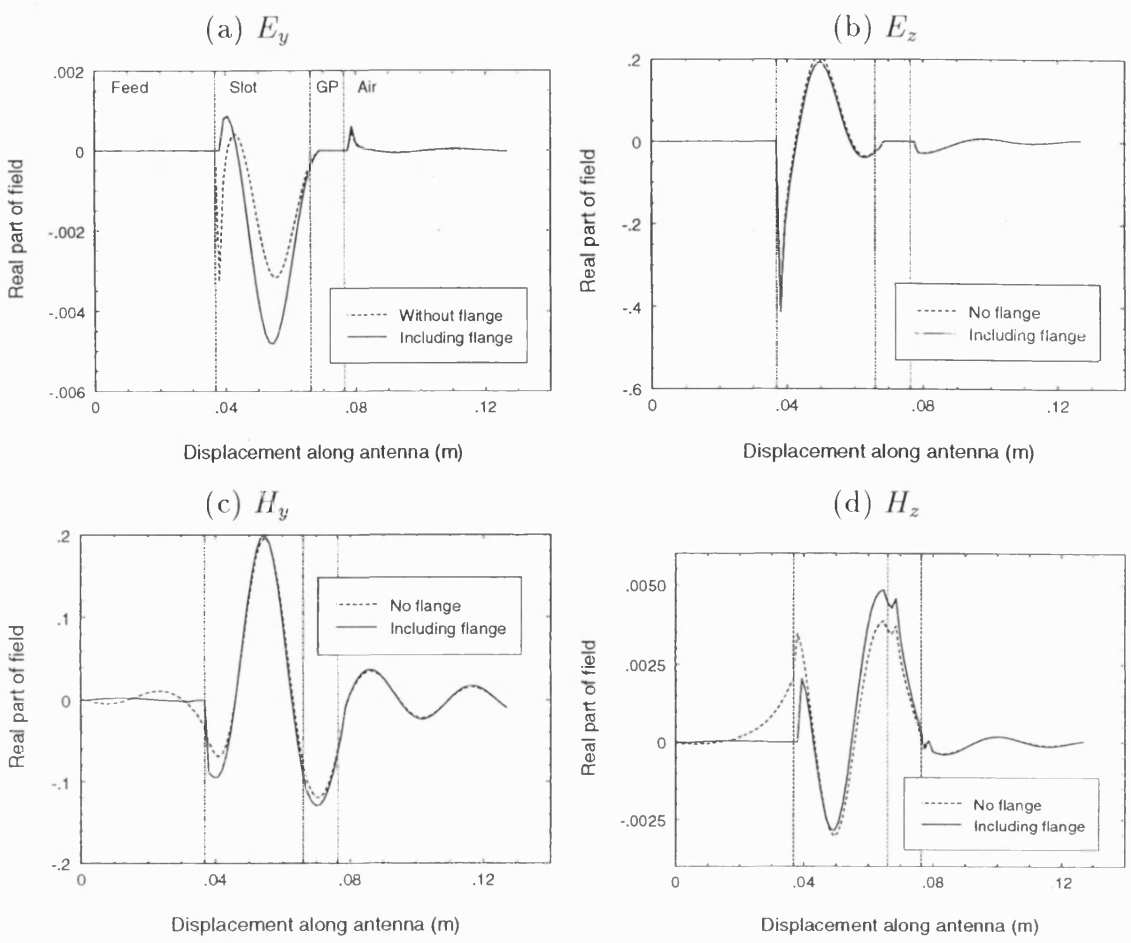

Figure 8.9: Full FDTD model with and without RWG flange. Frequency domain fields along the centre of the air/dielectric interface and ground plane.

8.6 Radiation from the End and Side Faces, and the Flange

The previous sections have demonstrated the effect of including the radiation from other surfaces of the antenna. In this section the elevation plane patterns of the individual surfaces are presented. Fig. 8.12 shows results for the short shallow antenna. Part (a) of the figure shows that of the subsidiary surfaces, the end face of the metal block contributes the most to the radiation pattern. As may be expected, the flange radiates mainly upwards, the end face downwards. The side faces of the structure do not play a significant role.

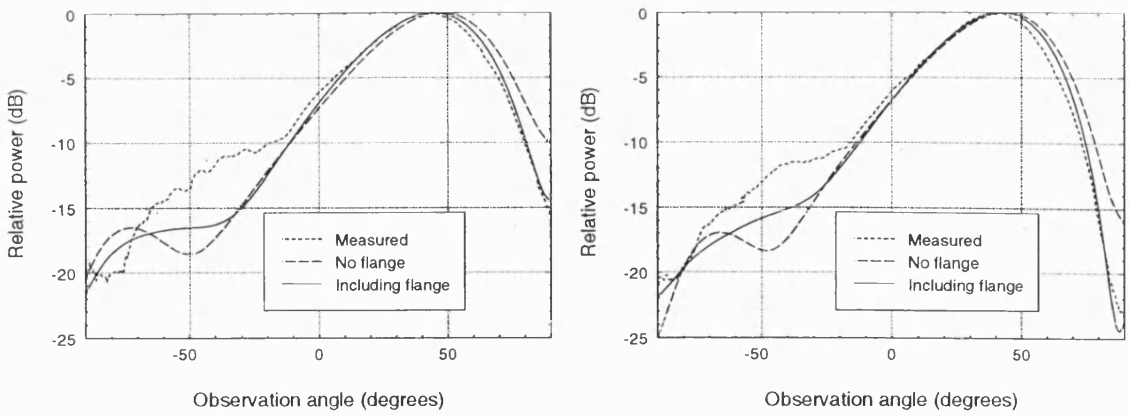

Figure 8.10: The effect of the RWG flange on the calculated radiation from the top of the antenna at (a) 9GHz, and (b) 10GHz.

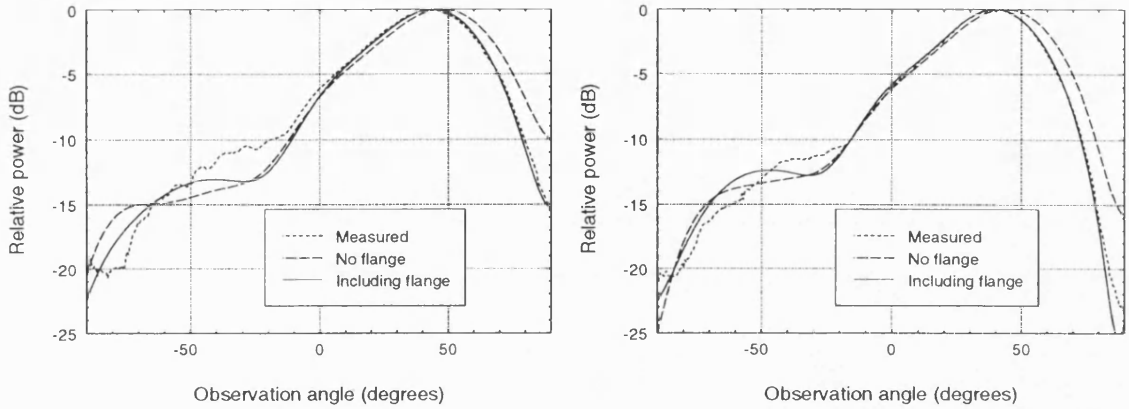

Figure 8.11: The effect of the RWG flange on the total calculated radiation from the structure at (a) 9GHz, and (b) 10GHz.

Part (b) of the figure shows the above components in relation to the top face radiation. Although only 10% of the top face peak magnitude, the end face peak is located at an angle where the top face radiation is low so that its effect is significant, as has already been seen. Radiation from the flange is less significant as its peak is near that of the top face radiation, but it provides a slight modification to the main beam shape of the overall structure.

Fig. 8.13 shows similar results for the long shallow structure. In this case the side of the block has a much greater relative area than that of the short structure and it therefore provides the highest contribution of the subsidiary surfaces to the overall pattern. However, it is still the end face and flange that have the greatest overall

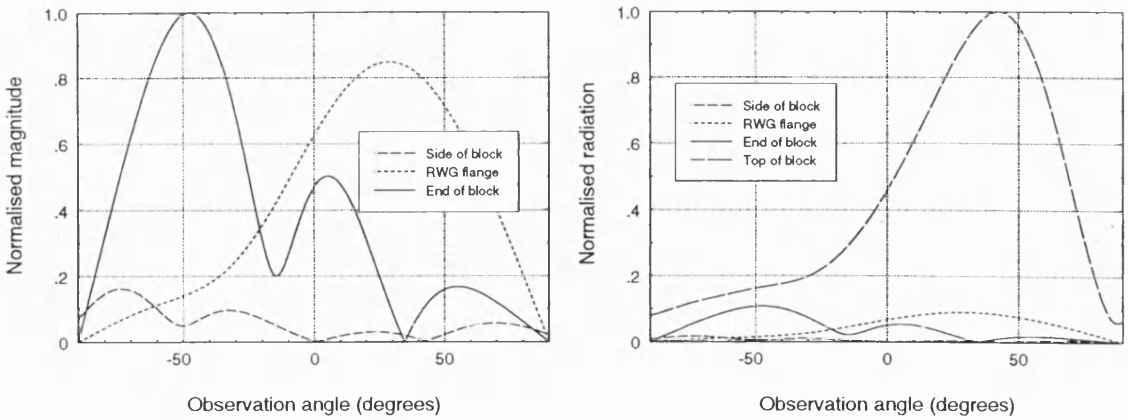

Figure 8.12: Elevation plane patterns for short shallow antenna at 10GHz: (a) Side, end, and flange radiation, and (b) Side, end, flange, and top face radiation.

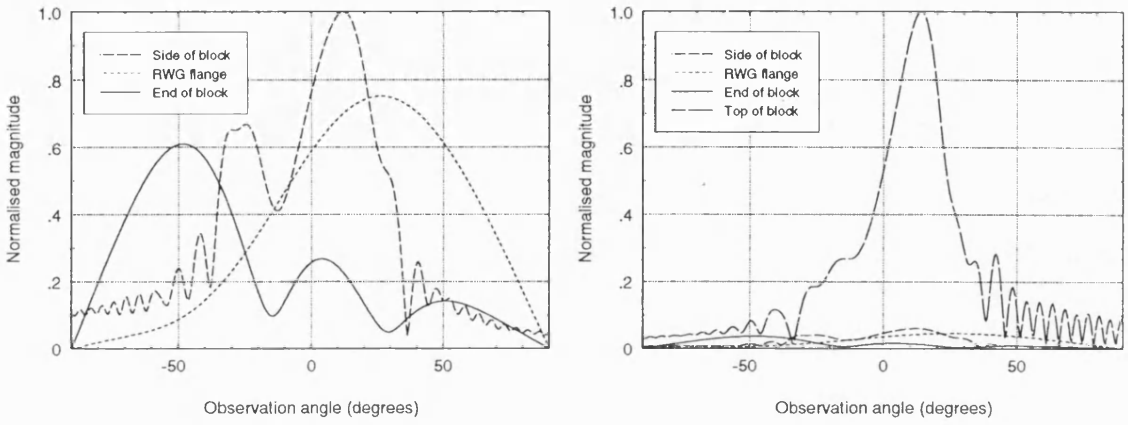

Figure 8.13: Elevation plane patterns for long shallow antenna at 10GHz: (a) Side, end, and flange radiation, and (b) Side, end, flange, and top face radiation.

effect as their radiation peaks coincide with lower top face radiation. The peak side face radiation coincides with the top face maximum so has negligible effect.

8.7 The Validity of Walter's Ground Plane Approximation

FDTD can be used to consider the validity of Walter's ground plane approximation. The technique is based on the assumption that the components of the calculated

radiation pattern due to the surface electric and magnetic fields have the same maximum value. As has been seen this approximate method can work well, both as part of a purely analytical method and when combined with FDTD. The results in combination with FDTD are particularly good, due to the more accurate electric field radiation pattern onto which the analytical magnetic field radiation pattern is superimposed. In Fig. 8.14 the individual components, due to H_y and E_z, of the pattern calculated by the full FDTD model are shown for two structures.

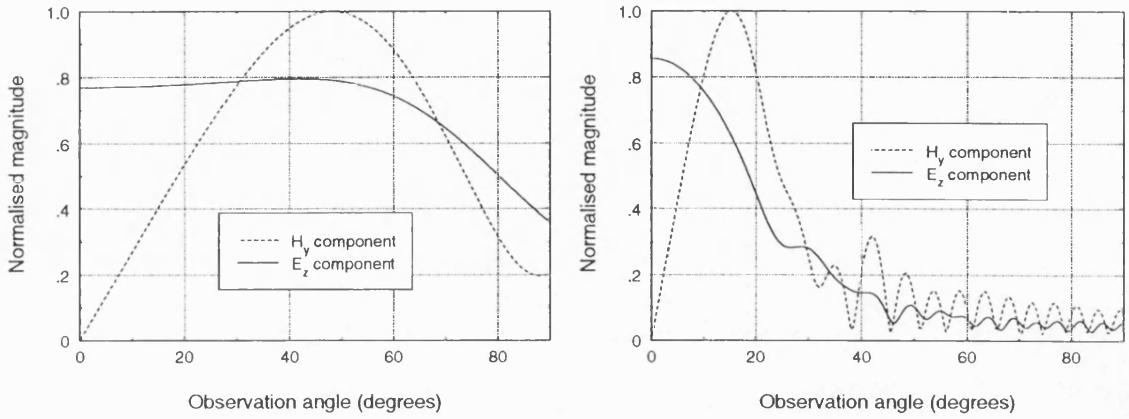

Figure 8.14: E_z and H_y contributions to the total pattern calculated by the full FDTD model: (a) Short shallow antenna at 9GHz, and (b) long shallow antenna at 10GHz.

The individual components are of similar magnitude but are not the same, differing by about 15% and 20% for the long and the short antenna respectively in the examples given. Thus, the earlier theoretical models that rely on this approximation incorporate an error of this order when they combine the calculated components to give the overall radiated far field.

8.8 Special Cells in FDTD IDG Analysis

8.8.1 Introduction

Having established the nature of the behaviour of the IDG fields at the slot edges in the analysis of Section 7.8, and having observed these effects in the numerical results of Chapter 5, it was decided to carry out an investigation into the effect of incorporating this field behaviour into special FDTD cells. As was stated in Section 3.2.8 the principal aim of doing this is to reduce the number of cells needed in the FDTD model to achieve a particular degree of accuracy.

In this section, the correction factors given in equations (3.30) and (3.31) are calculated for the IDG edge using the Van Bladel theory detailed in Section 3.3. The analysis is three dimensional and has been performed for the cells located next to the edge. The following sections give typical examples of the analysis, so that for many of the field components numerical results only are given. This is done because the general method, once established and its common variants identified, changes only slightly from node to node.

8.8.2 Analysis

This analysis relates to the FDTD cell shown in Fig. 3.5. Parts of this figure are reproduced in the current section as required for the analysis. The FDTD lattice is arranged such that the edge is located as shown in Fig. 8.15.

Only the three cells around the edge are shown in the figure, labelled as positions 1, 2, and 3. These are the only cells for which correction factors are sought as the field components located in these cells are the most affected by the presence of the edge. Below are four examples of typical calculations for the FDTD correction

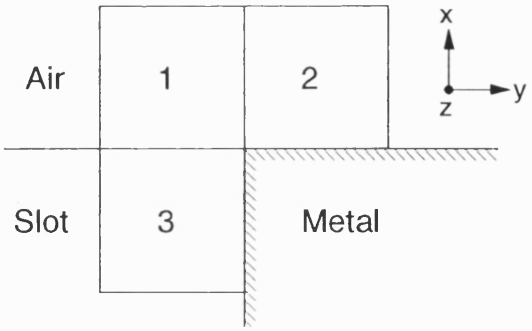

Figure 8.15: FDTD cells next to the IDG edge.

factors.

The analysis is based on the analytical expressions for the fields close to the edge in the air (equation (7.7)) and in the dielectric (equations (3.42) and (3.43)). These are expressed in Cartesian co-ordinates below:

In the air:

$$\begin{aligned}
E_x &\propto r^{\kappa-1}\sin\left[\left(\frac{3\pi}{2}-\phi\right)\kappa+\phi\right] \\
E_y &\propto r^{\kappa-1}\cos\left[\left(\frac{3\pi}{2}-\phi\right)\kappa+\phi\right] \\
E_z &\propto r^{\chi}\sin\left(\frac{3\pi}{2}-\phi\right)\chi \\
H_x &\propto r^{\chi-1}\cos\left[\left(\frac{3\pi}{2}-\phi\right)\chi+\phi\right] \\
H_y &\propto r^{\chi-1}\sin\left[\left(\frac{3\pi}{2}-\phi\right)\chi+\phi\right] \\
H_z &\propto r^{\kappa}\cos\left(\frac{3\pi}{2}-\phi\right)\kappa
\end{aligned} \tag{8.1}$$

and in the dielectric:

$$
\begin{aligned}
E_x &\propto r^{\kappa-1}\sin(\kappa-1)\phi \\
E_y &\propto r^{\kappa-1}\cos(\kappa-1)\phi \\
E_z &\propto r^{\chi}\sin\chi\phi \\
H_x &\propto r^{\chi-1}\cos(\chi-1)\phi \\
H_y &\propto r^{\chi-1}\sin(\chi-1)\phi \\
H_z &\propto r^{\kappa}\cos\kappa\phi
\end{aligned} \tag{8.2}
$$

The above are expressed as proportionalities as it is only the terms depending on the radial distance, r, of a field component from the edge and its angle, ϕ, measured from the slot wall that are of interest here.

Cell in Position 1, H_z Update

The H_z update depends on the E_x and E_y components surrounding it. This contour is depicted in Fig. 8.16.

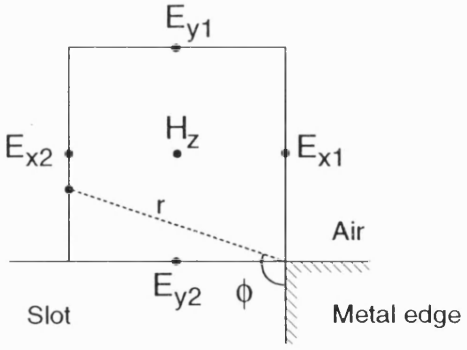

Figure 8.16: FDTD cell in position 1: H_z update contour.

The cell shown has sides of length Δx and Δy in the x and y directions respectively. The length r relates to the E_{x2} calculation only.

E_{x1} :

This calculation uses the correction factor definition given in equation (3.31). Let the calculated average value assigned to the line integral by FDTD be $\widehat{E_{x1}}\Delta x$. The analytical expression for the field is given by equation (8.1) as:

$$E_{x1}(r,\phi) = Ar^{\kappa-1}\sin\left[\left(\frac{3\pi}{2}-\phi\right)\kappa+\phi\right] \tag{8.3}$$

where A is a constant, ϕ is fixed at π and the distance to the edge, r is simply x so:

$$E_{x1}(x) = Ax^{\kappa-1}\sin\left(\frac{\kappa}{2}+1\right)\pi \tag{8.4}$$

It is known that at $x = \Delta x/2$ the field component has the final calculated value of $\widehat{E_{x1}}$, thus:

$$A = \frac{\widehat{E_{x1}}\left(\frac{\Delta x}{2}\right)^{1-\kappa}}{\sin\left(\frac{\kappa}{2}+1\right)\pi} \tag{8.5}$$

Now the integral of equation (8.4) can be performed:

$$\int_0^{\Delta x} E_{x1}(x)\,dx = \widehat{E_{x1}}\left(\frac{\Delta x}{2}\right)^{1-\kappa}\int_0^{\Delta x} x^{\kappa-1}\,dx = \widehat{E_{x1}}\Delta x\frac{1}{\kappa 2^{1-\kappa}} \tag{8.6}$$

Thus the correction factor is $1/\kappa 2^{1-\kappa}$. For a dielectric constant of 2.3, κ is 0.7455 so that the correction factor has the value 1.1245. According to equation (3.32) this value is used as a multiplier to the relevant E_x value in the H_z update equation.

E_{x2} :

Again, the calculated field value is denoted by $\widehat{E_{x2}}$. The analytical field value is given by equation (8.1) as above but now:

$$\begin{aligned} r &= (\Delta y^2 + x^2)^{\frac{1}{2}} \\ \phi &= \frac{\pi}{2} + \arctan\left(\frac{x}{\Delta y}\right) \end{aligned} \tag{8.7}$$

It is known that when:

$$\begin{aligned} r = r_a &= (\Delta y^2 + \Delta x^2/4)^{\frac{1}{2}} \\ \phi = \phi_a &= \frac{\pi}{2} + \arctan\left(\frac{\Delta x}{2\Delta y}\right) \end{aligned} \tag{8.8}$$

the field component has the final calculated value, so that:

$$A = \frac{\widehat{E_{x2}} r_a^{1-\kappa}}{\sin\left[\left(\frac{3\pi}{2} - \phi_a\right)\kappa + \phi_a\right]} \tag{8.9}$$

The line integral can now be performed, giving the correction factor as:

$$CF = \frac{r_a^{1-\kappa}}{\Delta x \sin\left[\left(\frac{3\pi}{2} - \phi_a\right)\kappa + \phi_a\right]} \int_0^{\Delta x} r^{\kappa-1} \sin\left[\left(\frac{3\pi}{2} - \phi\right)\kappa + \phi\right] dx \tag{8.10}$$

Given that κ is 0.7455 and assuming that the cell is square ($\Delta x = \Delta y$), performing the above integration numerically gives the value of the correction as 0.9884. This value is independent of the cell size, as indeed was the correction factor for E_{x1}

Cell in Position 1, E_y Update

The correction required by the E_y surface integration is considered here. From the FDTD expressions listed in Section 3.2.2, the E_y update can be seen to depend on H_x and H_z in the manner shown in Fig. 8.17, which shows the front and side views of the contour.

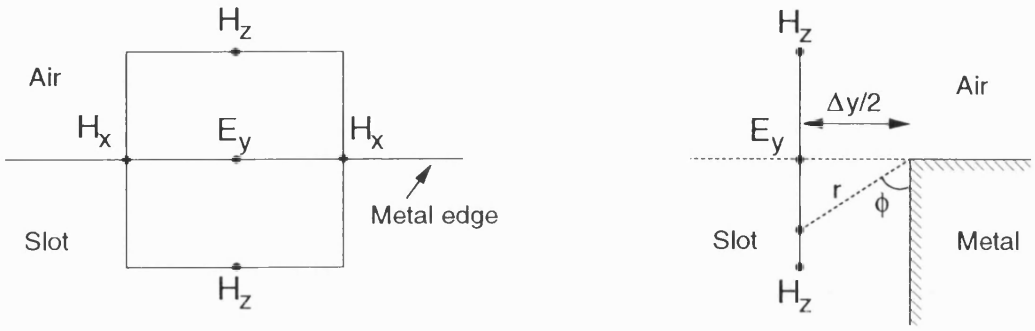

Figure 8.17: FDTD cell in position 1: E_y update contour (a) front view, and (b) side view.

The contour has sides of length Δx and Δz. It is clear from the figure that the lower half of the surface is in the dielectric region, and the upper half is in the air region. The calculation must perforce be carried out in two parts. It should be noted that the $x = 0$ axis is located on the dielectric surface, so that in this dimension the integration limits are $\pm\Delta x/2$. As before, let $\widehat{E_y}$ be the calculated value. Considering first $x < 0$:

The field is given by equation (8.2) as:

$$E_y(r, \phi, z) = Ar^{\kappa-1}(Bz + C)\cos(\kappa - 1)\phi \tag{8.11}$$

where A, B, and C are constants. As the integration surface runs parallel with the edge, some z dependence must be assumed. The standard FDTD assumption of linearity is used, and it will be seen that this term drops out of the subsequent

calculation. In the above equation:

$$\begin{aligned} r &= \left(\frac{\Delta y^2}{4} + x^2\right)^{\frac{1}{2}} \\ \phi &= \arctan\left(\frac{\Delta y}{2x}\right) \end{aligned} \tag{8.12}$$

It is known that the field value is $\widehat{E_y}$ when $r = r_a = \Delta y/2$ and $\phi = \phi_a = \pi/2$ and $z = z_a = \Delta z/2$. Thus:

$$A = \frac{\widehat{E_y} r_a^{1-\kappa}}{\cos(\kappa - 1)\frac{\pi}{2}(Bz_a + C)} \tag{8.13}$$

The surface integral can now be performed:

$$\int_{-\frac{\Delta x}{2}}^{0} \int_{0}^{\Delta z} E_y(r, \phi, z)\, dx\, dz = \frac{\widehat{E_y} \Delta z\, r_a^{1-\kappa}}{\cos(\kappa - 1)\frac{\pi}{2}} \int_{-\frac{\Delta x}{2}}^{0} r^{\kappa - 1} \cos(\kappa - 1)\phi\, dx \tag{8.14}$$

Considering now $x > 0$: The field is given by equation (8.2) as:

$$E_y(r, \phi, z) = Dr^{\kappa - 1}(Ez + F) \cos\left[\left(\frac{3\pi}{2} - \phi\right)\kappa + \phi\right] \tag{8.15}$$

where D, E, and F are constants, r is defined as for $x < 0$, and:

$$\phi = \frac{\pi}{2} + \arctan\left(\frac{2x}{\Delta y}\right) \tag{8.16}$$

Using the same conditions as were applied in the $x < 0$ case, D is obtained as:

$$D = \frac{\widehat{E_y} r_a^{1-\kappa}}{\cos\left(\kappa + \frac{1}{2}\right)\pi(Ez_a + F)} \tag{8.17}$$

The surface integral is:

$$\int_0^{\frac{\Delta x}{2}} \int_0^{\Delta z} E_y(r, \phi, z)\, dx\, dz = \frac{\widehat{E_y} \Delta z\, r_a^{1-\kappa}}{\cos\left(\kappa + \frac{1}{2}\right)\pi} \int_0^{\frac{\Delta x}{2}} r^{\kappa-1} \cos\left[\left(\frac{3\pi}{2} - \phi\right)\kappa + \phi\right] dx \tag{8.18}$$

The correction factor is given by the sum of equations (8.14) and (8.18) divided by $\Delta x\, \widehat{E_y}$. Numerical integration gives the value of the correction factor as 0.9301.

Cell in Position 3, H_z Update

As a final example, consider the correction factor for the H_z contour integral for the configuration shown in Fig. 8.18.

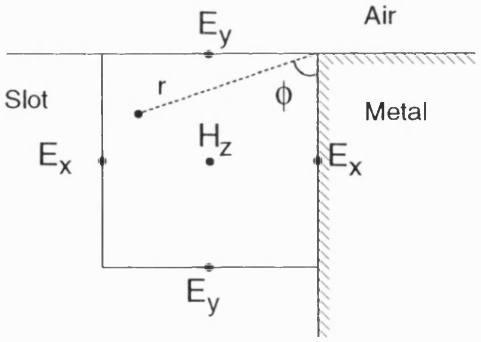

Figure 8.18: FDTD cell in position 3: H_z update contour.

The H_z node is located in the dielectric and is updated from the E_x and E_y components surrounding it, as shown. Let the calculated value be denoted by $\widehat{H_z}$, and the H_z node be located at r_a, ϕ_a. The contour sides are of length Δx and Δy. Equation (8.2) gives the field as:

$$H_z(r,\phi) = Ar^{\kappa}\cos\kappa\phi \tag{8.19}$$

where A is a constant and:

$$\begin{aligned} r &= (x^2+y^2)^{\frac{1}{2}} \\ \phi &= \arctan\left(\frac{y}{x}\right) \end{aligned} \tag{8.20}$$

The field is $\widehat{H_z}$ at:

$$\begin{aligned} r_a &= \left(\frac{\Delta x^2}{4}+\frac{\Delta y^2}{4}\right)^{\frac{1}{2}} \\ \phi_a &= \arctan\left(\frac{\Delta y}{\Delta x}\right) \end{aligned} \tag{8.21}$$

so that:

$$A = \frac{\widehat{H_z} r_a^{-\kappa}}{\cos\kappa\phi_a} \tag{8.22}$$

Thus, the correction factor is:

$$CF = \frac{r_a^{-\kappa}}{\Delta x\Delta y\cos\kappa\phi_a}\int_0^{\Delta y}\int_0^{\Delta x} r^{\kappa}\cos\kappa\phi\; dx\, dy \tag{8.23}$$

Application of a two-dimensional numerical integration routine to this integral gives the value of the correction factor as 0.9983.

All of the correction factors that have been calculated for this configuration are

included in Appendix A.

8.8.3 Results

The effect of the correction factors is tested using a uniform IDG code. The program averages results from five sets of probes to calculate the guide propagation constant, β. For the LSM guides tested it was found that the insertion of the correction factors into the code made little difference to the calculated propagation constants.

For example, for a 22.86mm wide, 10.16mm deep guide at 8GHz and with $\epsilon_r = 2.3$, the calculated β using small (0.635mm) and large (1.27mm) cells without correction factors are 1.077190 and 1.083916 respectively. The values including correction factors are 1.077094 and 1.083744 respectively. The corrected β value using the larger grid is slightly closer to the more accurate smaller grid values than the non-corrected β. This is not significant, however, and does not hold true across all frequencies. In general for LSM structures, the corrected and non-corrected β values are extremely close.

From this it must be concluded either that FDTD is modelling the singularities sufficiently well without compensation, or that the edge effects have little bearing on the propagation constant value. The results of Section 5.2.1 support the latter conclusion in that for most shallow guide geometries the H-guide and FDTD calculated β values are close even though the H-guide model omits the edge effects.

In Fig. 5.4 the LSE H-guide propagation constant is shown to deviate significantly from FDTD and TRD values, suggesting that the singularities may play more of a role. This seems to be the case, as can be seen in the results of Fig. 8.19.

In this figure a 10.16mm wide, 15.24mm deep LSE guide with $\epsilon_r = 2.3$ is considered. Models with four sizes of cell within the slot have been used, with and without correction factors. The cell sizes are 0.3175mm (32 cells wide by 48 deep in the

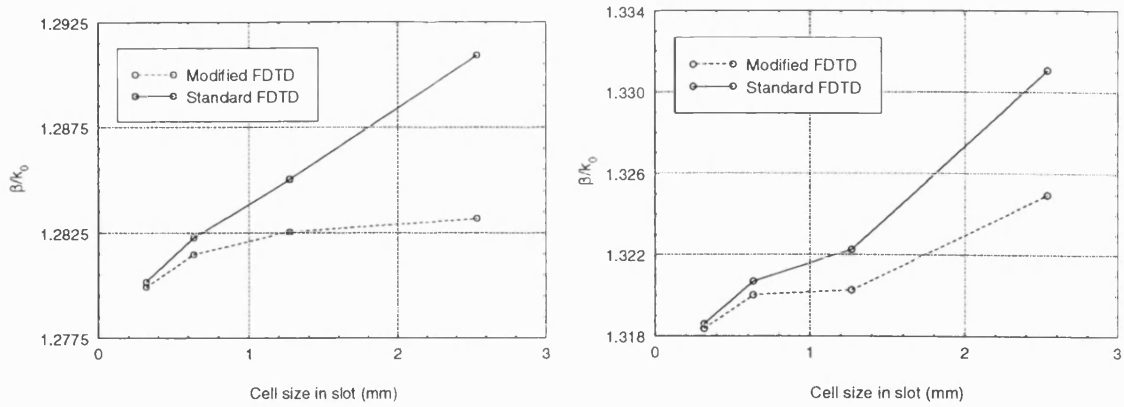

Figure 8.19: Effect of FDTD special cells for LSE guide at (a) 8GHz, and (b) 9GHz.

slot), 0.635mm (16 wide by 24 deep), 1.27mm (8 wide by 12 deep) and 2.54mm (4 wide by 6 deep).

The results show the propagation constants tending towards a given value as the cell size is decreased. However, when correction factors are included in the model the propagation constant is closer to the 'final' value for any given cell size. At 8GHz, for instance, a cell size of 2.54mm can be used in a modified model to obtain better accuracy than is achieved using a standard model with a 1.27mm cell size. This leads to a considerable saving in run time.

To quantify this, the details of the two latter models can be compared. The standard model with 1.27mm cell size takes 4 minutes 6 seconds to run. The number of cells in the slot is 4x12x250, in the air 15x25x250, and the model runs for 3000 time steps of 2.1ps. The modified model with 2.54mm cell size takes 19 seconds to run, with 2x6x125 cells in the slot, 8x13x125 cells in the air, and 1500 time steps of 4.2ps. Savings obtained by using the modified model are therefore of the order of a factor of 7 in terms of storage space and a factor of 13 in terms of the run time. It should be noted however that this represents a best case saving, as the extent of the advantage of using the modified model varies with frequency, as is clear from the results given above.

8.9 Chapter Summary

Improved FDTD models of the IDG-TSA have been presented. The most complete model includes all the faces of the antenna mounting block together with the RWG feed and flange. The importance of the radiation from the subsidiary faces of the structure has been demonstrated, as has the effect of the RWG flange on the aperture distribution. Results generated using the full model are in very close agreement with measured results, and are considerably better than those produced by the existing FDTD model which uses Walter's approximation to cater for the ground plane fields.

Special FDTD cells have been developed in an attempt to improve the modelling of the singularities around the slot edges. Inclusion of these cells in a uniform IDG FDTD model produced no significant change in calculated propagation constant values for shallow guides, but produced an improvement in the deep slot case. By using the correction factors, the model cell size for a given degree of accuracy may be increased. This leads to savings in computer time and storage requirements, with factors of up to 13 times and 7 times respectively having been observed.

Chapter 9

Further Application of the Models

This chapter is split into three main sections. In the first, the possible effects on the radiation pattern of installing an IDG-TSA in a surface are considered. This subject is returned to later on in the chapter. The effect of small variations in the dielectric constant of the slot filling is then examined. In the second section, the wider validity of the theoretical models developed in Chapters 7 and 8 is demonstrated by considering results over a wide range of observation angles. Results for novel short structures, both shallow and deep, are given. In the final section, a number of FDTD results depicting the fields around the IDG-TSA are presented which give insight into the operation of the structure. The details of the antennas considered in this chapter are listed in Section 7.2.

9.1 Near-Antenna Environment Issues

The objective of this section is to demonstrate the extent to which the radiation pattern of an IDG-TSA can be modified by the environment in which it is installed. That the radiation pattern of the shallow slot IDG-TSA is sensitive to its environment is already apparent from the FDTD results of Chapter 8. These results show

significant downward directed radiation and radiation from the subsidiary surfaces of the antenna, both of which will be disturbed by flush mounting it in a surface.

The ease with which the elevation pattern of a shallow IDG-TSA can be disrupted is shown in Fig. 9.1.

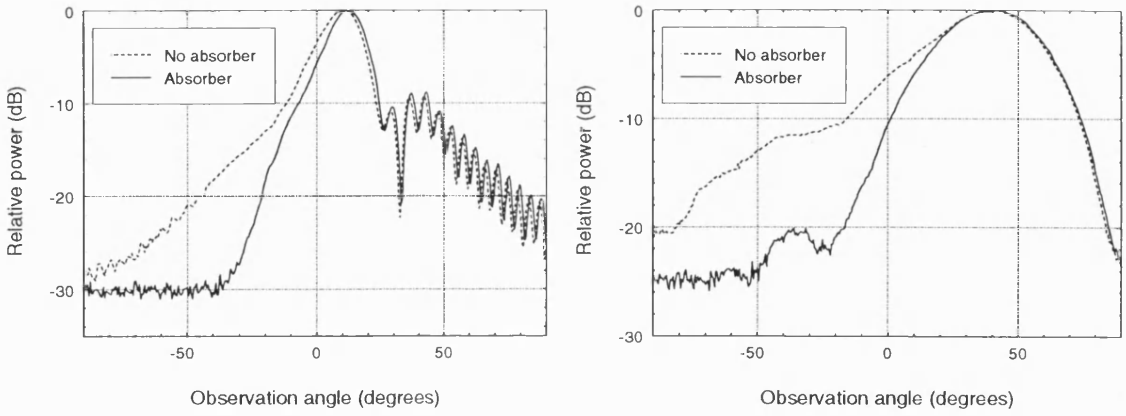

Figure 9.1: Measured elevation plane patterns for shallow antennas. Effect of masking mounting block end face: (a) Long, and (b) short antenna.

For these measurements two cones of absorbing material are fixed onto the end face of the antenna, entirely covering it and flush with the aperture surface. This prevents the end face from radiating and stops some of the downward radiation caused by the end edge of the structure. The reduction in downward radiation is clear in the results, and there is a subsequent narrowing of the main forward beam.

Going a stage further, the results of Fig. 9.2 show the effects of placing the antenna in a surface constructed from absorbing material.

The absorber is placed all around the edges of the ground plane, flush with it in order to try to simulate an infinite surface. Absorbing material is an extreme example and a metal surface, for instance, would produce very different results, but it is illustrative.

In the shallow slot case the downward radiation is now much reduced as the effects of the side faces and edges have been removed. In addition, the shape of the main

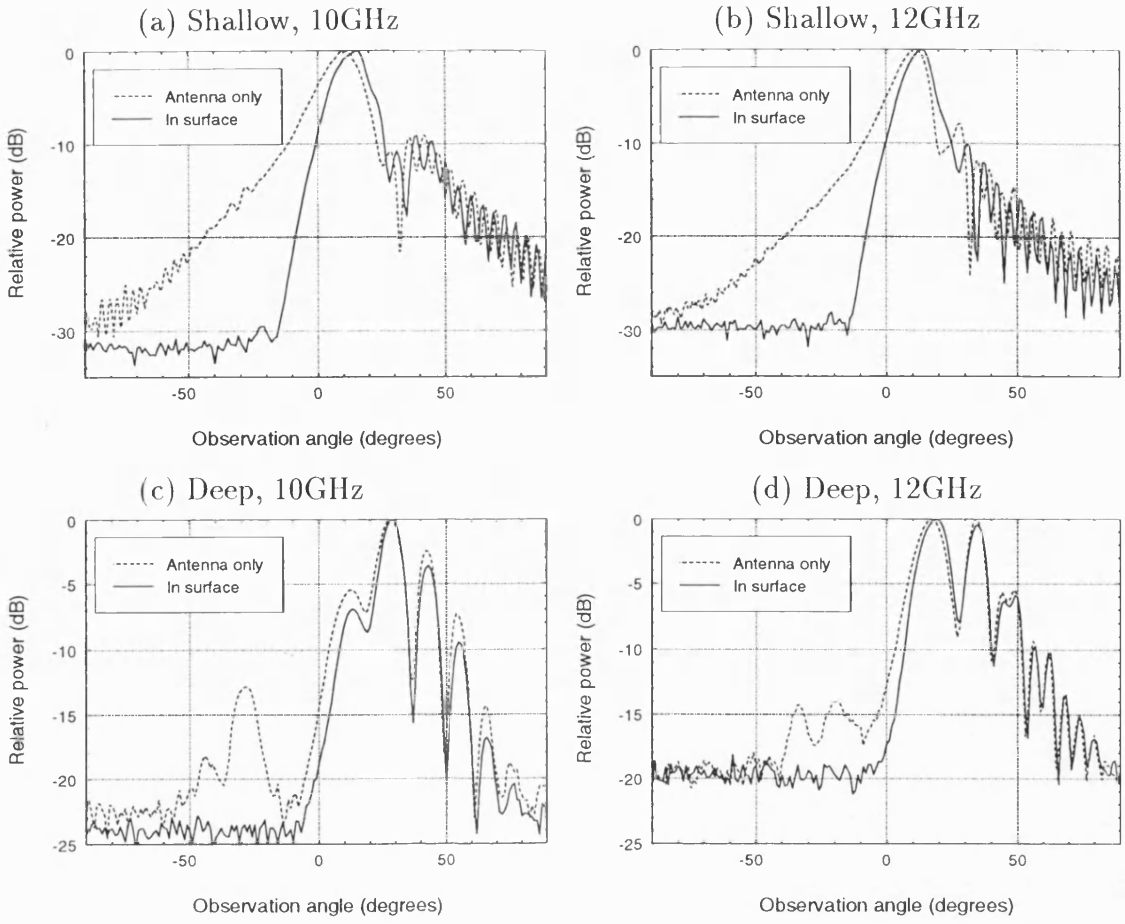

Figure 9.2: The effect of a surface of absorbing material on the measured elevation plane patterns of long antennas.

beam has been modified and shifted to a higher angle. This effect can to some extent be explained by considering the individual FDTD calculated components of the elevation pattern as depicted in Fig. 8.14. This figure shows the E_z components to have a high value, near to maximum, along the axis of the antenna whilst the H_y component pattern is tilted off the surface so is zero along this axis. The E_z pattern is therefore more susceptible to disturbance by the installation surface. In this case, its influence appears to be reduced, allowing the H_y pattern to dominate and increase the beam tilt.

Very little effect is seen in the case of the deep slot structure. Although the downward radiation is reduced the upward radiation is little affected by the absorber

surface. This is due in part to the fact that there is little radiation along the axis, and demonstrates that the ground plane plays a much less significant role for deep structures.

The conclusion to be drawn from the above is that for accurate prediction of the radiation behaviour of the IDG-TSA it is necessary to include details of the surrounding environment in the model. This was to some extent already apparent from the work of Chapter 8 where it was found that only by inclusion of a number of the IDG-TSA surfaces could measurement be accurately matched. Extension of the theoretical models to include the surrounding environment is potentially problematic. Whilst the main limitation in the FDTD case is the size of the model, the extension of the H-guide model to include more surfaces, possibly with curved profiles, could become very involved.

9.1.1 Implications for the Analytical Model

The H-guide model of Section 7.9 does not model the side or end faces of the antenna mounting block, nor the edges of the top face. It is possible therefore that the agreement between theory and measurement achieved in Section 7.9 might be improved by comparing to measured values where these effects have been masked out to some extent. This is indeed the case, as evidenced by Fig. 9.3.

In these figures the end face of the antenna has been masked with absorber. The discrepancy between theory and measurement around the main beam has been reduced and the sidelobe agreement is now very good.

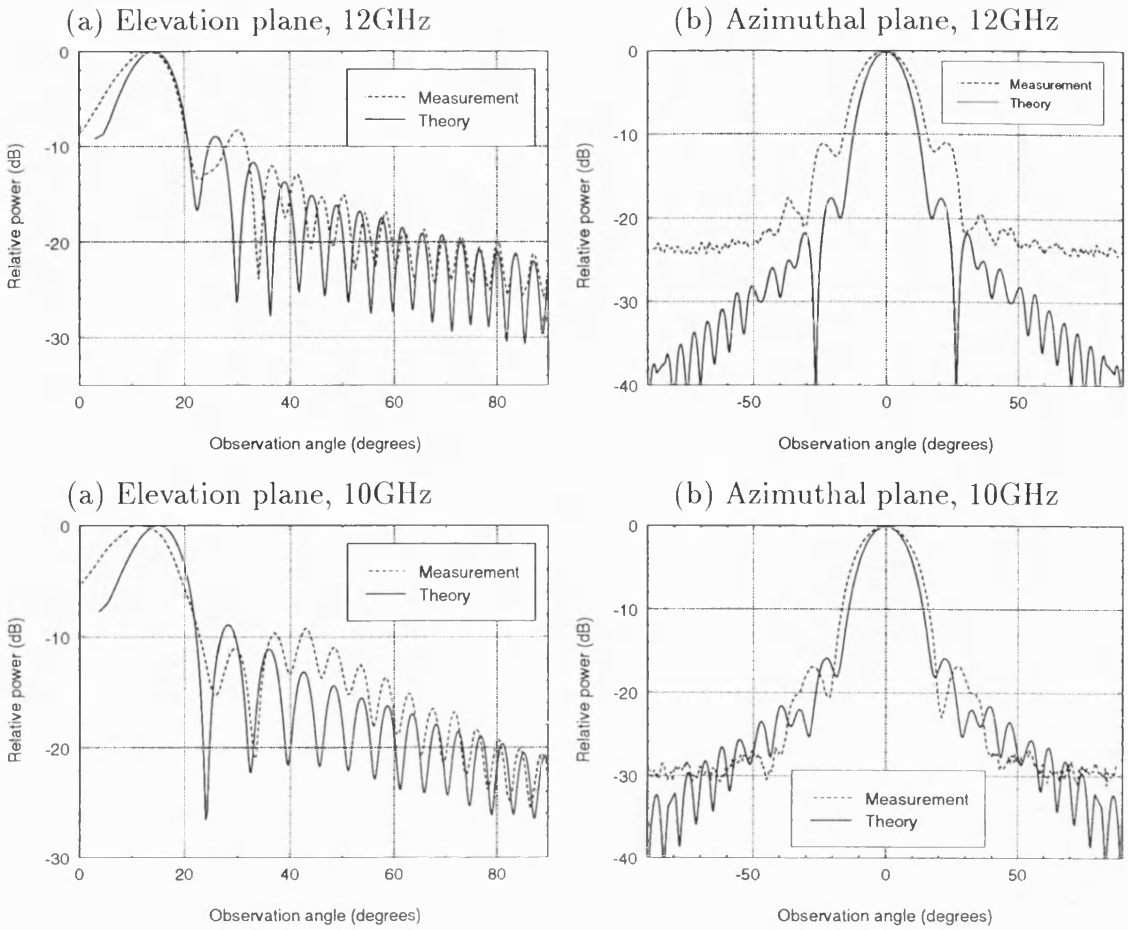

Figure 9.3: Radiation patterns of a long shallow antenna. End face of mounting block is masked in the measured data.

9.2 Small Variations in Dielectric Constant

For most of the work presented in this thesis, IDG with a nominal dielectric constant of 2.3 has been used. It is known that this material does not maintain the same dielectric constant across the frequency band of interest [4]. Clearly, a variation in ϵ_r will affect the propagation constant and thus the radiation pattern of the IDG-TSA. Figures 9.4 and 9.5 show the extent of this variation as calculated by the FDTD and H-guide methods.

For the short structure, there is little variation in the upward directed radiation when ϵ_r is changed by $\pm 10\%$ at 8GHz. The impact is much more pronounced

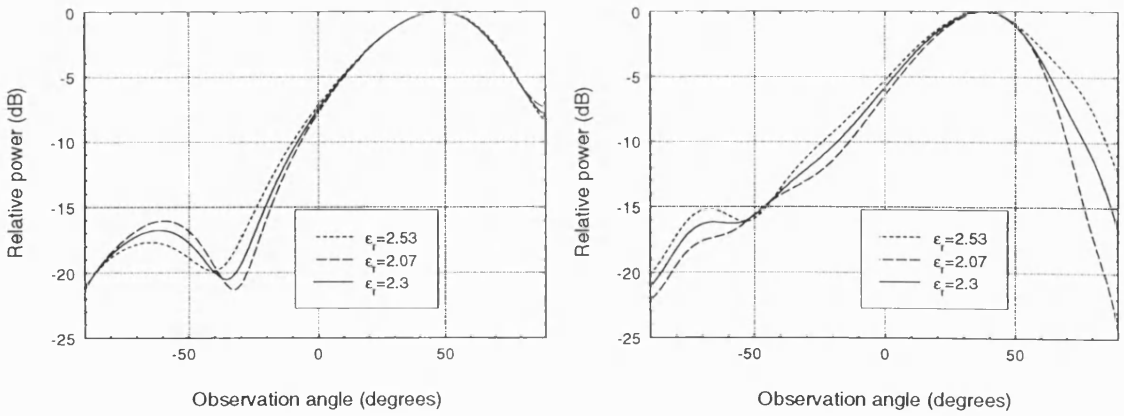

Figure 9.4: Short shallow antenna elevation plane radiation pattern by FDTD. Effect of varying ϵ_r by $\pm 10\%$ at (a) 8GHz, and (b) 12Ghz.

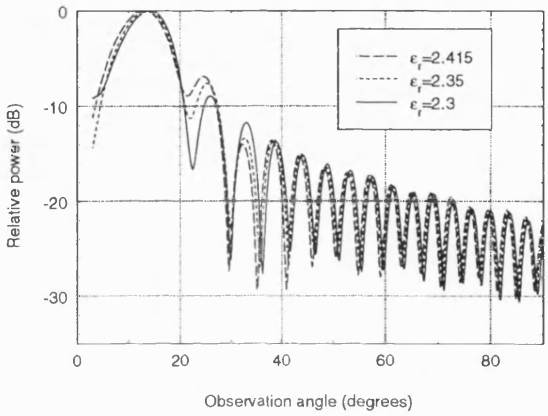

Figure 9.5: Long shallow antenna elevation plane radiation pattern by the H-guide method. Effect of varying ϵ_r by 5% at 12Ghz.

at 12GHz. At 8GHz, the propagation constant at the antenna feed is close to k_0 and reduces quickly to k_0 as the guide depth reduces. At 12GHz the propagation constant is higher and remains above k_0 for much of the taper so that changes in propagation constant due to ϵ_r variation have a greater net effect.

Varying ϵ_r by 5% for the long antenna has little effect on the lower sidelobes but produces significant variation in the first and second sidelobes.

Small changes in the dielectric constant are therefore a factor that can have a significant bearing on the radiation pattern but the effects are hard to predict. In a real IDG-TSA it is likely that ϵ_r will vary along the taper and that air bubbles in the

dielectric and irregularities in the surface finish will also exist. These unmodelled effects can all serve to degrade the apparent performance of the prediction tools.

9.3 Results Over a Broader Angular Range

This section presents four sets of results, one for each of the principal antenna geometries, that show for the first time the performance of the two theoretical methods, H-guide and FDTD, over a broad range of observation angles and make comparison to measurements. The models used here are the most complete that were developed in Chapters 7 and 8 respectively. The results are presented in Figures 9.6 to 9.9, grouped as four sets of three plots.

In each plot 0dB is defined as the maximum value of that particular plot, and the contours have been chosen such that the white part of each plot shows the 3dB beamwidth. Note also that some of the deep troughs in the theoretical results are not repeated in the measurements due to the noise floor of the measurement system having been reached.

In general, agreement between both theoretical methods and experiment is good, making allowance for the fact that the non-graded contour system adopted can sometimes accentuate small differences between results. A possible cause for differences between the H-guide and measured results has already been considered in Section 9.1.1. The FDTD results for the short deep antenna do not compare well with measurement. A set of results presented in the next chapter, Fig. 10.29, may help to explain this. Between 9 and 10GHz, the measured main beam undergoes a significant shift in position. It is possible that better comparison with measured results may be obtained at a lower frequency as inaccuracies in the FDTD model, such as an incorrect ϵ_r or ϵ_r distribution, or poor modelling of the sharp IDG taper, may be causing the theoretical results to be effectively frequency shifted.

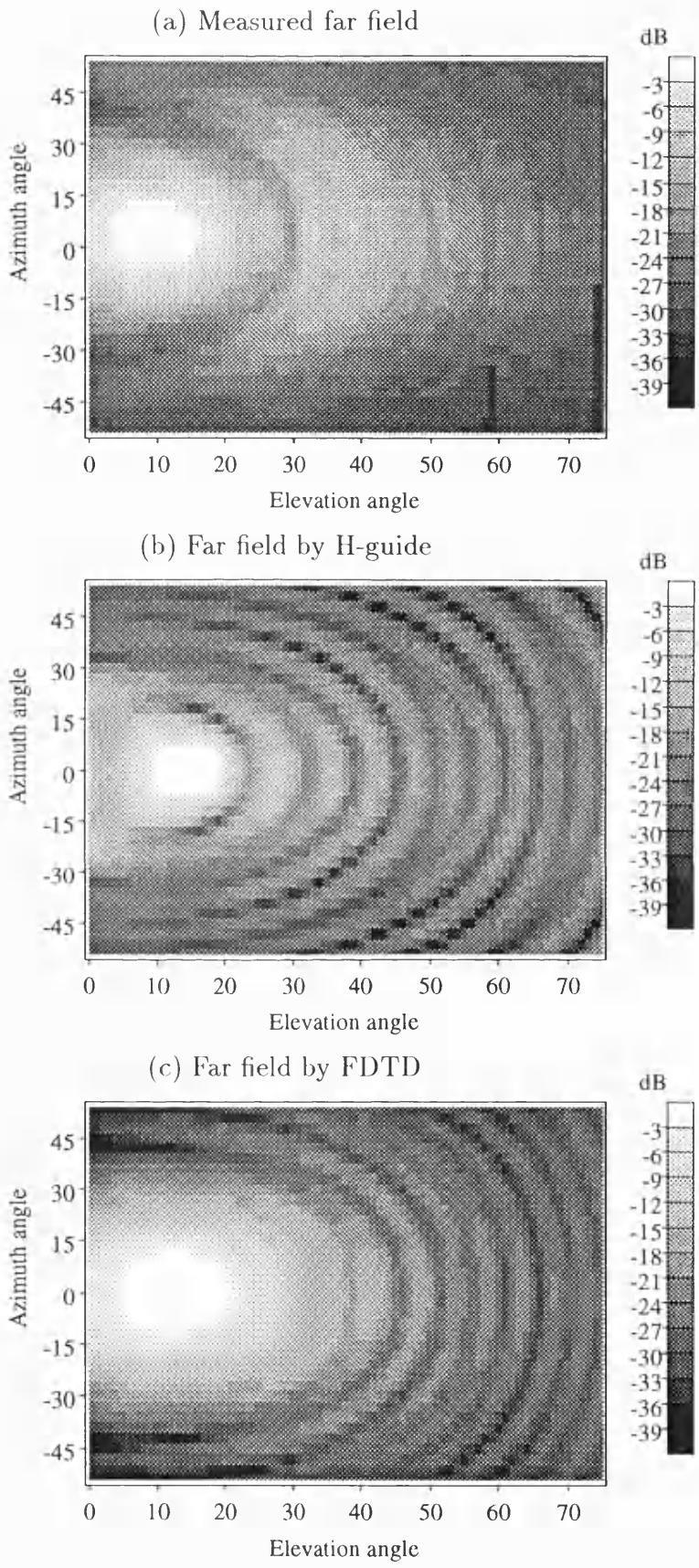

Figure 9.6: Far field of long shallow antenna at 10GHz.

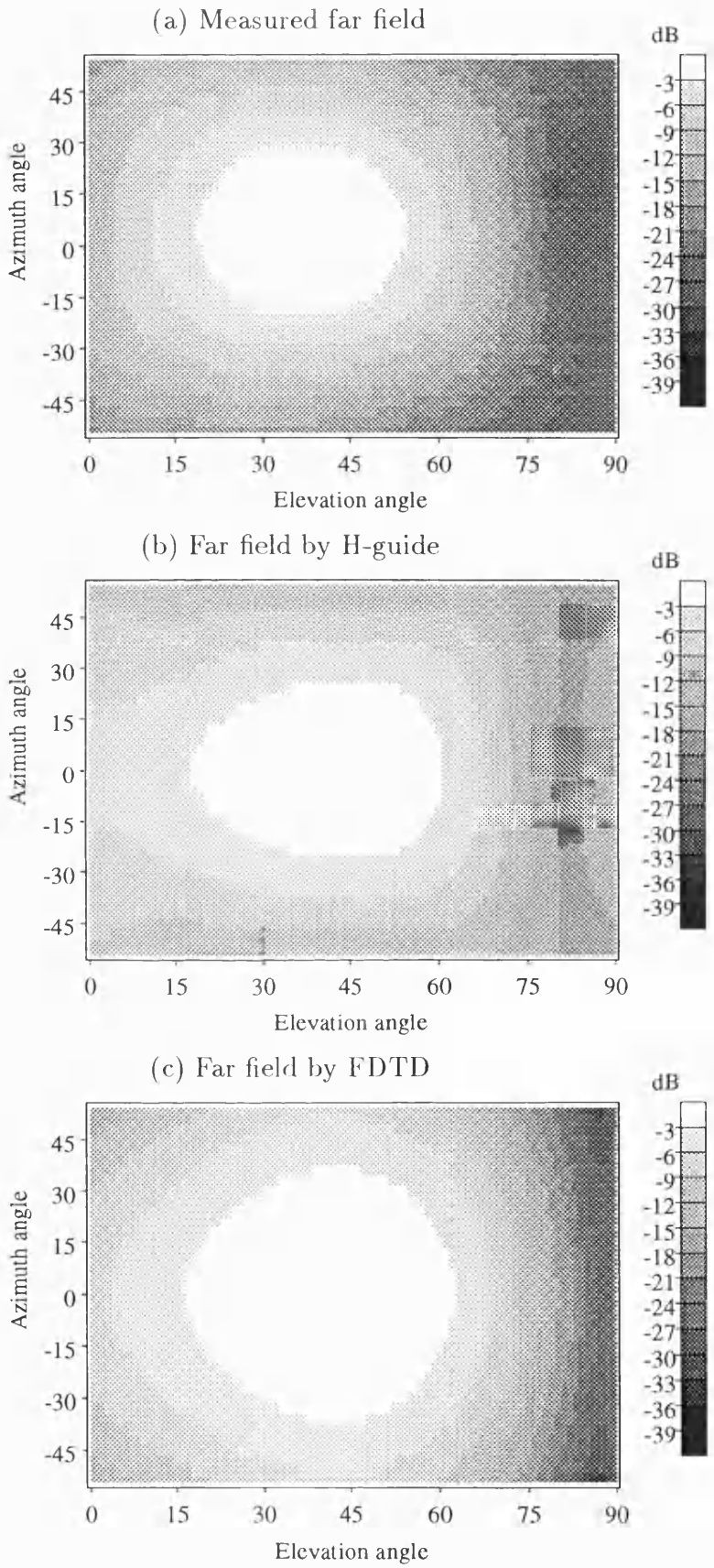

Figure 9.7: Far field of short shallow antenna at 10GHz.

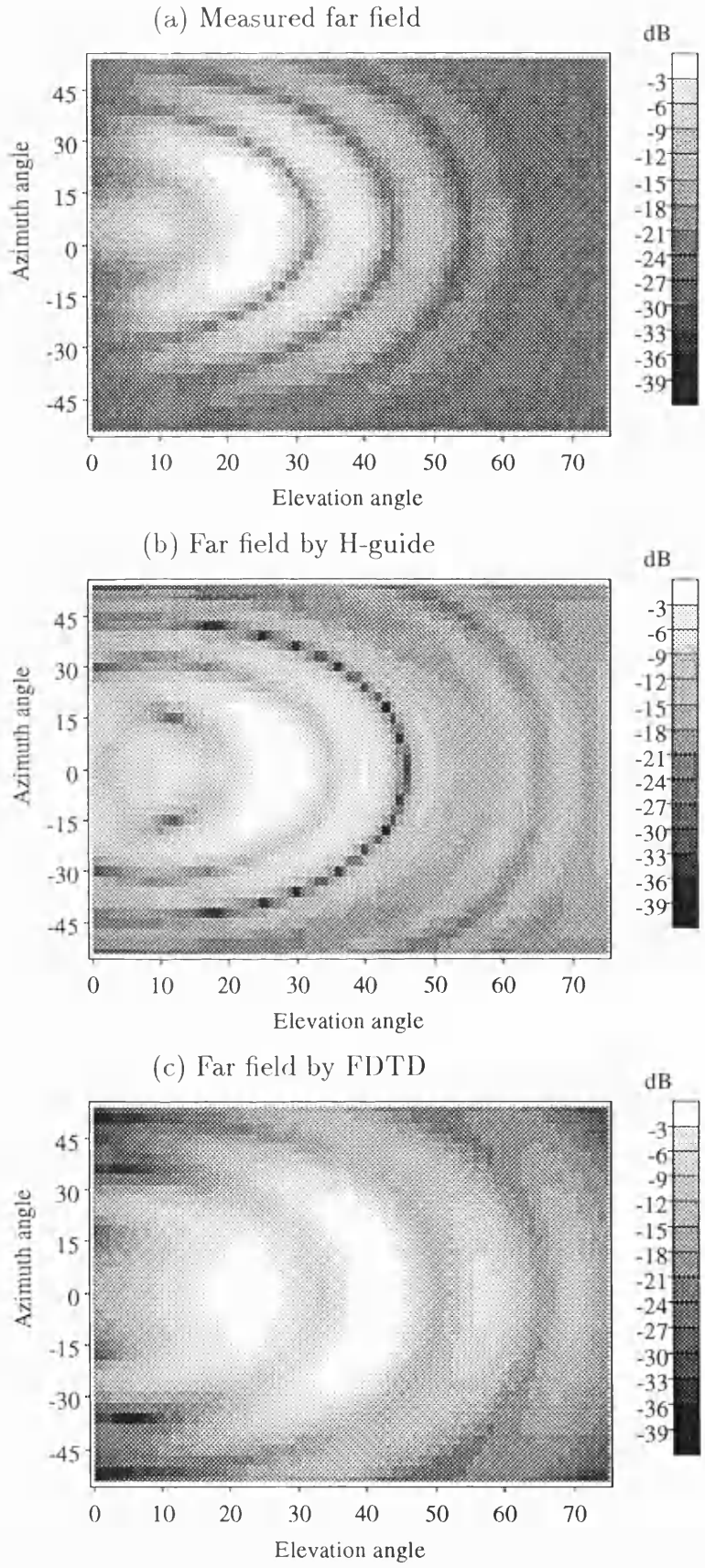

Figure 9.8: Far field of long deep antenna at 10GHz.

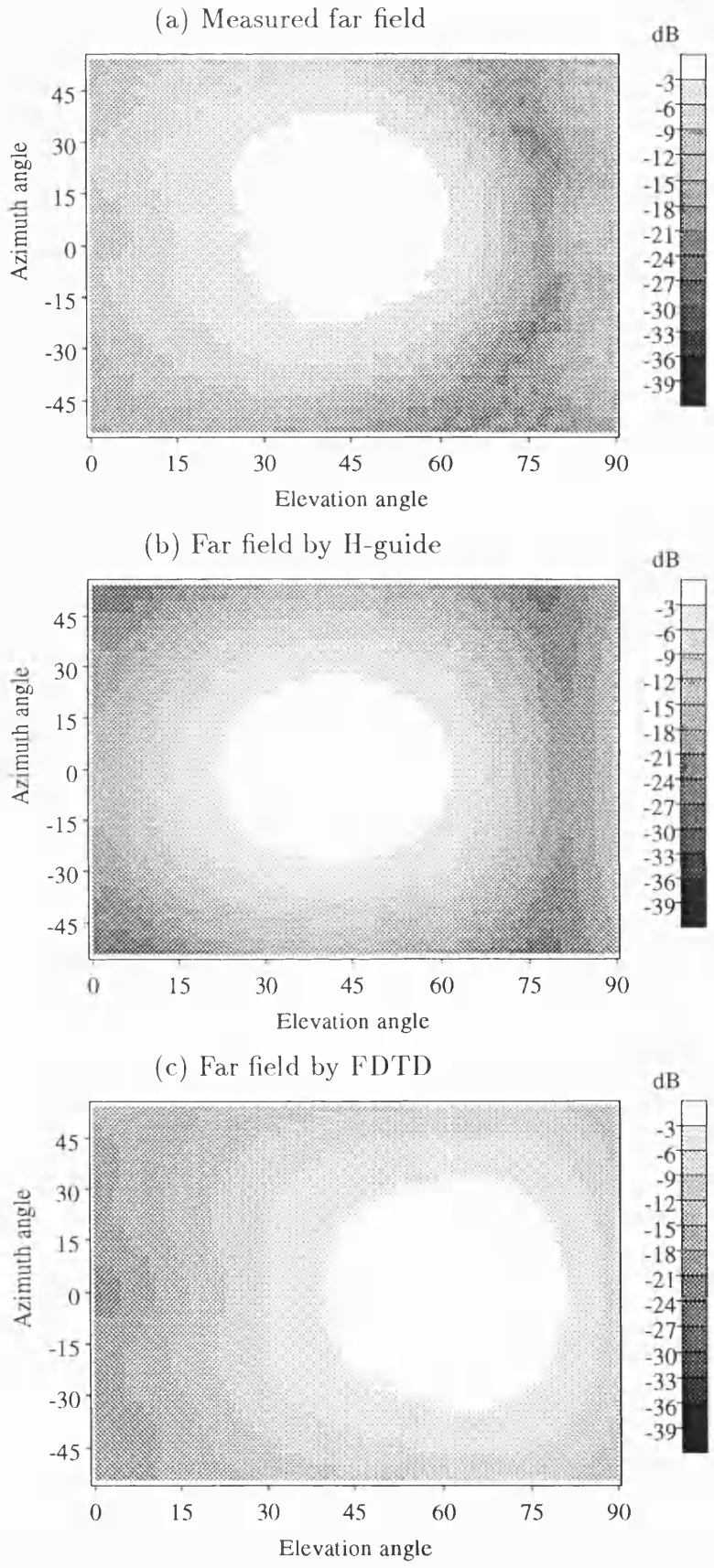

Figure 9.9: Far field of short deep antenna at 10GHz.

The short antennas considered in this section have not been studied in previous work. These elements can be seen to produce single very wide beams. Such structures may be suitable for application as elements in phased arrays.

9.4 IDG-TSA Field Distributions by FDTD

With the full FDTD model of Chapter 8 established, it is a straightforward matter to extract from this calculation the time or frequency domain fields on any plane within the structure. A number of such results are included in this section in order to give insights into the mode of operation of the IDG-TSA.

9.4.1 A Study of the Fields of a Short Shallow IDG-TSA

In this section the fields in three planes cut through the short shallow IDG-TSA FDTD model are presented. The E_z and H_y components only are considered as these are combined in the calculation to give the elevation plane pattern. All the results show time domain data extracted at the end of the FDTD run.

Fig. 9.10 shows the fields on a longitudinal cut through the centre of the structure.

Only the air fields are shown, which leads to the antenna and feed appearing as a black silhouette. The feed is 37mm long, the slot ends at a longitudinal distance of 66mm and the ground plane ends at 76mm. On the vertical axis the zero coincides with the plane of the aperture, and the antenna mounting block is 37mm deep. The RWG flange can clearly be seen on the top side of the structure.

An approximation in the FDTD model is apparent in these figures; the external vertical dimension of the feed waveguide has been extended so that it is as deep as the mounting block. The internal dimension is unchanged. This reduces the

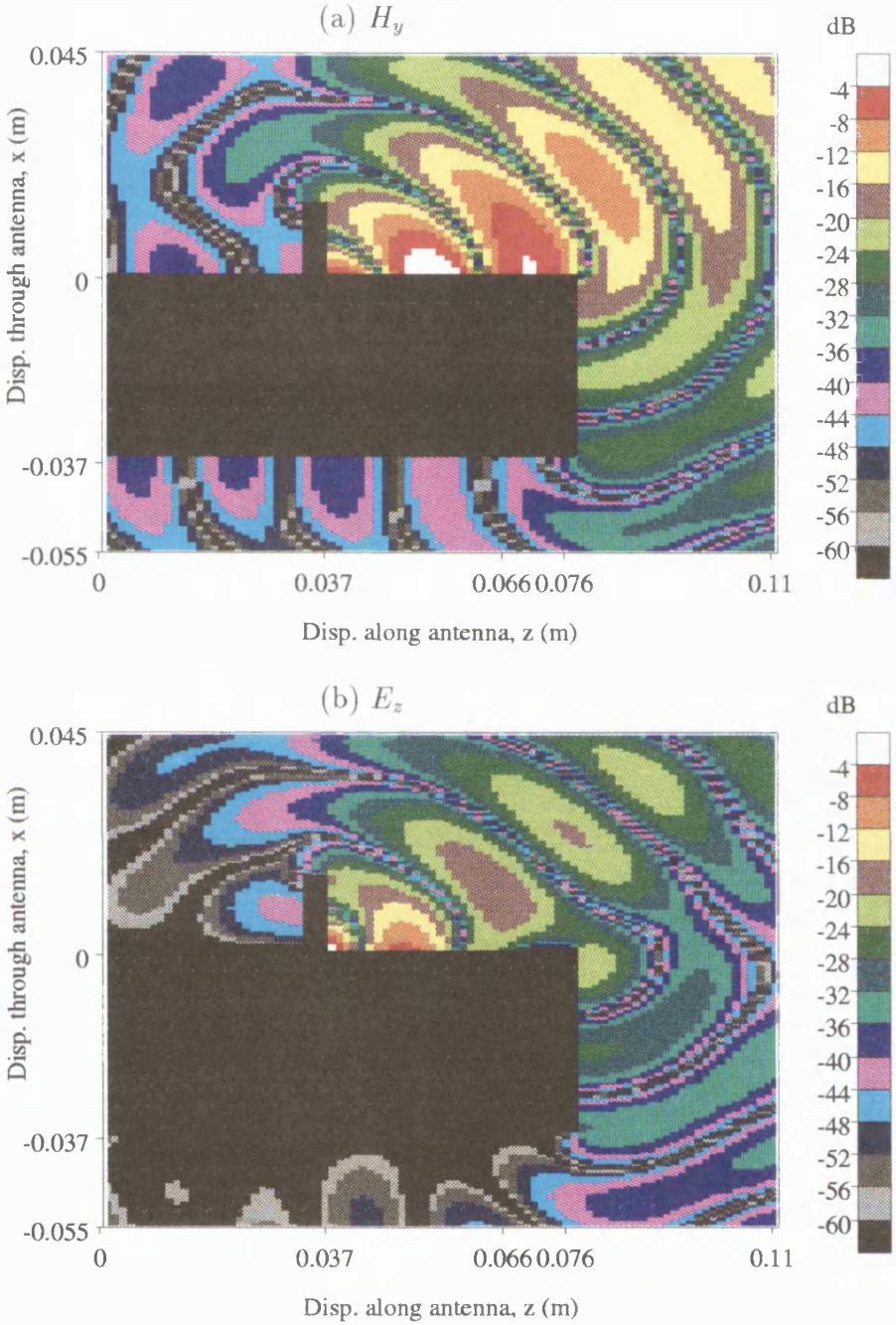

Figure 9.10: Fields on a cut through the centre of a short shallow antenna at 10GHz, excited from RWG with the flange located at $z = 0.037m$.

number of surfaces to be modelled and prevents further fragmentation of the air space. It is clear from these results that the fields on the underside of the feed are not high, so this approximation is likely to have little detrimental effect on the overall model performance.

These plots show clearly the wave travelling along the antenna surface and the power being radiated into space. The RWG flange prevents any significant spread of field onto the feed surface. It is interesting to note the extent to which the end edge and face of the mounting block play a role in the field distribution. For both field components the propagating wave extends around the end edge, leading to the significant downward directed radiation that has already been observed in Chapter 8.

The magnitude of the radiation below the aperture can be seen more distinctly in Fig. 9.11.

These figures show the field in a transverse plane 10 cells beyond the end edge of the ground plane block. Only the right hand half of the antenna is shown so that the zero on the horizontal axis corresponds to the centre of the structure. The half width of the mounting block is 45mm. It can be observed that whilst the main part of the radiation is upwards there is significant field below the aperture plane, particularly in the E_z case. As a final illustration for this structure, consider Fig. 9.12.

This data is taken in a longitudinal plane as used in Fig. 9.10 but is located just in front of the side face of the mounting block. Both components show much field below the level of the aperture, with the E_z component again being the most active in this respect. As well as being affected by the end edge of the ground plane it can be seen here how the field is also spilling over its side edges.

The results presented here correspond well with the measurements given in Section 9.1 where an antenna was located in a simulated installation surface. These

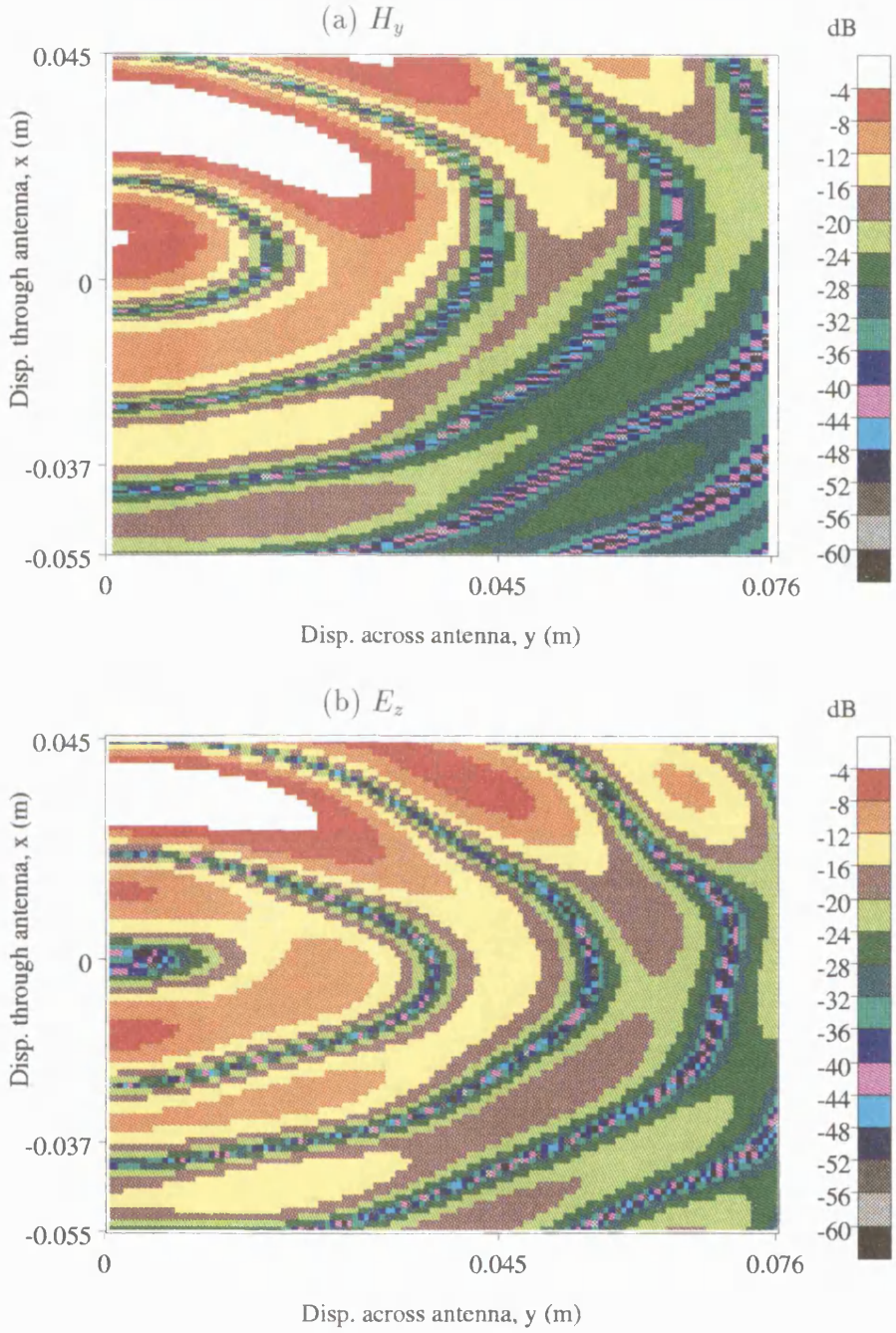

Figure 9.11: Short shallow antenna at 10GHz. Fields on a cut 10 cells (6.35mm) beyond the end edge of the mounting block.

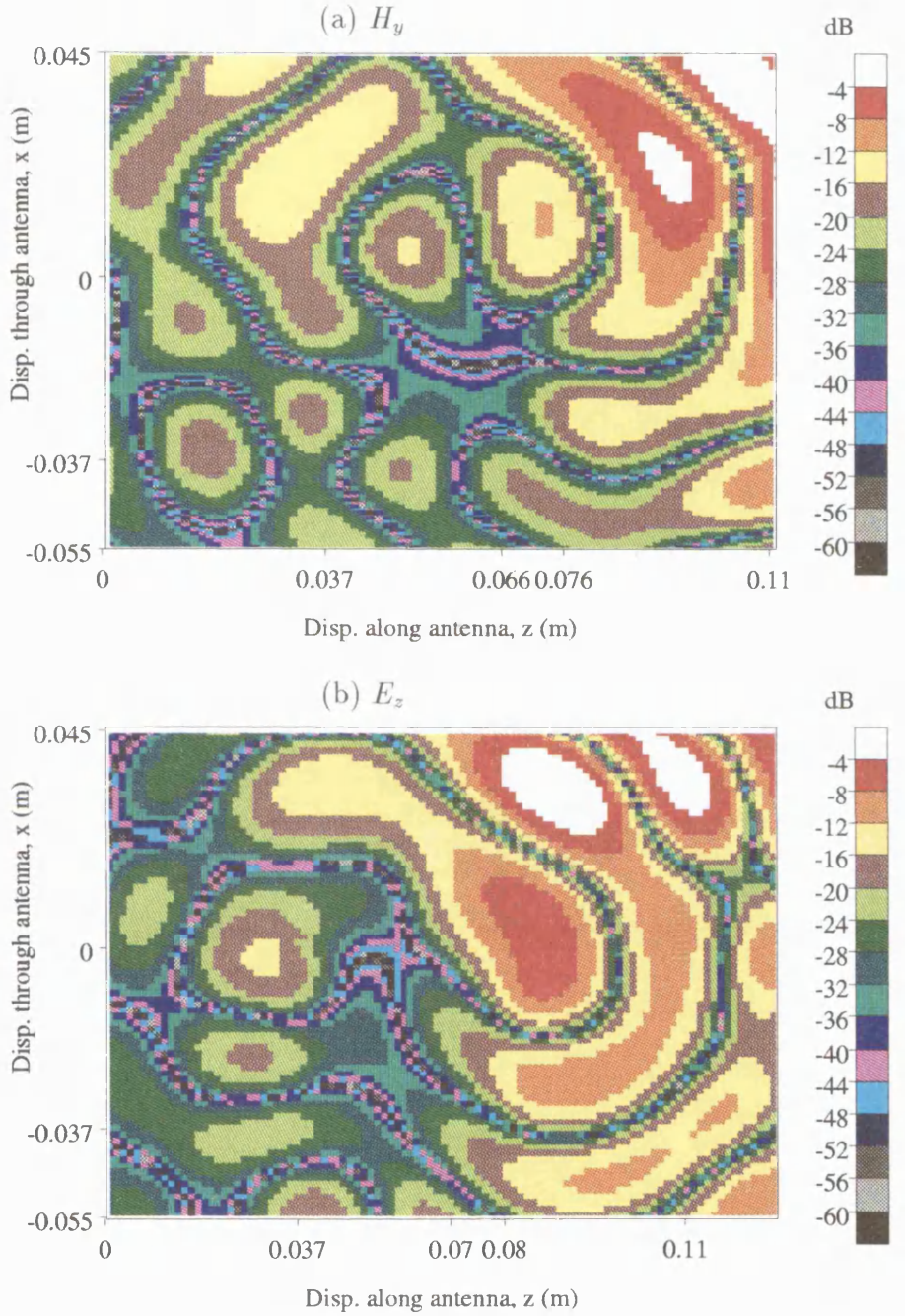

Figure 9.12: Short shallow antenna at 10GHz. Fields on a cut 10 cells (6.35mm) in front of the side face of the structure.

measurements demonstrate that the radiation pattern can be noticeably disturbed simply by masking the antenna end face, and that by masking all the edges a significant modification can be brought about. The plots given in this section show that the absorber used in the experimental work is in fact cutting through areas of significant field and underline once more the need to consider the installation environment when modelling an IDG-TSA.

9.4.2 Longitudinal Deep IDG-TSA Fields

For the purposes of comparison with the results of the foregoing section two results for a short deep IDG-TSA are included in Fig. 9.13. This shows longitudinal cuts through the centre of the structure and can be compared directly with Fig. 9.10, although the aperture and ground plane lengths are slightly different.

The tendency of the short deep antenna to radiate closer to broadside is evident from the results, as well as markedly less radiation below the level of the aperture when compared to the shallow slot case. Again, this is consistent with the experimental results of Section 9.1 where little disruption to the deep IDG-TSA radiation pattern was caused by its installation in a surface.

9.4.3 Aperture Fields

In this section the magnetic fields on the aperture surface of the principal antenna geometries are presented. The primary objective of doing this is to consider the validity of the analytical model of the aperture fields developed in Chapter 7.

Figures 9.14 and 9.15 show time domain magnetic field components on long shallow and deep structures. Both these results show the air around the ground plane surface, with the deep slot result additionally including 43mm of feed. The hori-

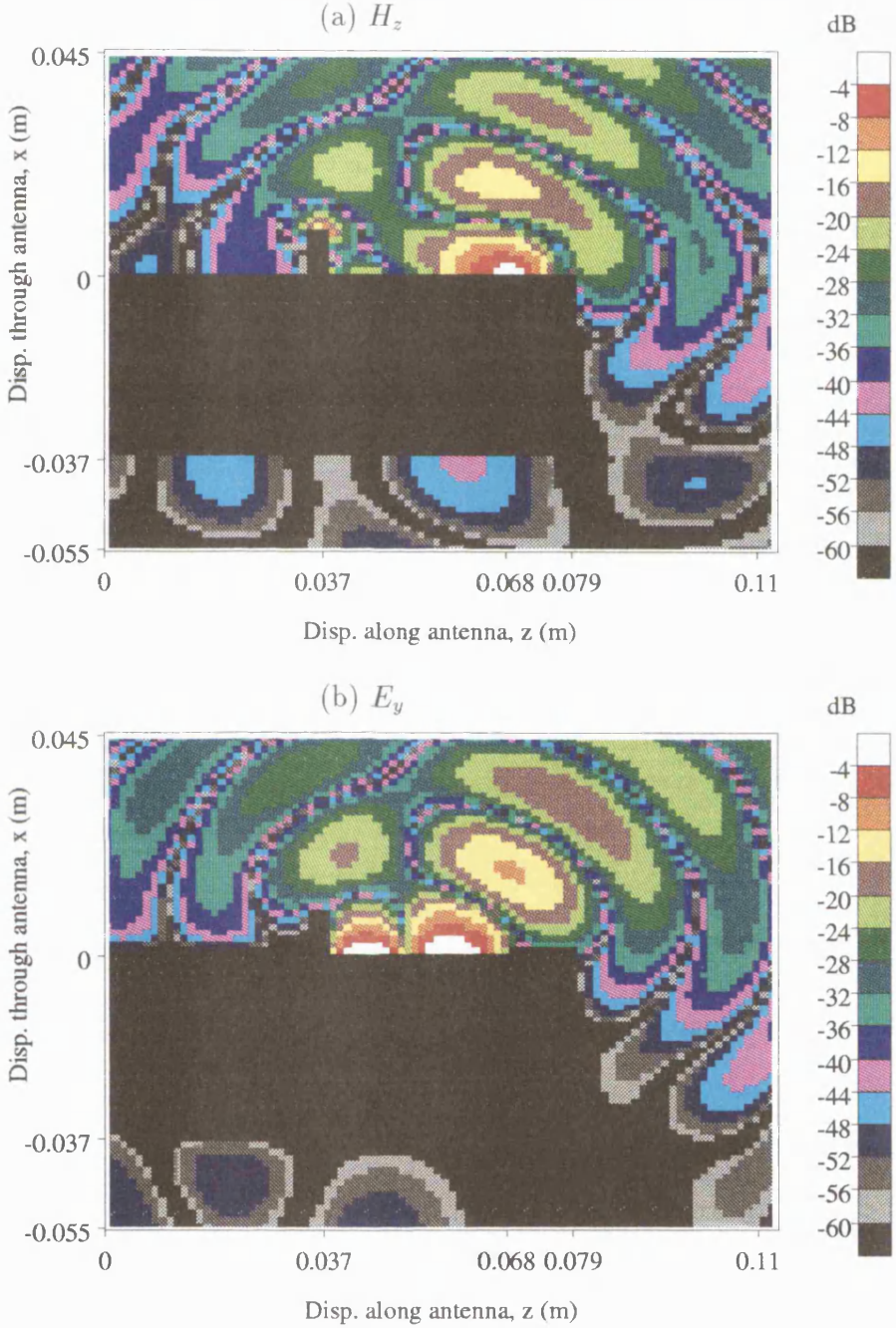

Figure 9.13: Fields on a cut through the centre of a short deep antenna at 10GHz, excited from RWG with the flange located at $z = 0.037m$.

zontal axes show the locations of the slot and ground plane ends, the vertical axis shows the half widths of the slot and ground plane. It is interesting to note here the higher concentration of field within the slot in the deep slot case; the spread of field onto the ground plane is much greater for the shallow slot and starts to build up soon after the feed. It has already been shown in Chapter 7 how the analytical model matches the long antenna distribution reasonably well.

The final three results, Figures 9.16 to 9.18, relate to shorter structures; the medium plastic and short shallow and deep antennas. The result for the medium plastic antenna, for which only the slot and ground plane are shown, conforms reasonably closely to the analytical model, with nearly plane wavefronts travelling with the slot propagation constant along the ground plane. There is rather more deviation from the model for the short structures, where the wavefronts on the ground plane are more curved. Despite this deviation from the model, the results of Section 9.3 show that the H-guide method still generates reasonable results for these structures. This is not inconsistent, as the curvature of the wavefronts in the FDTD results becomes most marked only further away from the slot where the field strength has decayed considerably.

9.5 Chapter Summary

It has been shown using measurement that the radiation characteristics of the shallow IDG-TSA are highly sensitive to changes in the environment in which it is installed, whereas the deep IDG-TSA is little affected by such changes. Cuts through the fields calculated by FDTD for both antenna types highlight the greater role played by the mounting block in the distribution of the fields in the shallow slot case. The full H-guide model introduced in Section 7.9 does not include details of the mounting block. It has been shown how results generated by this method match measurement more closely if some of the mounting block surfaces are masked

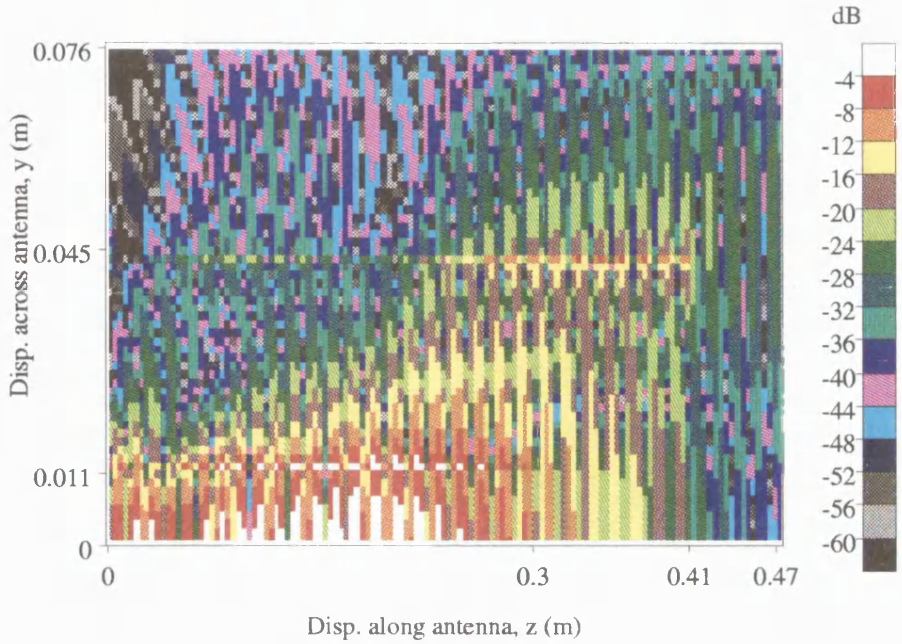

Figure 9.14: Long shallow antenna at 10GHz. Time domain H_y on the aperture surface.

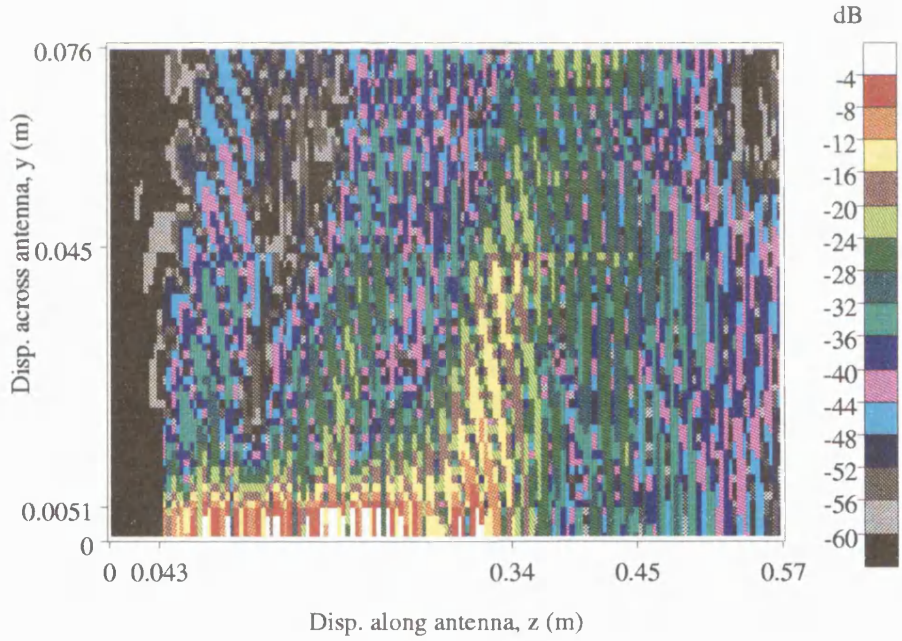

Figure 9.15: Long deep antenna at 10GHz. Time domain H_z on the aperture surface.

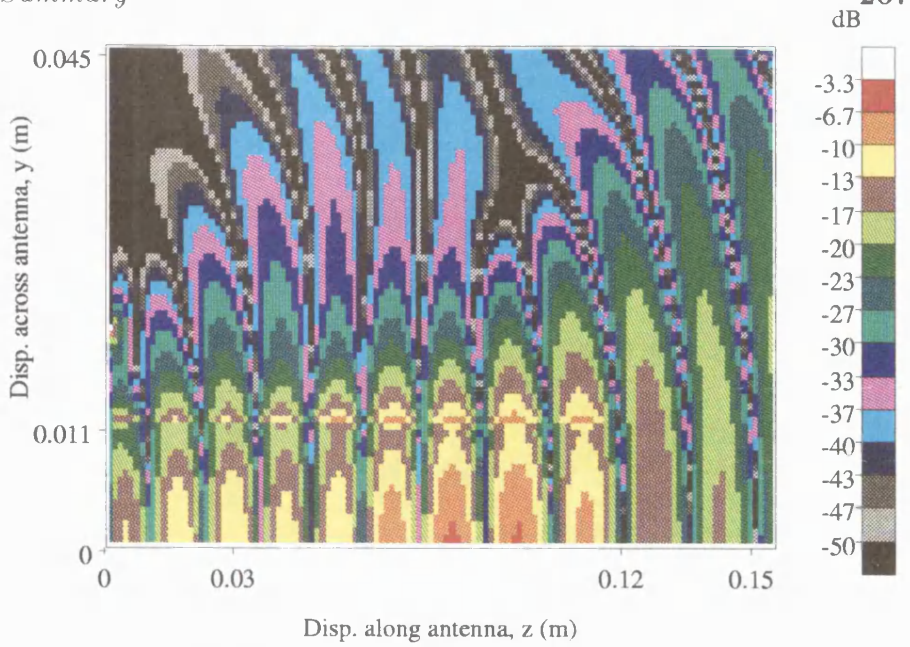

Figure 9.16: Medium plastic antenna at 10GHz. Frequency domain H_y on the aperture surface.

out during the measurements.

Thus, the material in this chapter and Chapter 8 indicates that details of the environment surrounding the antenna must be included in the theoretical models if highly accurate predictions are required. Such details are rather more straightforward to incorporate into FDTD than the H-guide model.

The performance of both the theoretical methods has been tested across a wide range of observation angles and agreement with measured values is generally good. Results for novel short shallow and deep structures have been presented. These antennas produce single broad beams, so may be suitable for application as elements in phased arrays. That said, the deep slot types appear to be more suitable for this application than the shallow slot structures as field leakage onto the ground plane is much less. Problems with cross coupling between array elements may be experienced if short shallow IDG-TSAs are used in an array.

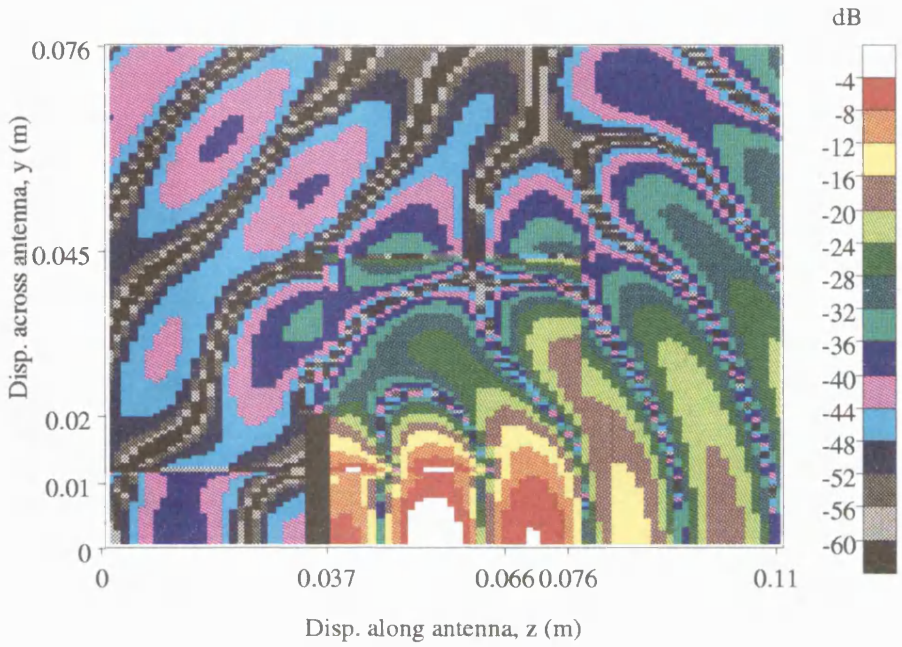

Figure 9.17: Short shallow antenna at 10GHz. Time domain H_y on the aperture surface.

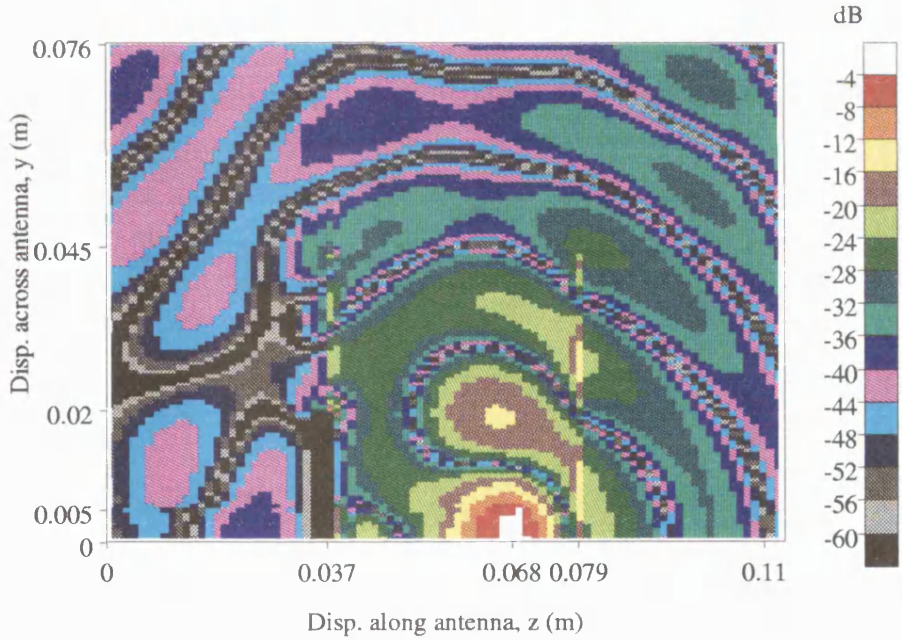

Figure 9.18: Short deep antenna at 10GHz. Time domain H_z on the aperture surface.

Chapter 10

Study of IDG-TSA Characteristics

In this chapter, a number of characteristics of the IDG-TSA are investigated through the medium of a variety of measured results. Firstly, transitions onto IDG are examined; new methods of feeding the IDG-TSA are introduced and their performance compared to RWG. Consideration is then given to the gain, input impedance, and radiation behaviour of the antenna with frequency. Previous work in this area is restricted to some input impedance, gain, and beamwidth results for long shallow antennas [3, 4]. Further, a first attempt at a novel dual polarised IDG-TSA is documented and some encouraging results from this are presented. In addition, a practical study of the fields on the antenna surface using probe measurements is given.

10.1 Transitions onto IDG

The small body of published work relating to transitions onto IDG was reviewed in Section 3.5. Only the RWG to shallow slot IDG junction has been fully char-

acterised experimentally [48]. Microstrip feeding of IDG has not previously been considered although the laying of metal strips on the IDG surface has been examined several times, as discussed in Section 2.1.3. In the present section a method of feeding IDG with microstrip is proposed. The design is empirical - no theoretical model of this junction has been developed - but is based on a knowledge of the fields of IDG and on the work carried out by Ma *et al.* [8, 9].

In [9], transverse metal strips are placed on the surface of deep slot IDG in order to couple to the strong electric field component across the slot and so act as dipole radiators. In [8], longitudinal strips are placed on the surface of shallow IDG to couple to the strong longitudinal electric field component. Thus, in order to feed deep slot guide a microstrip line can be laid across the IDG. To feed the shallow slot IDG, however, it has been found advantageous to fix the microstrip line onto the open end of the IDG rather than to lay the line longitudinally on the guide surface as suggested by Ma's work. This arrangement leads to easier development of the junction, as will be seen. A design for a shallow slot microstrip feed board is shown in Fig. 10.1.

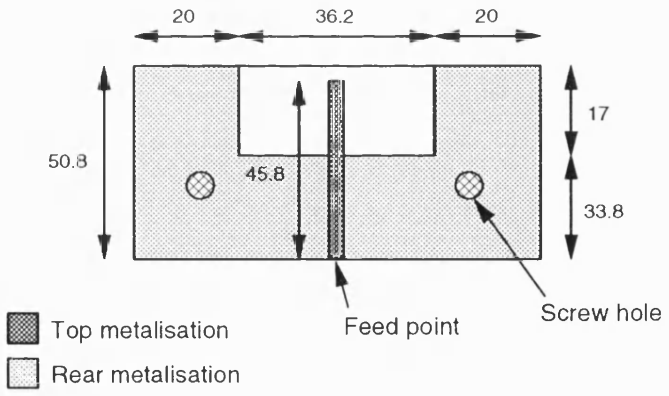

Figure 10.1: A microstrip feed board for shallow slot IDG.

This board is intended for feeding IDG which is 22.86mm wide by 10.16mm deep. It consists simply of a length of 50Ω microstrip line with a section of the metalisation on the rear of the board cut away. The rear metalisation contacts with the

metal face of the IDG end, whilst the cut-away section is in contact with the open dielectric end of the guide. The board is screwed onto the IDG using the same screw holes as utilised by the RWG feed. In reality the screw holes in the board have been enlarged to slots to allow various board positions to be tested. A deep slot feed board has been constructed and is very similar to the above, although a narrower board is used and the rear metalisation is removed across the full board width.

Experimental characterisation of the junction is performed by measuring the S-parameters of two sets of back-to-back transitions separated by different lengths of IDG, and by then applying a de-embedding procedure as described in Section 3.5.1.

Back-to-back measurements have been made with three types of feed; probe, microstrip, and RWG. The RWG configurations, both deep and shallow slot, are straightforward and need not be recorded, but the probe and microstrip arrangements are pictured in longitudinal cross section in Figures 10.2 and 10.3.

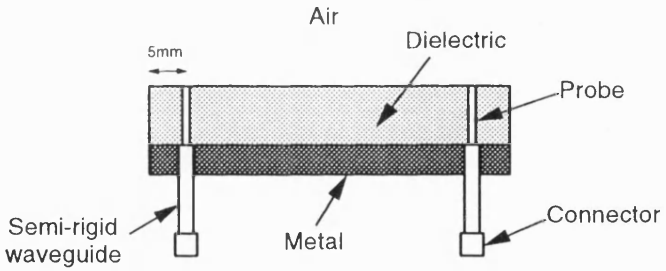

Figure 10.2: Shallow slot IDG: back-to-back measurements using probe feeds.

The probe feeds are simply lengths of semi-rigid waveguide with one end stripped back to leave the inner conductor exposed. The probes are fitted through holes drilled in the metal floor of the IDG and through the dielectric.

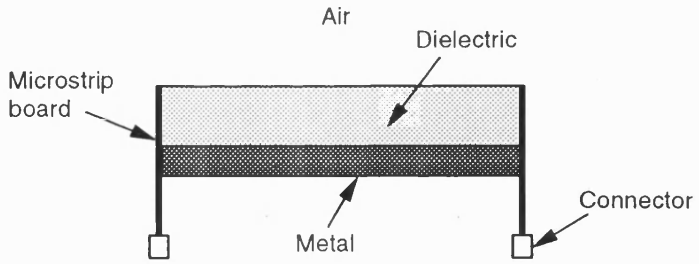

Figure 10.3: Shallow slot IDG: back-to-back measurements using microstrip feed boards. Retaining screws are not shown.

10.1.1 Measured Results - Shallow IDG

A number of back-to-back measurements have been taken for shallow slot IDG, with four feed arrangements.

1. Rectangular waveguide.
2. Microstrip, as pictured in Fig. 10.3.
3. Probe feed with IDG ends open, as shown in Fig. 10.2.
4. Probe feed with absorbing material covering the dielectric faces at the ends of the IDG.

The IDG in between the transitions has an ϵ_r of 2.08 and is 10.16mm deep by 22.86mm wide. The two lengths of IDG used for the measurements are 279mm and 285mm long, i.e. a separation of 6mm. It is important not to use very short lengths of guide between the transitions as this can lead to power coupling between the junctions directly, distorting the measurements. Values for the magnitudes of S_{21} and S_{11} between 7 and 12GHz have been extracted from the measurements and are plotted in Figures 10.4 and 10.5. The RWG results obtained here are similar to those presented by Stoiljković *et al.* in [48].

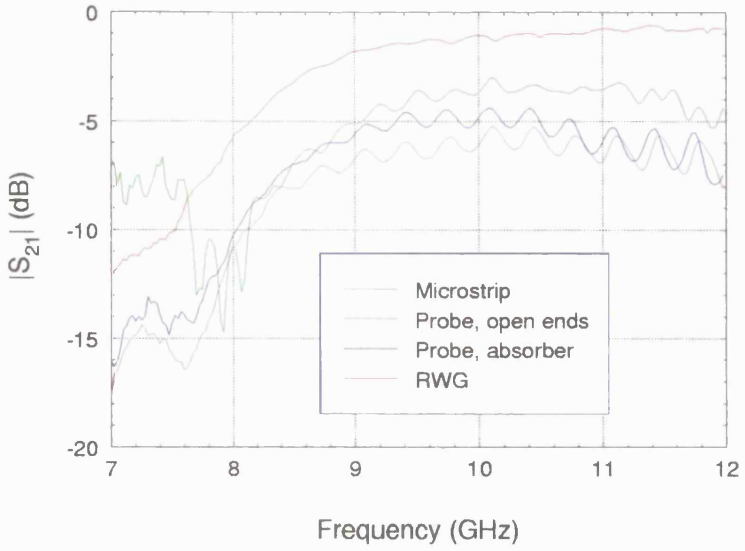

Figure 10.4: Comparison of measured $|S_{21}|$ for various transitions onto shallow IDG.

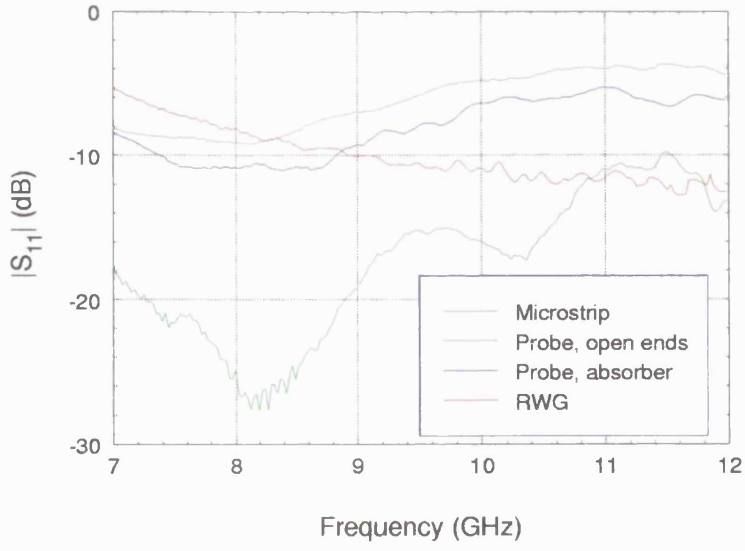

Figure 10.5: Comparison of measured $|S_{11}|$ for various transitions onto shallow IDG.

Considering first the results for $|S_{21}|$. As might be expected, the RWG feed is much more effective than the others at getting power into the guide across the whole frequency range. For all the feeds, transmission deteriorates below 9GHz. Above this threshold, though, RWG transmission is between -1dB and -2dB (i.e. 63% to 79%) whereas the next most effective feed, the microstrip, is between -3db and -4dB (i.e. 40% to 50%). The results for the probe are poor, the best results being around 32% transmission for the case where the IDG ends are covered with absorbing material.

Looking now at the $|S_{11}|$ plots of Fig. 10.5, poor results are again exhibited by the probe configuration. The microstrip feed shows the lowest reflection coefficient, but in the light of the above transmission results it is clear that this junction must be radiating to a much greater extent than the RWG/IDG junction. Given the rather open nature of the microstrip/IDG junction, it is encouraging that as much as 50% of the input power is coupling into the IDG.

Thus, a new way of feeding shallow slot IDG has been identified. Whilst the microstrip arrangement used here is not as efficient as feeding with RWG, its performance is sufficiently good to demonstrate the soundness of the technique. Besides having the obvious advantage of allowing integration with microstrip circuits, the use of the microstrip feed allows the IDG-TSA to have dimensions other than those matching standard rectangular waveguide. This feature is utilised in Section 10.7 where a design for a dual polarised structure is considered.

The board used here is an empirical design. Even without developing a theoretical model of the transition, there is the possibility of improving its performance through further experimental work using various different profiles for the metalisation on the top of the board instead of the basic 50Ω line of Fig. 10.1. Indeed, considerable variation in $|S_{21}|$ and $|S_{11}|$ can be achieved simply by varying the vertical position of the existing feed board. The extent of this variation is shown in Figures 10.6 and 10.7 on which the results for six board positions are recorded.

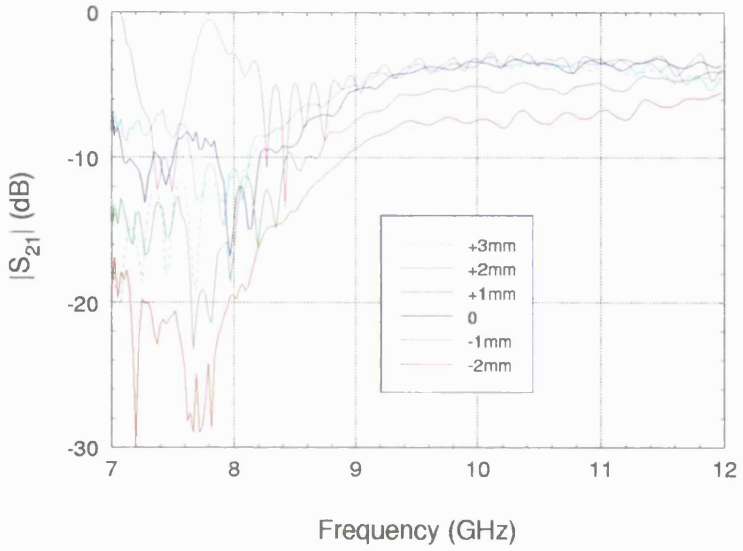

Figure 10.6: Variation of measured $|S_{21}|$ for microstrip fed shallow IDG achieved by moving the feed position.

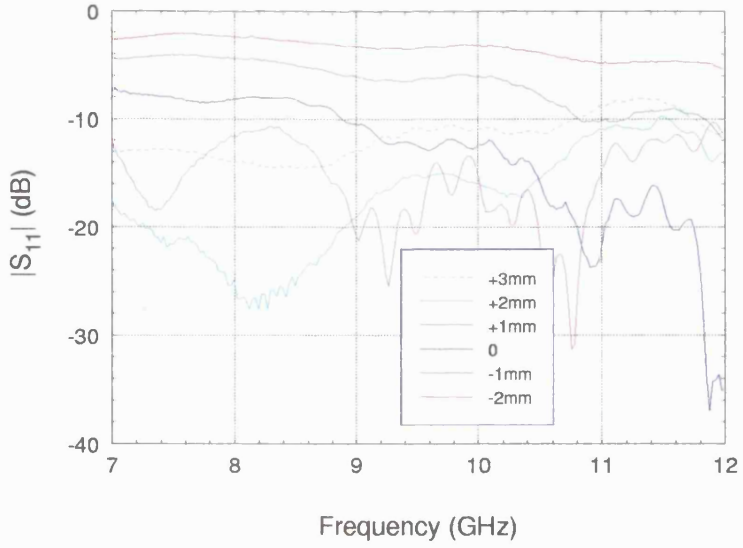

Figure 10.7: Variation of measured $|S_{11}|$ for microstrip fed shallow IDG achieved by moving the feed position.

In both plots the dark blue trace, labelled '0', relates to the situation where the top of the feed board is level with the surface of the IDG. The other traces are referred to this position. Note that the microstrip line itself ends 5mm away from the edge of the board. The lowest two positions, i.e. those with the least overlap between the microstrip and IDG end, can be seen at once to be of little use at these frequencies as they provide lower transmission and higher reflection than the other positions. For the remaining positions, it is interesting to note that $|S_{21}|$ over 9GHz varies only slightly as the board is moved. Under 9GHz, though, considerable variation is seen with the '+1mm' position appearing to offer improved performance.

A further advantage of the microstrip over the RWG feed is the possibility of using the antenna over a broader range of frequencies. Fig. 10.8 shows de-embedded S-parameters for the microstrip junction up to 20GHz.

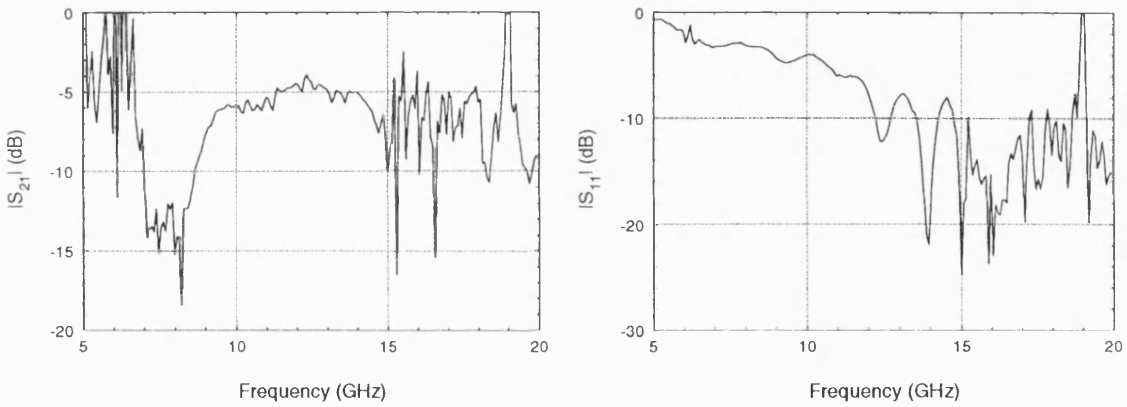

Figure 10.8: Measured (a) $|S_{21}|$, and (b) $|S_{11}|$ for microstrip to shallow IDG transition. Extended frequency range.

The board position here has been set to obtain the best results. The figures between 10 and 20GHz are reasonable, with $|S_{11}|$ generally lower than -10dB and $|S_{21}|$ around -5dB. Note that the first shallow slot mode does not start to propagate until approximately 7GHz so there is little transmission up to this frequency. The results are somewhat oscillatory. This could be due to error in the calculated propagation constants used in the de-embedding calculations. The cut-in of higher order modes at 10 and 17GHz may cause problems in this respect. In [135] Pennock *et al.*

conclude that separation differences in the lines used in the back-to-back measurements should be less than $\lambda_g/2$ to give the most accurate results, with $\lambda_g/4$ being the optimum difference required to minimise errors due to inaccurate propagation constant data. The 6mm separation used here is greater than $\lambda_g/2$ for frequencies above 18.5GHz and greater than $\lambda_g/4$ for frequencies above 10.6GHz. Pieces of IDG with less than 6mm separation are not currently available.

The results of Figures 10.4 and 10.5 indicate that the microstrip to IDG junction is radiative. An attempt has been made to reduce the radiation by building a stripline to IDG junction with a structure based on that of the well-known co-axial to RWG transition [136, 137]. The new junction consists of two boards pressed together to form a 50Ω stripline mated with the open end of the IDG in a similar manner to the microstrip to IDG junction. A 5.5mm shorted length of IDG (i.e. $\lambda_g/4$ at 11.3GHz, with $\epsilon_r = 2.3$) is then placed over the stripline to complete the junction. The physical structure of this transition is more satisfactory than the basic junction described above as better contact between the various components can be achieved due to the 'sandwich' construction. Only one of these junctions is currently available so de-embedding of its S-parameters is not possible. However, the effect of using one of these junctions in a back-to-back arrangement with a microstrip junction can be compared to the case where both transitions are of the microstrip type. This comparison is presented in Fig. 10.9.

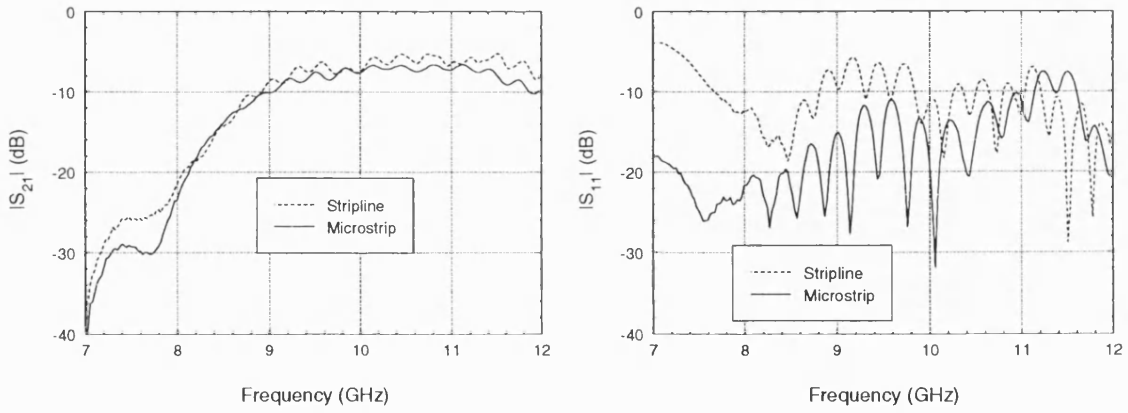

Figure 10.9: Measured (a) $|S_{21}|$, and (b) $|S_{11}|$ for back-to-back transition onto shallow IDG. Effect of replacing one microstrip transition with a stripline transition.

The use of the stripline junction in the place of one of the microstrip junctions can be seen to have generally increased $|S_{11}|$. This is not necessarily a negative result as the $|S_{21}|$ figures show that more of the power entering the junction is transmitted to the other end of the line rather than being radiated. The stripline feed, therefore, represents an improvement over the microstrip feed. The extent of this improvement is investigated further in the radiation measurements of Section 10.4.

10.1.2 Measured Results - Deep IDG

The focus of this work has been the feeding of shallow slot IDG. However, microstrip excitation of the LSE mode is given some consideration in Section 10.7 where a dual polarised structure is considered. In this section, RWG feeding of a deep slot is considered. De-embedded S-parameters from back-to-back measurements (with 486mm and 476mm IDG lengths) are shown in Fig. 10.10.

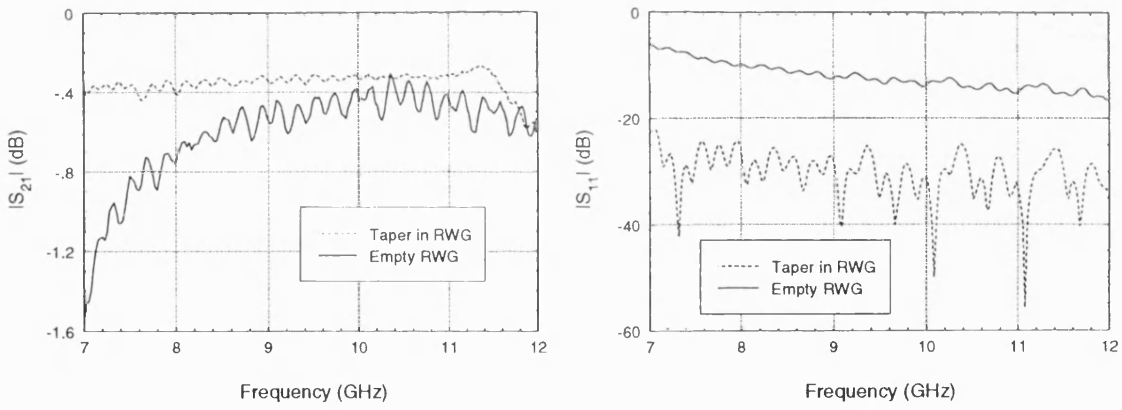

Figure 10.10: Measured (a) $|S_{21}|$, and (b) $|S_{11}|$ for RWG to deep IDG transitions.

The guide used here has an ϵ_r of 2.08 and is 10.16mm wide by 15mm deep. In the figure the case with an empty feed waveguide is compared to that with a dielectric taper discontinuity minimiser fitted in the guide, the use of which was first proposed by Rozzi and Hedges [6]. Without the taper, the transmission and reflection are good, better than the shallow slot data given in Figures 10.4 and 10.5. With the taper fitted the results are improved, producing a very efficient transition. This

good match compared to the shallow slot case can be explained by considering the FDTD IDG field plots presented in Section 5.2.2. The LSE fields are similar to those in one half of a rectangular waveguide, leading to a smooth transition and good coupling, whereas no such relationship exists in the LSM case.

10.2 IDG-TSA Input Impedance

The results of the previous sections demonstrate that most of the feed transitions with which this work is concerned are radiative. As such, measurements of the input impedance of IDG-TSAs are less useful than they might be for antennas which exhibit minimal feed radiation. Even so, such measurements still provide useful information and are a first step in determining whether a particular feed/antenna combination is viable.

Fig. 10.11 displays $|S_{11}|$ data for four shallow slot antennas. Note that this figure is concerned only with RWG fed structures. Details of the antennas used here are given in Section 7.2.

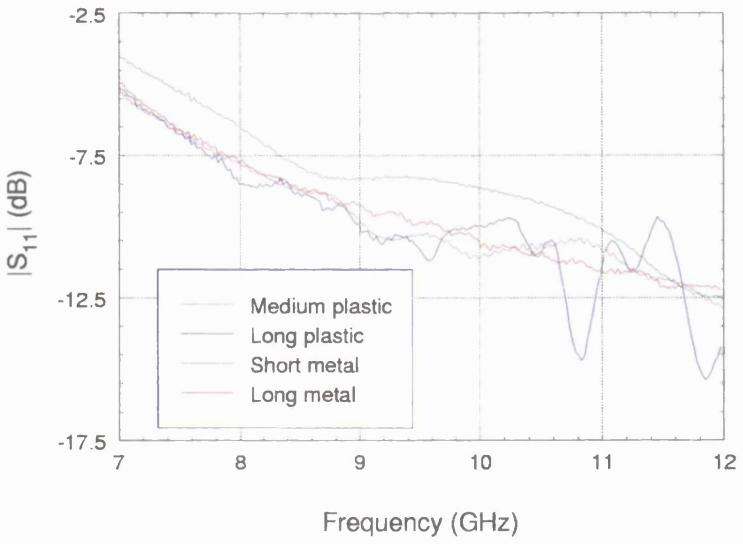

Figure 10.11: RWG fed shallow slot IDG-TSA measured input impedances.

The results shown in the figure show a reasonable match for the long antennas,

for which $|S_{11}|$ is lower than -10dB for frequencies over 9.5GHz. The results for the long plastic and long metal antennas are close, demonstrating the usefulness of the plastic build technique. The increased variations at higher frequencies for the plastic antenna may be due to the reduced uniformity of the structure.

The results for the short metal antenna show a higher reflection coefficient than for the long structures, reducing below -10dB only at 11GHz. This is to be expected as the short structure is a very much sharper discontinuity than the long antenna, tapering from 10.16mm deep to zero over 30mm rather than 300mm. The medium plastic antenna exhibits better reflection properties than the short metal. This improvement is most probably due to the section of uniform IDG included in the plastic design which serves to lessen, or distribute, the discontinuity.

Figures 10.12 and 10.13 show $|S_{11}|$ for the long and short metal antennas for RWG, stripline, and two positions of the microstrip feed.

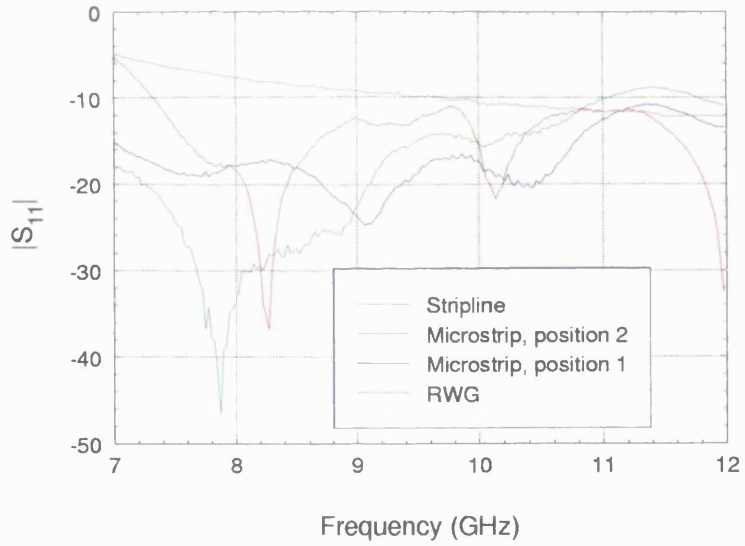

Figure 10.12: Measured input impedance of long metal shallow antenna with RWG, microstrip, and stripline feeds.

All the strip feeds offer lower $|S_{11}|$ than the RWG feed, but the results of the previous section indicate that a higher proportion of the power entering the strip feeds is radiated than is the case for the RWG feed. The stripline feed result is

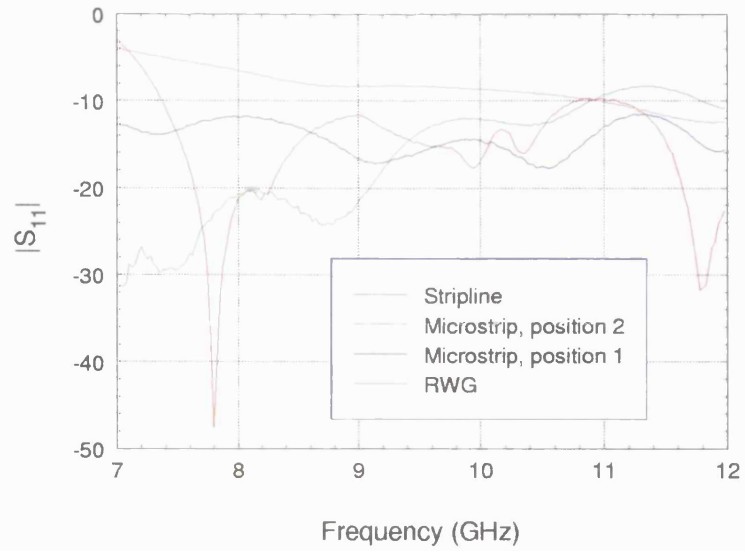

Figure 10.13: Measured input impedance of short metal shallow antenna with RWG, microstrip, and stripline feeds.

encouraging in that this feed is known to couple more power into the IDG than the microstrip.

Finally, Fig. 10.14 shows $|S_{11}|$ for RWG fed deep slot antennas. The figures also show the effect of inserting a dielectric taper into the feed waveguide. Even without the taper, the $|S_{11}|$ of the long antenna is lower than the shallow case, with the taper lowering it still further. The short antenna shows a comparatively poor match, even with the taper fitted, due to the sharp discontinuity presented by this antenna (which tapers from 22.86mm deep to zero over a length of 30mm).

10.3 IDG-TSA Gain

Further information on the performance of both the antenna and the feed can be obtained by measuring the gain. For instance, as the various antennas considered in this section are fed with the same input power, the results give some indication of the antenna efficiency. The gain is calculated using the well-known radar equation. This equation assumes a configuration of two antennas with gain G_1 and G_2

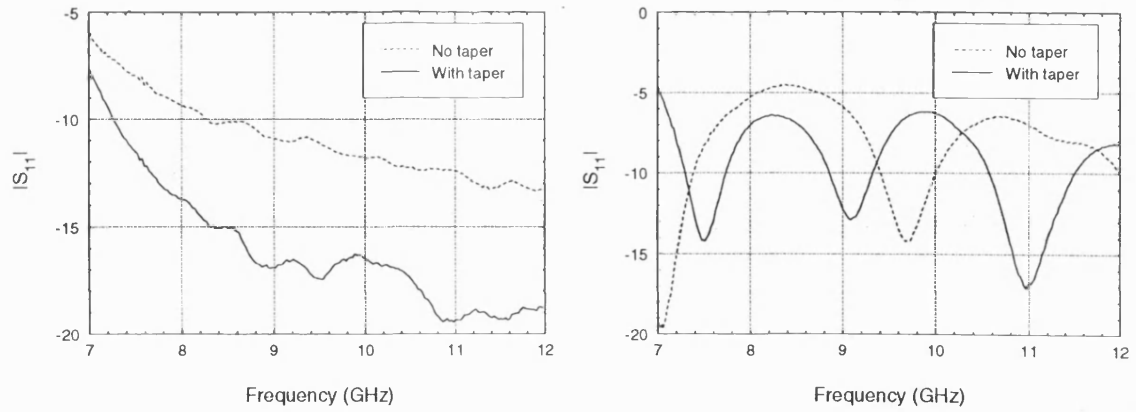

Figure 10.14: Measured input impedance of (a) long, and (b) short deep antennas with and without a dielectric taper fitted into the feed RWG.

separated by a distance S. The antenna with gain G_1 receives power P_R from the antenna with gain G_2, which transmits power P_T:

$$\frac{P_R}{P_T} = \left(\frac{\lambda}{4\pi S}\right)^2 G_1 G_2 \tag{10.1}$$

If the antennas are the same then $G_1 = G_2 = G$ and:

$$\frac{P_R}{P_T} = \left(\frac{\lambda}{4\pi S}\right)^2 G^2 \tag{10.2}$$

The transmitted and received powers are measured using a power meter; a Boonton Model 4220A RF Power Meter connected to a Boonton Model 51072 Power Sensor. The first task is to measure the gain of the X-band horn used as the transmitter for the IDG-TSA measurements. Using two such horns the results in Fig. 10.15 are obtained. Part (a) of this figure shows the horn gain, whilst part (b) shows the offset that will later be subtracted from IDG-TSA radiation measurements in order to compensate for the gain of the transmit antenna.

Having established G_2 in equation (10.1) the gain of any receiving antenna can now be measured. Fig. 10.16 shows the gain of three RWG fed shallow antennas; long

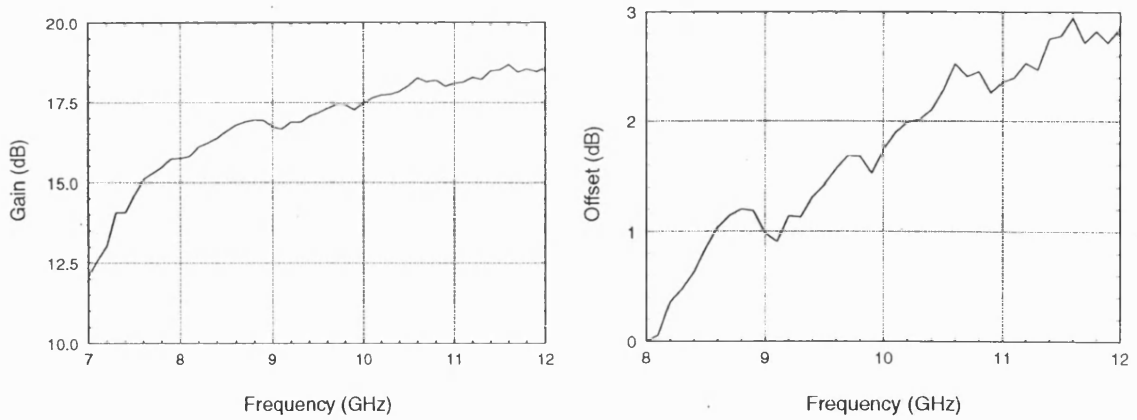

Figure 10.15: (a) Measured gain of waveguide horn, and (b) Offset to be subtracted from measured radiation patterns to compensate for variations in horn gain with frequency.

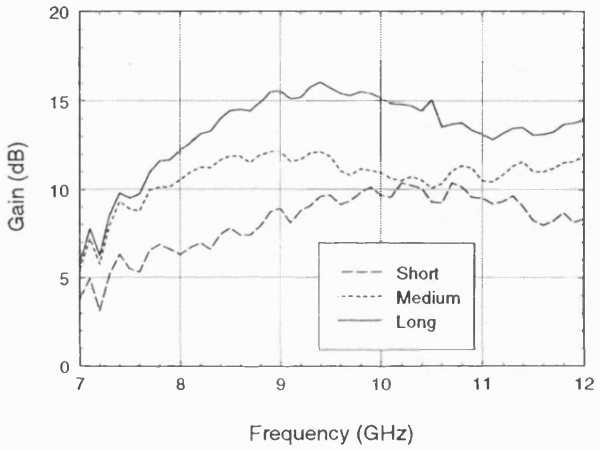

Figure 10.16: Measured gain of shallow antennas with RWG feed.

and short metal and medium plastic. The long antenna produces a moderate gain peaking around 16dB, the short metal antenna produces lower gain, peaking at around 10dB. The medium plastic antenna is in fact a much longer structure than the short metal antenna, with 30mm of uniform IDG and an additional 20mm of ground plane, all of which contributes to the radiation and leads to a higher gain.

The gain of microstrip fed shallow structures is given in Fig. 10.17. As anticipated, the microstrip fed structure exhibits lower gain, although the long antenna still shows reasonable figures between 9 and 10GHz. The results for the stripline feed show a significant improvement on those for the microstrip feed. The measurements

of Section 10.1.1 suggest that the stripline feed is more efficient at coupling power into IDG; the current results demonstrate clearly that this is indeed the case. In fact, for a small number of frequencies the gain of stripline fed structures equals or exceeds that of RWG fed structures.

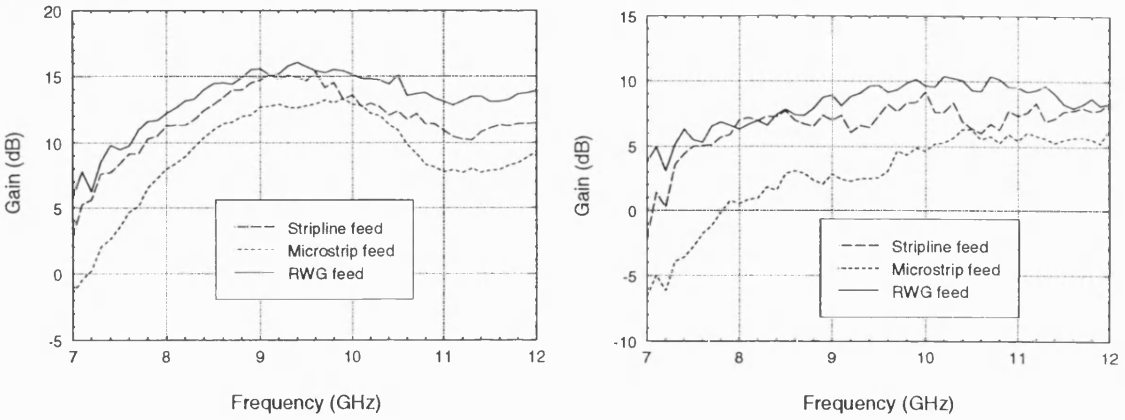

Figure 10.17: Measured gain for shallow antennas with RWG, stripline, and microstrip feeds: (a) long antenna, and (b) short antenna.

Fig. 10.18 shows the gain of long and short RWG fed deep antennas. The gain of these structures is well below that shown by their shallow counterparts. In the previous section, the high $|S_{11}|$ of the short deep antenna was noted and this poor figure is reflected in the gain results. It will be recalled from Chapter 7 that the radiation pattern of the long LSE antenna contains only a few lobes, some of which are of similar magnitude. As such the input power is split between two or more beams so that high gain is not to be expected. Some of the features of these results can be explained by considering Figures 10.28 and 10.29, where the high degree of mobility of the main beams compared to the shallow slot case (Figures 10.25 and 10.26) can be seen clearly, together with the existence of three 'main' beams. In the short antenna gain results, the higher gain at lower frequencies can be seen to be linked to a shift in the position of the main radiated beam. The long antenna gain is low at lower frequencies but increases markedly after 9.5GHz when one of the three main beams drops away.

In performing the gain measurements, it was necessary to move the antenna posi-

tion much more frequently for the deep structure than for the shallow in order to take readings at the main beam maximum. These frequent realignments are visible in the more oscillatory nature of the deep slot gain results.

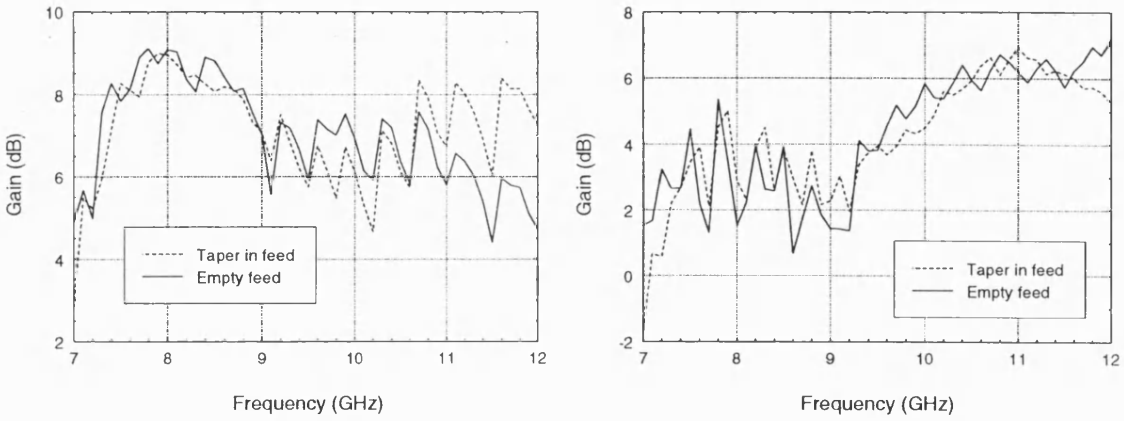

Figure 10.18: Measured gain for deep antennas with RWG feed: (a) long antenna, and (b) short antenna.

A potential source of inaccuracy in the measurements for the long antennas lies in the fact that the anechoic chamber available for this work may be too small for measurements to be taken in the Fraunhofer region of the antennas' radiation pattern. An antenna separation of $2d^2/\lambda_0$, where d is the greatest aperture dimension of the antenna, is usually assumed to be required for far-field measurements to be taken. This criteria cannot be met for the long antennas. This comment can be applied equally to the measurement of radiation patterns, the theoretical predictions for which assume far-field operation. However, if the main radiating section of the long antenna is considered as being rather less than the physical length of the aperture, as suggested by the work presented in Chapter 6, then the above may not represent a problem.

10.4 The Radiation Behaviour of Shallow Slot Feeds

The transition measurements of Section 10.1.1 indicate that the microstrip shallow IDG feed is much more radiative than the RWG feed. The stripline feed was proposed as a means of reducing this radiation, and back-to-back transition measurements suggested that this objective had been achieved. The gain measurements presented above support this conclusion. In this section, the behaviour of these feeds is scrutinised further using radiation measurements.

For the long and short shallow metal antennas, elevation plane radiation pattern measurements have been taken over the complete 360° range so that the backward radiation can be examined. Measurements have been obtained for the RWG, microstrip, and stripline feeds in 1GHz steps from 8GHz to 12GHz inclusive. The results are presented in Figures 10.19 to 10.21 for the long antenna and in Figures 10.22 to 10.24 for the short antenna.

In these figures 0°, coinciding with the antenna surface, is defined from the right hand horizontal axis. Thus, the top right quadrant of each figure shows the forward radiation above the plane in which the aperture sits, the lower right quadrant shows the forward radiation below this plane. The top left quadrant depicts backward radiation directed upwards from the antenna and the lower left quadrant shows backward radiation directed below the level of the antenna surface.

The first important point to note from the results is the magnitude of the backward radiation produced by each of the feeds. The microstrip feed radiates in this direction to a considerable degree. Indeed, in the case of the lower gain short antenna the peak of the forward radiation is only just greater than that of the reverse radiation; the 8GHz result is the best example of this.

The RWG radiates the least power backwards but it is interesting to note how

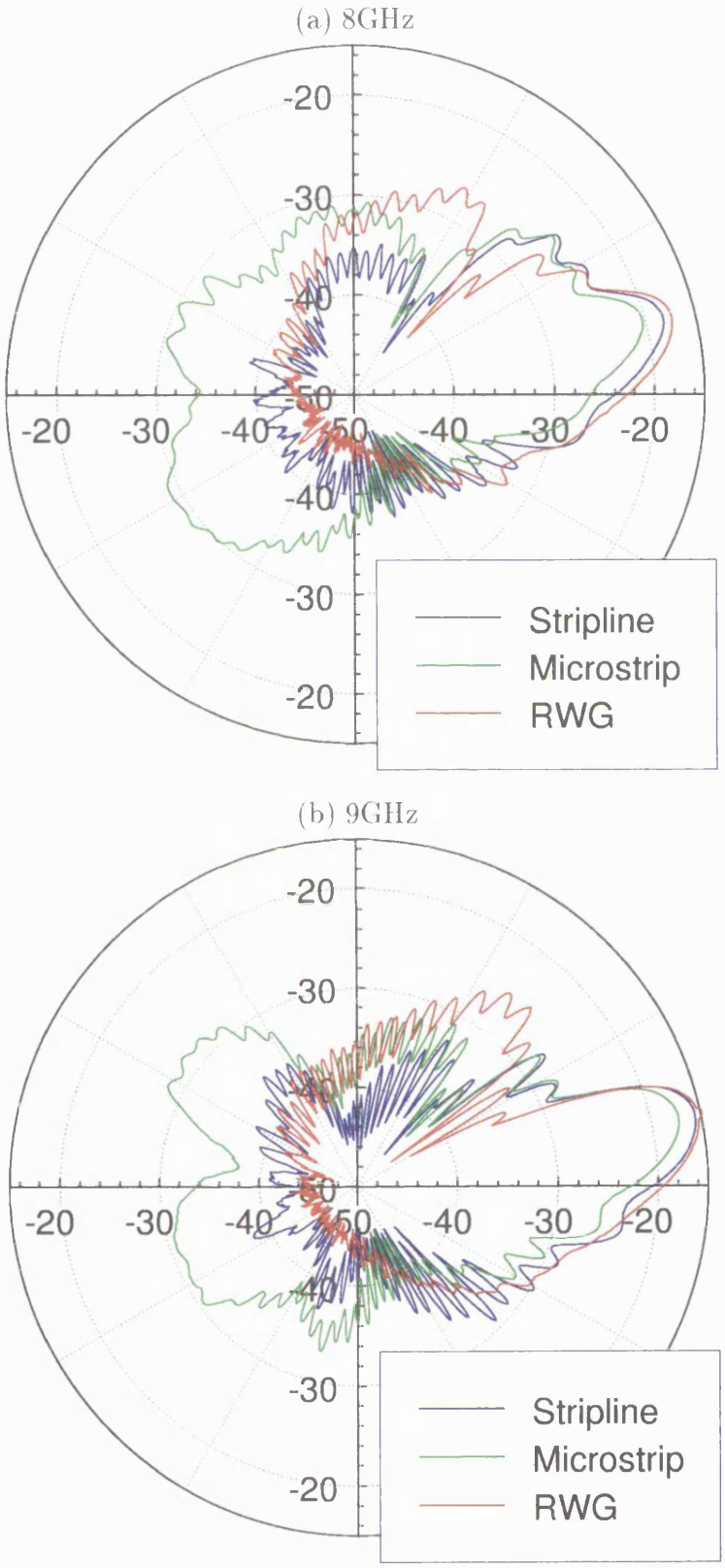

Figure 10.19: Comparison of long shallow antenna feeds.

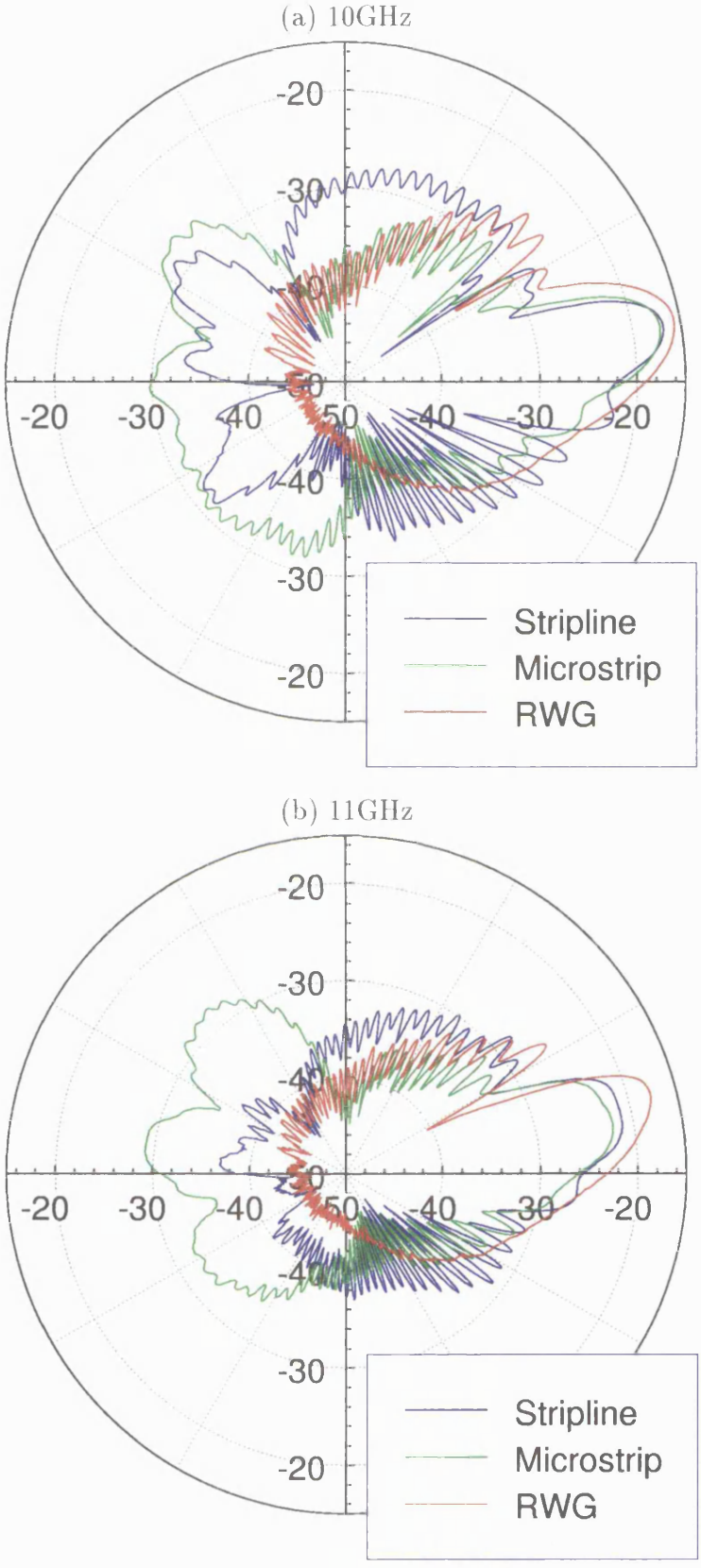

Figure 10.20: Comparison of long shallow antenna feeds.

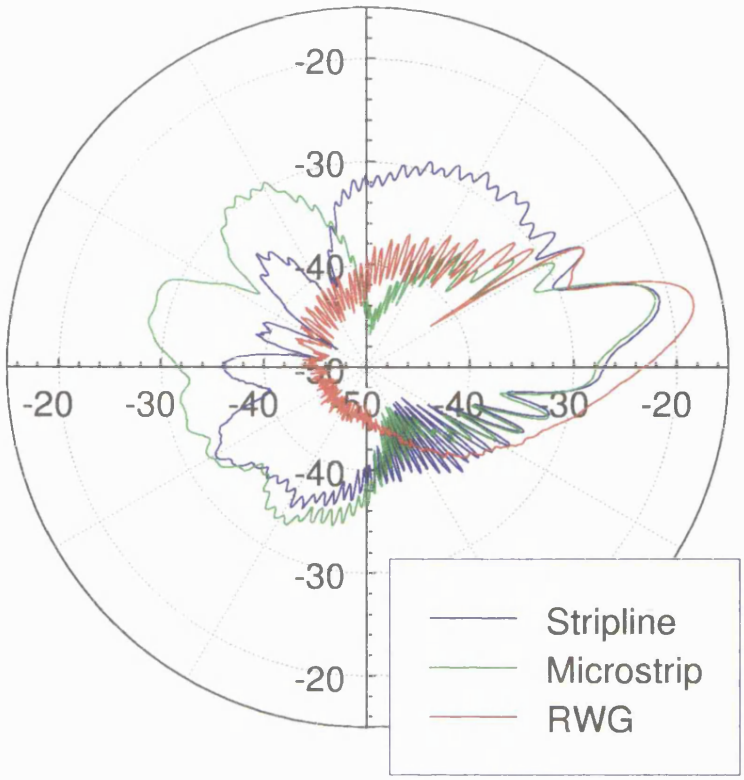

Figure 10.21: Comparison of long shallow antenna feeds at 12GHz.

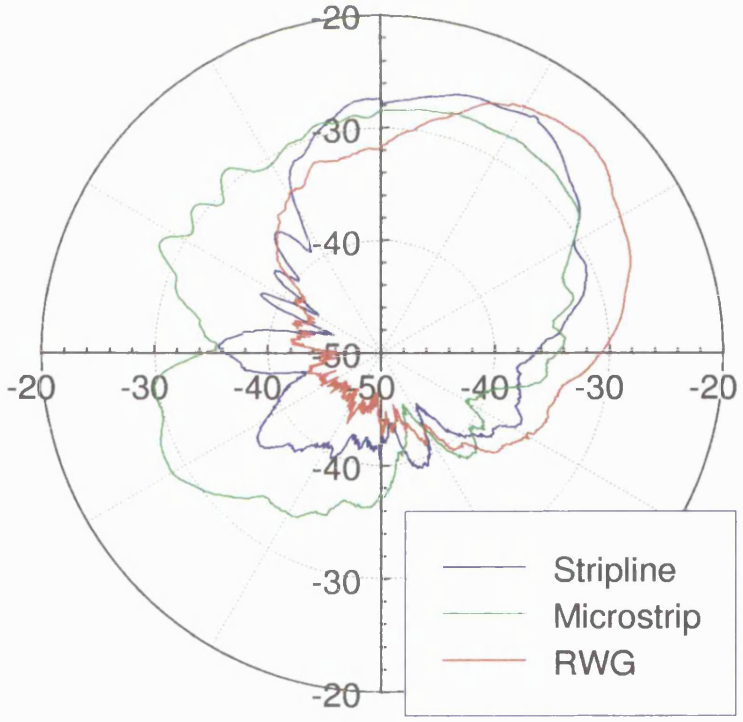

Figure 10.22: Comparison of short shallow antenna feeds at 8GHz.

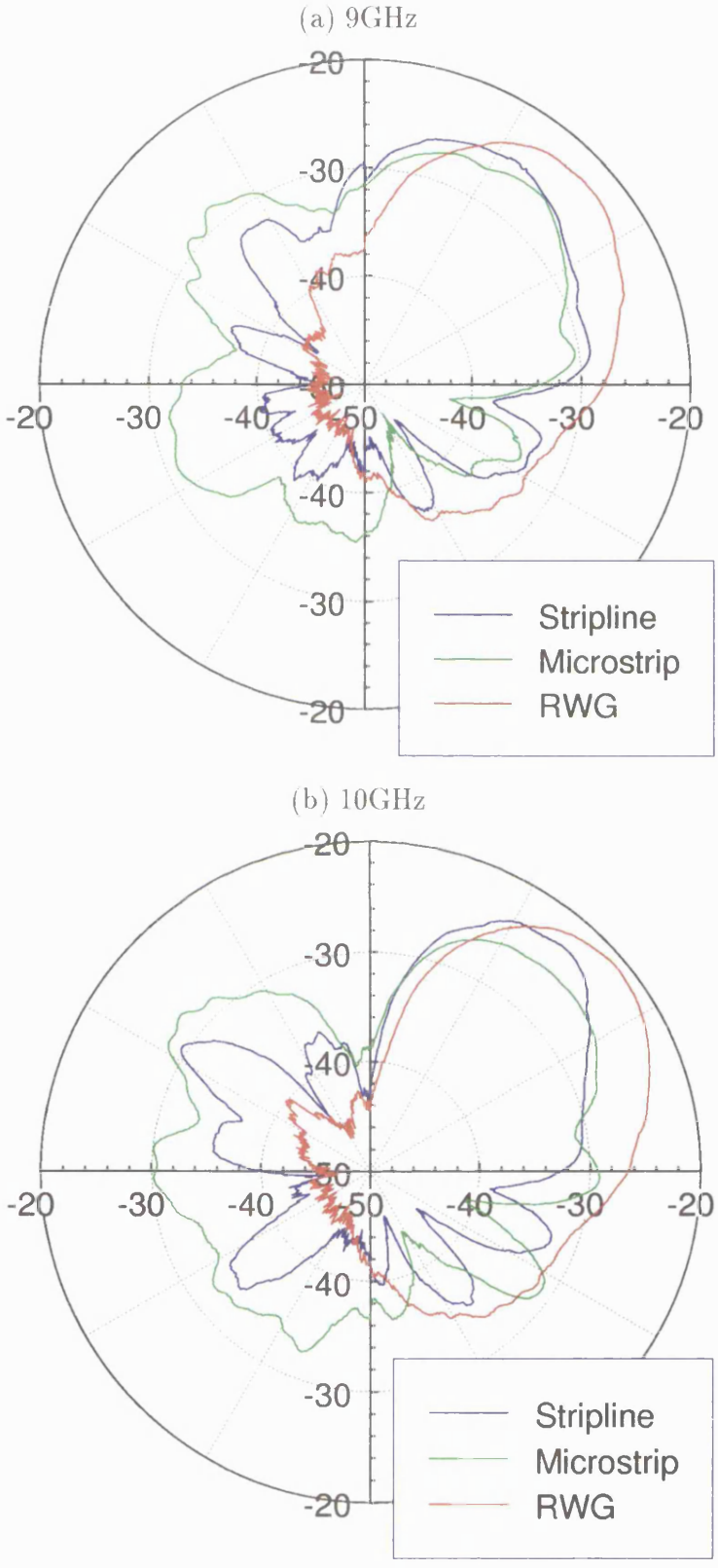

Figure 10.23: Comparison of short shallow antenna feeds.

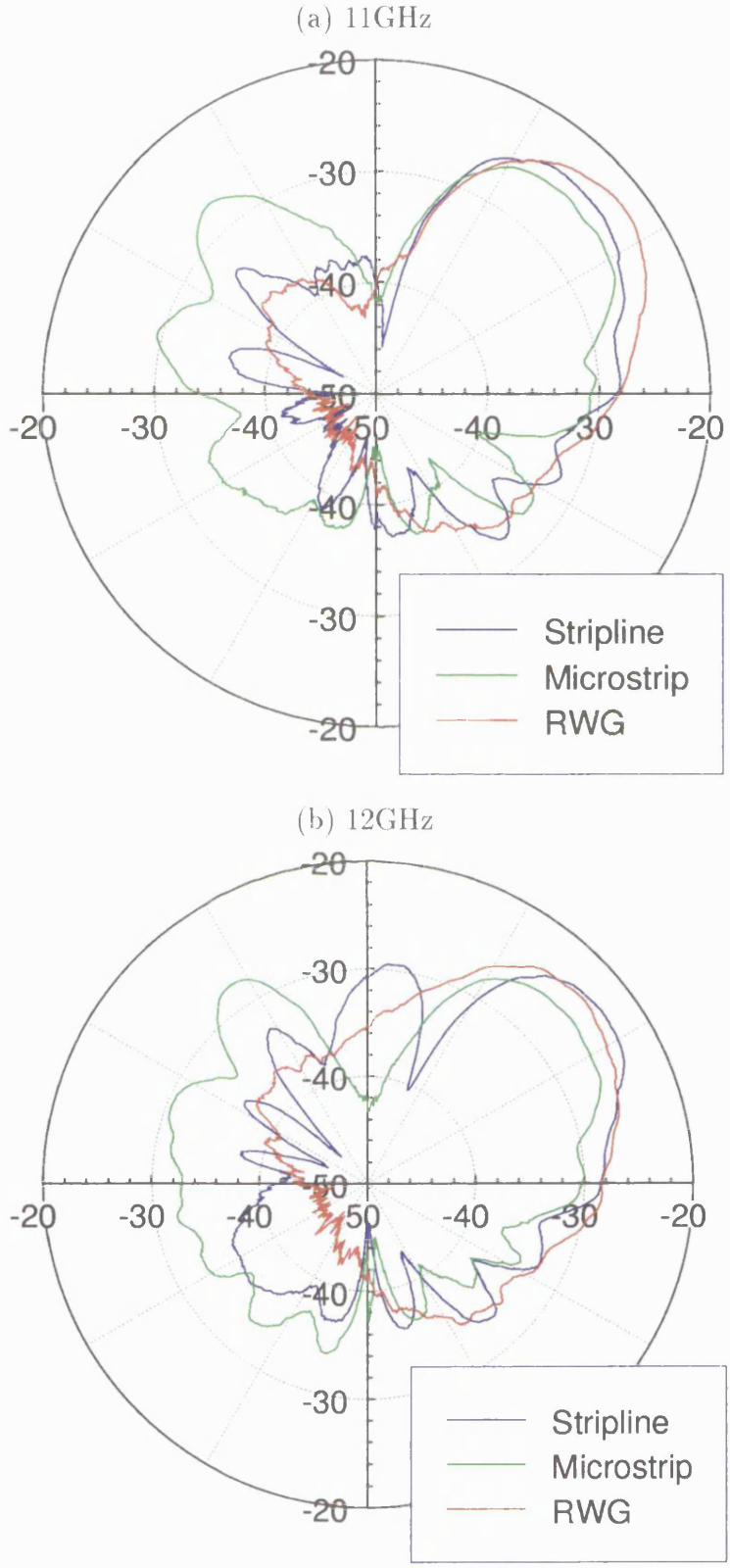

Figure 10.24: Comparison of short shallow antenna feeds.

effective the stripline feed is at cutting the reverse radiation. For both antennas the results at 8, 9, and 11GHz are particularly good in this respect.

As a result of the amount of power that it is spreading behind the antenna, the microstrip feed produces the minimum peak radiation in the forward direction. Conversely, the RWG feed produces, almost uniformly, the maximum peak forward radiation. Again, though, the stripline feed performs well, particularly at certain frequencies. For the long antenna the 8 and 9GHz results are good, there being little to choose between the RWG and stripline feeds in the latter case. For the short antenna, the stripline feed performs particularly well at 12GHz where its peak radiation exceeds that of the RWG fed structure, due largely to the slightly different beam shape.

So it can be seen that the stripline feed offers a viable alternative to RWG. With further development it is anticipated that the performance of this feeding structure could be improved still further.

As an aside, the results in this section highlight one of the difficulties encountered when trying to produce theoretical models for prediction of the radiation characteristics of the IDG-TSA; the feed radiation affects the overall radiation pattern in a manner that is very difficult to characterise analytically.

10.5 IDG-TSA Radiation Behaviour with Frequency

In this section measurements depicting IDG-TSA radiation behaviour over the 8 to 12GHz frequency range are presented. These results are presented here as a reference, to highlight general trends that are not apparent from single frequency results of the type given in Chapters 7 and 8, and in all previously published work. For all the results in this section, measurements are spaced at 0.1GHz intervals.

In Fig. 10.25(a) the behaviour of the elevation plane radiation pattern of a long shallow slot IDG-TSA is shown.

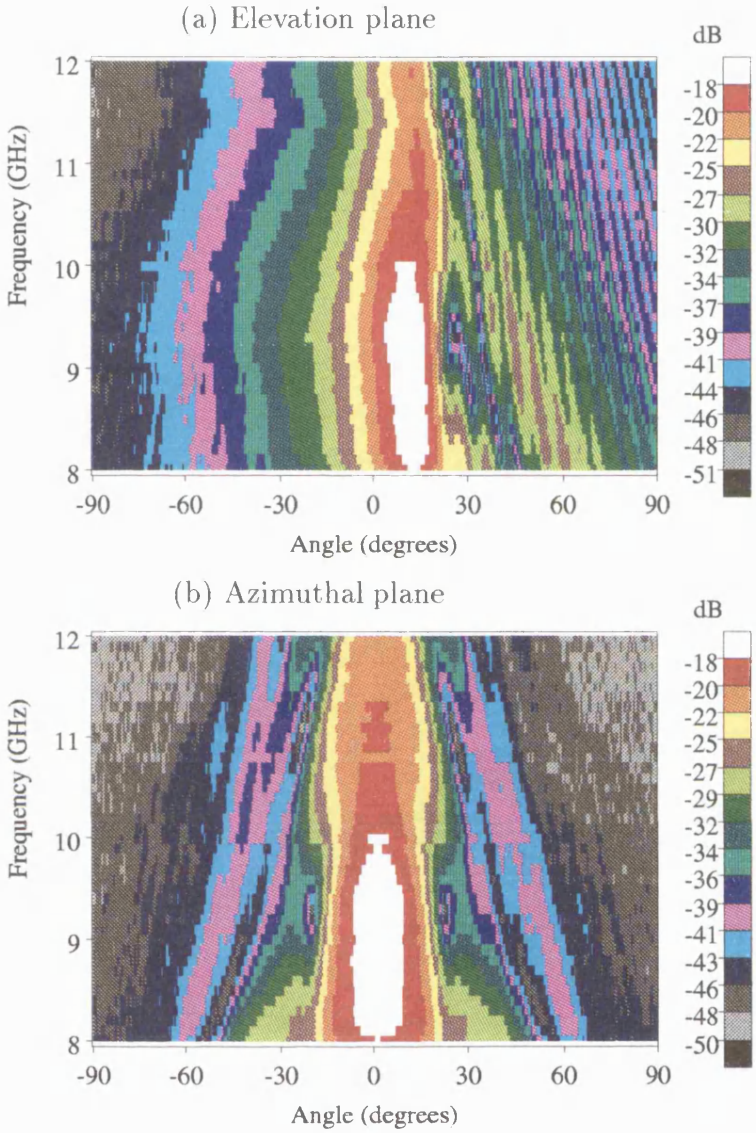

Figure 10.25: Long shallow antenna: variation of radiation pattern with frequency, incorporating compensation for measurement system gain. Elevation is fixed at 13° for azimuthal plane data.

Only the forward radiation is considered, with 0° being defined from the aperture surface so that negative angles relate to radiation below the level of the aperture and positive angles relate to that above it. These results have had the offset due to the gain of the measuring system, as shown in Fig. 10.15(b), removed from them so that they reflect the true gain of the IDG-TSA. The antenna gain can be seen to

reduce after 10GHz. The increase in the number of sidelobes and the reduction in the amount of power being directed into them is clear from the plot. Fig. 10.25(b) shows the azimuthal pattern for the same antenna. These results were measured at an elevation angle of 13°, which is at or close to the maximum of the elevation pattern.

Fig. 10.26 shows similar plots for a short shallow antenna. The same features are in evidence here as were observed above, but here the main beam is much wider in both dimensions. In the azimuthal plane there is some oscillation evident in the vicinity of the peak value causing the rather broken up effect between 8 and 9GHz.

In Fig. 10.27 the elevation and azimuthal plane 3dB beamwidths are extracted from the above data. The short antenna produces a considerably wider beam than the long, with nearly constant dimensions of 40° by 50° from 9.5 to 12GHz. The results of Section 10.3 show that the short antenna gain is also nearly constant across this frequency range. The long antenna beamwidths are rather more variable, as anticipated by the theoretical results of Chapter 7, in Sections 7.6 and 7.7 for example. The beamwidths can be seen to be in general agreement with theoretical predictions if the results of Section 9.3 are considered, showing radiation patterns over a broad angular range.

The variation with frequency of the elevation plane patterns of long and short deep slot antennas are studied in Figures 10.28 and 10.29. These show interesting features that differentiate them from the shallow slot structures. For the long antenna the radiated power is split between two or even three beams, with the position of the main beam jumping to over 30° above 10GHz. The FDTD results of Section 8.3 are in general agreement with these results in that they show two or three main beams whose relative magnitudes vary significantly with frequency. The same drawing in of the sidelobes with frequency can be seen here as was observed for the shallow structure, but the radiation below the level of the aperture (-90° to 0°) is much less.

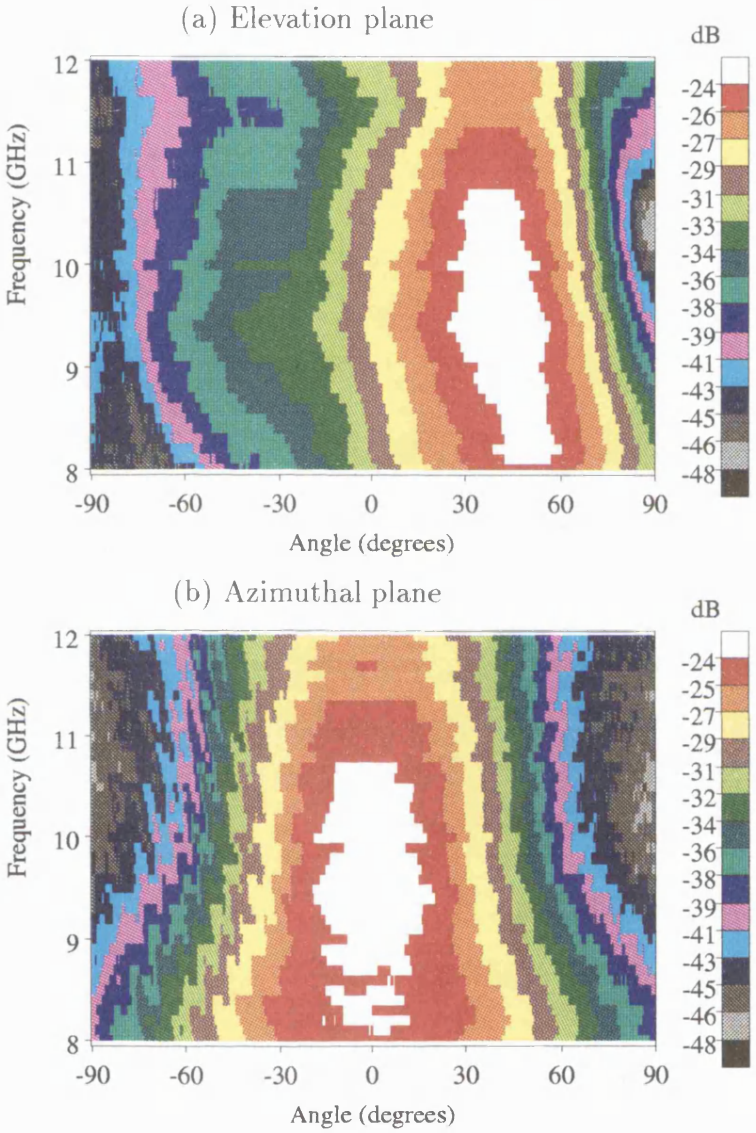

Figure 10.26: Short shallow antenna: variation of radiation pattern with frequency, incorporating compensation for measurement system gain. Elevation is fixed at 40° for azimuthal plane data.

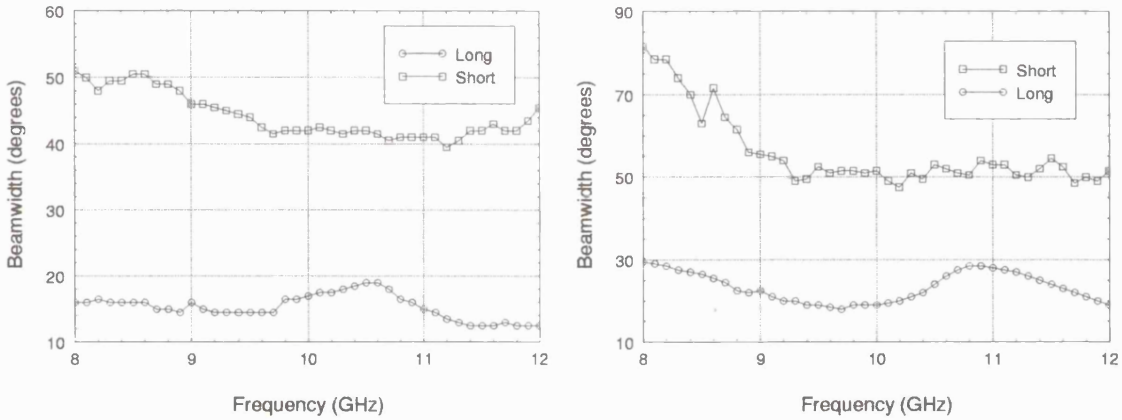

Figure 10.27: Measured 3dB beamwidths for long and short shallow antennas: (a) elevation plane, and (b) azimuthal plane.

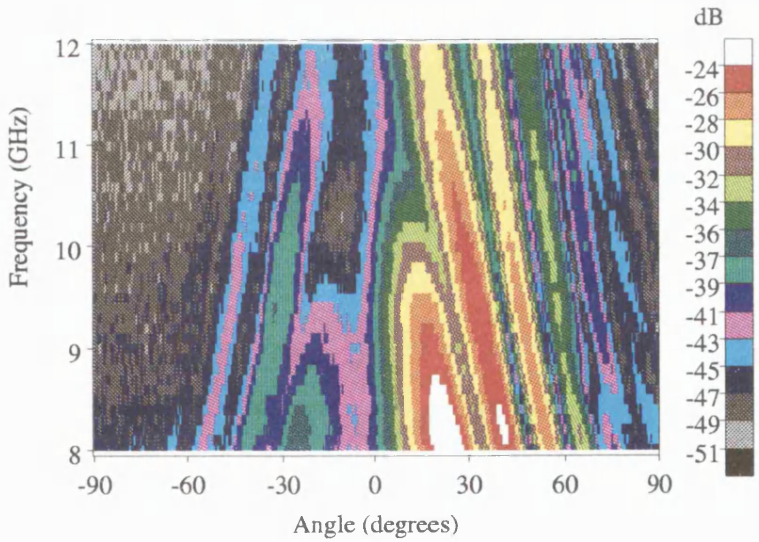

Figure 10.28: Long deep antenna: variation of elevation pattern with frequency, incorporating compensation for measurement system gain.

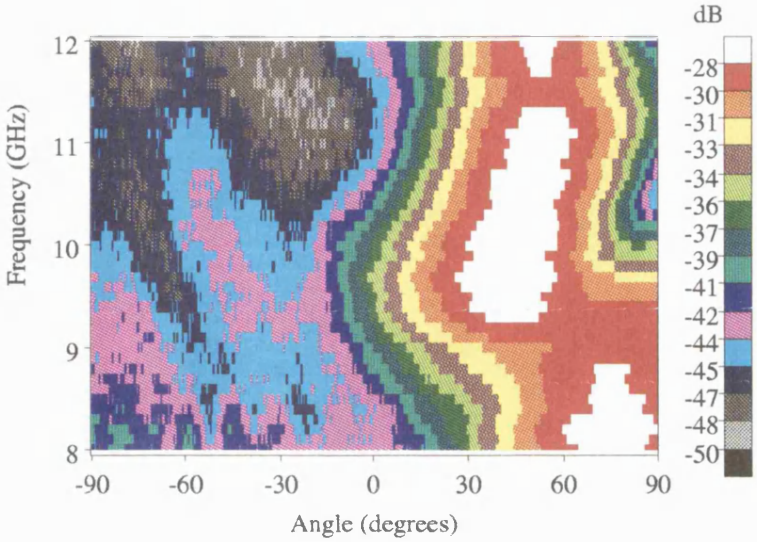

Figure 10.29: Short deep antenna: variation of elevation pattern with frequency, incorporating compensation for measurement system gain.

The short deep antenna exhibits a significant jump in the position of the main beam as the frequency is increased; this time the shift occurs above 9GHz, and in this case the gain does not decrease at the top of the frequency band. Although FDTD successfully predicts this jump in the position of the main beam, it was noted in Section 9.3 that it does not accurately predict the frequency at which the transition takes place.

10.6 IDG-TSA Polarisation Properties

The pure polarisation properties of IDG have been mentioned already in this thesis, in Section 7.4 for example. It has been claimed that shallow slot (LSM) IDG-TSAs produce nearly pure vertically polarised radiation whilst deep slot (LSE) IDG-TSAs give nearly pure horizontally polarised radiation. In this section measurements are presented which justify these claims. Results are given for the 'extremes' of antenna geometry that have already been considered in the foregoing sections, i.e. very short and very long shallow and deep structures. This section deals exclusively

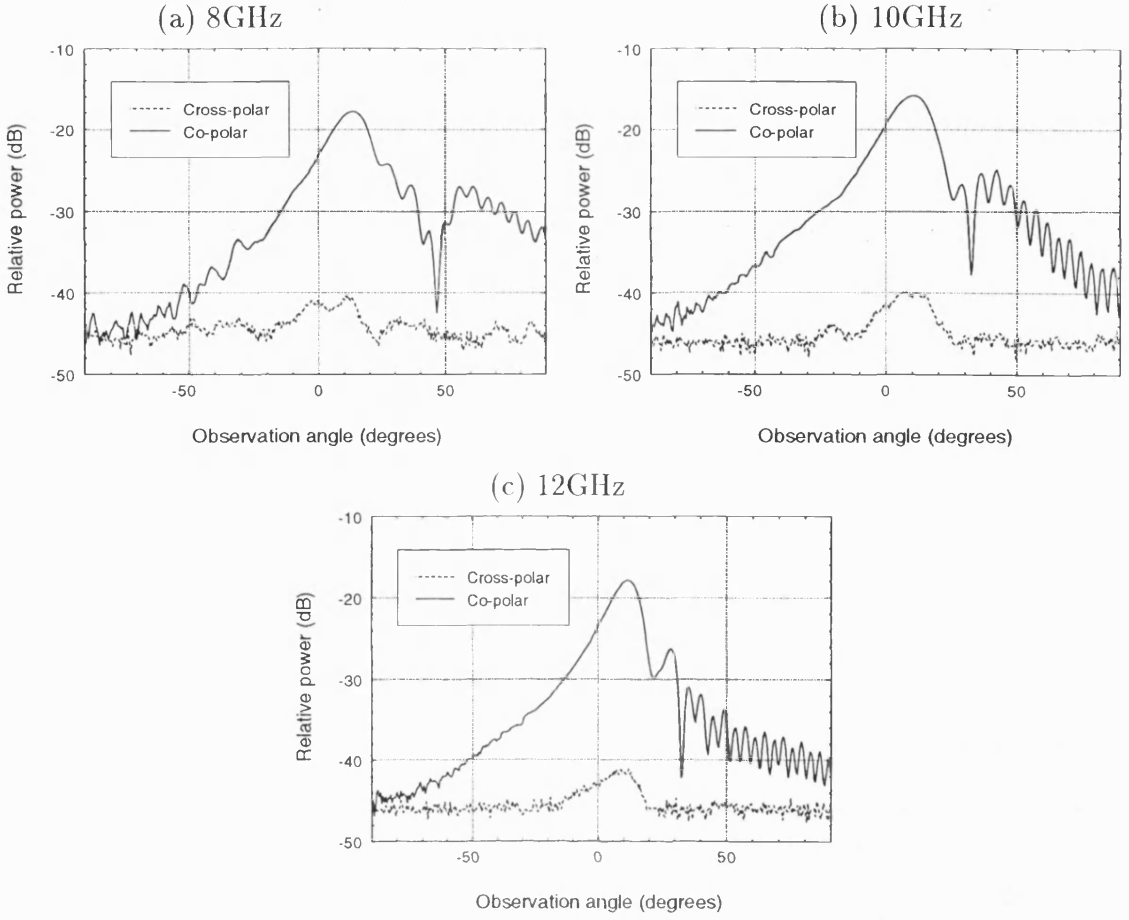

Figure 10.30: Measured co-polarised and cross-polarised elevation plane patterns for a long shallow slot antenna.

with RWG fed structures.

Long and short shallow IDG-TSAs are considered in Figures 10.30 and 10.31 at 8, 10, and 12GHz.

The figures show the elevation plane radiation patterns measured between -90° and 90° using transmitting waveguide horns oriented both parallel and perpendicular to the long dimension of the slot.

For both geometries, the cross-polarisation when the co-polarised radiation is maximum is very low, more than 20dB lower than the co-polarised radiation for the long antenna. The results for the short antenna are at least this good; the cross-

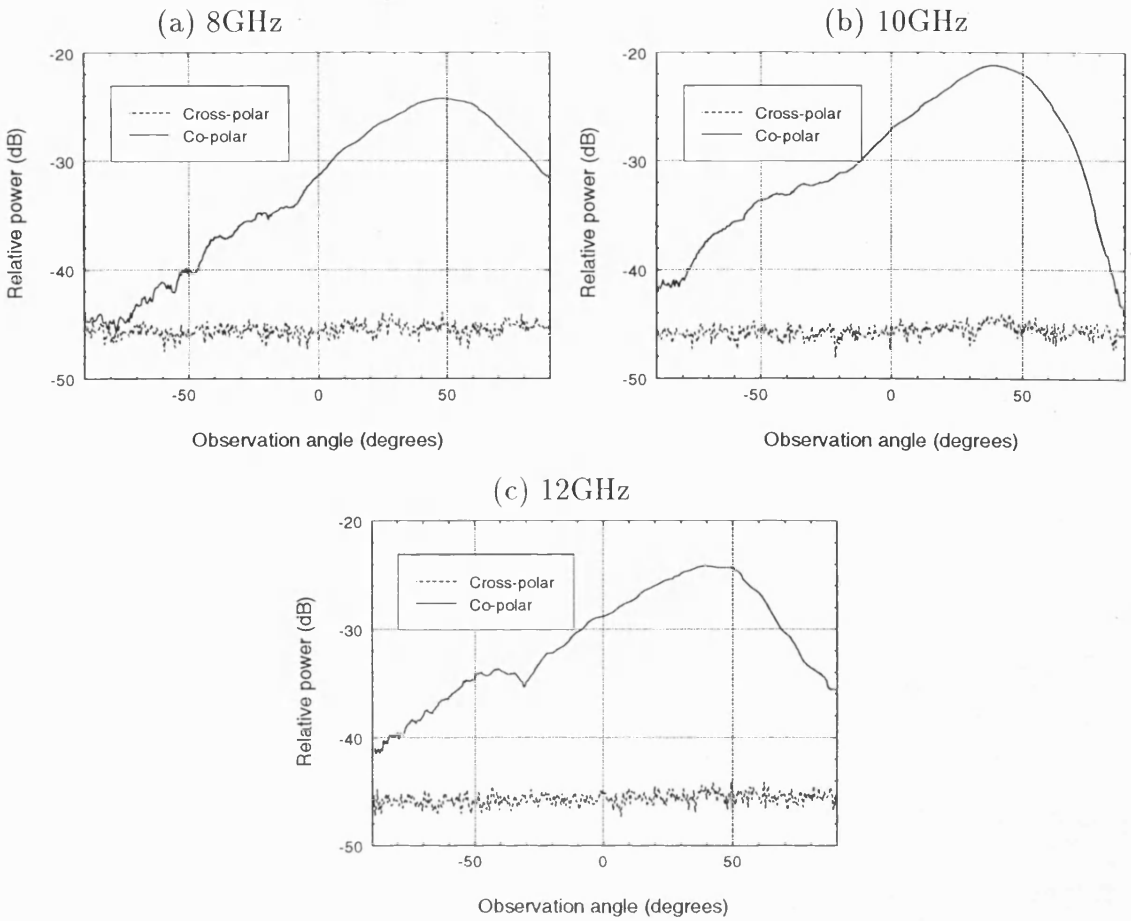

Figure 10.31: Measured co-polarised and cross-polarised elevation plane patterns for a short shallow slot antenna.

polarised radiation in this case is at or below the lower limit of the measurement system.

A similar set of results are given for long and short deep slot antennas in Figures 10.32 and 10.33.

For both structures, the cross-polarised radiation at the co-polarised radiation peak is generally between 15 and 20dB lower than the co-polarised radiation. Slightly worse results, around 13.5dB, are shown by the long antenna at 12GHz. This is due to the co-polarised radiated power being split into two 'main' beams of almost the same magnitude, which has the effect of reducing the measured power below -30dB. With the exception of the latter structure, the IDG-TSA exhibits lower levels of

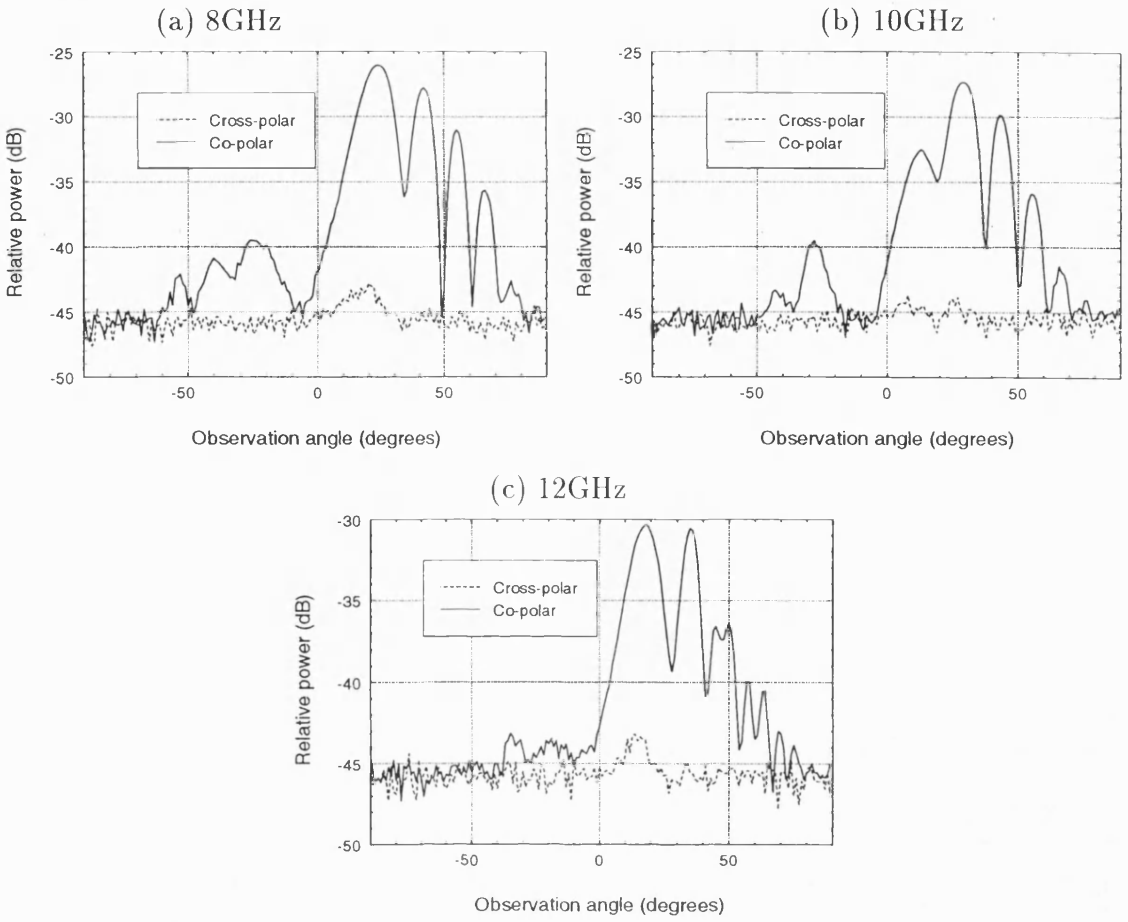

Figure 10.32: Measured co-polarised and cross-polarised elevation plane patterns for a long deep slot antenna.

cross-polarised radiation than have been reported for the Vivaldi and antipodal Vivaldi antennas [64].

10.7 Dual Polarised IDG-TSA: Feasibility Study

Having demonstrated that deep and shallow slot IDG exhibit nearly pure polarised radiation, the possibility of using a slot with intermediate dimensions to support both polarisations simultaneously is investigated. Ideally, such an antenna should produce the same radiation pattern in each polarisation, both with very low cross-polarisation. Antennas with these characteristics have a number of applications;

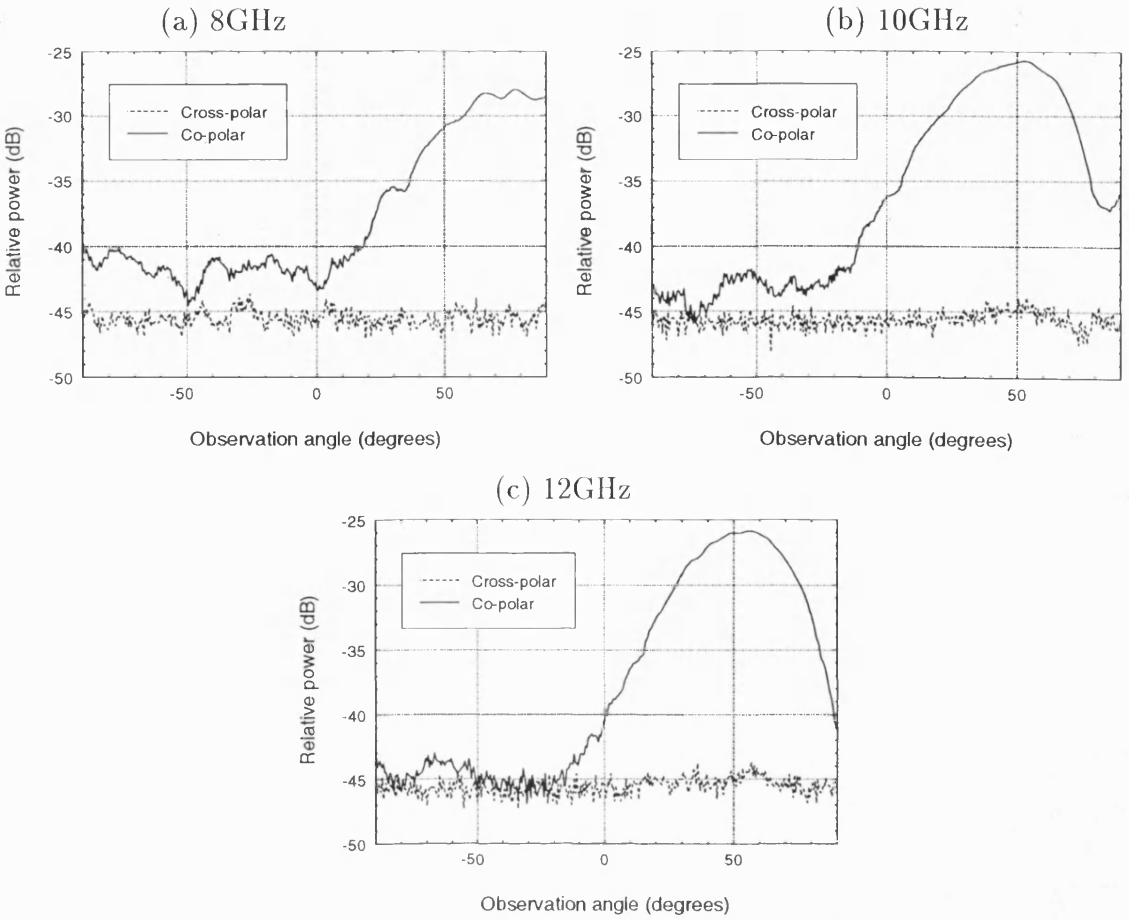

Figure 10.33: Measured co-polarised and cross-polarised elevation plane patterns for a short deep slot antenna.

for example, the polarisation diversity provided by such antennas can be used in indoor wireless schemes to improve reception.

As part of this feasibility study, an IDG-TSA capable of accepting feeds of both vertical and horizontal polarisation was constructed. The antenna was designed early on in the project in a relatively unsophisticated manner; this is very much a first attempt at a dual polarised structure. Two key physical requirements of the antenna - the necessity of fitting two feeds simultaneously, and the need to have complete control over the feed dimensions - meant that it was not possible to test the prototype until towards the end of the project when microstrip feeds were available. Feeding with RWG is not an option in this case.

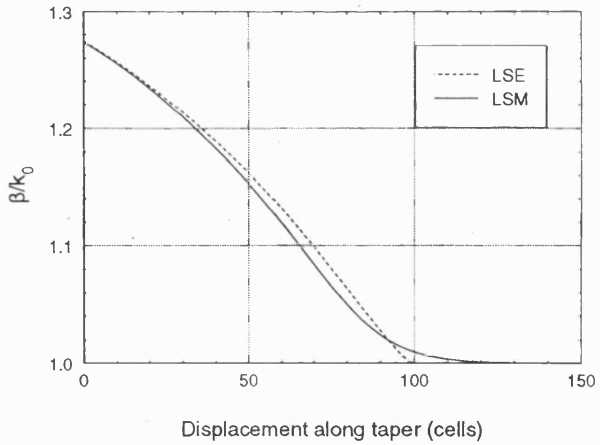

Figure 10.34: Dual polarised antenna propagation constants at 10GHz by TRD.

The approach taken in the design was as follows. Having noted that the increased spread of field onto the ground plane in the shallow slot case produced extremely dissimilar patterns for long deep and shallow antennas of the same dimensions, it was decided to construct a short structure. Short deep and shallow antennas exhibit more similar elevation plane radiation patterns, consisting in the main of one broad beam, so it seems possible that a short dual polarised structure could be designed to produce similar radiation patterns in each polarisation. To try to achieve this, a taper was designed on which the LSE and LSM propagation constants at 10GHz are almost equal, as shown in Fig. 10.34.

The figure shows TRD predictions of the LSE and LSM propagation constants along a taper with an ϵ_r of 2.3, broken up into 128 longitudinal elements. In order to keep the propagation constants as close as this it was necessary to use a taper where the width is varied as well as the depth. The antenna and its dimensions are shown in Fig. 10.35 in both top view and cross section. The feed board positions are also shown.

To feed the shallow slot mode, a microstrip board such as that shown earlier in Fig. 10.1 is used. The LSE feed board is placed across the 40mm uniform section of IDG prior to the taper, which was provided for this purpose. As discussed in Section 10.1 the LSE feed is of a similar design to the LSM feed. Its placement

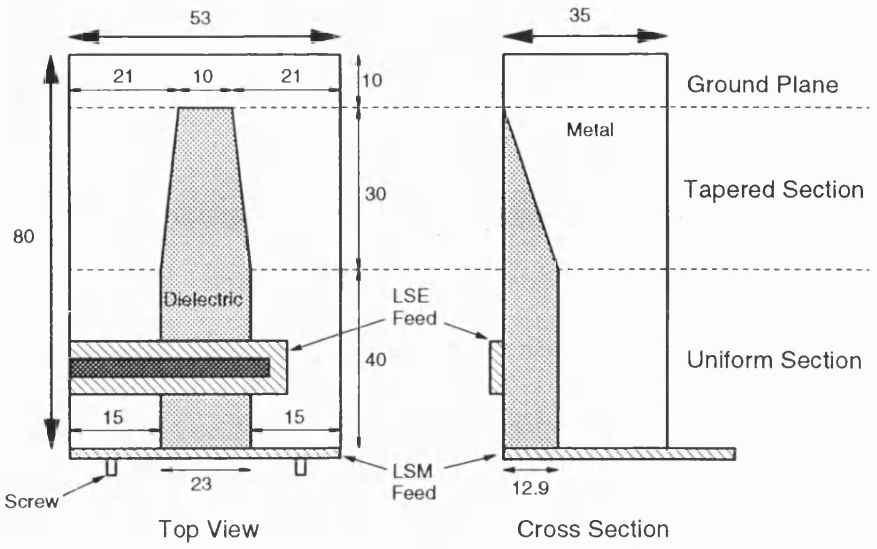

Figure 10.35: Dimensions of the dual polarised antenna.

across the top surface of the IDG is reminiscent of the microstrip to slot-line transition [61]. With both feeds attached the measured input reflection is as shown in Fig. 10.36.

The feeds are positioned here for minimum $|S_{11}|$ with the best results in the LSE case being obtained with the feed line extending beyond the IDG by approximately one quarter of a guided wavelength at 7.5GHz. The LSM input exhibits a reflection of around -10dB across the band. The LSE input is better than this, being lower than -15dB across the greater part of the band.

The feeding of shallow IDG with microstrip has already been considered in this chapter. Its performance when connected to the dual polarised antenna is similar to that seen earlier. However, more difficulty was experienced with the deep slot feed. Despite the low $|S_{11}|$ it was found difficult to excite the deep slot mode in the 8 to 12GHz range. In fact, in this range the 'LSE' feed operates as a reasonably effective LSM feed. Only below 8GHz was significant LSE polarised radiation excited.

A possible cause for the above problems is revealed by considering the modes of the

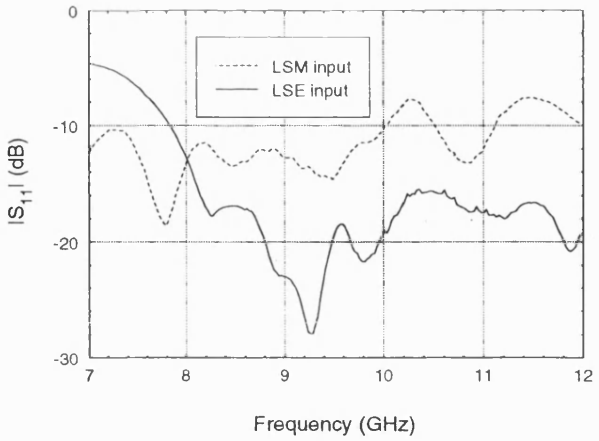

Figure 10.36: Measured input impedance of the dual polarised antenna.

uniform section of IDG. The first LSE mode exists between 5.1 and 12.1GHz, at which point the second mode begins to propagate. However, the LSM single-mode region is narrower, between 6.4 and 8.1GHz. The third LSM mode appears at 13.1GHz. The cut-in of the second LSM mode at 8.1GHz coincides with the point at which the LSE feed performance rapidly degenerates and it begins to excite LSM polarised radiation. As it stands, therefore, the LSE feed seems to be more effective at exciting the second LSM mode than the fundamental LSE mode. This seriously limits the operating bandwidth of this particular antenna.

Despite the foregoing, some dual polarised functionality can be observed, although it does not meet the requirement of exhibiting the same radiation pattern in each polarisation. Fig. 10.37 shows the co- and cross-polar radiation measured at 7.5 and 7.6GHz for both LSE and LSM excitation.

In all cases, the cross-polar radiation at the peak of the co-polar pattern is between 10 and 15dB down. This is satisfactory, but if the patterns are combined as in Fig. 10.38 at 7.6GHz then the dissimilarity of the patterns is clear. Only around 60° elevation are the co-polarised patterns of the same magnitude. As the original design frequency of the antenna is 10GHz the discrepancy between the patterns at 7.5GHz is to be expected; the LSE and LSM propagation constants are quite dissimilar at this frequency.

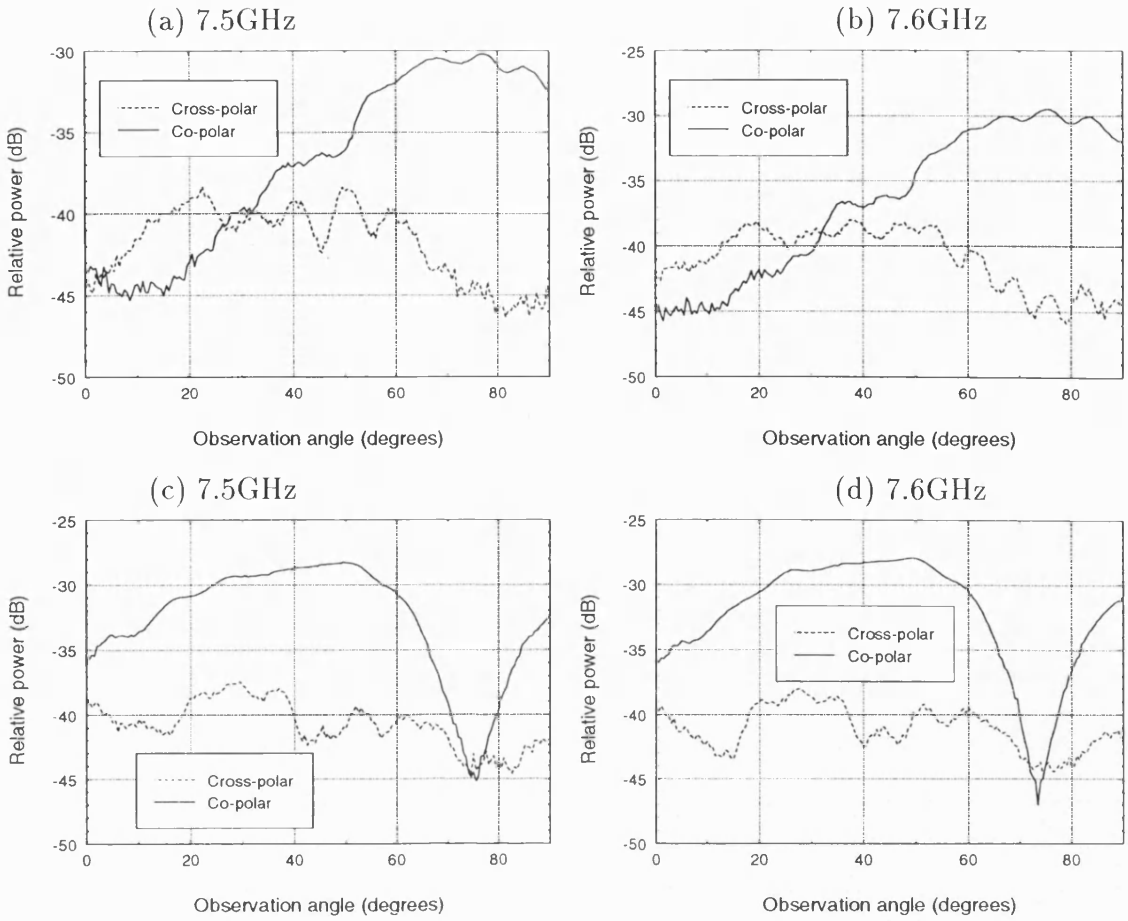

Figure 10.37: Measured elevation plane patterns for the dual polarised antenna. (a)-(b): LSE feed, (c)-(d) LSM feed.

This study has shown that the IDG-TSA does possess the capability for dual polarised operation. The results obtained from the prototype are imperfect but encouraging. It is thought that further effort in this area may well yield an IDG-TSA with satisfactory dual-polarised performance.

10.8 Higher Frequency Operation

In this section, the possibility of using a microstrip fed IDG-TSA at frequencies above X-Band is investigated. It was pointed out in Section 10.1 that the development of the microstrip feed opens up the possibility of higher frequency IDG-TSA

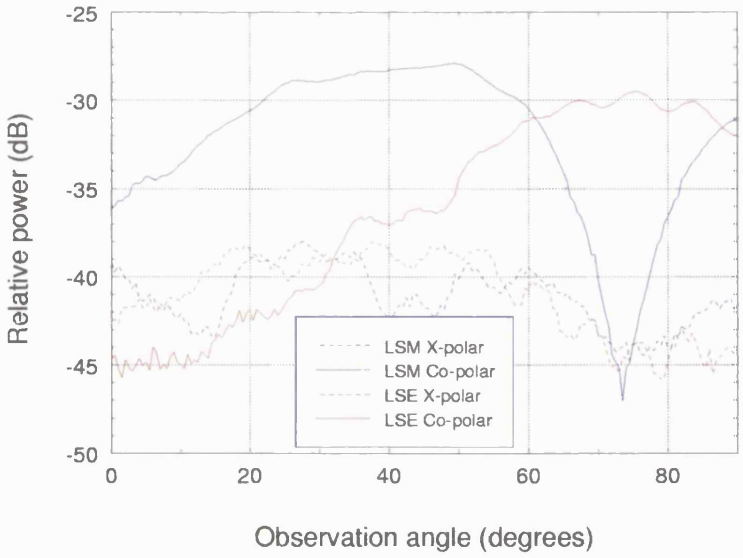

Figure 10.38: Measured elevation plane patterns for the dual polarised antenna at 7.6GHz. Results for both feeds superimposed.

operation. In Fig. 10.8 the performance of this feed up to 20GHz is shown. These results are tolerable, so it is worthwhile to test the operation of the transition in conjunction with an IDG-TSA. Measurements up to 21GHz were taken using this feed attached to the short shallow IDG-TSA. Results at 15, 17, 19, and 21GHz are depicted in Fig. 10.39.

Comparisons with predictions made using the full H-guide model of Section 7.9 and the simpler line source model used in Section 7.6 are also included. Although no gain measurements were taken, comparison with theory shows that the IDG-TSA is operating in a reasonably predictable manner at these higher frequencies. The fundamental LSM mode at the feed end of the antenna cuts in at 6.7GHz so that an operating bandwidth of 3:1 is demonstrated here. Previous bandwidth measurements on related structures have claimed operation over 2:1 [1] and 4:1 [2] bands. The latter measurements were taken at rather lower frequencies than the current work, 2.5 to 10GHz.

It is possible that operation above 21GHz could be achieved, but this could not be tested. Indeed, the measurement equipment is well outside its specification at

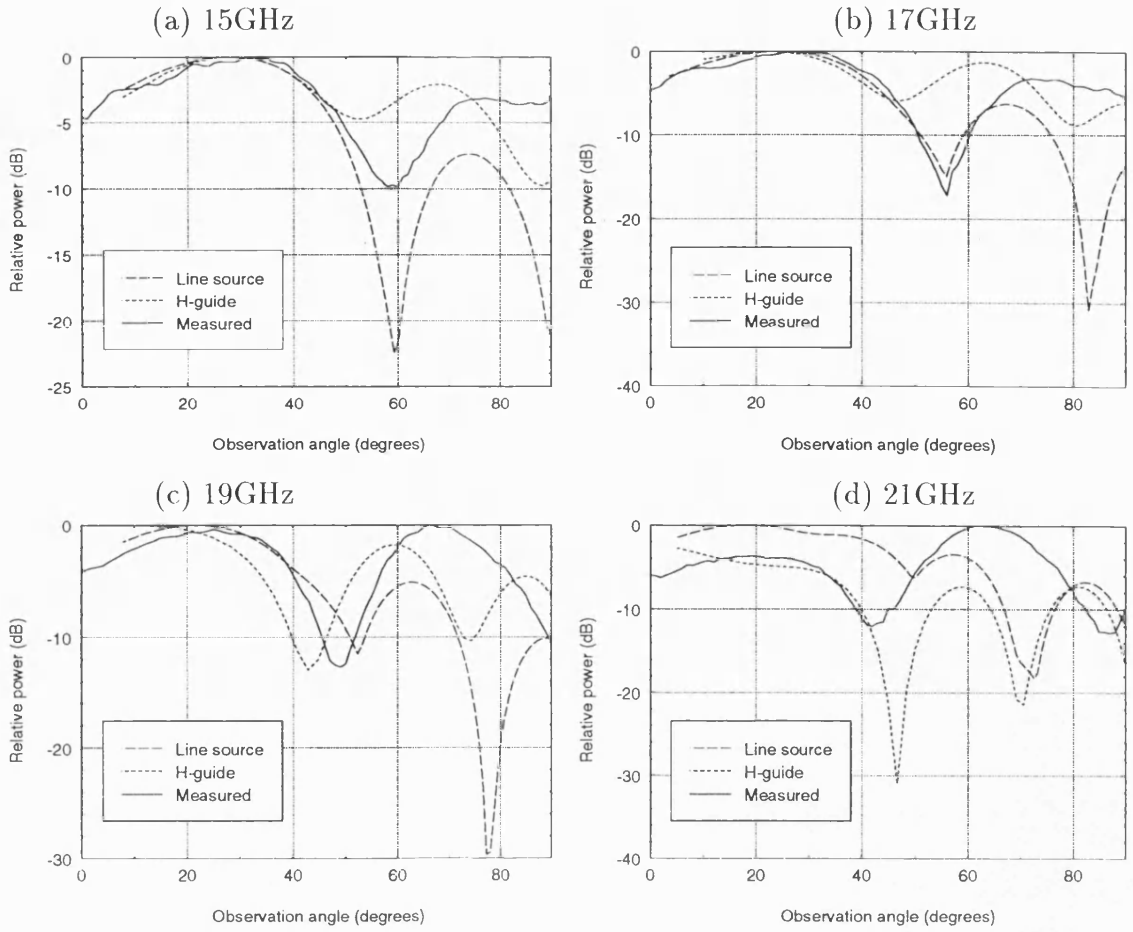

Figure 10.39: Elevation plane patterns at higher frequencies for a short shallow antenna with microstrip feed.

21GHz, which may have some bearing on the imperfect match to theory at the higher frequencies. Another possible cause for the degraded performance at these frequencies is the likelihood that higher order modes are being excited by the microstrip feed. There is evidence for this in the transition measurements of Fig. 10.8. At the feed higher order modes cut in at 9.2, 15.7, 18.2, and 19.6GHz. The theoretical methods only model the fundamental mode, so that deviation between theory and measurement should be expected as the frequency is raised. The full H-guide model may be particularly affected in this respect as it makes assumptions about the transverse variation of the aperture fields. Hence the inclusion of results from the simpler line source model.

10.9 Measured Field Distributions

A number of probe measurements of the fields on the IDG-TSA surface have been taken. As well as providing insight into the operation of the structure, these measurements allow at least qualitative verification of aspects of the theoretical models. No IDG-TSA surface measurements have been taken previously; in fact the only set of comparable measurements of which the author is aware relate to a linear tapered slot antenna (LTSA) in [57, Chapter 9].

The measurements were made using probes constructed from semi-rigid waveguide located one or two millimetres from the antenna surface. For electric field probes a length of the inner conductor was allowed to continue beyond the end of the waveguide, and this length of wire was then orientated with the field component to be measured. For magnetic field probes, the length of inner conductor was folded back and soldered to the outer conductor to form a loop. Measurements were made using a crystal detector and VSWR meter.

It should be noted that the results given in this section do not accurately depict specific Cartesian field components. Each probe couples to a number of these components. A probe such as that nominally detecting E_z is a good example of this. Here the wire of the probe is bent through 90° to align with the E_z component, so that the top section of the probe is in fact at right angles to the desired field.

A source of inaccuracy in these measurements is due to the disturbance that the probes cause to the fields on the surface of the antenna; performing the measurements requires a metal object of not inconsiderable size to be inserted into the IDG-TSA near field.

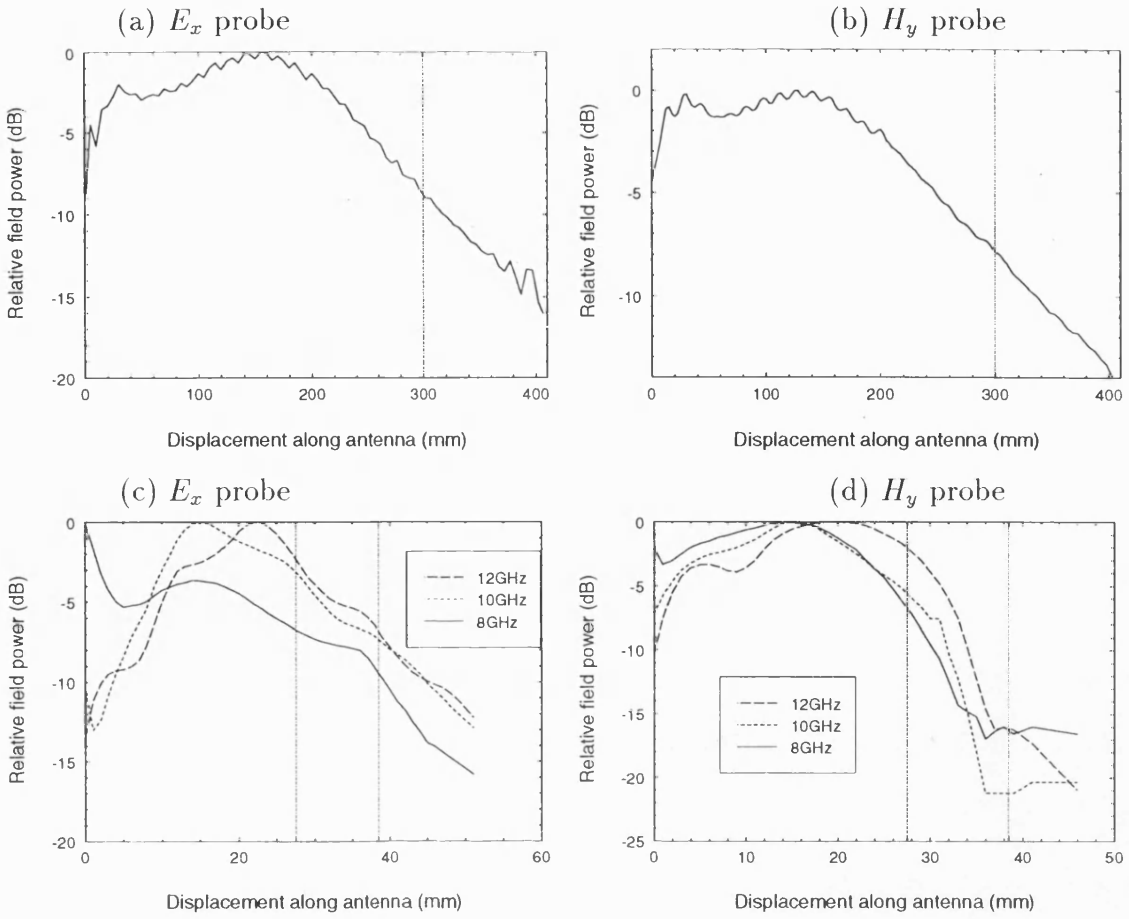

Figure 10.40: Field power measured along the centre of shallow structures. (a)-(b): Long antenna, (c)-(d): Short antenna.

10.9.1 Shallow Slot Results

In Fig. 10.40 are depicted measurements taken along the centre of the antenna.

For the short structure, the end of the slot and ground plane are marked on the figures whilst only the slot end is marked in the long antenna results as no measurements were taken off the end of the ground plane for this structure. The results show standing wave patterns, as expected, with many peaks for the long antenna and few for the short. A reduction in the power along the slot can be observed, corresponding to power losses to radiation. In all cases the field continues onto the ground plane with significant magnitude.

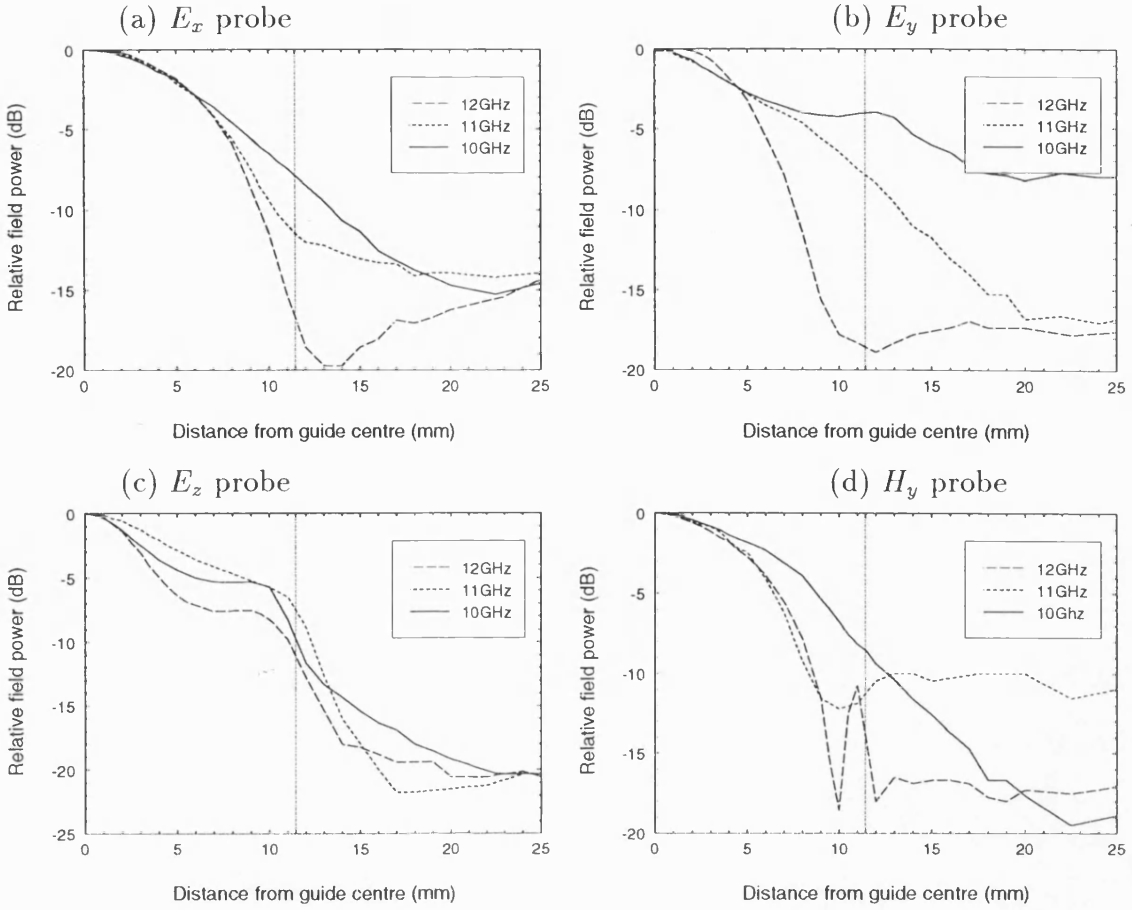

Figure 10.41: Field power measured across the half-width of a short shallow antenna.

The features of these results correspond well with those displayed by the FDTD results given in Chapter 8, Figures 8.2 and 8.9. Further, the results support the power loss characteristics calculated by FDTD and VBMM given in Section 6.6.1.

Fig. 10.41 depicts fields measured across the antenna, starting at the guide centre and working outwards to a point 25mm distant. The half-width of the slot, 11.43mm, is marked on the plots. These measurements can be compared to the surface fields calculated by FDTD given in Fig. 5.12. It is clear that the fields have an approximately sinusoidal variation within the slot. For the E_x, E_z, and H_y components therefore, the measurements support the FDTD results. Also, the H-guide assumption of a sinusoidal variation across the slot can be seen to be reasonable.

However, there is some deviation between FDTD and measurement in the case of the E_y component, which theory states is zero at the guide centre. The E_y probe consists of a short x directed section, a 90° bend, and then a longer y directed length of wire. As can be seen in Fig. 5.12 the E_x component is of much larger magnitude than E_y. Thus, the power measured by the x directed section of the probe is dominating the y directed measurement causing the E_y probe measurement to have a similar shape to the E_x measurement. The E_z probe results are also affected, though to a lesser extent.

The foregoing can be tested by simulating the probes in FDTD, rather than considering only the field at a point. This is done in Fig. 10.42 for the transverse E_x and E_y components, and for the longitudinal E_x component. Part (a) of the figure shows the calculated E_y component now has a similar shape to that measured.

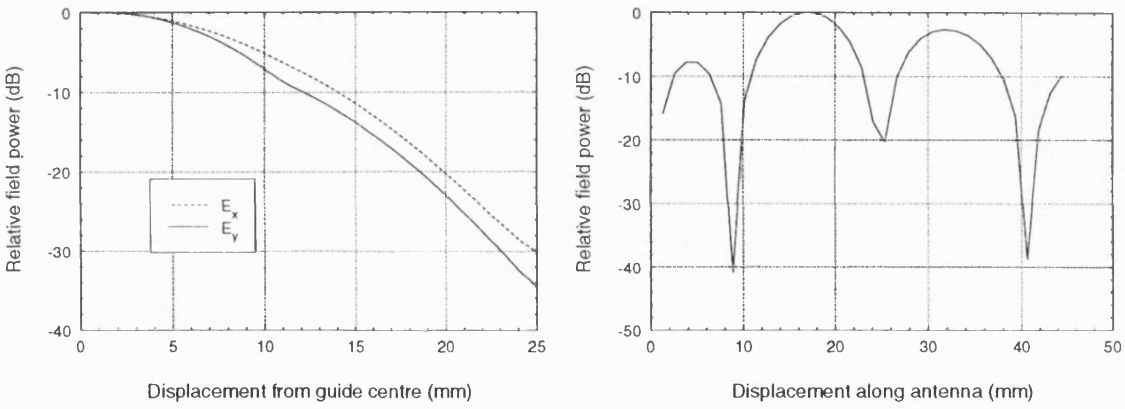

Figure 10.42: FDTD simulations of probe measurements for short shallow antenna at 10GHz. (a) Across antenna surface, and (b) E_x along centre of antenna surface.

Finally, it is interesting to look at how the field decays in the air above the guide. Fig. 10.43 shows the E_x component over a long shallow antenna. Starting 1mm above the guide, the probe is lifted until its end is 18mm above it.

The field can be seen to decay in an approximately exponential manner. This supports the hypothesis that the antenna is a surface wave structure (Section 2.2.2). It will be recalled that the H-guide fields derived in Chapter 5 decay exponentially in the air region. Note that these measurements were taken towards the feed end

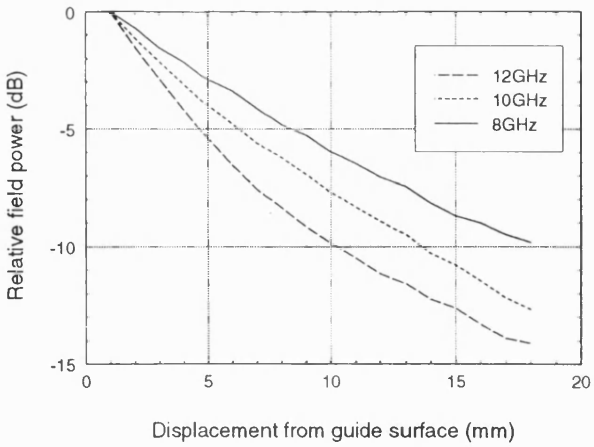

Figure 10.43: Decay of field power away from the long shallow antenna surface measured using an E_x probe.

of a long structure so that the measurements were not swamped by radiation from the antenna. The results given earlier in this section and in Chapter 6 indicate that there is little radiation from this part of the long antenna.

10.9.2 Deep Slot Results

Measurements taken along the centre of long and short deep antennas are shown in Fig. 10.44.

These figures show similar standing wave patterns to those seen in the shallow slot case above. For the long antenna, no power could be detected on the ground plane beyond the end of the aperture, so the results depict the aperture only. For the short structure, the end of the slot and the end of the ground plane are marked on the figures. Results taken in the transverse direction are given in Fig. 10.45, where the half-width of the slot is 5.08mm.

These results should be compared with the components calculated by FDTD in Fig. 5.13. There is good agreement between the predicted and measured field shapes, although the spread onto the ground plane is more significant in the lat-

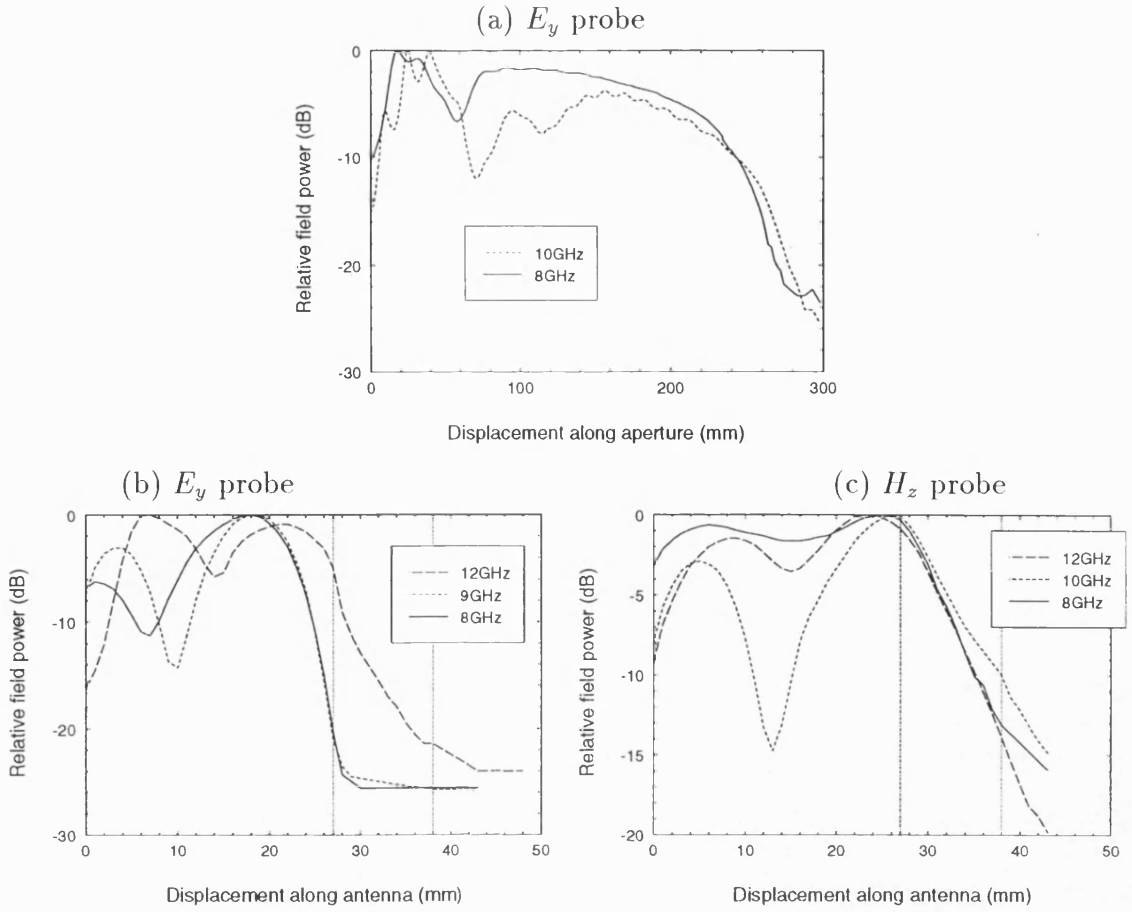

Figure 10.44: Field power measured along the centre of deep structures. (a): Long antenna, (b)-(c): Short antenna.

ter case as the measurements were taken approximately 2mm above the antenna surface. Again, the E_y and E_z measurements contain an element of the E_x measurement due to the shape of the probes. In this case however, the E_x measurement is zero at the guide centre so that the E_y and E_z components within the slot are clearly visible in the E_y and E_z probe measurements.

So, in both the deep and shallow slot cases the surface measurements can be seen to support the FDTD predictions and the results of the H-guide analysis. The measurements demonstrate that the IDG-TSA is indeed a travelling wave structure, and that ground plane fields play an important role in defining its radiation properties.

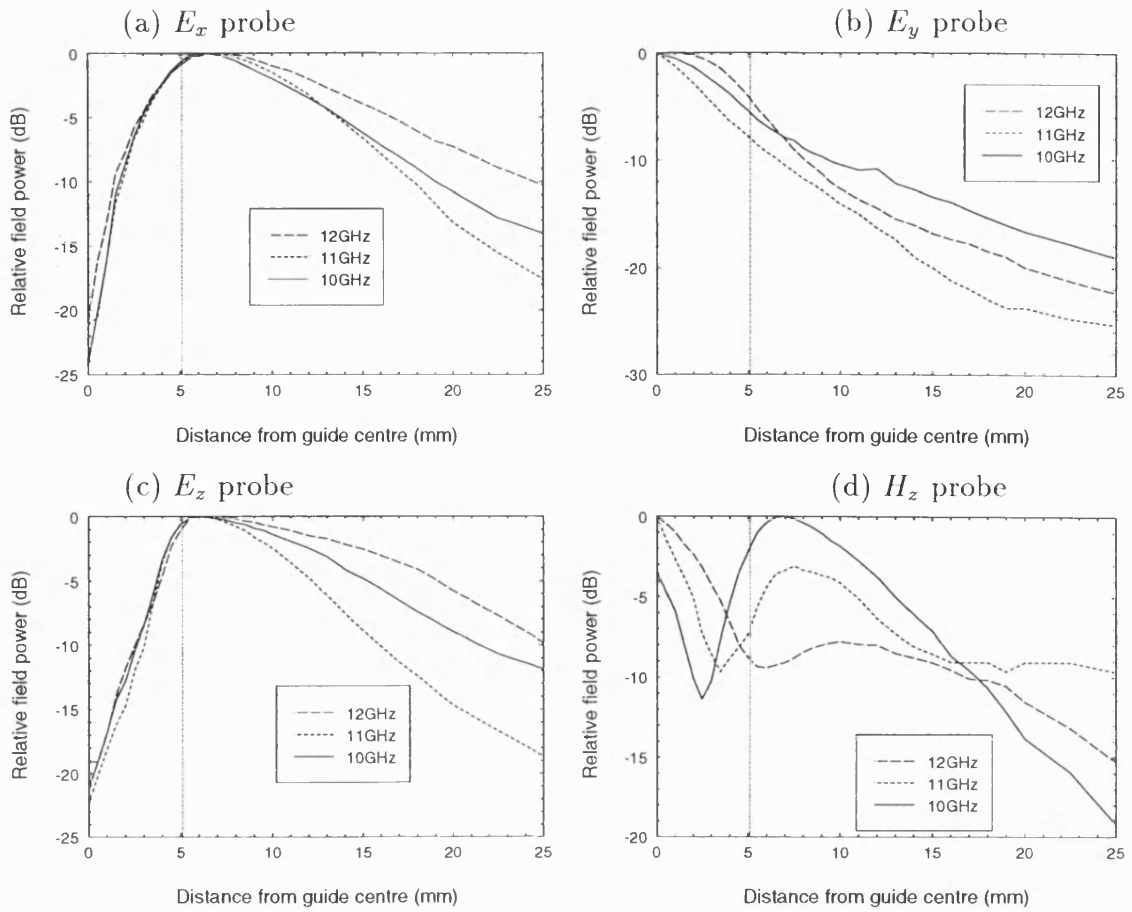

Figure 10.45: Field power measured across the half-width of a short deep antenna.

10.10 Chapter Summary

Various transitions onto IDG have been experimentally investigated. New microstrip and stripline based transitions have been introduced. As an IDG-TSA feed the latter structure performs well, having a lower input reflection coefficient than the conventional RWG feed and providing comparable, sometimes better, antenna gain. This development allows the IDG-TSA to be integrated with planar circuitry and frees the designer from the need to adhere to feed dimensions matching those of standard rectangular waveguides.

In order to obtain a broader picture of the characteristics of the IDG-TSA, a number of measured results have been presented. These include input impedance,

gain, and beamwidth measurements, as well as plots showing the manner in which the radiation characteristics of the structure vary with frequency. The low cross-polarisation of IDG-TSA radiation has been demonstrated for the first time, and the measurements indicate that the IDG-TSA exhibits lower levels of cross-polarisation than the Vivaldi and antipodal Vivaldi structures. A novel prototype dual polarised IDG-TSA has been constructed from which some encouraging results have been obtained.

Higher frequency IDG-TSA operation using the microstrip feed has been tested, and a 3:1 operating bandwidth has been measured. At these higher frequencies, the antenna has been shown to perform in a predictable manner. Probe measurements of the fields on the IDG-TSA surface have been taken. These give insights into the mode of operation of the antenna, and also support the results of the theoretical models.

Chapter 11

Conclusions

11.1 Introduction

In this chapter, the work presented in the thesis is reviewed, its achievements are highlighted and any outstanding problems are identified. In the final section, areas for possible future study are proposed.

11.2 Review and Concluding Remarks

This thesis is chiefly concerned with the development of analytical and numerical methods for the prediction of the radiation characteristics of the inset dielectric guide tapered slot antenna. Experimental investigations into the antenna properties have supported and informed the theoretical work, as well as providing new insight into the properties of the structure.

The early chapters of the thesis, Chapters 2 to 4, provide a review of past developments in research relevant to the IDG-TSA, and then focus on specific elements of

the previously developed theory that are of particular importance to the material presented in the later chapters. These subsequent chapters detail the various pieces of work that were carried out for this project, most of which represent a development of, or an addition to, the existing body of work. The main achievements of the work presented here are given below, listed in the order in which they appear in the thesis:

The H-guide model of IDG has been developed and its validity checked against FDTD and transverse resonance diffraction results. The H-guide field distributions are similar to those of IDG, and the propagation constants of the two structures are close except where the IDG propagation constant approaches that of free space. The lack of modelling of edge effects in the H-guide analysis means that its fields least resemble those of IDG in the vicinity of the dielectric surface, which is the region of principal interest in the antenna analysis.

The bounded mode matching method has been successfully applied to step discontinuities in LSE and LSM polarised H-guide. A transmission line model of an IDG taper has been constructed from these elements. This model predicts the power loss of the fundamental mode on the taper well, showing reasonable agreement with FDTD results. However, the usefulness of this method is limited to that part of the IDG taper where the propagation constant is greater than that of free space.

A new analytical method for prediction of the IDG-TSA radiation characteristics has been developed. This method includes a full model of the slot and ground plane fields which incorporates a theory for linking the fields across the slot edge. Results generated using the new method show improvements over those produced by the previously developed analytical method. FDTD simulation has shown that the surface field model used by the new analytical model is realistic. The theoretical methods developed prior to the current work used an approximate method to cater for the fields on the ground plane. It has been shown here that this method cannot be used with LSE polarised structures, and FDTD results have demonstrated that

it introduces significant error into the calculation when applied to LSM polarised structures.

A full FDTD model of the IDG-TSA has been developed which dispenses with various approximations and limitations of the existing FDTD code [4]. The new model allows the effects on the radiation pattern of the faces of the mounting block and the RWG flange to be investigated. These additional surfaces have been shown to have a significant effect, and very close agreement between theory and measurement has been achieved using this model, as well as an improvement over results generated using the earlier code.

Special FDTD cells have been developed in order to model the singularities at an IDG edge. For an FDTD model for calculating the propagation constant of uniform deep IDG it was found that application of the special cells allowed a given degree of accuracy to be achieved using larger cells. This leads to savings in computer storage requirements and run times. Inclusion of the special cells was found to have little effect on a similar model for shallow slot IDG.

Results from the new analytical and FDTD methods have been compared with each other and measured data across a wide range of observation angles for four antenna geometries. Agreement between the three sets of data is in general good.

It has been shown by experiment that the environment in which a shallow slot IDG-TSA is installed has a significant effect on its radiation pattern. Deep slot antenna radiation patterns are largely unaffected in this respect. These results indicate that ground plane currents are a much more significant factor in determining the radiation pattern of the shallow slot antenna. For antennas located in a metal block, this hypothesis is supported by field cuts calculated by FDTD which demonstrate that that the fields interact with the edges and surfaces of the mounting block to a much greater extent in the shallow slot case. If this antenna is then installed in an infinite surface these fields will be disturbed and the radiation characteristics

will change. Indeed, predictions made using the new FDTD method show how excellent agreement between theory and measurement can only be obtained by including details of the environment in the model.

Various types of transition onto IDG have been evaluated, including new microstrip and stripline structures. These new feeds have been used in conjunction with the IDG-TSA. The microstrip feed is radiative, but the stripline feed offers better performance, close to or better than that of the conventional RWG feed. The stripline feed allows, for the first time, direct integration of IDG-TSAs with planar circuitry, and facilitates a free choice of the dimensions of the IDG at the feed end of the antenna.

The pure polarisation properties of the IDG-TSA have been established. Both shallow and deep slot structures produce low levels of cross-polarised radiation, although performance is degraded in the case of the long deep antenna due to the existence of two or three main beams in the radiation pattern. A novel dual-polarised antenna has been built where a slot of intermediate dimensions is fed using vertically and horizontally orientated microstrip boards. Performance of this structure is not perfect, apparently due to the excitation of higher order modes, but reasonable dual-polarised operation has been observed over a limited range of frequencies.

The broadband properties of the IDG-TSA have been demonstrated. Using a microstrip feed, a nominally X-band structure has been operated successfully and in a predictable manner up to 21GHz. A bandwidth of approximately 3:1 has thus been established.

A number of the antenna geometries studied in this work have not previously been considered, namely the very short deep and shallow structures and the long deep antenna. Whilst an examination of the properties of the latter has helped to demonstrate the reduced role played by the ground plane fields in the deep slot

case, it is the short structures that show the most interesting properties. Both the deep and shallow short structures produce a single broad main beam, so may be useful for array applications. The shallow structure considered here exhibits nearly constant beam dimensions and gain over a 4GHz band. For both of the deep slot geometries, measurements of the radiation pattern over a range of frequencies are interesting, showing significant shifts in the main beam positions with frequency.

Probe measurements of the fields on the IDG-TSA surface have supported aspects of both theoretical models and confirm the antenna's classification as a slow wave travelling wave antenna.

A number of the difficulties associated with producing an accurate analytical method for the IDG-TSA have become apparent over the course of this work. The need to include the complete near-antenna environment has already been mentioned; this can be a difficult task. The work on feed structures has shown the extent to which radiation from the feed can alter the overall radiation pattern. Further, it is clear that variations in the dielectric constant and its distribution along the taper can have a significant effect on the radiation properties. All of these factors can have a deleterious effect on the agreement between measurement and theory.

11.3 Further Work

A number of the areas studied in this thesis could benefit from further work. The most important of these are considered below.

Broadband operation of the IDG-TSA has been demonstrated in this thesis. It is known that the bandwidth of IDG can be significantly extended by using a layered dielectric in the slot [14, 15]. It would be of interest to investigate whether a twin layer dielectric filling would produce an IDG-TSA with a very wide operating

bandwidth. The performance of the microstrip or stripline feeds in conjunction with such a structure would also need to be tested. Building a layered dielectric into the theoretical models should be straightforward, certainly in FDTD, and the H-guide analysis could be modified using the transverse resonance method.

The measurements taken from the dual-polarised structure reported in this thesis are encouraging but not good enough for practical application. Further work here could yield much better performance. When designing this antenna the possibility that the deep slot feed may couple to higher order LSM polarised modes needs to be borne in mind. The prospect of extending the monomode bandwidths of the fundamental LSE and LSM modes on the dual-polarised taper using a layered dielectric as mentioned above is appealing, and needs to be investigated.

Promising new IDG and IDG-TSA feeds have been introduced in this thesis. The designs for these were largely empirical although based on the results of earlier work carried out by a number of researchers. There is great scope for improving the performance of these feeds, even without developing theoretical models of the junctions, by experimental investigation of various microstrip and stripline board layouts. At present, straight 50Ω lines are used.

Currently, the FDTD model of the IDG-TSA has no capability for modelling antennas whose width varies. This would be a straightforward addition, though conformal modelling of the slot sides would be required. Modifying the model such that a dual-polarised antenna could be analysed is a little more involved, with the aforementioned modelling of width variations being a first step, but is necessary if any serious development of this structure is to be carried out. At present the model only includes half of the antenna and enforces either LSE or LSM symmetry at the guide centre. For a dual-polarised model it is likely that the entire structure would need to be modelled as both symmetries are present. The increased computing power now available means that such a model could be successfully run. A further complication, however, is the modelling of two microstrip feeds in place of

the single RWG feed currently employed.

11.4 Chapter Summary

The work presented in this thesis has been reviewed, and options for further work discussed. As a result of this project, the modelling tools for use with the IDG-TSA have been significantly improved, the manner in which it operates is now much better understood, and methods now exist for integrating it with microstrip circuitry. A number of the antennas discussed in this work demonstrate useful properties, whilst others show considerable promise, so it is to be hoped that this versatile structure can soon find practical application.

Appendix A

FDTD Correction Factors

The following correction factors relate to the arrangement shown in Fig. 8.15 with $\epsilon_r = 2.3$. The nomenclature for the FDTD cells is defined in Section 3.2.2 and Fig. 3.5. Correction factors for the surface integrals are denoted CF_s, and for the line integrals CF_l

Cells in Position 1:

- EX update: $CF_s = 0.9944717$,
  $CF_l[HZ] = 1.0$, $CF_l[HY] = 1.0245602$.
- EY update: $CF_s = 1.0274641$,
  $CF_l[HZ] = 1.0$, $CF_l[HX] = 0.9449408$.
- EZ update: $CF_s = 1.0004539$,
  $CF_l[HY(I-1,J,K)] = 0.9748446$, $CF_l[HY(I,J,K)] = 1.0245602$,
  $CF_l[HX(I,J-1,K)] = 0.9921049$, $CF_l[HX(I,J,K)] = 0.9449408$.
- HX update: $CF_s = 1.19055079$,
  $CF_l[EZ] = 1.0$, $CF_l[EY] = 1.1211952$.

- HY update: $CF_s = 0.9792931$,
  $CF_l[EX] = 0.9884315$, $CF_l[EZ] = 1.0$.

- HZ update: $CF_s = 0.997878$,
  $CF_l[EY(I+1,J,K)] = 0.9798906$, $CF_l[EY(I,J,K)] = 1.1211952$,
  $CF_l[EX(I,J+1,K)] = 1.1211952$, $CF_l[EX(I,J,K)] = 0.9884315$.

Cells in Position 2:

In this case the EY, EZ, and HX components are zero as they are on the ground plane surface. Correction factors for the remaining three components are calculated as follows:

- EX update: $CF_s = 0.9606473$,
  $CF_l[HZ] = 1.0$, $CF_l[HY] = 0.9449408$.

- HY update: $CF_s = 1.1905508$,
  $CF_l[EZ] = 1.0$, $CF_l[EX] = 1.1211952$.

- HZ update: $CF_s = 0.9983105$,
  $CF_l[EY(I+1,J,K)] = 1.0204797$, $CF_l[EY(I,J,K)] = 1.0$,
  $CF_l[EX(I,J+1,K)] = 0.9944931$, $CF_l[EX(I,J,K)] = 1.1211952$.

Cells in Position 3:

In this case, only the HZ update contains components that are significantly affected by the IDG edge:

- HZ update: $CF_s = 0.9983105$,
  $CF_l[EY(I+1,J,K)] = 1.1211952$, $CF_l[EY(I,J,K)] = 0.9978608$,
  $CF_l[EX(I,J+1,K)] = 1.0$, $CF_l[EX(I,J,K)] = 1.0032511$.

Appendix B

Solution of Bounded H-Guide Characteristic Equations

This appendix shows how the characteristic equations for the slow and fast modes of the PMC bounded LSE H-guide, equation (6.6), are rearranged for computer solution. The procedure for the bounded LSM H-guide equations (6.11) and (6.14) is similar, so specific details are not given here.

Slow Modes:

Repeating the slow mode characteristic equation given by equation (6.6):

$$k_{dn}\cos\left(k_{dn}t_1\right)\cosh\left[\gamma_{an}(t_1-t_B)\right]-\gamma_{an}\sinh\left[\gamma_{an}(t_1-t_B)\right]\sin\left(k_{dn}t_1\right)=0 \qquad \text{(B.1)}$$

From equation (6.5):

$$k_{dn}^2-k_{an}^2=(\epsilon_r-1)k_0^2 \qquad \text{(B.2)}$$

For the slow modes it is known that k_{an} is imaginary, i.e. $k_{an} = j\gamma_{an}$, so that:

$$\gamma_{an}^2 = (\epsilon_r - 1)k_0^2 - k_{dn}^2$$

This equation can be used to eliminate γ_{an} from equation (B.1):

$$\begin{aligned} k_{dn}\cos(k_{dn}t_1)\cosh\left[(t_1 - t_B)\sqrt{(\epsilon_r - 1)k_0^2 - k_{dn}^2}\right] \\ -\sqrt{(\epsilon_r - 1)k_0^2 - k_{dn}^2}\sinh\left[(t_1 - t_B)\sqrt{(\epsilon_r - 1)k_0^2 - k_{dn}^2}\right]\sin(k_{dn}t_1) \;&=\; 0 \end{aligned} \tag{B.3}$$

This equation is solved for k_{dn} using the modified bisection method [126].

Fast Modes:

Repeating the fast mode characteristic equation given by equation (6.6):

$$k_{dn}\cos(k_{dn}t_1)\cos[k_{an}(t_1 - t_B)] + k_{an}\sin[k_{an}(t_1 - t_B)]\sin(k_{dn}t_1) = 0 \tag{B.4}$$

Equation (B.2) gives:

$$k_{dn}^2 = k_{an}^2 + (\epsilon_r - 1)k_0^2$$

This equation can be used to eliminate k_{dn} from equation (B.4):

$$\sqrt{k_{an}^2+(\epsilon_r-1)k_0^2}\cos\left(t_1\sqrt{k_{an}^2+(\epsilon_r-1)k_0^2}\right)\cos\left[k_{an}(t_1-t_B)\right]$$
$$+k_{an}\sin\left[k_{an}(t_1-t_B)\right]\sin\left(t_1\sqrt{k_{an}^2+(\epsilon_r-1)k_0^2}\right) = 0 \tag{B.5}$$

This equation is used for computer solution.

References

[1] B.T. Stephenson and C.H. Walter. Endfire slot antennas. *IRE Transactions on Antennas and Propagation*, volume AP-3:pp. 81–86, April 1955.

[2] J.W. Eberle, C.A. Levis, and D. McCoy. The flared slot: A moderately directive flush-mounted broad-band antenna. *IRE Transactions on Antennas and Propagation*, volume AP-8:pp. 461–468, September 1960.

[3] V. Stoiljković, S.R. Pennock, and P.R. Shepherd. Numerical analysis of flared IDG antennas. In *Proceedings of the 9th International Conference on Antennas and Propagation*, volume 1, pages 520–523. IEE, 1995.

[4] V. Stoiljković, S.R. Pennock, and P.R. Shepherd. The use of the FDTD method in the design of IDG antennas. In *Proceedings of the 3rd International Conference on Computation in Electromagnetics*, pages 67–71. IEE, 1996.

[5] T. Itoh and B. Adelseck. Trapped image guide for millimeter-wave circuits. *IEEE Transactions on Microwave Theory and Techniques*, volume MTT-28:pp. 1433–1436, December 1980.

[6] T.E. Rozzi and S.J. Hedges. Rigorous analysis and network modeling of inset dielectric guide. *IEEE Transactions on Microwave Theory and Techniques*, volume MTT-35:pp. 823–834, September 1987.

[7] T. Rozzi and L. Ma. Mode completeness, normalization, and Green's function

of the inset dielectric guide. *IEEE Transactions on Microwave Theory and Techniques*, volume MTT-36:pp. 542–551, March 1988.

[8] L. Ma, T. Rozzi, and S. Pennock. Linear arrays realized in IDG. In *Proceedings of IEE Colloquium on Components for Novel Transmission Lines*, pages 6/1–6/3, 1990.

[9] T. Rozzi, L. Ma, R. De Leo, and A. Morini. Equivalent network of transverse dipoles on inset dielectric guide: application to linear arrays. *IEEE Transactions on Microwave Theory and Techniques*, volume MTT-38:pp. 380–385, March 1990.

[10] L. Ma, T. Rozzi, and S. Pennock. Design of multiple array flat millimetric antennas in IDG. In *Proceedings of the 21st European Microwave Conference*, volume 1, pages 641–646, 1991.

[11] T. Rozzi, R. De Leo, and A. Morini. Analysis of the "microstrip-loaded inset dielectric waveguide". In *IEEE MTT-S Digest*, volume 3, pages 923–926, 1989.

[12] T. Rozzi, A. Morini, and G. Gerini. Analysis and applications of "Microstrip-Loaded Inset Dielectric Waveguide" (Mig). *IEEE Transactions on Microwave Theory and Techniques*, volume MTT-40:pp. 272–278, February 1992.

[13] N. Izzat, S.R. Pennock, and T. Rozzi. Space domain analysis of micro-IDG structures. *IEEE Transactions on Microwave Theory and Techniques*, volume MTT-42:pp. 1074–1078, June 1994.

[14] S.R. Pennock, N. Izzat, and T. Rozzi. Very wideband operation of twin-layer inset dielectric guide. *IEEE Transactions on Microwave Theory and Techniques*, volume MTT-40:pp. 1910–1917, October 1992.

[15] T. Rozzi, S.R. Pennock, and N. Izzat. Bandwidth control in multilayer inset dielectric guide. In *Proceedings of the 20th European Microwave Conference*, volume 2, pages 1169–1174, 1990.

[16] Z. Fan and S.R. Pennock. Propagation characteristics of ferrite loaded inset dielectric guide. In *Proceedings of the 23rd European Microwave Conference*, volume 1, pages 129–131, 1993.

[17] Z. Fan, Y.M.M. Antar, L.E. Davis, and Z. Wu. Analysis of multilayer inset dielectric guides containing magnetised ferrites. *IEE Proceedings Part H*, volume 143:pp. 390–396, October 1996.

[18] Z. Fan and S.R. Pennock. Characteristics of coplanar waveguide loaded inset dielectric guide. In *Proceedings of the 24th European Microwave Conference*, pages 1409–1414, 1994.

[19] S.R. Pennock, D.M. Bošković, and T. Rozzi. Analysis of coupled inset dielectric guides under LSE and LSM polarisation. *IEEE Transactions on Microwave Theory and Techniques*, volume MTT-40:pp. 916–924, May 1992.

[20] Z. Fan and S.R. Pennock. Rigorous analysis of coupled inset dielectric guides. In *Proceedings of IEEE workshop on CAE, modelling and measurement verification*, pages 91–96, 1994.

[21] Z. Fan and S.R. Pennock. Broadside coupled strip inset dielectric guide and its directional coupler application. *IEEE Transactions on Microwave Theory and Techniques*, volume MTT-43:pp. 612–619, March 1995.

[22] Z. Fan and S.R. Pennock. Analysis of broadside coupled strip inset dielectric guide. In *IEEE MTT-S Digest*, volume 2, pages 839–842, 1993.

[23] Z. Fan and Y.M.M. Antar. Analysis of edge coupled strip inset dielectric guide. *IEEE Transactions on Microwave Theory and Techniques*, volume MTT-44:pp. 349–352, February 1996.

[24] Z. Fan and Y.M.M. Antar. Broadband overlaid inset dielectric guide coupler with very flat coupling. *IEEE Transactions on Microwave Theory and Techniques*, volume MTT-44:pp. 2058–2063, November 1996.

[25] S.R. Pennock, T. Rozzi, and A. DiFilippo. Inset dielectric guide mounting of a detector diode. *IEEE Microwave and Guided Wave Letters*, volume 2:pp. 168–170, May 1992.

[26] W. Zhou and T. Itoh. Analysis of trapped image guides using effective dielectric constant and surface impedances. *IEEE Transactions on Microwave Theory and Techniques*, volume MTT-30:pp. 2163–2166, December 1982.

[27] C.A. Balanis. *Antenna Theory, Analysis and Design.* Harper and Row, New York, 1982.

[28] T. Rozzi and P.D. Sewell. The continuous spectrum of open waveguides of nonseparable cross section. *IEEE Transactions on Microwave Theory and Techniques*, volume MTT-40:pp. 1283–1291, November 1992.

[29] P.D. Sewell and T. Rozzi. The continuous spectrum of the inset dielectric guide and its application to waveguide transitions. *IEEE Transactions on Microwave Theory and Techniques*, volume MTT-41:pp. 282–289, February 1993.

[30] Z. Ma, T. Ishikawa, and E. Yamashita. An efficient analysis approach for inset dielectric guide (IDG) structures and its variations. *IEEE Microwave and Guided Wave Letters*, volume 5:pp. 117–118, April 1995.

[31] Z. Ma, E. Yamashita, and S. Xu. Transverse scattering matrix formulation for a class of waveguide eigenvalue problems. *IEEE Transactions on Microwave Theory and Techniques*, volume MTT-41:pp. 1044–1051, June/July 1993.

[32] T. Itoh and R. Mittra. Spectral-domain approach for calculating the dispersion characteristics of microstrip lines. *IEEE Transactions on Microwave Theory and Techniques*, (Short Papers), volume MTT-21:pp. 496–499, July 1973.

[33] T. Itoh and R. Mittra. A technique for computing dispersion characteristics

of shielded microstrip lines. *IEEE Transactions on Microwave Theory and Techniques*, volume MTT-22:pp. 896–898, October 1974.

[34] T. Itoh. Analysis of microstrip resonators. *IEEE Transactions on Microwave Theory and Techniques*, volume MTT-22:pp. 946–952, November 1974.

[35] T. Itoh. Spectral domain immitance approach for dispersion characteristics of generalized printed transmission lines. *IEEE Transactions on Microwave Theory and Techniques*, volume MTT-28:pp. 733–736, July 1980.

[36] Z. Fan and Y.M.M. Antar. An extended spectral domain approach and its applications to a class of quasiplanar structures. *International Journal of Microwave and Millimetre Wave Computer Aided Engineering*, volume 7(number 6):pp. 468–482, 1997.

[37] K.S. Yee. Numerical solution of initial boundary value problems involving Maxwell's equations in isotropic media. *IEEE Transactions on Antennas and Propagation*, volume AP-14:pp. 302–307, May 1966.

[38] K.S. Kunz and R.J. Luebbers. *The Finite Difference Time Domain Method for Electromagnetics.* CRC Press, Boca Raton, Florida, 1993.

[39] A. Taflove and M.E. Brodwin. Numerical solution of steady-state electromagnetic scattering problems using the time-dependent Maxwell's equations. *IEEE Transactions on Microwave Theory and Techniques*, volume MTT-23:pp. 623–630, August 1975.

[40] G. Mur. Absorbing boundary conditions for the finite-difference approximation of the time-domain electromagnetic-field equations. *IEEE Transactions on Electromagnetic Compatibility*, volume EMC-23:pp. 377–382, November 1981.

[41] P.Y. Zhao, J. Litva, and K.L Wu. A new stable and very dispersive boundary condition for the FD-TD method. In *IEEE MTT-S Digest*, volume 1, pages 35–38, 1994.

[42] J.P. Berenger. A perfectly matched layer for the absorption of electromagnetic waves. *Journal of Computational Physics*, volume 114:pp. 185–200, 1994.

[43] D.L. Paul, N.M. Pothecary, and C.J. Railton. Calculation of the dispersive characteristics of open dielectric structures by the finite-difference time-domain method. *IEEE Transactions on Microwave Theory and Techniques*, volume MTT-42:pp. 1207–1212, July 1994.

[44] C. Wu, K.L. Wu, Z.Q. Bi, and J. Litva. Accurate characterization of planar printed antennas using finite-difference time-domain method. *IEEE Transactions on Antennas and Propagation*, volume AP-40:pp. 526–534, May 1992.

[45] R.J. Luebbers and J. Beggs. FDTD calculation of wide-band antenna gain and efficiency. *IEEE Transactions on Antennas and Propagation*, volume AP-40:pp. 1403–1407, November 1992.

[46] P.A. Tirkas and C.A. Balanis. Finite-difference time-domain method for antenna radiation. *IEEE Transactions on Antennas and Propagation*, volume AP-40:pp. 334–340, March 1992.

[47] V. Stoiljković, S.R. Pennock, and P.R. Shepherd. FDTD modelling of IDG structures. In *Proceedings of the 25th European Microwave Conference*, pages 751–754, 1995.

[48] V. Stoiljković, S.R. Pennock, and P.R. Shepherd. Finite-difference time-domain analysis of inset dielectric guide and its application to waveguide transitions. *IEE Proceedings Part H*, volume 144:pp. 477–481, December 1997.

[49] F.J. Tischer. The H-guide, a waveguide for microwaves. *IRE National Convention Record*, Part 5:pp. 44–47, 1956.

[50] F.J. Tischer. The properties of H-guide at microwave and millimetre-wave regions. *Proceedings of the IEE*, volume 106, Part B, Supplement No. 13:pp. 47–53, 1959.

[51] C.H. Walter. *Traveling Wave Antennas.* McGraw-Hill, New York, 1965.

[52] C. Di Nallo, F. Frezza, A. Galli, P. Lampariello, and A.A. Oliner. Properties of NRD-guide and H-guide higher-order modes: physical and nonphysical ranges. *IEEE Transactions on Microwave Theory and Techniques*, volume MTT-42:pp. 2429–2434, December 1994.

[53] V. Stoiljković, S.R. Pennock, and P.R. Shepherd. Wideband flared IDG slot millimetre wave antenna. In *Proceedings of the 26th European Microwave Conference*, volume 2, pages 790–793, 1996.

[54] P.J. Gibson. The Vivaldi aerial. In *Proceedings of the 9th European Microwave Conference*, pages 101–105, 1979.

[55] S.N. Prasad and S. Mahapatra. A new MIC slot-line aerial. *IEEE Transactions on Antennas and Propagation*, volume AP-31:pp. 525–527, May 1983.

[56] K.S. Yngvesson, D.H. Schaubert, T.L. Korzeniowski, E.L. Kollberg, T. Thungren, and J.F. Johansson. Endfire tapered slot antennas on dielectric substrates. *IEEE Transactions on Antennas and Propagation*, volume AP-33:pp. 1392–1400, December 1985.

[57] K.F. Lee and W. Chen, editors. *Advances in Microstrip and Printed Antennas.* John Wiley and Sons, New York, 1997.

[58] K.S. Yngvesson, T.L. Korzeniowski, Y.S. Kim, E.L. Kollberg, and J.F. Johansson. The tapered slot antenna - a new integrated element for millimeter-wave applications. *IEEE Transactions on Microwave Theory and Techniques*, volume MTT-37:pp. 365–374, February 1989.

[59] P.R. Acharya, H. Ekström, S.S. Gearhart, S. Jacobsson, J.F. Johansson, E.L. Kollberg, and G.M. Rebeiz. Tapered slotline antennas at 802GHz. *IEEE Transactions on Microwave Theory and Techniques*, volume MTT-41:pp. 1715–1719, October 1993.

[60] S. Sugawara, Y. Maita, K. Adachi, K. Mori, and K. Mizuno. A mm-wave tapered slot antenna with improved radiation pattern. In *IEEE MTT-S Digest*, pages 959–962, 1997.

[61] J.B. Knorr. Slot-line transitions. *IEEE Transactions on Microwave Theory and Techniques*, volume MTT-22:pp. 548–554, May 1974.

[62] R.N. Simons, R.Q. Lee, and T.D. Perl. New techniques for exciting linearly tapered slot antennas with coplanar waveguide. *Electronics Letters*, volume 28(7):pp. 620–621, March 1992.

[63] E. Gazit. Improved design of the Vivaldi antenna. *IEE Proceedings Part H*, volume 135(2):pp. 89–93, April 1988.

[64] J.D.S. Langley, P.S. Hall, and P. Newham. Balanced antipodal Vivaldi antenna for wide bandwidth phased arrays. *IEE Proceedings - Microwaves, Antennas and Propagation*, volume 143(2):pp. 97–102, April 1996.

[65] N. Fourikis, N. Lioutas, and N.V. Shuley. Parametric study of the co- and crosspolarisation characteristics of tapered planar and antipodal slotline antennas. *IEE Proceedings Part H*, volume 140(1):pp. 17–22, February 1993.

[66] E. Thiele and A. Taflove. FD-TD analysis of Vivaldi flared horn antennas and arrays. *IEEE Transactions on Antennas and Propagation*, volume AP-42:pp. 633–641, May 1994.

[67] R. Janaswamy and D.H. Schaubert. Analysis of the tapered slot antenna. *IEEE Transactions on Antennas and Propagation*, volume AP-35:pp. 1058–1065, September 1987.

[68] R. Janaswamy. An accurate moment method model for the tapered slot antenna. *IEEE Transactions on Antennas and Propagation*, volume AP-37:pp. 1523–1528, December 1989.

[69] F. Ndagijimana, P. Saguet, and M. Bouthinon. Tapered slot antenna analysis with 3-D TLM method. *Electronics Letters*, volume 26(7):pp. 468–470, March 1990.

[70] P.J.B. Clarricoats and K.R. Slinn. Numerical solution of waveguide-discontinuity problems. *Proceedings of the IEE*, volume 114:pp. 878–886, July 1967.

[71] N. Marcuvitz. *Waveguide Handbook.* McGraw-Hill Book Company, New York, 1951.

[72] R.E. Collin. *Field Theory of Guided Waves.* McGraw-Hill, New York, 1st edition, 1960.

[73] P.H. Masterman and P.J.B. Clarricoats. Computer field-matching solution of waveguide transverse discontinuities. *Proceedings of the IEE*, volume 118:pp. 51–63, January 1971.

[74] P.J.B. Clarricoats and K.R. Slinn. Numerical method for the solution of waveguide-discontinuity problems. *Electronics Letters*, volume 2(6):pp. 226–228, June 1966.

[75] D. Marcuse. Mode conversion caused by surface imperfections of a dielectric slab waveguide. *Bell System Technical Journal*, pages pp. 3187–3215, December 1969.

[76] P.J.B. Clarricoats and A.B. Sharpe. Modal matching applied to a discontinuity in a planar surface waveguide. *Electronics Letters*, volume 8(2):pp. 28–29, January 1972.

[77] G.A. Hockham and A.B. Sharpe. Dielectric-waveguide discontinuities. *Electronics Letters*, volume 8(9):pp. 230–231, May 1972.

[78] V.V. Shevchenko. *Continuous Transitions in Open Waveguides.* Golem Press, Boulder, Colorado, 1971.

[79] S.F. Mahmoud and J.C. Beal. Scattering of surface waves at a dielectric discontinuity on a planar waveguide. *IEEE Transactions on Microwave Theory and Techniques*, volume MTT-23:pp. 193–198, February 1975.

[80] T.E. Rozzi. Rigorous analysis of the step discontinuity in a planar dielectric waveguide. *IEEE Transactions on Microwave Theory and Techniques*, volume MTT-26:pp. 738–746, October 1978.

[81] T.E. Rozzi. Network analysis of strongly coupled transverse apertures in waveguide. *International Journal of Circuit Theory and Applications*, volume 1:pp. 161–178, 1973.

[82] T.E. Rozzi. The variational treatment of thick interacting inductive irises. *IEEE Transactions on Microwave Theory and Techniques*, volume MTT-21:pp. 82–88, February 1973.

[83] T.E. Rozzi and G.H. in't Veld. Field and network analysis of interacting step discontinuities in planar dielectric waveguides. *IEEE Transactions on Microwave Theory and Techniques*, volume MTT-27:pp. 303–309, April 1979.

[84] G.H. Brooke and M.M.Z. Kharadly. Step discontinuities on dielectric waveguides. *Electronics Letters*, volume 12(18):pp. 473–475, September 1976.

[85] G.H. Brooke and M.M.Z. Kharadly. Scattering by abrupt discontinuities on planar dielectric waveguides. *IEEE Transactions on Microwave Theory and Techniques*, volume MTT-30:pp. 760–770, May 1982.

[86] T.J. Chen and H.C. Chang. Radiation from dielectric waveguide step discontinuities - a bounded approach. *Microwave and Optical Technology Letters*, volume 5(4):pp. 188–191, April 1992.

[87] G. Reiter. Generalized telegraphist's equation for waveguides of varying cross-section. *Proceedings of the IEE*, volume 106, Part B, Supplement No. 13:pp. 54–57, September 1959.

[88] W.A. Huting and K.J. Webb. Comparision of mode-matching and differential equation techniques in the analysis of waveguide transitions. *IEEE Transactions on Microwave Theory and Techniques*, volume MTT-39:pp. 280–286, February 1991.

[89] A.W. Snyder. Coupling of modes on a tapered dielectric cylinder. *IEEE Transactions on Microwave Theory and Techniques*, volume MTT-18:pp. 383–392, July 1970.

[90] D. Marcuse. *Theory of Dielectric Optical Waveguides.* Academic Press Inc., San Diego, 2nd edition, 1991.

[91] H. Flügel. Taper analysis of the 150GHz KfK-gyrotron including the electron beam. *International Journal of Electronics*, volume 64(1):pp. 95–106, 1988.

[92] B.Z. Katsenelenbaum. On the theory of irregular acoustic waveguides. *Soviet Physics - Acoustics*, volume 7(2):pp. 159–164, October-December 1961.

[93] B.Z. Katsenelenbaum. *The Theory of Irregular Waveguides with Slowly Varying Parameters.* Moscow, 1961.

[94] B.Z. Katsenelenbaum, L.M. del Rio, M. Pereyaslavets, M.S. Ayza, and M. Thumm. *Theory of Nonuniform Waveguides: the Cross-Section Method.* The Institution of Electrical Engineers, London, 1998.

[95] T. Rozzi, D. Cerri, F. Chiaraluce, R. De Leo, and R.F. Ormondroyd. Finite curvature and corrugations in dielectric ridge waveguides. *IEEE Transactions on Microwave Theory and Techniques*, volume MTT-36:pp. 68–79, January 1988.

[96] T. Rozzi and M. Mongiardo. *Open Electromagnetic Waveguides.* The Institution of Electrical Engineers, London, 1997.

[97] S.S. Saad, J.B. Davies, and O.J. Davies. Computer analysis of gradually tapered waveguide with arbitrary cross section. *IEEE Transactions on Microwave Theory and Techniques*, volume MTT-25:pp. 437–440, May 1977.

[98] D. Mirshekar-Syahkal and J.B. Davies. Accurate analysis of tapered planar transmission lines for microwave integrated circuits. *IEEE Transactions on Microwave Theory and Techniques*, volume MTT-29:pp. 123–128, February 1981.

[99] H. Flügel and E. Kühn. Computer-aided analysis and design of circular waveguide tapers. *IEEE Transactions on Microwave Theory and Techniques*, volume MTT-36:pp. 332–336, February 1988.

[100] W.A. Huting and K.J. Webb. Numerical solution of the continuous waveguide problem. *IEEE Transactions on Microwave Theory and Techniques*, volume MTT-37:pp. 1802–1808, November 1989.

[101] J. Shafii and R.J. Vernon. Mode coupling in coaxial waveguides with varying-radius center and outer conductors. *IEEE Transactions on Microwave Theory and Techniques*, volume MTT-43:pp. 582–591, March 1995.

[102] N. Izzat. *Space domain analysis of inhomogeneous waveguides of the microstrip and inset guide families.* PhD thesis, University of Bath, 1991.

[103] I.S. Gradshteyn and I.M. Ryshik. *Table of Integrals, Series and Products.* Academic Press, New York, 1965.

[104] A. Taflove. *Computational Electrodynamics: The Finite-Difference Time-Domain Method.* Artech House, Norwood, 1995.

[105] T.G. Jurgens, A. Taflove, K. Umashankar, and T.G. Moore. Finite-difference time-domain modeling of curved surfaces. *IEEE Transactions on Antennas and Propagation*, volume AP-40:pp. 357–366, April 1992.

[106] A. Taflove, K.R. Umashankar, B. Beker, F. Harfoush, and K.S. Yee. Detailed FD-TD analysis of electromagnetic fields penetrating narrow slots and lapped joints in thick conducting screens. *IEEE Transactions on Antennas and Propagation*, volume AP-36:pp. 247–257, February 1988.

[107] D.B. Shorthouse and C.J. Railton. The incorporation of static field solutions into the finite difference time domain algorithm. *IEEE Transactions on Microwave Theory and Techniques*, volume MTT-40:pp. 986–994, May 1992.

[108] D.H. Choi and W.J.R. Hoefer. A graded mesh FD-TD algoritm for eigenvalue problems. In *Proceedings of the 17th European Microwave Conference*, pages 413–417, 1987.

[109] I.S. Kim and W.J.R. Hoefer. A local mesh refinement algorithm for the time domain-finite difference method using Maxwell's curl equations. *IEEE Transactions on Microwave Theory and Techniques*, volume MTT-38:pp. 812–815, June 1990.

[110] D.H. Choi and J.R. Hoefer. The finite-difference time-domain method and its application to eigenvalue problems. *IEEE Transactions on Microwave Theory and Techniques*, volume MTT-34:pp. 1464–1470, December 1986.

[111] X. Zhang and K.K. Mei. Time-domain finite difference approach to the calculation of the frequency-dependent characteristics of microstrip discontinuities. *IEEE Transactions on Microwave Theory and Techniques*, volume MTT-36:pp. 1775–1787, December 1988.

[112] C.J. Railton and J.P. McGeehan. An analysis of microstrip with rectangular and trapezoidal conductor cross sections. *IEEE Transactions on Microwave Theory and Techniques*, volume MTT-38:pp. 1017–1022, August 1990.

[113] B. Engquist and A. Majda. Absorbing boundary conditions for the numerical simulation of waves. *Mathematics of Computation*, volume 31(number 139):pp. 629–651, July 1977.

[114] J. Mao. Twofold Mur's first order ABC in the FDTD method. *IEEE Transactions on Microwave Theory and Techniques*, volume MTT-46:pp. 299–301, March 1998.

[115] Z. Bi, K. Wu, C. Wu, and J. Litva. A dispersive boundary condition for microstrip component analysis using the FD-TD method. *IEEE Transactions on Microwave Theory and Techniques*, volume MTT-40:pp. 774–777, April 1992.

[116] G. Mur. The modeling of singularities in the finite-difference approximation of the time-domain electromagnetic-field equations. *IEEE Transactions on Microwave Theory and Techniques*, volume MTT-29:pp. 1073–1077, October 1981.

[117] K. Beilenhoff and W. Heinrich. Treatment of field singularities in the finite-difference approximation. In *IEEE MTT-S Digest*, pages 979–982, 1993.

[118] N. Huynh and W. Heinrich. Efficient finite-difference description of 3D edge singularities for coplanar MMICs including metalization thickness. In *Proceedings of the 29th European Microwave Conference*, Oct. 1999.

[119] J. Meixner. The behaviour of electromagnetic fields at edges. *IEEE Transactions on Antennas and Propagation*, volume AP-20:pp. 442–446, July 1972.

[120] R.A. Hurd. The edge condition in electromagnetics. *IEEE Transactions on Antennas and Propagation*, volume AP-24:pp. 70–73, January 1976.

[121] G.H. Brooke and M.M.Z. Kharadly. Field behaviour near anisotropic and multidielectric edges. *IEEE Transactions on Antennas and Propagation*, volume AP-25:pp. 571–575, July 1977.

[122] J.B. Andersen. Field behavior near a dielectric wedge. *IEEE Transactions on Antennas and Propagation*, volume AP-26:pp. 598–602, July 1978.

[123] R.E. Collin. *Field Theory of Guided Waves.* IEEE Press, New York, 2nd edition, 1991.

[124] J Van Bladel. Field singularities at metal-dielectric wedges. *IEEE Transactions on Antennas and Propagation*, volume AP-33:pp. 450–455, April 1985.

[125] S. Ramo, J.R. Whinnery, and T. Van Duzer. *Fields and Waves in Communication Electronics.* John Wiley and Sons, New York, 2nd edition, 1984.

[126] A. Reverchon and M. Duchamp. *Mathematical Software Tools in C++.* Wiley, Chichester, 1993. Translated from the French, by Fally, V. and Schaer, S.

[127] S.A. Schelkunoff. Some equivalence theorems of electromagnetics and their application to radiation problems. *Bell System Technical Journal*, volume 15:pp. 92–112, 1936.

[128] R.F. Harrington. *Time Harmonic Electromagnetic Fields.* McGraw-Hill Book Company, New York, 1961.

[129] R.E. Collin. *Antennas and Radiowave Propagation.* McGraw-Hill, New York, 1985.

[130] K. Umashankar and A. Taflove. A novel method to analyse electromagnetic scattering of complex objects. *IEEE Transactions on Electromagnetic Compatability*, volume EMC-24:pp. 397–405, November 1982.

[131] A. Taflove and K. Umashankar. Radar cross section of general three-dimensional scatterers. *IEEE Transactions on Electromagnetic Compatability*, volume EMC-25:pp. 433–440, November 1983.

[132] K.S. Yee, D. Ingham, and K. Shlager. Time-domain extrapolation to the far field based on FDTD calculations. *IEEE Transactions on Antennas and Propagation*, volume AP-39:pp. 410–413, March 1991.

[133] R.J. Luebbers, K.S. Kunz, M. Schneider, and F. Hunsberger. A finite-difference time-domain near zone to far zone transformation. *IEEE Transactions on Antennas and Propagation*, volume AP-39:pp. 429–433, April 1991.

[134] W.H. Press, B.P. Flannery, S.A. Teukolsky, and W.T. Vetterling. *Numerical Recipes in C.* Cambridge University Press, Cambridge, 1988.

[135] S. Pennock, C.M.D. Rycroft, P.R. Shepherd, and T. Rozzi. Transition characterisation for de-embedding purposes. In *Proceedings of the 17th European Microwave Conference*, pages 355–360, 1987.

[136] S.B. Cohn. Design of simple broad-band wave-guide-to-coaxial-line junctions. *Proceedings of the I.R.E.*, volume 35:pp. 920–926, September 1947.

[137] W.W. Mumford. The optimum piston position for wide-band coaxial-to-waveguide transducers. *Proceedings of the I.R.E.*, pages 256–261, February 1953.